DOCTORAT MATIERE BRETAGNE MOLECULES LOIRE ET MATERIAUX

UNIVERSITÉ DE NANTES

THESE DE DOCTORAT DE

L'UNIVERSITE DE NANTES

ECOLE DOCTORALE N° 596
Matière, Molécules, Matériaux
Spécialité : « *(Sciences des Matériaux)* »

Par
Julio César ESPINOSA-ANGELES

Multicationic tungsten-based oxides as electrode materials for fast energy storage devices

Thèse présentée et soutenue à Nantes, le 08 Décembre 2021
Unité de recherche : Institut des Matériaux Jean Rouxel (IMN), UMR 6502

Rapporteurs avant soutenance :

Laurence CROGUENNEC	Directrice de Recherche, CNRS – ICMCB, UMR 5026 Université de Bordeaux
Frédéric FAVIER	Directeur de Recherche, CNRS – ICGM, UMR 5253 Université de Montpellier

Composition du Jury :

Président :	Patrice SIMON	Professeur, CIRIMAT, UMR 5085 Université Paul Sabatier
Examinateurs :	Francesca SOAVI	Associate Professor, Department of Chemistry University of Bologna
	Christel LABERTY-ROBERT	Professeur, LCMCP, UMR 7574 Sorbonne Université
Dir. de thèse :	Thierry BROUSSE	Professeur, IMN, UMR 5026 Université de Nantes
Co-dir. de thèse :	Olivier CROSNIER	Maître de conférences, IMN, UMR 5026 Université de Nantes
Co-dir. de thèse :	Eric QUAREZ	Chargé de Recherche, IMN, UMR 5026 CNRS
Invité(s)		
	Laurent CARIO	Directeur de Recherche, IMN, UMR 5026 CNRS

Multicationic tungsten-based oxides as electrode materials for fast energy storage devices

By Julio César ESPINOSA-ANGELES

THESE DE DOCTORAT DE L'UNIVERSITE DE NANTES
ECOLE DOCTORALE N 596
Matière, Molécules, Matériaux

Thèse présentée et soutenue à Nantes, le 08 Décembre 2021
Unité de recherche : Institut des Matériaux Jean Rouxel (IMN),
UMR 6502

Acknowledgments

First of all, I would like to immensely acknowledge my supervisors for all the support, advice, and guidance they gave me throughout these more than three years, ever since I came to do my last semester of master to the lab. To Thierry and Olivier, they always had some time for me to answer and discuss my experiments. More than a few times it was me who had to almost haunt their time to discuss and answer my questions, but they always were accessible and nice with me to explain to me and discuss.

Thanks to Olivier, I still remember his enthusiasm for me to come and do my internship with them in their lab. He did not tell me much about work but about how Nantes was a great city to live in and to have some fun. And how the lab was really great and with so many collaborations. Finally, he convinced me, and thanks to him I'm here now, after more than three years, I'm a complete and full doctor. Thank you Olivier for all the good moments, all the funny and wonderful stories, they always made me laugh and sure you knew how to tell them. Thanks for all the support and all the help you provided me, it was really significant for me, and even though you had a million things to do you always took some time for me.

Thanks to Eric who always was there to discuss my XRD results and all the crystallographic work I was doing. He always took his time and as the expert on the matter that he is, he shared with me what he knew and helped me to actually understand how my materials were formed and where the atoms were located. All the work he does taking into account until the last tiny detail to improve the refinement is really impressive and I admire that of him.

Thanks to Mr. Prof. Thierry Brousse. I couldn't be happier and grateful to be one of his alumni. He is just an exceptional scientist and a wonderful human being. He has a strong and well-defined character and he always tells you what is in his mind, but don't be afraid, he is indeed a very nice and friendly man. Thank you Thierry for all the memorable discussions and all the good moments we spent, along with Olivier, simply I couldn't have asked for a better supervision team.

I would like to thank the reporters and all the members of my jury. Laurence Croguennec and Fred Favier, for taking their time to read and comment carefully on my manuscript. I appreciated all the comments and the interesting discussion we had during the defense. I would like to thank Prof. Francesca Soavi and Dr. Christ

el Laberty-Robert for taking their time to attend, physically and online to my defense. And of course, I couldn't be more happier and grateful to Prof. Patrice Simon, my ex-professor during and one of the co-coordinators of my master. Thank you professor for the hard work and the very interesting pieces of advice. I would like to give a big acknowledgment to Laurent Cario who was a member of my CSI (Individual Ph.D. Committee) who actually recognize my work and the struggles I had during the sanitary crisis being all by myself. It was a very nice gesture of him and I will keep his words with me.

I would like to greatly acknowledge the University of Nantes (Université de Nantes) for the funding dedicated to this project. Moreover, I deeply acknowledge IMN (Institut des Matériaux Jean Rouxel de Nantes) for selecting this Ph.D. topic and providing financial support, as well as for the warm welcoming, especially to the IMN direction, under Florent Boucher management, and the leader of the ST2E team, Olivier Joubert.

My sincere acknowledgment to all the scientists from the IMN and other institutions that were involved in this project. Thanks to Dr. Moulay Tahar Sougrati from ICGM in Montpellier, for all his expertise in mössbauer spectroscopy. A huge thank you to Dr. Antonela Iadecola, for all her help, patient, and understanding regarding all the data analysis that she helped me with. Thanks a lot, Anto for all your knowledge regarding the XAS, having the chance to perform experiments with synchrotron radiation was just magnificent and a really amazing experience for me. From the IMN, thanks to Spetphane Grolleau in charge of the TGA and BET experiments. To Nicolas Gautier for the great TEM pictures of my materials. And to Christophe Payen who actually gave the very first idea to study the Fe-W-O system for possible supercap applications. Moreover, he performed the magnetic measurements which were included in the manuscript. From IMN (Chantrerie-site) thanks to Fanch who is a very nice guy and an excellent engineer that actually can design and fabricate almost everything. Thanks to Marion who gave me really useful tips while using the SEM and she was always very supportive while manipulating both SEM and XRD equipment.

I couldn't be happier and grateful to all the supercaps team from La Chantrerie. Camille, Etienne, Thibaud, Nicolas, Laurence, and David too. Camille was always there for me while looking for a beaker that was just in front of me until helping to look for some random French administration service that I had to do to not get kicked out of the country (LOL). Thanks to David for the great music recommendations and the terrific radio emissions about Depeche Mode.

My sincere appreciation to Thibaud (a.k.a Tibidubidu) with whom we began this adventure together and who always stood all my craziness and silly dances in his office. He's is a very kind and sweet guy, He can never lose his temper and admire him a lot. In a similar way, my huge acknowledgment goes to Etienne (a.k.a mon chaton and le weonito) I never spent a day without cracking my laugh with this guy and of course without shouting at each other and saying the most random jokes in French. Thanks for the whole time you were there for me and all the help you provided me. You are now one of the most important people in my life.

Continuing with La Chantrerie team from the metallurgist guys (les metalos) I have to mention Madeleine, Mathieu, Dinesh, Aman, Franck, Laurent, and the new guys Juliette, Huge, and Louise. Moreover, the old guys that were there when I was still an intern, Jeremy, Anne-Lise, and Quentin. I had a great time at the lab and all of you made special in your own and significant way.

From the Lombarderie site, I would like to thank all the ST2E members, especially all the Ph.D. students with whom I created nice bonding and with whom I spent the nicest time. Among these guys special recognition to Khryslyn and Sacris, my best philippine friends, and former MESC students too. They helped me a lot in my transition master-Ph.D and as foreigners in a strange country, we could really relate to each other. Thanks to Angy and Lucas, without them I couldn't have survived what all that we have been through. Angy, you are just the kindest, sweetest, and funniest Italian that I have ever met. And Lucas (a.k.a le lulu), my best bud in whole France. We did the internship together and ever since we got along pretty well, now been almost four years that we know each other. Lulu, you are one of the few people I have created this special bond and with you, I have spent a few of the craziest experiences of my life, I wouldn't regret it for one second, thank you for that. Thanks, Angy and Lulu for the best memories here in France. Furthermore, another special one that came into my life the last year was Joël (a.k.a. Joelita or now Dr. Jay). Even though we started hanging out only over the last few months I feel like I know you for a long time. You're incredible and I appreciate every moment we spent talking and talking. You're really the best Dr. Jay!

I would like to express all my gratitude and admiration to my Mexican friends. To Adrian, Porfirio, Ana and Alexis. You guys motivated me, inspired me, and made me always look forward ahead to accomplishing what I have got so far. Thanks to you guys, I fought to come here to Europe and to stay, and now to have obtained my doctorate. In this list, I couldn't leave out Adriana, Cyn, and Chuy, my oldest friends and the ones I can tell literally everything

about. Thanks for everything we have lived together. All of you, I can consider you as part of my family now. Thanks for everything.

Last but not least to my family. All of this work is dedicated to my beautiful nephew and niece, Mate and Pau. And to my dad, Ezequiel, even though that he is no longer with us, wherever he is, he would have been proud, I know. To my mom, Lourdes, my sisters and brother-in-law, Paola, Karla, and Juan. All you gave me the strength to continue every day and despite that, we are so far away I always and I will always carry you with me. Thank you for supporting all my crazy ideas about coming to study abroad, I know it was a hard time for all of you but ever since you have been nothing but comprehensive and supportive with me. We all experienced a loss in the family and as difficult as it was we have been strong enough to keep going. I love you all very much and thank you!

Table of Contents

Résumé de Thèse

L'objectif de cette thèse concerne la synthèse d'oxydes multicationiques contenant du tungstène avec pour but leur utilisation dans des systèmes de stockage d'énergie de forte puissance, de type supercondensateur, fonctionnant avec un électrolyte aqueux. Plus précisément, ce travail concerne principalement l'oxyde Fe_2WO_6 ainsi que des bronzes de tungstène stabilisés avec des ions lithium, sodium ou potassium de formule générale A_xWO_3 (A=Li, Na, K, x~0.3). Le schéma général consiste en la synthèse de matériaux finement divisés qui sont ensuite caractérisés d'un point de vue structural et microstructural. Les poudres synthétisées sont ensuite utilisées comme matériaux d'électrodes dont le comportement et les propriétés électrochimiques sont étudiés. Le stockage des charges a également été étudié à l'aide d'analyses *in-situ* et *operando* afin de comprendre le mécanisme à l'origine de ces performances.

Les supercondensateurs sont des systèmes de stockage électrochimique de l'énergie destinés à des applications de puissance. Les systèmes commerciaux utilisent des matériaux d'électrodes à base de carbone qui développent de grandes surfaces spécifiques et stockent les charges principalement par des réactions électrostatiques à leur surface. Ils peuvent alors stocker peu d'énergie, mais peuvent la restituer très rapidement. Pour augmenter leur densité d'énergie (c'est-à-dire leur autonomie), il peut être intéressant de remplacer les matériaux carbonés par des oxydes de métaux de transition qui peuvent avoir un comportement pseudo-capacitif. Celui-ci a été démontré pour des matériaux tels que RuO_2, MnO_2 et Fe_3O_4. Le mécanisme de stockage des charges dans ces composés repose sur des réactions d'oxydoréduction rapides et réversibles qui se produisent à la surface du matériau d'électrode, à l'interface avec l'électrolyte. Ce comportement pseudo-capacitif dépend principalement de la présence de cations électrochimiquement actifs dans les matériaux d'électrode.

Les oxydes multi-cationiques, comme ceux étudiés dans cette thèse, possèdent un effet pseudo-capacitif et ont été présentés comme des alternatives aux oxydes métalliques simples. Divers matériaux ont été synthétisés en faisant intervenir des cations électroactifs tels que Mn, Fe, Co et Ni couplés à des cations dits spectateurs, situés à l'intérieur de la structure cristalline dont le seul rôle est de maintenir la stabilité des réseaux sans aucune activité électrochimique. Les exemples de cations spectateurs peuvent être Sr, Ba, Zn, La ou W. L'association des cations

appropriés (spectateurs et électroactifs, par exemple dans les composés $MnFe_2O_4$, $ZnMn_2O_2$ et $FeWO_4$) dans des structures cristallographiques distinctes (par exemple spinelle, perovskite, wolframite, columbite) peut donner lieu à des comportements pseudocapacitifs intéressants et à des performances volumétriques plus élevées que celles des carbones activés utilisés dans les dispositifs commerciaux en raison de la densité élevée de ces oxydes.

De plus, différents paramètres tels que la surface spécifique, la morphologie et l'accessibilité des sites actifs sont également importants pour l'obtention de propriétés électrochimiques intéressantes car le stockage des charges s'effectue grâce à une réaction de surface qui se produit à l'interface électrode/électrolyte.

Parmi les matériaux potentiellement intéressants, le système Fe-W-O a été étudié dans notre équipe dans la phase wolframite $FeWO_4$, montrant des performances prometteuses en tant que matériau d'électrode pour les supercondensateurs fonctionnant dans un électrolyte aqueux neutre. Dans ce composé, il a été récemment démontré que le couple redox Fe^{3+}/Fe^{2+} était responsable de ce comportement pseudo-capacitif.

Par conséquent, d'un point de vue fondamental et appliqué, nous avons décidé de poursuivre l'étude du système Fe-W-O avec le composé Fe_2WO_6. Différentes études ont rapporté les propriétés de ce composé en tant qu'électrode négative pour les batteries lithium-ion, comme photocatalyseur et comme matériau de photoélectrodes, motivant ainsi son étude en tant qu'électrode pseudocapacitive pour supercondensateur fonctionnant en milieu aqueux. De plus, contrairement à $FeWO_4$, cet oxyde ternaire ne contient que du Fe^{3+} dans sa structure cristalline, ce qui devrait avoir un impact sur ses performances électrochimiques finales.

Cependant, dans la littérature, Fe_2WO_6 n'a été synthétisé que par voie céramique, dans des conditions de synthèse à haute température (>800°C), ce qui a conduit à l'obtention de particules de grande taille, et donc à une faible surface spécifique, peu favorables aux réactions de surface nécessaires à un comportement électrochimique de type pseudo-capacitif. Nos travaux ont donc tout d'abord porté sur la recherche de méthodes de synthèse alternatives à plus basse température. Dans cette optique, l'utilisation de polyols a été privilégiée pour la synthèse de Fe_2WO_6 à basse température (~220 °C), qui permettent de limiter la croissance des particules conduisant ainsi à une plus grande surface spécifique de la poudre associée.

Ce type de synthèse est un processus à basse température impliquant un polyol liquide agissant à la fois comme un solvant pour les précurseurs dissous et comme un agent réducteur doux. Les principales caractéristiques de cette méthode sont les suivantes : 1) la possibilité

d'utiliser des alcools multivalents à haut point d'ébullition dans des milieux en phase liquide ayant une solubilité comparable à celle de l'eau pour les précurseurs métal-sel simples. 2) les propriétés réductrices et coordinatrices pour la nucléation et la croissance des particules et 3) une possibilité d'utiliser des polyols de faibles masses moléculaires comme l'éthylène glycol (EG) jusqu'à des masses élevées comme les polyéthylène glycols (PEG). La synthèse en milieu polyol offre donc la possibilité d'adapter différents paramètres, tels que les précurseurs, la température, le pH de la solution et la durée de la réaction qui contrôlent la cinétique de la précipitation, permettant ainsi l'obtention de particules de forme et de taille bien définies. Toutes ces caractéristiques en font une méthode de synthèse très attractive et relativement simple à utiliser, comme cela a déjà été montré dans la littérature où des particules d'oxydes métalliques simples ainsi que des oxydes multicationiques ont été synthétisés, ce qui motive notre principal intérêt à poursuivre l'utilisation de cette voie de synthèse. Ainsi, Fe_2WO_6 a été synthétisé pour la première fois par la méthode polyol. Les matériaux obtenus ont été comparés à ceux obtenus par voie céramique classique (à haute température).

Le diagramme de diffraction des rayons X (XRD) enregistré à température ambiante pour le matériau Fe_2WO_6 synthétisé par voie polyol a montré qu'on obtenait par cette voie de synthèse un matériau amorphe, contrairement à certains autres tungstates synthétisés par la même méthode et déjà publiés dans la littérature. Ceci a soulevé quelques questions concernant les conditions de synthèse et la pureté du matériau. Pour cette raison, nous avons décidé de réaliser une étude en diffraction des rayons X en température *in situ* en suivant l'état de cristallisation du matériau en fonction de la température entre la température ambiante et 900 °C. Une phase amorphe est encore observable lorsque la température atteint 400 °C et ce n'est qu'à partir de 600 °C que certaines raies de diffraction très larges, caractéristiques de la phase cristalline, commencent à apparaître, pour former un matériau bien cristallisé aux alentours de 800 °C. Les paramètres de maille déterminés pour ce matériau ont été affinés dans un premier temps dans le groupe d'espace *Pbcn* avec a = 4.5995(15) Å, b = 5.6043(19) Å, c = 4.9718(19) Å (25) avec une occupation aléatoire des sites cationiques par Fe et W dans un rapport 2:1, en bon accord avec la formulation Fe_2WO_6.

Contrairement au matériau synthétisé à haute température, les observations au microscope électronique à balayage (MEB) montrent que les particules obtenues par la synthèse polyol à basse température semblent être complètement différentes. Elles sont plus agglomérées entre elles, avec un nombre plus élevé de défauts à la surface et une distribution granulométrique plus importante.

Des électrodes composites ont ensuite été réalisées avec les matériaux synthétisés, en les mélangeant avec du noir de carbone (pour assurer la bonne conductivité électronique) et un liant polymère (pour maintenir la cohésion mécanique). Les tests électrochimiques en voltammétrie cyclique ont été effectués dans une solution aqueuse de $LiNO_3$ 5M. Pour tous les échantillons, aucun pic redox ne peut être observé, ce qui exclut une réponse faradique pour les matériaux d'électrode. Au lieu de cela, les voltammogrammes ont une forme rectangulaire légèrement déformée pour tous les matériaux, mais avec toutefois des différences significatives. Nous pouvons remarquer que les échantillons à basse température FWO-RT et FWO-400 (respectivement sans recuit, et après recuit à 400°C) présentent un voltammogramme en forme de "ballon de rugby", correspondant à une électrode composite très résistive, avec une capacité spécifique de 17 $F.g^{-1}$ et 15 $F.g^{-1}$, respectivement. L'échantillon FWO-800 (recuit à 800°C) présente une forme plus rectangulaire typique des oxydes pseudo-capacitifs mais avec une valeur de capacité très faible (3 $F.g^{-1}$). En revanche, l'échantillon recuit à 600°C présente une forme de voltammétrie cyclique (CV) quasi-rectangulaire avec une capacité spécifique de 23 $F.g^{-1}$ à une vitesse de cyclage de 20 $mV.s^{-1}$. Un tel comportement est très similaire à celui observé pour le matériau $FeWO_4$ cyclé dans des conditions similaires, pour lequel cette capacité avait été associée au couple redox Fe^{3+}/Fe^{2+}. De plus, ce matériau présente un très bon compromis entre sa capacité (38 $F.g^{-1}$, soit 240 $F.cm^{-3}$) et sa tenue en cyclage, avec une rétention de 85% de la capacité initiale après 10 000 cycles de charge/décharge. Aussi, nous avons souhaité étudier les changements structuraux et microstructuraux se produisant après le cyclage long (plusieurs milliers de cycles) afin d'expliquer cette perte de capacité. Les observations en microscopie électronique en transmission n'ont pas permis de montrer une dégradation du matériau d'électrode, ni aucune dissolution du matériau dans la cellule électrochimique. La spectroscopie Mössbauer utilisant une source de ^{57}Fe n'a pas non plus permis de mettre en évidence des changements notables après 10 000 cycles. Les mesures de susceptibilité magnétique tendent également à indiquer qu'il n'y a pas d'amorphisation ni de modification de l'environnement des cations de fer lors du cyclage, montrant donc la très bonne résistance du matériau aux conditions de cyclage. Cependant, une légère corrosion du collecteur de courant à l'interface avec l'électrode a été observée, ce qui pourrait être dû à la présence d'oxygène dissous dans l'électrolyte aqueux, expliquant ainsi la légère baisse de capacité après 10 000 cycles.

La structure cristalline des matériaux Fe_2WO_6 obtenus par ces différents modes de synthèse a également été étudiée de manière approfondie. Pour la première fois, la structure de

la poudre de Fe_2WO_6, préparée par deux méthodes de synthèse différentes et recuite à 900 ou 950°C a été résolue, et a montré que les phases obtenues présentaient une structure modulée de façon incommensurable. Cette étude cristallographique a permis de mettre en évidence la relation entre les méthodes de synthèse utilisées, conduisant à une forte influence sur le vecteur de modulation incommensurable q et, par extension, sur la taille des domaines ordonnés. Elle a également permis de mieux comprendre la structure cristalline des composés polycristallins de type A_2BO_6, ce qui peut être bénéfique pour les recherches futures visant à déterminer la relation structure-propriété de composés analogues.

Le matériau Fe_2WO_6 représente donc une nouvelle approche d'oxyde multicationique présentant des performances pseudo-capacitives très prometteuses en termes de densité, de capacité volumétrique et de tenue en cyclage. De plus, ce matériau peut être intéressant pour l'assemblage d'un condensateur électrochimique asymétrique complet, avec un électrolyte aqueux neutre, associant Fe_2WO_6 comme matériau d'électrode négative et, par exemple, MnO_2 comme électrode positive.

Tous ces résultats ont apporté une nouvelle contribution sur le mécanisme régissant la stabilité des oxydes multicationiques lors des cycles électrochimiques. L'ajustement de différents paramètres tels que la cristallinité, la microstructure ou la surface spécifique du matériau d'électrode pourrait permettre d'optimiser les propriétés électrochimiques des matériaux de type oxydes utilisés dans les supercondensateurs fonctionnant en milieu aqueux.

Suite à ces travaux, une étude sur les bronzes de tungstène hexagonaux (HTBs, hexagonal tungsten bronzes) avec la formule générale A_xWO_3 ($0 < x < 0.33$, et A=Li, Na ou K) a été menée. Elle a concerné particulièrement la compréhension du rôle du cation A à l'intérieur du réseau, impactant à la fois la structure cristalline et les propriétés électrochimiques finales. Le nom de bronze provient de la synthèse rapportée pour la première fois en 1824 lorsque Wöhler fit passer un flux d'hydrogène sec sur du tungstate de sodium tout en le chauffant. Il a observé la croissance de cristaux jaunes présentant un aspect métallique. C'est ainsi qu'il a baptisé ces matériaux "bronzes" en raison de leur brillance caractéristique.

L'étude des bronzes de tungstène s'est poursuivie avec Magnéli dans les années 1950, qui s'est attaché à relier la composition de ces phases à leur structure cristalline. A cette époque, des articles de Hägg avaient été publiés sur différents bronzes de tungstène alcalins avec différentes symétries, où les compositions irrégulières pour Na_xWO_3 dépendaient de la quantité de sodium dans la structure. Ces études ont conduit à la célèbre publication de Magnéli dans le journal *Nature* en 1952, où il a décrit pour la première fois des structures en anneaux à six

membres avec l'association d'octaèdres WO_6 pour les bronzes de tungstène. La formulation générale était M_xWO_3, avec M=K, Rb ou Cs, et une teneur approximative de x = ~0,3. Dans notre étude, trois bronzes de tungstène ont été synthétisés avec M=Li, Na, K, par voie hydrothermale. Les conditions expérimentales ont été ajustées pour obtenir des produits de grande pureté. Comme nous l'avons déjà mentionné, la structure des bronzes de tungstène hexagonaux est formée d'un cadre rigide de tungstène-oxygène constitué de couches contenant des octaèdres WO_6 qui partagent des sommets, disposés en anneaux à six chaînons. Les couches sont empilées dans la direction [00l], ce qui donne lieu à des tunnels unidimensionnels. La synthèse de ces bronzes de tungstène hexagonaux en présence de métaux alcalins conduit à la formation de composés qui présentent des différences structurales. Celles-ci sont par exemple un agencement différent des atomes occupant les tunnels, la présence ou l'absence de molécules d'eau et la formation d'octaèdres de tungstène réguliers ou déformés.

Les différentes analyses ont conduit aux formules chimiques suivantes pour les trois types de composés synthétisés : $Li_{0.167}WO_{3.333}$ (ou $Li_{0.167}WO_{3.083}(H_2O)_{0.25}$), $Na_{0.278}WO_{3.139}(H_2O)_{0.083}$ et $K_{0.33}WO_3$. Contrairement aux composés à base de Li et Na, le paramètre *c* est doublé pour la phase au potassium, et les atomes de K sont situés dans la cavité hexagonale et désordonnés le long de l'axe *c*. Les octaèdres WO_6 sont légèrement plus déformés que ceux des HTB de Li et Na, avec des distances W-O allant de 1,84(7) à 2,03(7) Å. La morphologie des différents matériaux se présente sous la forme de nanocylindres.

Les matériaux ont ensuite été testés électrochimiquement. Toutes les expériences ont été réalisées en voltammétrie cyclique (CV) dans la fenêtre de potentiel [-0.6 V; 0 V] *vs*. Ag/AgCl. Un électrolyte aqueux de $LiNO_3$ 5M a tout d'abord été utilisé avec le composé au lithium comme matériau actif d'électrode. La forme du CV correspond clairement à un comportement de type faradique. Lorsque le balayage se déplace vers un potentiel plus négatif, un pic faradique lors de la réduction est observé à -0.432 V *vs* Ag/AgCl. Puis, lors de l'oxydation, un pic à -0.322 V *vs* Ag/AgCl apparaît. De plus, une forme quasi-rectangulaire est observée lorsque le balayage se déplace vers les potentiels positifs. Les réactions électrochimiques peuvent être résumées par la réaction suivante:

$$Li_{0.167}WO_{3.333} + 0.175\,Li^+ + 0.175\,e^- \leftrightarrow Li_{0.342}WO_{3.333}$$

De plus, la sphère de solvatation du Li^+ peut être une autre caractéristique importante à prendre en compte. Il s'agit de savoir si les cations Li^+ sont complètement désolvatés ou s'ils sont accompagnés de molécules d'eau au moment de l'intercalation. Les bronzes au sodium

montrent le même comportement avec des capacités assez similaires, laissant penser à un comportement pseudocapacitif (stockages des charges en surface) couplé à de l'intercalation dans la structure des matériaux. On peut noter que ce n'est pas le cas pour le bronze de tungstène au potassium qui montre uniquement un caractère capacitif qui peut donc être attribué au stockage de charges dans la double couche électrochimique.

Les rayons ioniques effectifs pour les différents cations alcalins (Li^+, Na^+ et K^+) sont respectivement de 0,76 Å, 1,02 Å et 1,38 Å. Le lithium étant le plus petit, il peut avoir un accès plus facile dans les phases HTBs, comme le montrent les réponses faradiques observées. Après le lithium, on trouve les phases au sodium, avec un comportement électrochimique similaire mais avec une réponse plus faible. Et enfin les phases au potassium, qui ne montrent aucune activité d'intercalation dans les matériaux.

Une étude plus poussée sur l'influence de la concentration en électrolyte a également été menée. Le LiTFSI (Lithium bis (trifluorométhanesulfonyl) imide) avec une très forte concentration de 21 m (moles de soluté par kilogramme de solvant) a été utilisé en plus des différentes concentrations d'électrolytes aqueux : du $LiNO_3$ 1 M (LNO 1M), du $LiNO_3$ 5 M (LNO 5M) et du $LiNO_3$ 10 M (LNO 10M). On peut alors observer une grande différence entre le LNO 1M et le LNO 5M, avec une différence d'environ ~75 moles de H_2O par mole de Li^+ entre les deux. Avec une concentration supérieure à 5M, la différence est moins importante, respectivement ~11 et ~ 7 moles de H_2O par mole de Li^+ pour LNO 10M et LiTFSI 21 m. Pour les matériaux testés dans ces différents électrolytes, le potentiel de demi-onde a été tracé en fonction du ratio de moles de H_2O par moles de Li^+. Cette étude confirme que l'eau entourant les cations Li^+ (c'est-à-dire la sphère de solvatation) joue un rôle important lorsque le Li^+ est intercalé dans les phases HTBs contenant du lithium et du sodium. Lorsque moins de molécules d'eau sont disponibles pour le Li^+, il y a moins d'eau pour former les sphères d'hydratation respectives (~6 et ~14, pour la première et la seconde sphère). Ainsi, une diminution de l'énergie de solvatation rendra plus facile la désolvatation du Li^+ à intercaler dans les bronzes de tungstène hexagonaux. Ceci n'avait jamais été montré auparavant pour ce type de matériau en électrolyte aqueux.

Comme établi précédemment, Li^+ est un élément important du mécanisme de stockage de charge pour les bronzes de tungstène hexagonaux, lorsque ceux-ci sont utilisés comme matériaux d'électrode pour le stockage d'énergie fonctionnant dans des électrolytes aqueux. Il a été démontré que la concentration et le rapport entre les molécules de Li^+ et de H_2O facilitent (ou non) le processus d'intercalation. Afin d'évaluer ce rôle important du Li^+ et du contre-ion

dans les performances électrochimiques, des expériences utilisant du nitrate de sodium et du nitrate de potassium avec la même concentration que le $LiNO_3$ (5 M) ont été réalisées. Dans le cas des HTBs à base de Li et de Na, le mécanisme d'intercalation est facilement mis en évidence. Quand la concentration en $LiNO_3$ atteint une valeur de 1,2 M, jusqu'à atteindre une concentration de 5 M, la forme du CV commence à changer, pour former un comportement de type faradique. D'autre part, la forme classique quasi-rectangulaire pour la phase HTB au potassium est observée, même avec un électrolyte KNO_3 de concentration 2,5 M sans ions Li^+. Les résultats montrent également des valeurs de capacité très proches pour tous les électrolytes testés, y compris pour la concentration maximale de Li^+. Cela ne fait que confirmer le fait qu'aucune réponse faradique n'a lieu dans la phase HTB K et que les contributions du mécanisme de stockage de charge sont définitivement des comportements capacitifs et pseudo-capacitifs.

Les conclusions sur cette étude sont les suivants :

- il existe une relation claire entre la structure des HTBs et leurs performances électrochimiques. Les phases à base de Li et Na présentent des caractéristiques structurales similaires ainsi que des signatures électrochimiques très semblables. En revanche, le K HTB présente un comportement complètement différent ;

- pour les HTBs de Li et de Na, on observe une insertion de Li^+ dans la structure, mise en évidence par la présence des pics redox, alors que pour le HTB de K, le mécanisme de stockage de charge est un mélange de contributions pseudo-capacitives et capacitives ;

- le rôle important du ratio H_2O/Li^+ a été mis en évidence lorsque les HTBs Li et Na ont été testés dans différentes concentrations de $LiNO_3$, en comparaison avec l'électrolyte de type « water in salt ».

Ce travail de thèse mérite des études plus poussées dans la compréhension des mécanismes de stockage des charges notamment en milieu aqueux. Autant les comportements électrochimiques ont été clairement établis en milieu organique avec un électrolyte à base de lithium, consistant en une intercalation lente des ions lithium dans les structures Li et Na HTB, autant la rapidité de cette intercalation des cations accompagnés de molécules d'eau n'est pas évidente à décrire. La spectroscopie XAS *operando* réalisée sur certains matériaux a cependant permis d'apporter des réponses sur l'implication des cations W^{6+} qui sont réduits lors de la charge de l'électrode en milieu $LiNO_3$.

Ces développements feront l'objet d'études plus poussées avec des électrodes déposées sur des substrats adaptés et permettant l'utilisation de diverses techniques spectroscopiques comme le Raman.

Pour conclure, les différents matériaux étudiés dans cette thèse, comme Fe_2WO_6 et les bronzes de tungstène, ont montré qu'ils représentaient une catégorie de matériaux adaptés comme électrodes pour les dispositifs de stockage d'énergie de forte puissance. Les mécanismes de stockage de charge sont originaux et mettent en œuvre l'intercalation d'ions lithium partiellement désolvatés. Ce travail, à l'interface entre la chimie du solide et l'électrochimie, offre de nombreuses perspectives vers des matériaux permettant l'intercalation rapide d'ions alcalins pour le stockage de l'énergie.

General Introduction

The global consumption of energy increases day by day. The modernization of the society and the fast economic development of different regions causes a high demand for energy that needs to be satisfied, and energy production has to increase. Currently, fossil fuels (oil, coal, natural gas) represent more than 80% of global energy production. However, these resources are limited and non-renewable, and their exploitation generates significant greenhouse gas emissions responsible for an environmental crisis that only worsens.

In this way, the world's effort has switched to developing greener and safer energy sources. The interest in renewable energies has rapidly increased. Technologies like solar and wind power take advantage, and a complete energetic transition is achieved. However, this is accompanied by many issues. Most renewable energies (solar, wind, hydraulic, tidal, etc.) are notably only available intermittently (depending on the sunshine, the wind, etc.). Thus, they need to be stored to be returned on demand. Consequently, the development of energy storage systems is essential to address these issues, whether for stationary applications (integration into "smart grids" electricity distribution networks, etc.) or mobile (electric and hybrid vehicles, portable electronic devices, etc.). Among these systems, electrochemical energy storage devices (in which electrical energy is stored in its chemical form) occupy an important place.

Generally, electrochemical energy storage systems are classified and compared according to three main criteria: their energy density, *i.e.*, the amount of energy they can store per unit of mass or volume (expressed in $Wh.kg^{-1}$ or $Wh.L^{-1}$), their power density ($W.kg^{-1}$ or $W.L^{-1}$), corresponding to how fast these systems can restore the accumulated energy; and their lifespan, often assimilated to the number of charge/discharge cycles that they can withstand without significant loss of performance. In other words, high energy density will allow an electric car to travel a great distance on a single charge while high power density will let it go faster.

Two main electrochemical energy storage systems can be compared: batteries and electrochemical capacitors (ECs), also called supercapacitors (SCs). These devices consist of two conductive electrodes separated by a liquid electrolyte. However, they work according to different internal mechanisms, thus leading to various properties. Batteries store charges at the bulk of the electrodes through redox electrochemical reactions. They can store a large amount

of energy but have a lifespan limited to a few thousand cycles. Their charge/discharge cycles are restricted by the movement of ions (diffusion) within the electrode materials. Therefore, they present higher energy density but lower power density.

Electrochemical capacitors are based on different operating principles. They consist of electrodes with an extensively developed surface area and store the charges on their surface through adsorption reactions and fast redox reactions. Thus, they have intermediate performance between conventional capacitors and batteries and provide high power peaks withdrawals with moderate energy density. They are often used as complements to batteries. For example, the battery will provide autonomy in an electric vehicle, thanks to its high energy density. On the other hand, the high power density and excellent lifespan of the ECs will be instead used to provide or absorb the repeated peaks of power necessary for starting, climbing a hill, or recovering energy during braking.

The vast majority of ECs on the market today are the so-called Electric Double Layer Capacitors (EDLCs) and have two activated carbon electrodes with a very highly developed surface area, spaced by a porous separator soaked in the electrolyte (generally a salt dissolved in an organic solvent). The ions in the electrolyte are stored electrostatically at the surface of the electrodes. The good electronic conductivity, porosity distribution, and excellent thermal and electrochemical stability of activated carbons make them materials of choice for ECs. Nevertheless, their low density (~0.7 $g.cm^{-3}$) due to their very high porosity, combined with a low surface capacity limited to the capacity of electrochemical double-layer (<20 $\mu F.cm^{-2}$, compared to their specific surface) weaken them for hoping to achieve high volumetric energy densities.

Contrary to the standard activated carbons aforementioned, oxides and multicationic oxides present a pseudocapacitive mechanism due to the fast and reversible surface redox reactions to store energy and can thus reach capacities much higher than those of carbons in aqueous electrolytes. Moreover, due to the high density of oxides, they can achieve higher volumetric performances without being detrimental to their lifespan.

This thesis will study materials based on tungsten oxides (Fe_2WO_6 and the hexagonal bronzes of WO_3) as possible electrode materials for fast energy storage systems. The focus will be to understand the charge storage mechanism transitioning from a pseudocapacitive behavior material towards a more battery-like material at high rates.

The first chapter of this manuscript will present state of the art on electrochemical energy storage systems, focusing on electrode materials used for capacitive and pseudocapacitive energy storage. Moreover, fast intercalation materials will be described, highlighting, and comparing the differences in their charge storage mechanisms.

The second chapter will focus on the work carried out on iron tungstate (Fe_2WO_6) as new pseudocapacitive material. This oxide has been studied in the literature only by high-temperature synthesis routes. In contrast, in this thesis, a low-temperature method is proposed for the first time to obtain the pure phase of the material. Several techniques will fully characterize Fe_2WO_6, and its electrochemical performance will be evaluated. Furthermore, a crystallographic study of the high-temperature form of the polycrystalline sample will be presented, addressing the structural determination using the superspace formalism.

In the third chapter, the interest on the hexagonal tungsten bronzes (HTBs) A_xWO_3 (with A= Li, Na and K and $0<x<0.33$) will be presented as a metastable phase of WO_3 with potential applications as electrode materials for fast energy storage. The hydrothermal synthesis of these phases will be discussed, emphasizing the role of the alkali cation in the structure to determine the final structural and morphological properties. The physicochemical characterization will be shown to understand the growth of the nanorod-like particles, and the crystal structure of such phases will be elucidated. Furthermore, an extensive electrochemical characterization in different aqueous electrolytes will be presented to understand the role of the alkali cations in the electrolyte and inside the structure. Afterwards, a comparison with water-in-salt and organic electrolytes will also be discussed.

The fourth chapter will go deeper into understanding the charge storage mechanism of the hexagonal tungsten bronzes. An electrochemical deconvolution of the different contributions, capacitive and diffusion-controlled, will be shown. Moreover, powerful and non-conventional techniques such as *in situ* Electrochemical Quartz Crystal Microbalance (EQCM), *in situ* X-ray diffraction (XRD), and *operando* synchrotron X-ray Absorption Spectroscopy (XAS) will be used to unveil and discuss how the cation intercalation in the lattice of the HTBs takes place.

Chapter I: Literature review

I.1. Introduction: Energy storage systems

Electrochemical energy storage (EES) systems like batteries and electrochemical capacitors (ECs) have been developed and enhanced for the past few years. Depending on the application, energy storage systems can store a high amount of energy or a high amount of power. If one of these devices is used to power a vehicle, the amount of energy stored will tell how far the vehicle can go. On the other hand, the amount of power will tell how fast the vehicle can go on a single charge, in the case of an electric vehicle. In this regard, the Ragone plots (see Figure I-1) provide information on the relationship of power versus energy density of EES[1,2]. The filled areas correspond to the performance obtained using the same charge and discharge current. In contrast, areas dashed lines refer only to discharge performance (with a recharge at a low rate). With the high demand on energy storages system capable of charging and discharging rapidly and delivering a high amount of energy and power, all the research and development efforts aim to push ECs and batteries performances towards the star highlighted in Figure I-1, where the boundaries between both EES will be overlapping.

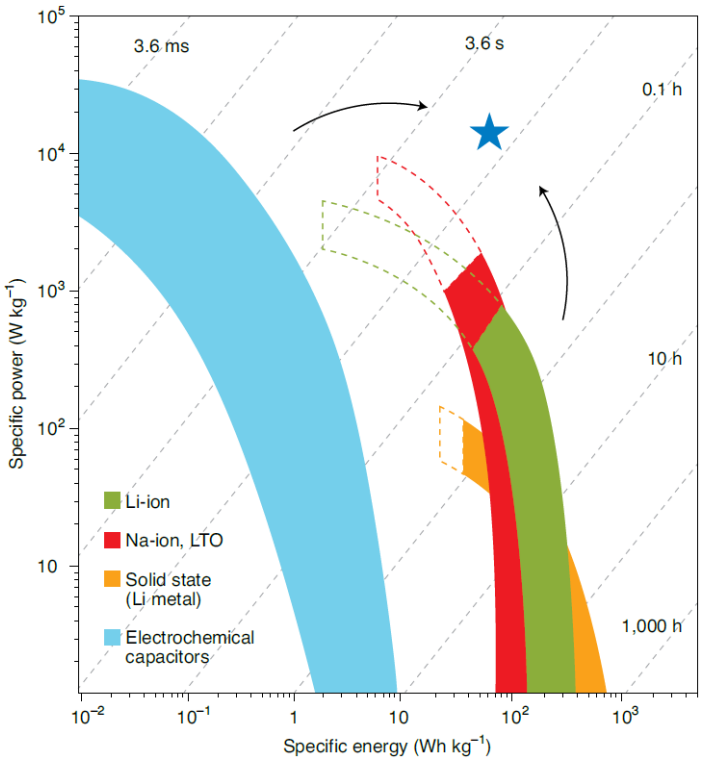

Figure I-1. *Ragone plot. Specific power versus specific energy of common electrical energy-storage devices. The plot shows the trends towards greater specific power for batteries and specific energy for electrochemical capacitors (arrows), blurring the boundaries between the two as the trends approach the star.*[1,2]

EES can be differentiated depending on their charge storage mechanism[3], either at the surface (double-layer) or in the bulk of the material (faradaic). Electric double-layer capacitors or EDLCs store charge by pure electrostatic interactions of accumulated charge at the electrode/electrolyte interface (see Figure I-2a). They must present high and accessible specific surface area electrode materials. In the case of batteries, charge storage occurs through reversible faradaic reactions throughout the bulk of the electrode materials (see Figure I-2b). Thus, the material must be designed to allow the intercalation/de- intercalation of the reacting species throughout the material. On the other hand, charge storage based on fast and reversible faradaic redox reactions at the surface or at the vicinity of the electrode active material, receives the name of pseudocapacitance (see Figure I-2c).[4–6]

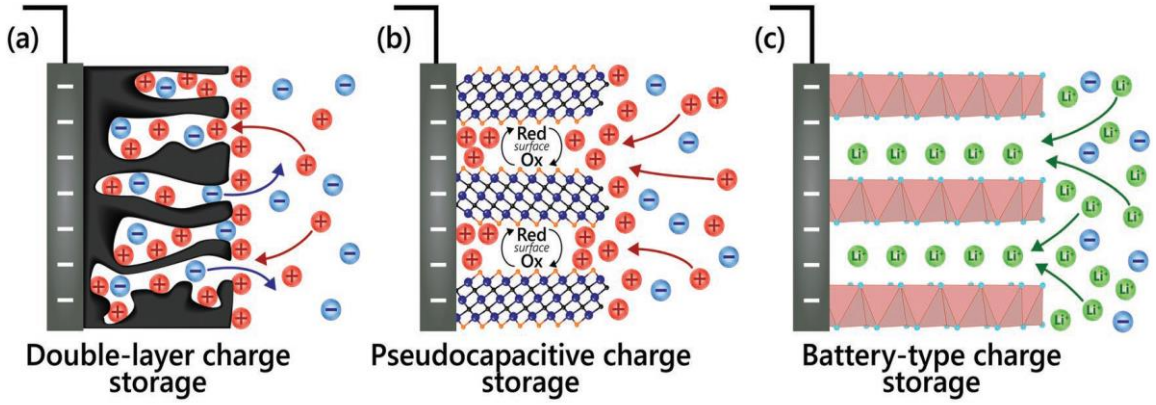

***Figure I-2**. Illustration of the electrode processes occurring at a) electrical double-layer capacitive, b) pseudocapacitive, and c) faradaic electrodes.*[5]

One way to distinguish the charge storage mechanism is to look at the electrochemical signature. EDLC charge storage will depict a rectangular cyclic voltammogram (CV) and a triangular galvanostatic charge/discharge (GCD) profile (see Figure I-3a and d). In this case, the amount of charges stored varies linearly as a function of potential. A single value of capacitance can be easily calculated and reported for capacitive energy storage systems. In the case of a pseudocapacitive behavior, the signature will be a quasi-rectangular CV where the redox peaks can be slightly appreciated and a quasi-triangular GCD profile (see Figure I-3b and e). On the other hand, well-defined peak-shaped CVs or nonlinear GCD profiles with one or more obvious potential plateaus are characteristics of faradaic, or battery-type, material (see Figure I-3c and f).[4–6]

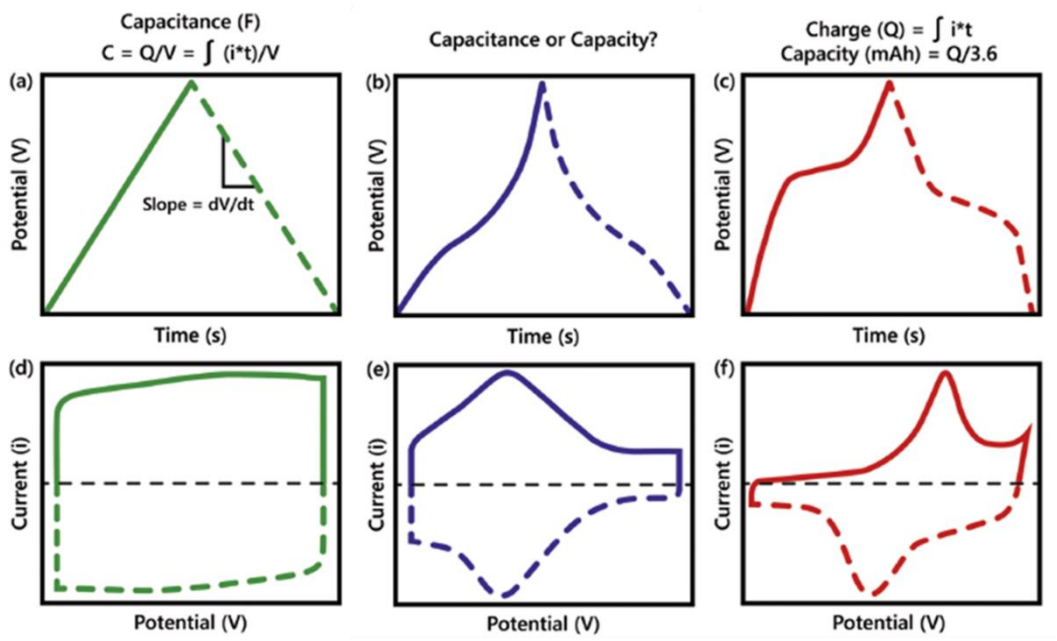

***Figure I-3**. Archetypal electrical output behavior of three main types of electrodes, including a, d) electrical double-layer, b, e) pseudocapacitive, and c, f) battery type. a)-c) Schematic of galvanostatic charge-discharge profiles showing linear and nonlinear responses with time and d)-f) corresponding CV profiles.*[4,5]

Thus, different charge storage mechanisms can be categorized as (1) capacitive non-faradaic charge storage, (2) capacitive faradaic charge storage, and (3) non-capacitive faradaic charge storage. Moreover, the correct metrics for characterization of capacitive charge storage processes is capacitance (in Farads, F, *i.e.*, C=Q/V with Q being the capacity in Coulombs, C), and that of non-capacitive faradaic processes is the specific charge capacity (m.Ah, *i.e.*, Q/3.6). Therefore, the performance of materials exhibiting a clear peak-shaped CV must be reported in terms of m.Ah, and not with capacitance units.[4–6]

In this chapter, a literature review of materials presenting a capacitive and mainly a pseudocapacitive mechanism will be presented. Moreover, in the last section, tungsten oxide (WO_3) applications in different EES will be highlighted.

I.2. Materials with capacitive behavior

I.2.1. Electric double-layer

EDLCs offer excellent power performance and cycle life and are characterized by rectangular CVs and triangular GCD profiles. The adsorption and desorption of ions originate the electric double-layer (EDL) charge storage at the electrode/electrolyte interface with no diffusion limitation.[7] There are several theories or models for this interface between a solid and a liquid. In Figure I-4, the Helmholtz model, the Gouy–Chapman model, and the Stern model are illustrated, where Ψ is the potential, Ψ_0 is the electrode potential, IHP refers to the inner Helmholtz plane, and OHP refers to the outer Helmholtz plane explained in the Stern model.[8]

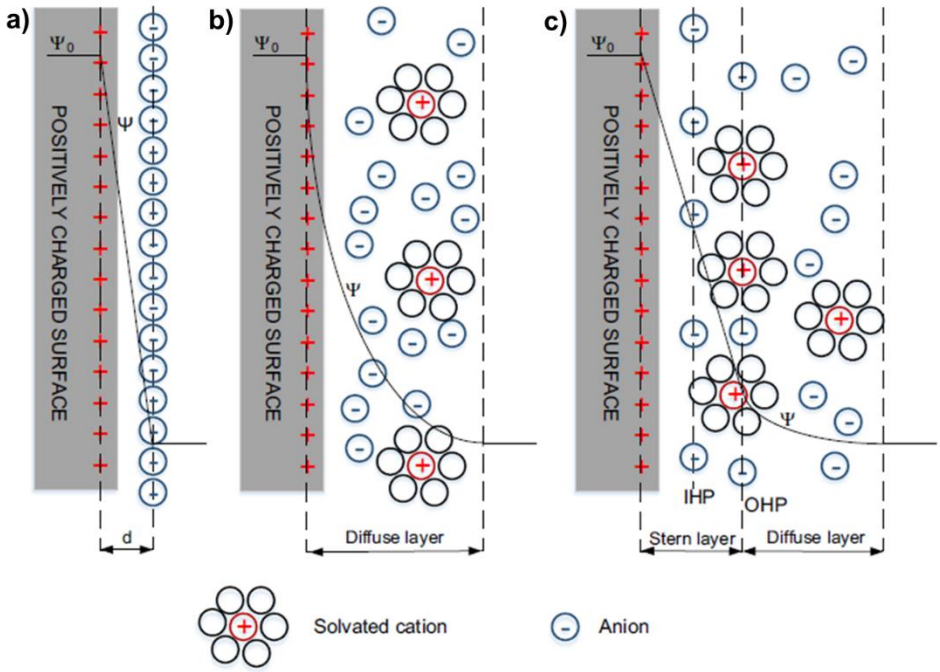

***Figure I-4**. EDL models, a) Helmholtz model, b) Gouy–Chapman model, and c) Stern model.*[8]

Helmholtz is the simplest. It describes that the electrode attracts the counter-ions under an applied potential while repelling the co-ions at a *d* distance (see Figure I-4a). Thus, two compact layers of charges form at the electrode-electrolyte interfaces, called the ‘‘electric double-layer’’. The double-layer capacitance, C_{dl}, at each electrode-electrolyte interface resembles that of a conventional parallel plate capacitor.[6,8] In contrast to the Helmholtz assumption, in the Gouy–Chapman model, the charged ions are mobile in the electrolyte solutions and are under the influence of both diffusion and electrostatic forces. Gouy suggests that the same amount of opposite ionic charge appears in a liquid surrounding a charged solid. However, the ions are not rigidly attached to the surface, and the concentration of the ions in the solution near the surface follows a Boltzmann distribution (see Figure I-4b). Although this

makes a better approach to reality, the Gouy– Chapman model fails for highly charged double-layers. The most sophisticated post-Helmholtz EDL model is the Gouy– Chapman–Stern model, which combines the Helmholtz and the Gouy–Chapman ideas.[6,8]

Based on the Gouy– Chapman–Stern model, the EDL has, in fact, a multi-layer structure, including the inner Helmholtz plane (IHP), outer Helmholtz plane (OHP), and a diffuse layer that is next to the bulk electrolyte solution. In the Stern layer, which comprises the IHP and OHP, counter-ions are unsolvated or partially solvated due to the strong interactions with the ions and the electrode surfaces and pores (see Figure I-4c).[6,8]

I.2.2. Carbon-based materials

EDLCs use activated porous carbon with pervasive specific surface area (SSA), as electrode materials. These are obtained from carbon-rich organic precursors through heat treatment (carbonization) and an activation process. The precursors can be coconut shells, wood, fossil fuels and their derivatives like pitch, coal and coke.[9,10]

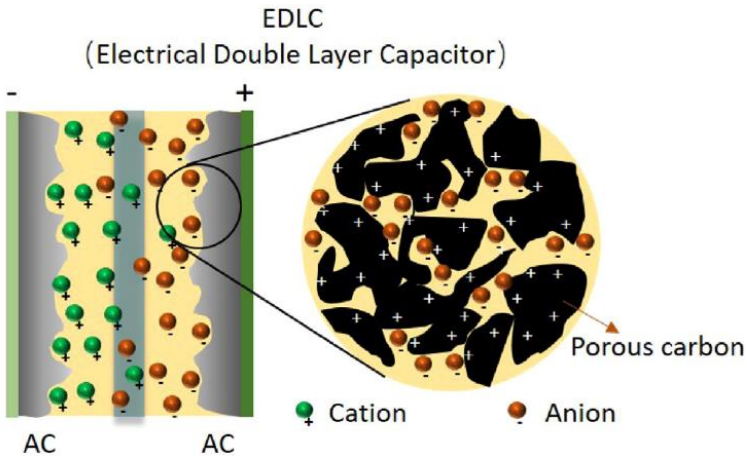

Figure I-5. *Scheme of an electrical double-layer capacitor (EDLC) with an amplification of porous activated carbon electrode interface.*[11]

The large number of ions from the electrolyte capable of being accumulated at the surface of this carbonaceous materials give rise to specific capacitance up to 100 F g^{-1} (Farads per gram) in organic electrolytes with a cell operating voltage of 2.7 V, (see Figure I-5). In aqueous electrolytes capacitance can go up to 200 F g^{-1} but with a cell voltage limitation of 0.9 V[12,11] (see Figure I-6). Moreover, many studies refer to the use of different carbon forms for

EDLCs, like carbon blacks, carbon aerogels, carbon fibers, glassy carbon, and carbon nanostructures.[13]

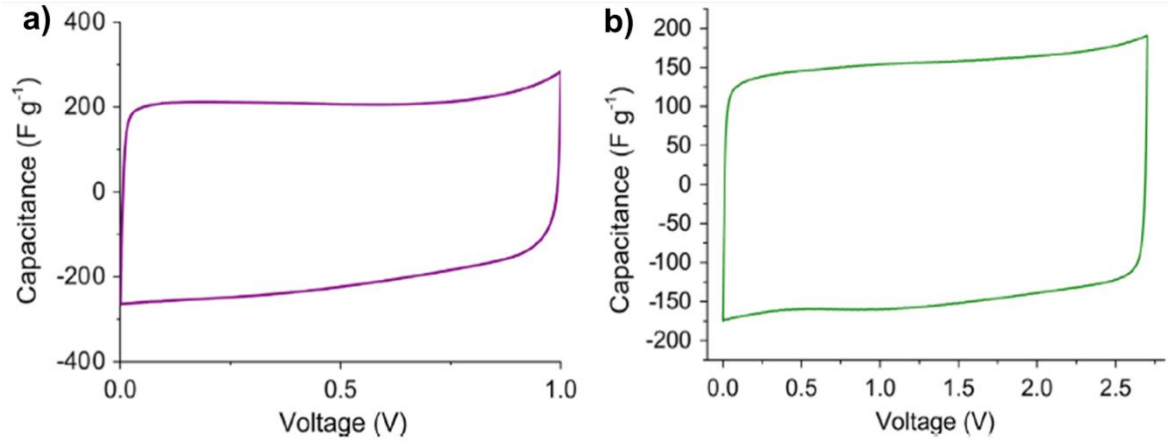

Figure I-6. *Cyclic voltammogram of an EDLC cell at 5 mV.s^{-1} in a) aqueous 6 M KOH and b) organic1M tetraethylammonium tetrafluoroborate electrolytes.*[8]

I.2.3. Key parameters of ECs

The following parameters and the way they are adjusted are critical for the better performance of electrochemical capacitors.

a) Cell voltage *V*: Maximum potential defined at the electrodes used on the SC. It depends mainly on the type of electrolyte used. Organic electrolytes provide a broader potential window up to 2.7-3 V, unlike aqueous electrolytes which thermodynamically can only reach up to 1.2 V. However, the first ones suffer a drop in conductivity that water based electrolytes can compensate.[7]

b) Capacitance: The capacitance is given in Farads (F) and it depends directly on the active materials and the electrolyte. For aqueous systems, maximum capacitance values are around 300 F g$^{-1,}$ contrary to organic systems, which can reach 150-200 F g^{-1}, for EDLCs.[7]

c) Series resistances *R*: This is the entire resistance of the SC, which sums the electrolyte resistance, electrode resistances from the materials, and the contacts. The resistance dictates the maximum power that a supercapacitor can deliver.[7]

d) Energy: The energy stored in an SC is given by Eq. I-1, where W is the energy (J), C is the capacitance (F), and V is the voltage (V). As the potential window for organic electrolytes systems is higher, they can store a more considerable amount of energy.[7]

$$W=\frac{1}{2}CV^2 \qquad \text{Eq. I-1}$$

e) Power: The power is defined by the product between voltage and current, or the energy delivered per unit of time. For supercapacitors, the parameter used is the maximum power P_{max}, it is given by Eq. I-2.[7]

$$P_{max}=\frac{V_{max}^2}{4R} \qquad \text{Eq. I-2}$$

I.3. Materials with pseudocapacitive behavior

I.3.1. Pseudocapacitance phenomenon

As aforementioned, a rectangular cyclic voltammogram and a linear time-dependent change in potential at constant current characterize the EDLCs. On the other hand, cyclic voltammograms for batteries display the corresponding reduction and oxidation peaks caused by a faradic response and the voltage plateau in a galvanostatic experiment indicating the presence of two phases[14]. In addition, Conway *et al.*[3] acknowledged different materials capable of carrying out fast and reversible redox reactions at or near their surface with a similar electrochemical signature to that of EDLCs, although with much greater charge storage[14]. This phenomenon was called "pseudocapacitance"[3] and represents another mechanism for capacitive energy storage. Conway later extended the concept of pseudocapacitance to monolayer adsorption (adsorption pseudocapacitance, Figure I-7a and d)[15], faradaic reactions of hydrous RuO_2 in H_2SO_4 (redox pseudocapacitance, Figure I-7b and e[16,17]), and solid-solution electrochemical intercalation (intercalation pseudocapacitance, Figure I-7c and f).[18] In the following subsections a few examples of materials presenting such behavior will be described.

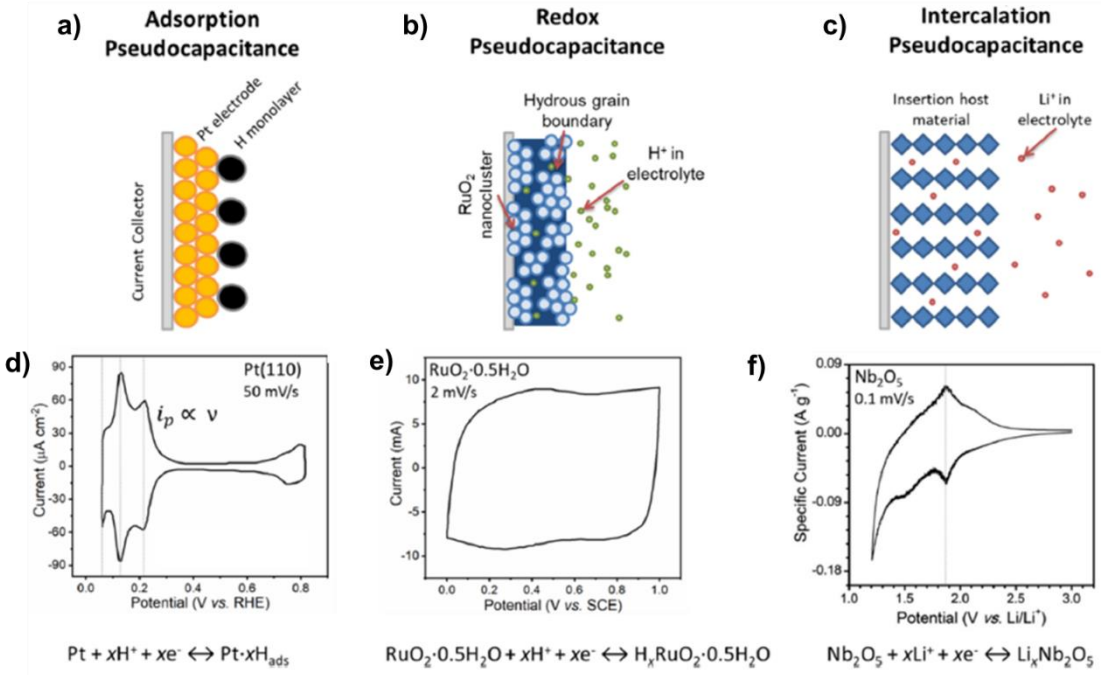

***Figure I-7**. Illustrations of the three types of pseudocapacitance (a-c) and their corresponding CV profiles and reactions (d-f): (a) adsorption pseudocapacitance, (b) redox pseudocapacitance and (c) intercalation pseudocapacitance. CV profiles of (d) a Pt (110) surface in 0.1M aqueous $HClO_4$, (e) RuO_2•$0.5H_2O$ in 0.5M aqueous H_2SO_4, and (f) T-Nb_2O_5 in a nonaqueous Li^+ electrolyte. Adapted from.*[19]

I.3.2. Metal oxides pseudocapacitive materials

Hydrous RuO_2 (RuO_2•nH_2O), iridium oxide (IrOx), and MnO_2 (typically birnessite δ-MnO_2, of the type K_xMnO_2•nH_2O) are among the most-studied materials exhibiting a pseudocapacitive mechanism and continue to serve as model materials for the fundamental understanding of such phenomenon. The surface area-normalized capacitance for hydrous RuO_2 is about 150−1200 μF.cm^{-2}, depending on the preparation method, with an almost ideally rectangular capacitive CV response for the optimum water content of 0.5•H_2O per RuO_2 (see Figure I-8).[20–22]

This capacitance is at least an order of magnitude greater than what is typically measured for carbon materials (~4−16 μF.cm^{-2})[23]. Moreover, this mechanism is described as a series of fast, reversible electron-transfer reactions that are coupled with protons H^+ adsorption at or near the electrode surface where the Ru oxidation states can change from (II) up to (IV) (Eq. I-3).

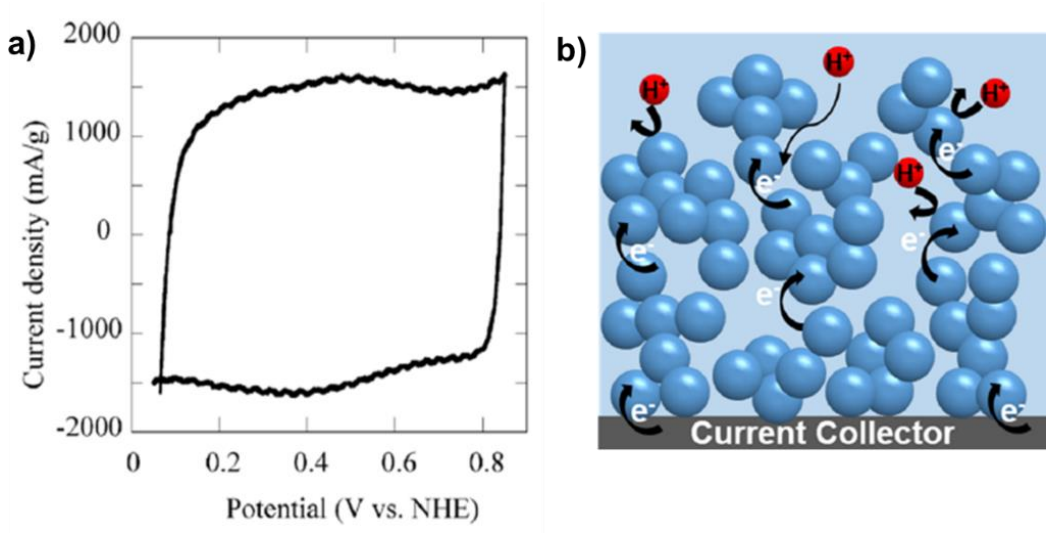

Figure I-8. *a) Representative cyclic voltammogram of RuO_2•0.58H_2O measured in an acidic electrolyte at a sweep rate of 2 mV.s^{-1}. b) Schematic of RuO_2•nH_2O, depicting clusters of rutile RuO_2 formed into loose aggregates separated by hydrous grain boundaries.*[20–22]

$$Ru^{IV}O_2 + xH^+ + xe^- \leftrightarrow Ru^{IV}{}_{1-x}Ru^{III}{}_xO_2H_x \qquad \text{Eq. I-3}$$

However, the high cost of ruthenium-based materials has limited their applications to a few high-value electronic devices. In contrast, manganese oxides present a relatively low cost, low toxicity, environmental safety, and a high theoretical capacitance of up to 1300 F.g^{-1}, making it a suitable alternative to RuO_2.[6,19]

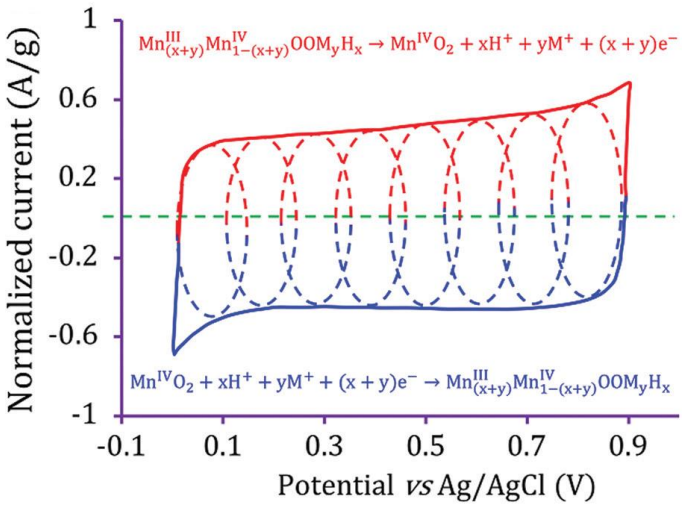

Figure I-9. *Schematic CV for a MnO_2 electrode in a mild aqueous electrolyte (0.1 M K_2SO_4) shows the successive multiple surface redox reactions leading to the pseudocapacitive charge storage mechanism.*[1,2]

The different polymorphs MnO_x (amorphous to highly crystalline) and different electrode structures (powder, composites, thin films) represent an extensive range of electrochemical performance metrics. Further studies have already disclosed an apparent mechanism where the average oxidation state alternates between 4^+ and 3^+ being compensated by cations insertion (Na^+, K^+) or protons from the aqueous electrolyte (see Eq. I-4 and Figure I-9).[24–29]

$$MnO_2 + xC^+ + yH^+ + (x+y)e^- \leftrightarrow MnOOC_xH_y \qquad \text{Eq. I-4}$$

Example materials presenting the third pseudocapacitive mechanism indicated in Figure I-7c and f will be described in the next section, highlighting the fast intercalation behavior.

I.4. Fast intercalation materials

I.4.1. TiO_2 and titanates

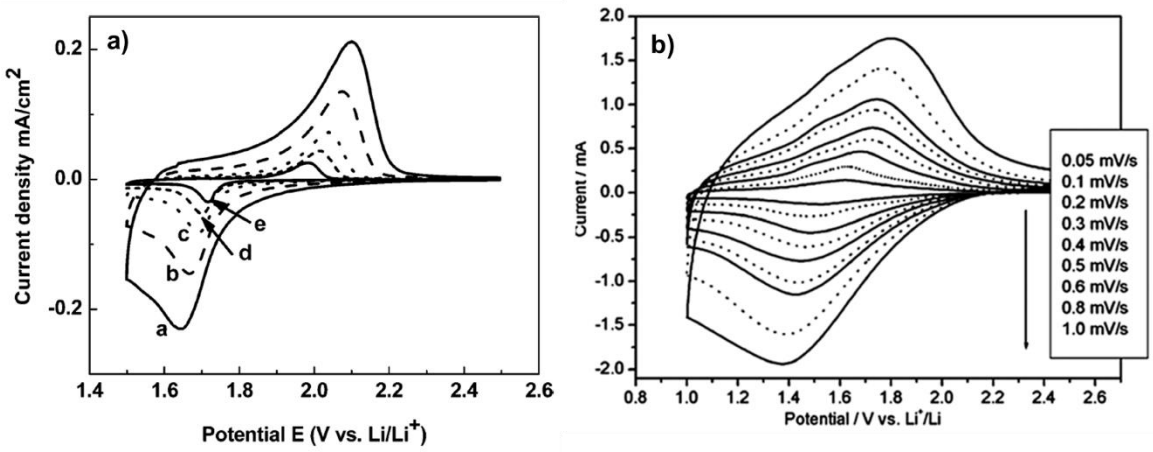

***Figure I-10**.a) CV for the 7 nm nanocrystalline TiO_2 film. The sweep rates were (from out to in) (a) 10, (b) 5, (c) 2, (d) 1, and (e) 0.5 mV/s, 1.0 M $LiClO_4$ in PC. And b) CVs of $H_2Ti_3O_7$ nanowires in a non-aqueous lithium ion electrolyte 1M $LiPF_6$ + EC/DMC (1/1, v/v).*[30,32]

TiO_2 presents a fast intercalation behavior as reported by Dunn[30] and Zukalov[31] (see Figure I-10). The charge storage in TiO_2(B) occurs *via* the intercalation of lithium ions in a non-aqueous electrolyte (see Eq. I-5). TiO_2(B) exhibits two sets of cathodic redox peaks, at 1.5 and 1.6 V *vs.* Li^+/Li, which are located at lower potentials than for lithium-ion intercalation into

anatase TiO_2, (~1.75 V). In bulk TiO_2(B), these peaks exhibit a linear dependence on the sweep rate indicative of a pseudocapacitive process. Moreover, the theoretical capacity for a full one electron redox reaction is 335 $mAh.g^{-1}$ (1206 $C.g^{-1}$).[31]

$$TiO_2(B) + xLi^+ + xe^- \leftrightarrow Li_xTiO_2(B) \qquad \text{Eq. I-5}$$

Furthermore, the layered structures of hydrogen titanates ($H_2Ti_3O_7$) have been investigated for pseudocapacitive EES. In these materials, as in other titanium oxides, charge storage occurs due to the $Ti^{+4/+3}$ redox couple, and lithium-ion intercalation occurs below 2 V *vs.* Li^+/Li. These investigations have been primarily carried out on nanostructured materials such as nanowires and nanotubes, and a reversible capacity of 597 $C.g^{-1}$ (~ 5 min charge/discharge) was obtained.[32–36]

I.4.2. T-Nb_2O_5

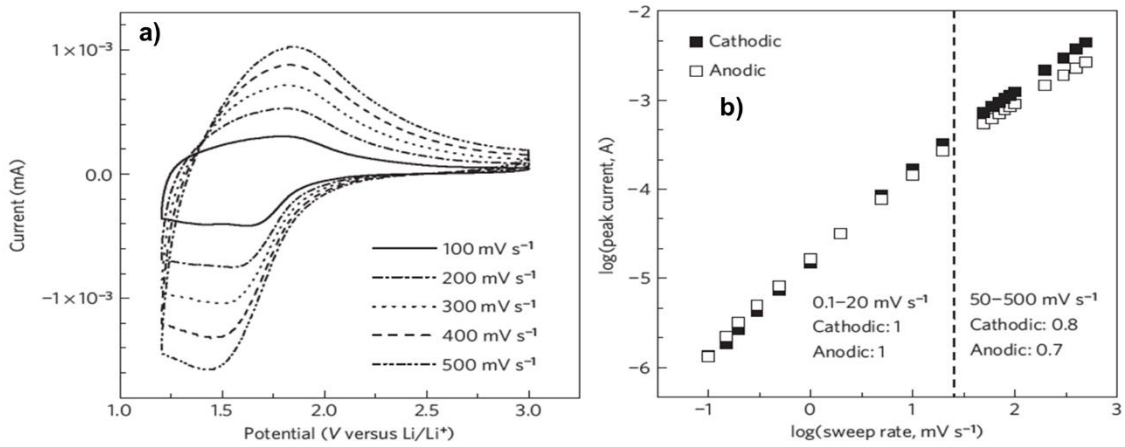

Figure I-11. *a) Cyclic voltammograms from 100 to 500 $mV.s^{-1}$ demonstrate the high-rate capability of the material. And b), b-value determination of the peak anodic and cathodic currents shows that this value is approximately 1 up to 50 $mV.s^{-1}$.*[40]

Recent reports have demonstrated the fast intercalation behavior (pseudocapacitive in nature) of orthorhombic T-Nb_2O_5. In general, the charge storage of T-Nb_2O_5 occurs due to the insertion of lithium ions in non-aqueous electrolytes at a potential of < 2 V *vs.* Li^+/Li. Based on the redox of the $Nb^{+5/+4}$ couple. The charge storage occurs up to 2 Li^+/Nb_2O_5 for a maximum capacity of 720 $C.g^{-1}$ (see Eq. I-6).[37–40] The T-Nb_2O_5 material exhibits the features representative of pseudocapacitive charge storage for sweep rates up to 50–60 $mV.s^{-1,}$ which

corresponds to 1-minute charge-discharge times. The CVs (see Figure I-11a) exhibit broad redox peaks below 2 V. The peak current scales linearly with sweep rate over a wide range of sweep rates as shown in Figure I-11b.[40]

$$Nb_2O_5 + xLi^+ + xe^- \leftrightarrow Li_xNb_2O_5 \quad \text{Eq. I-6}$$

T-Nb_2O_5 along with TiO_2 and the hydrogen titanates present a fast intercalation process for Li^+ in non-aqueous electrolytes. This behavior has been suggested as a pseudocapacitive behavior in nature; however, one must be careful when reporting the values in capacity ($C.g^{-1}$ and not capacitance for those materials exhibiting a clear faradaic signature in their CVs.[41] These high-rate materials present an exciting alternative for fast and high-power devices; nonetheless, they operate in an organic electrolyte. In the next section, tungsten oxide will be introduced as another high-rate material presenting a very similar behavior to T-Nb_2O_5 and TiO_2 but in a water-based electrolyte.

I.4.3. Tungsten Oxide - WO_3

Tungsten oxide (WO_3) is a transition metal oxide characterized for a wide range of various applications.[42] Nanostructured WO_3 is an exceptionally versatile material and offers unique characteristics. It has become one of the most investigated functional metal oxides impacting many research fields, including condensed matter physics and solid-state chemistry. WO_3 has exceptional chromic properties, and thin films made of nanostructured WO_3 have been increasingly investigated and applied to develop photochromic and electrochromic devices.[43–46] WO_3 is a versatile transition metal oxide with different polymorphs, and because of these interesting structural properties, its range of applications can be even more spread.

I.4.3.1. Structural features

The crystal structure of WO_3 is composed of corner-sharing WO_6 octahedra. There are several polymorphs of the WO_3 compound: monoclinic II (ε-WO_3), triclinic (δ-WO_3), monoclinic I (γ-WO_3), orthorhombic (β-WO_3), tetragonal (α-WO_3), and cubic WO_3. However,

cubic WO_3 is not commonly observed experimentally. The detail of the polyhedral representations of these six structures is shown in Figure I-12.[47]

The phase classification is based on the tilting angles and rotation direction of WO_6 octahedra regarding the "ideal" cubic structure (ReO_3 type). Lattice constant data for WO_3 crystal phases are presented in Table I-1. Like other metal oxides, WO_3 crystal phase transitions can take place during annealing and cooling. It has been widely reported that for WO_3, in bulk form, phase transformation occurs in the following sequence: monoclinic II (ε- WO_3, < − 43 ° C) → triclinic (δ- WO_3, − 43 °C to 17 ° C) → monoclinic I (γ - WO_3, 17 ° C to 330 ° C) → orthorhombic (β - WO_3, 330 ° C to 740 ° C) → tetragonal (α - WO_3, > 740 ° C) The above phase transitions of WO_3 has been reported to be partially reversible. Monoclinic I (γ - WO3) has been reported as the most stable phase at room temperature, with triclinic (δ-WO_3) also being observed. When annealed at high temperature, WO_3 transforms to other crystal phases (usually β-WO_3 and α-WO_3). However, WO_3 is generally unable to retain these alternate phases when it is returned to room temperature. The monoclinic II phase (ε- WO_3) is only stable at subzero temperatures and is thus rarely encountered outside the laboratory.[42]

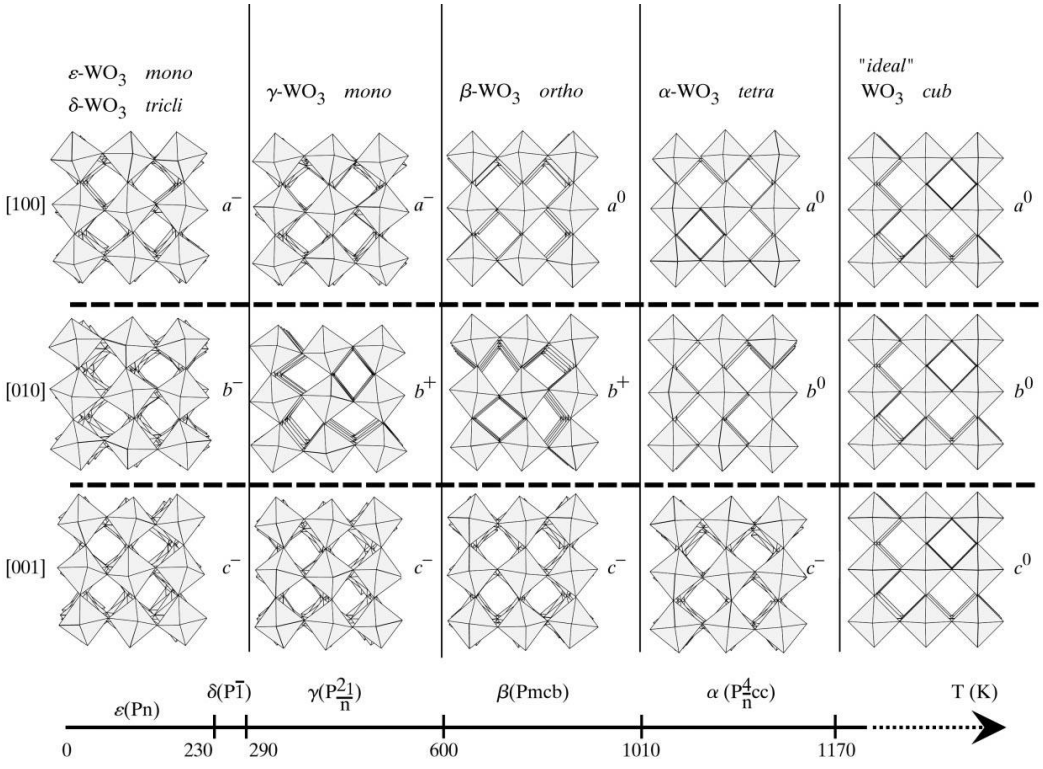

Figure I-12. *Tilt patterns and stability temperature domains of the different polymorphs of WO_3.*[47]

***Table I-1**. Lattice constant data for different WO_3 crystal phases.*

lattice constant (Å)	ε-WO_3[4]	δ-WO_3[4]	γ-WO_3[4]	β-WO_3[5]	α-O_3[5]	"ideal" cubic-WO_3[2]
a	7.378	7.309	7.306	7.384	5.25	3.84
b	7.378	7.522	7.540	7.512	N/A	N/A
c	7.664	7.686	7.692	3.846	3.91	N/A

In addition to the aforementioned crystal phases, another possible stable phase for WO_3 is the hexagonal (h-WO_3). Observation of this phase was first reported by Gerand *et al*. in 1979[48] and was originally obtained from the slow dehydration of tungstite. Figure I-13 presents a diagram of the crystal structure of h-WO_3. The crystal structure is again composed of corner-sharing WO_6 octahedra, but with the form of three and six-membered rings in the *ab*-plane. These three- and six-membered rings result in the appearance of trigonal cavities and hexagonal windows, respectively. In the *c*-axis, these octahedra stack by sharing the axial oxygen and form 4-coordinated square windows. However, this hexagonal crystal phase is metastable and reported to be transformed into a monoclinic structure when annealed at temperatures exceeding 400 °C. The lattice constants reported for h- WO_3 are a = 7.298 Å and c = 3.899 Å.[42]

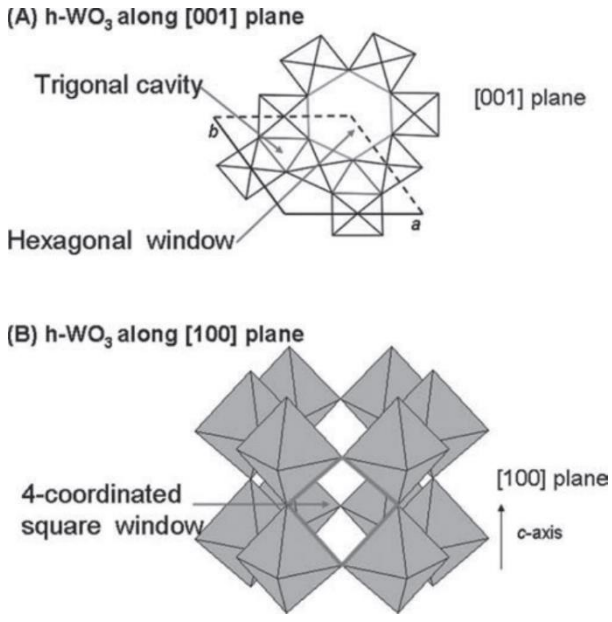

***Figure I-13.** a) The structure of h-WO_3 is shown with the c -axis perpendicular to the plane. b) The structure of h-WO_3 with the c- axis parallel to the plane.*[37]

I.4.3.2. WO_3 in energy storage

As mentioned above, tungsten oxide and related compounds show rich diversity in their structures. Among the different forms of tungsten oxide, WO_3 has been a versatile and capable electrode material for energy-storage applications, batteries, and electrochemical capacitors[49]. One of the most interesting reports is the one by Augustyn *et. al.*[50,51], where they studied the pseudocapacitive behavior of the hydrated phase of WO_3•$2H_2O$ (see Figure I-14). As a result, they found that it exhibits significantly improved capacity retention and energy efficiency for proton storage over monoclinic WO_3 at sweep rates as fast as 200 $mV.s^{-1}$. The theoretical capacity for the one-electron redox process is 360 $C.g^{-}1$. Cathodic current arises from reducing W^{6+} to W^{5+} with the concomitant intercalation of H^+ from the electrolyte (see Eq. I-7).

$$WO_3 \bullet 2H_2O + xH^+ + xe^- \leftrightarrow H_xWO_3 \bullet nH_2O \quad (0 \leq x \leq 1) \qquad \text{Eq. I-7}$$

The studies performed by Augustyn's group account to be one of the most interesting because they exhibit the fast intercalation mechanism of WO_3 in a water-based electrolyte. This will serve as an excellent reference for the study intended in this thesis.

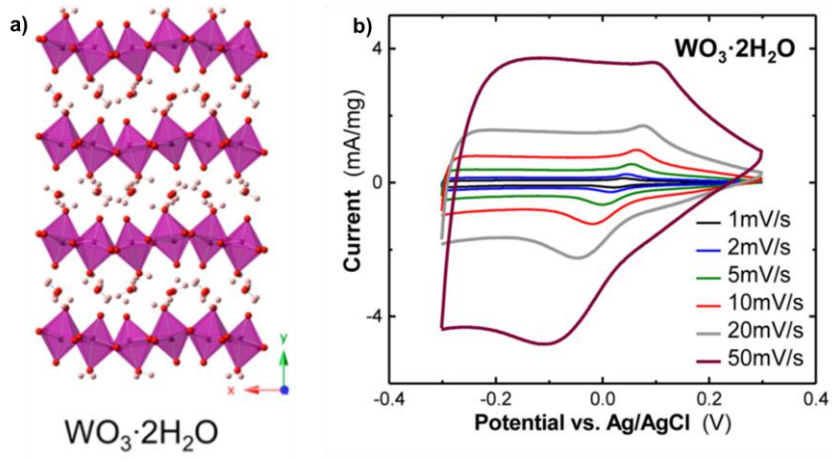

Figure I-14. *a) Crystallographic structures of monoclinic WO_3•$2H_2O$ and b) cyclic voltammograms at various sweep rates in 0.5 M H_2SO_4.*[50]

I.5. Conclusions and Objectives of the thesis

In this brief literature review the concepts and examples of pseudocapacitive and fast intercalation materials were introduced and described. Both mechanisms involve fast and reversible redox reactions occurring at the surface (or into) the electrode material. The electrochemical signature of the pseudocapacitive materials will depict most of the time a quasi-rectangular shape with slight or non-faradaic response, presenting a non-diffusion limited mechanism. Whereas, fast intercalation materials will present a defined faradaic behavior. However, the performance of the latter will be differentiated of that of a battery material because of the much faster times of operation. In addition, this material will present a diffusion-limited mechanism.

Thus, the main objective of this thesis is to study different tungsten-based oxides as electrode materials for fast energy storage systems and to unravel their charge storage mechanism, either a pseudocapacitive or a fast intercalation behavior.

The main goals are:

1) To synthesize by low-temperature Fe_2WO_6 and the Hexagonal Tungsten Bronzes. And to fully characterize the materials to understand how they will perform electrochemically in aqueous electrolytes.
2) To use different methods, physicochemical, electrochemical, *in situ* and *operando* to understand what type of charge storage predominates on each material.

I.6. References – Chapter I

1. Simon, P. & Gogotsi, Y. Materials for electrochemical capacitors. *Nat. Mater.* **7**, 845–854 (2008).
2. Simon, P. & Gogotsi, Y. Perspectives for electrochemical capacitors and related devices. *Nat. Mater.* **19**, 1151–1163 (2020).
3. Conway, B. E. *Electrochemical Supercapacitors: Scientific Fundamentals and Technological Applications*. (Springer US, 1999).
4. Gogotsi, Y. & Penner, R. M. Energy Storage in Nanomaterials – Capacitive, Pseudocapacitive, or Battery-like? *ACS Nano* **12**, 2081–2083 (2018).
5. Mathis, T. S. *et al.* Energy Storage Data Reporting in Perspective—Guidelines for Interpreting the Performance of Electrochemical Energy Storage Systems. *Adv. Energy Mater.* **9**, 1902007 (2019).
6. Noori, A., El-Kady, M. F., Rahmanifar, M. S., Kaner, R. B. & Mousavi, M. F. Towards establishing standard performance metrics for batteries, supercapacitors and beyond. *Chem. Soc. Rev.* **48**, 1272–1341 (2019).
7. Simon, P., Brousse, T. & Favier, F. *Supercapacitors Based on Carbon or Pseudocapacitive Materials*. (John Wiley & Sons, Inc., 2017).
8. González, A., Goikolea, E., Barrena, J. A. & Mysyk, R. Review on supercapacitors: Technologies and materials. *Renew. Sust. Energ. Rev.* **58**, 1189–1206 (2016).
9. Zhang, L. L. & Zhao, X. S. Carbon-based materials as supercapacitor electrodes. *Chem. Soc. Rev.* **38**, 2520–2531 (2009).
10. Wei, L. & Yushin, G. Nanostructured activated carbons from natural precursors for electrical double-layer capacitors. *Nano Energy* **1**, 552–565 (2012).
11. Lin, Z. *et al.* Materials for supercapacitors: When Li-ion battery power is not enough. *Mater. Today* **21**, 419–436 (2018).
12. Simon, P. & Burke, A. F. Nanostructured Carbons : Double-Layer Capacitance and More. *Electrochem. Soc. Interface* **17**, 38–43 (2008).
13. Wang, G., Zhang, L. & Zhang, J. A review of electrode materials for electrochemical supercapacitors. *Chem. Soc. Rev.* **41**, 797–828 (2012).
14. Simon, P., Gogotsi, Y. & Dunn, B. Where Do Batteries End and Supercapacitors Begin? *Science* **343**, 1210–1211 (2014).
15. Conway, B. E. & Angerstein-Kozlowska, H. The electrochemical study of multiple-state adsorption in monolayers. *Acc. Chem. Res.* **14**, 49–56 (1981).
16. Hadži-Jordanov, S., Angerstein-Kozlowska, H. & Conway, B. E. Surface oxidation and H deposition at ruthenium electrodes: Resolution of component processes in potential-sweep experiments. *J. Electroanal. Chem.* **60**, 359–362 (1975).

17. Hadži-Jordanov, S., Angerstein-Kozlowska, H., Vukovič, M. & Conway, B. E. Reversibility and Growth Behavior of Surface Oxide Films at Ruthenium Electrodes. *J. Electrochem. Soc.* **125**, 1471–1480 (1978).

18. Conway, B. E. Two-dimensional and quasi-two-dimensional isotherms for Li intercalation and upd processes at surfaces. *Electrochim. Acta* **38**, 1249–1258 (1993).

19. Fleischmann, S. *et al.* Pseudocapacitance: From Fundamental Understanding to High Power Energy Storage Materials. *Chem. Rev.* **120**, 6738–6782 (2020).

20. Zheng, J. P. Hydrous Ruthenium Oxide as an Electrode Material for Electrochemical Capacitors. *J. Electrochem. Soc.* **142**, 2699 (1995).

21. Long, J. W., Swider, K. E., Merzbacher, C. I. & Rolison, D. R. Voltammetric Characterization of Ruthenium Oxide-Based Aerogels and Other RuO_2 Solids: The Nature of Capacitance in Nanostructured Materials. *Langmuir* **15**, 780–785 (1999).

22. Choi, C. *et al.* Achieving high energy density and high power density with pseudocapacitive materials. *Nat Rev Mater* (2019).

23. Ji, H. *et al.* Capacitance of carbon-based electrical double-layer capacitors. *Nat Commun* **5**, 3317 (2014).

24. Kanoh, H., Tang, W., Makita, Y. & Ooi, K. Electrochemical Intercalation of Alkali-Metal Ions into Birnessite-Type Manganese Oxide in Aqueous Solution. *Langmuir* **13**, 6845–6849 (1997).

25. Lee, H. Y. & Goodenough, J. B. Supercapacitor Behavior with KCl Electrolyte. *J. Solid State Chem.* **144**, 220–223 (1999).

26. Toupin, M., Brousse, T. & Bélanger, D. Charge Storage Mechanism of MnO_2 Electrode Used in Aqueous Electrochemical Capacitor. *Chem. Mater.* **16**, 3184–3190 (2004).

27. Kuo, S.-L. & Wu, N.-L. Investigation of Pseudocapacitive Charge-Storage Reaction of MnO_2•nH_2O Supercapacitors in Aqueous Electrolytes. *J. Electrochem. Soc.* **153**, A1317 (2006).

28. Ghodbane, O., Pascal, J.-L. & Favier, F. Microstructural Effects on Charge-Storage Properties in MnO_2-Based Electrochemical Supercapacitors. *J. Power Sources* **1**, 1130–1139 (2009).

29. Wei, W., Cui, X., Chen, W. & Ivey, D. G. Manganese oxide-based materials as electrochemical supercapacitor electrodes. *Chem. Soc. Rev.* **40**, 1697–1721 (2011).

30. Wang, J., Polleux, J., Lim, J. & Dunn, B. Pseudocapacitive Contributions to Electrochemical Energy Storage in TiO_2 (Anatase) Nanoparticles. *J. Phys. Chem. C* **111**, 14925–14931 (2007).

31. Kavan, L. *et al.* Lithium Storage in Nanostructured TiO_2 Made by Hydrothermal Growth. *Chem. Mater.* **16**, 477–485 (2004).

32. Li, J., Tang, Z. & Zhang, Z. Layered Hydrogen Titanate Nanowires with Novel Lithium Intercalation Properties. *Chem. Mater.* **17**, 5848–5855 (2005).

33. Li, J., Tang, Z. & Zhang, Z. H-titanate nanotube: a novel lithium intercalation host with large capacity and high rate capability. *Electrochem. commun.* **7**, 62–67 (2005).

34. Wei, M., Wei, K., Ichihara, M. & Zhou, H. High rate performances of hydrogen titanate nanowires electrodes. *Electrochem. commun.* **10**, 1164–1167 (2008).

35. Zhu, G.-N., Wang, C.-X. & Xia, Y.-Y. Structural transformation of layered hydrogen trititanate ($H_2Ti_3O_7$) to TiO_2(B) and its electrochemical profile for lithium-ion intercalation. *Journal of Power Sources* **196**, 2848–2853 (2011).

36. Wang, Y., Hong, Z., Wei, M. & Xia, Y. Layered $H_2Ti_6O_{13}$-Nanowires: A New Promising Pseudocapacitive Material in Non-Aqueous Electrolyte. *Adv. Funct. Mater.* **22**, 5185–5193 (2012).

37. Ohzuku, T., Sawai, K. & Hirai, T. Electrochemistry of L-niobium pentoxide a lithium/non-aqueous cell. *J. Power Sources* **19**, 287–299 (1987).

38. Brezesinski, K. *et al.* Pseudocapacitive Contributions to Charge Storage in Highly Ordered Mesoporous Group V Transition Metal Oxides with Iso-Oriented Layered Nanocrystalline Domains. *J. Am. Chem. Soc.* **132**, 6982–6990 (2010).

39. Kim, J. W., Augustyn, V. & Dunn, B. The Effect of Crystallinity on the Rapid Pseudocapacitive Response of Nb_2O_5. *Adv. Energy Mater.* **2**, 141–148 (2012).

40. Augustyn, V. *et al.* High-rate electrochemical energy storage through Li+ intercalation pseudocapacitance. *Nat. Mater.* **12**, 518–522 (2013).

41. Brousse, T., Bélanger, D. & Long, J. W. To Be or Not To Be Pseudocapacitive? *J. Electrochem. Soc.* **162**, A5185–A5189 (2015).

42. Zheng, H. *et al.* Nanostructured Tungsten Oxide - Properties, Synthesis, and Applications. *Adv. Funct. Mater.* **21**, 2175–2196 (2011).

43. Granqvist, C. G. Electrochromic materials: Microstructure, electronic bands, and optical properties. *Appl. Phys. A* **57**, 3–12 (1993).

44. Gao, T. & Jelle, B. P. Visible-Light-Driven Photochromism of Hexagonal Sodium Tungsten Bronze Nanorods. *J. Phys. Chem. C* **117**, 13753–13761 (2013).

45. Gao, T. & Jelle, B. P. Electrochromism of hexagonal sodium tungsten bronze nanorods. *Sol. Energy Mater Sol. Cells.* **177**, 3–8 (2018).

46. Besnardiere, J. *et al.* Structure and electrochromism of two-dimensional octahedral molecular sieve h-WO_3. *Nat. Commun.* **10**, 327 (2019).

47. Roussel, P., Labbé, P. & Groult, D. Symmetry and twins in the monophosphate tungsten bronze series $(PO_2)_4(WO_3)_{2m}$($2 \leq m \leq 14$). *Acta Crystallographica Section B* **56**, 377–391 (2000).

48. Gerand, B., Nowogrocki, G., Guenot, J. & Figlarz, M. Structural study of a new hexagonal form of tungsten trioxide. *J. Solid State Chem.* **29**, 429–434 (1979).

49. Shinde, P. A. & Jun, S. C. Review on Recent Progress in the Development of Tungsten Oxide Based Electrodes for Electrochemical Energy Storage. *ChemSusChem* **13**, 11–38 (2020).

50. Mitchell, J. B., Lo, W. C., Genc, A., LeBeau, J. & Augustyn, V. Transition from Battery to Pseudocapacitor Behavior via Structural Water in Tungsten Oxide. *Chem. Mater.* **29**, 3928–3937 (2017).

51. Mitchell, J. B. *et al.* Confined Interlayer Water Promotes Structural Stability for High-Rate Electrochemical Proton Intercalation in Tungsten Oxide Hydrates. *ACS Energy Lett.* **4**, 2805–2812 (2019).

Chapter II: Multicationic oxides as electrode materials for electrochemical capacitors: Study of Fe_2WO_6 in mild aqueous conditions

II.1. Introduction

This chapter will present the study of iron tungsten oxide Fe_2WO_6 as a negative electrode material for electrochemical capacitors. The interest in such multicationic oxides and their advantages in terms of electrochemical performance in aqueous electrolytes will be highlighted.

The synthesis, the structural characterization, and the electrochemical performance of Fe_2WO_6 electrode material will be described and discussed in the second section.

Afterwards, in the third section, the stability of such material during long-term electrochemical cycling in 5M $LiNO_3$ aqueous electrolyte will be shown. The aim will be to shed light on this behavior using original characterization equipment.

Finally, the last section of the chapter will be dedicated to the crystallographic study of the Fe_2WO_6 synthesized at higher temperatures, solving for the first time the crystal structure using powder X-ray diffraction and the incommensurately modulated structural model.

II.2. Fe_2WO_6 as a pseudocapacitive electrode material

II.2.1. Introduction

The pseudocapacitive behavior of transition metal oxides has been demonstrated for materials such as RuO_2,[1] MnO_2,[2,3] and Fe_2O_3[4]. The charge storage mechanism in these compounds relies on fast and reversible redox reactions that occur at the vicinity of the electrode material. This pseudocapacitive behavior depends mainly on the existence of specific electroactive cations in the electrode materials.[5]

Multicationic oxides exhibiting a pseudocapacitive effect have been presented as alternatives to single metal oxides. Various oxides have been synthesized involving electroactive cations such as Mn, Fe, Co and Ni coupled to the so-called spectator cations. These are located inside the crystal structure and whose only role is to maintain the stability of the network without any electrochemical activity. Examples of spectator cations are Sr, Ba, Zn, La,

or W. The combination of appropriate cations (spectator and electroactive, *e.g.*, $MnFe_2O_4$,[6] $ZnMn_2O_2$,[7] and $FeWO_4$[8]) in distinct crystallographic structures (*e.g.*, spinel, perovskite, wolframite, columbite) can give rise to interesting pseudocapacitive behaviors and higher volumetric performances due to the high density of these oxides compared to usual activated carbon materials, 260 $F.cm^{-3}$ *vs.* 80-100 $F.cm^{-3}$, respectively.[5,8–12]

Moreover, parameters such as specific surface area, morphology, and accessibility of the active sites are also essential since the reaction remains a surface reaction that occurs at the electrode/electrolyte interface (see Figure II-1).[5]

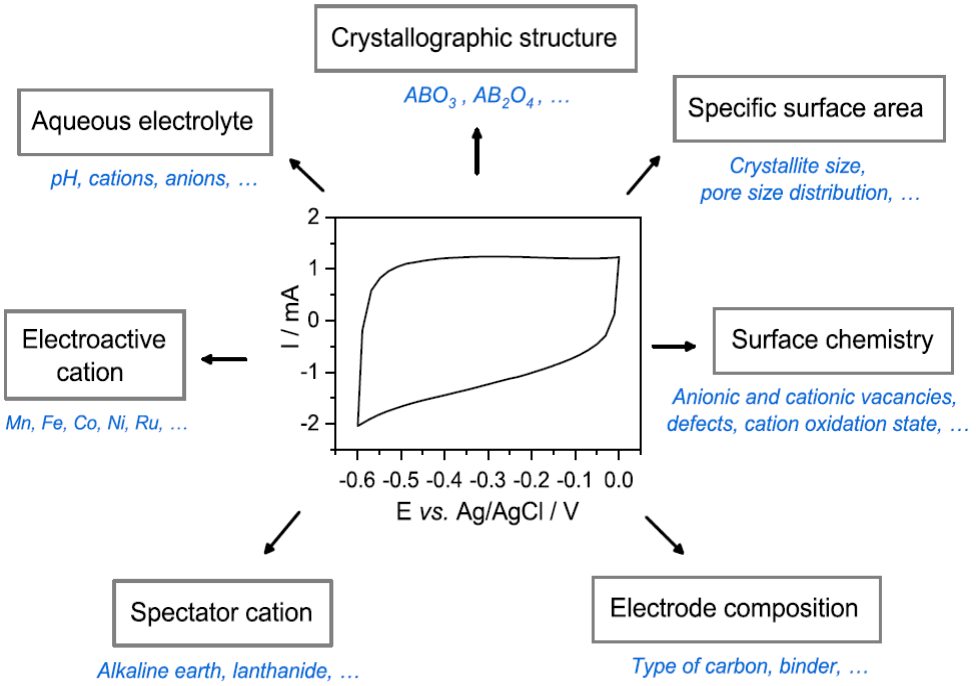

Figure II-1. *Schematic drawing of the different parameters that could possibly influence the electrochemical behavior and performance of multicationic oxides for aqueous electrochemical capacitors.*[5]

The Fe-W-O family has already been studied in our team, in particular the $FeWO_4$ wolframite phase, showing interesting performance as electrode material for electrochemical capacitors operated in a neutral aqueous electrolyte, about 35 $F.g^{-1}$ corresponding to about 260 $F.cm^{-3}$ (see Figure II-2).[8,13] The role of the Fe^{3+}/Fe^{2+} redox couple has been recently proven to be responsible of such a pseudocapacitive behavior.[14]

Therefore, from a fundamental and applied point of view, we decided to investigate the Fe-W-O system now as Fe_2WO_6. Different studies have reported the properties of such

compound as a negative electrode for lithium-ion batteries[15] photocatalyst[16] and photoelectrode,[17] motivating the use of this Fe-W-O material as a possible pseudocapacitive electrode material for aqueous electrochemical capacitors. Unlike $FeWO_4$, which depending on the synthesis conditions can present different ratios of Fe^{3+}/Fe^{2+}. Fe_2WO_6 contains only Fe^{3+} in the crystal structure, impacting the final electrochemical performance differently.

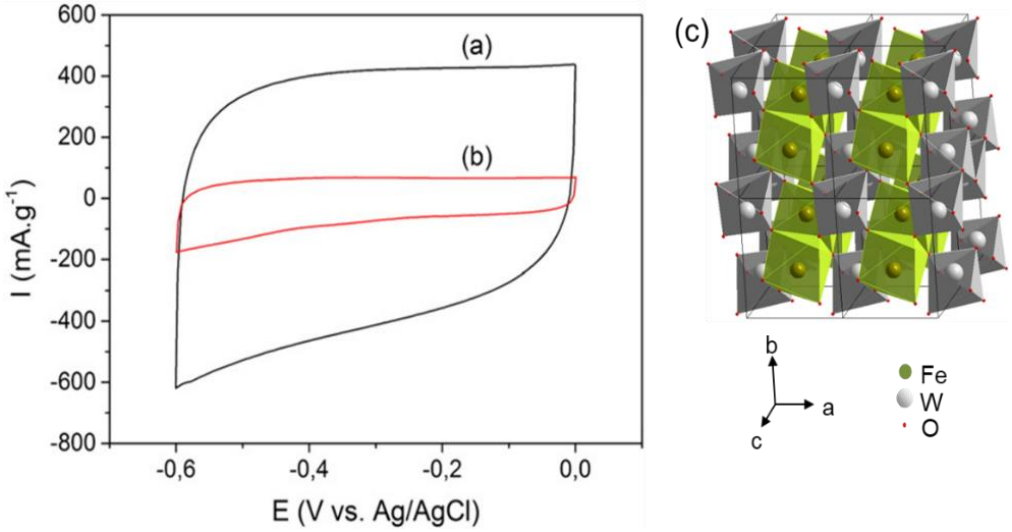

Figure II-2. *Cyclic voltammogram of $FeWO_4$ in aqueous $LiNO_3$ 5 M. (a) Polyol-mediated synthesis and (b) hydrothermal synthesis; scan rate: 10 $mV{\cdot}s^{-1}$, and (c) crystallographic representation of $FeWO_4$ wolframite structure.*[8]

Nevertheless, Fe_2WO_6 was only synthesized under high-temperature synthesis conditions, above 900 °C for more than 24 h,[18–20] leading to large average particle size and low specific surface area, both of which are detrimental to the surface reactions required for a pseudocapacitive electrochemical behavior. Therefore, in the next section, Fe_2WO_6 will be synthesized for the first time by a low-temperature (~220 °C) method, hence limiting particle growth and a possible increase in specific surface area. Moreover, this material will be compared to the one obtained by the classic ceramic route. Additionally, X-ray diffraction (XRD), scanning electron microscopy (SEM), and BET analysis will be used to study the crystal structure, morphology, and specific surface area of the as-synthesized particles and the heat-treated materials.

II.2.2. Polyol-mediated synthesis *vs.* Ceramic synthesis

The polyol-mediated route is a low-temperature process involving a liquid polyol acting both as a solvent for the dissolved precursors and as a mild reducing agent[21]. The main features of this method are: 1) the possibility of using high-boiling multivalent alcohols in liquid-phase media having a water-comparable solubility for simple metal-salt precursors. 2) The reducing and coordinating properties for the nucleation and growth of the particles and 3) An easy adaptability of the polyols from low-weight like ethylene glycol (EG) up to high-weight like polyethylene glycols (PEGs).[21,22] The polyol-mediated route can tune the different parameters such as the starting materials to be used, the temperature, pH of the solution, and the duration of the reaction that will control the kinetics of the precipitation, and then well-defined shape control-size particles can be obtained.[22] These characteristics make it an attractive and relatively simple synthesis method to produce single metal oxides such as CoNi,[23] ZnO,[23] and multimetallic oxides like FeCoNi.[24]

Therefore, Fe_2WO_6 was synthesized for the first time following the reported polyol-mediated synthesis of several nanoscale transition metal tungstates, such as $FeWO_4$.[8,25] First, 50 mL of diethylene glycol, DEG 99% $(HOCH_2CH_2)_2O$ (Alfa Aesar), was heated up to 80 °C to dissolve 10.55 mmol of iron (III) nitrate nonahydrate, $Fe(NO_3)_3 \cdot 9H_2O$ 98% (Alfa Aesar), under vigorous stirring until acquiring a homogeneous solution. Then, an aqueous solution of 5 mmol of sodium tungstate dihydrate, $Na_2WO_4 \cdot 2H_2O$ 99% (Acros Organics), was added dropwise, and directly after that, the pH was very carefully adjusted to 6 using a solution of ammonium hydroxide, NH_4OH 28% (Alfa Aesar), resulting in a reddish like suspension. Once the pH was stabilized, the mixture was heated up to 220 °C and kept for one hour until complete nucleation occurred (see Figure II-3). After natural cooling down to room temperature, the particles were purified by centrifugation (20 min, 10,000 rpm) and suspended in ethanol, glacial acetic acid, and distilled water three times to remove all the remaining salts and other non-desired products of the reaction. The obtained powder was then dried at 60 °C for 24 h in air and ground before several heat treatments under air at different temperatures, ranging from 400 °C up to 800 °C.

The proper ratio among iron and tungsten precursors had to be well defined to avoid either iron oxides or tungsten oxides precipitating as impurities. The average yield obtained in the reactions was about 90%, and it was noticed that washing and cleaning of the samples after

being synthesized was a vital parameter to take into account for the higher yield desired. Every time a brownish/reddish powder was obtained.

As a comparison and reference, a classic solid-state reaction (ceramic synthesis)[18–20] was carried out by mixing 1:1 molar ratio of iron (III) oxide red, Fe_2O_3 (Riedel-de Haën, purity > 95 %) and tungsten (VI) oxide, WO_3 (Sigma-Aldrich, 99.9%). The mixture was ground in an agate mortar until reaching a homogenous powder. Afterwards, the sample was placed in a ceramic crucible and then taken into a furnace to be heated under air at 950°C for 24h. Once the reaction concluded, the powder was recovered and ground one more time for further characterizations.

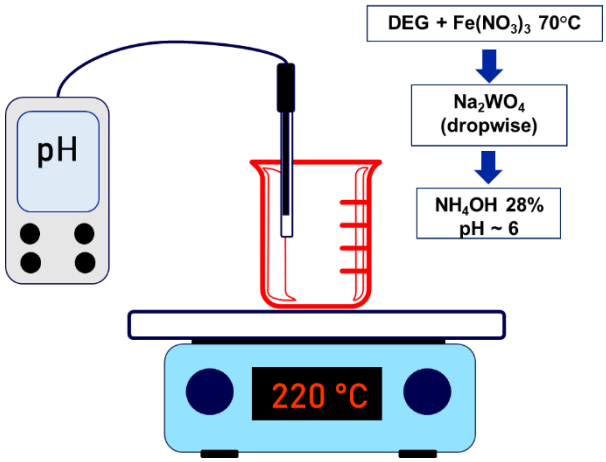

***Figure II-3**. Schematic drawing of the polyol mediated-route for the synthesis of low-temperature Fe_2WO_6.*

II.2.3. Physical and structural characterization

II.2.3.1. Crystal structure: X-ray diffraction

The crystallographic structure of the different samples was investigated by X-ray diffraction (XRD) using a PANalytical X'Pert Pro diffractometer (by Malvern Panalytical) with an X'Celerator detector and Cu-Kα1-Kα2 (λ = 1.54060, 1.54439 Å) radiation. The acceleration voltage and current were 40 kV and 40 mA, respectively. Diffraction patterns were collected in the 2θ range from 10 to 70° and a scan step of 0.0167°. For the *in situ* heat treatment study, a

high-temperature chamber XRK 900 (by Anton Paar) was used under air with a heating rate of 6 °C.min^{-1}. The patterns were acquired after 250 °C every 50°C degrees.

Surprisingly, the diffractogram taken at room temperature for the as-synthesized polyol Fe_2WO_6 showed an amorphous material, in contrast to some other tungstates synthesized by the same method and already reported in the literature.[8,25] For that reason, we decided to carry out *in situ* temperature X-ray diffraction study by following the crystallization as a function of temperature increase from the as-synthesized sample to 900 °C. An amorphous phase is still observable below 600 °C. At T = 600 °C, some broad features begin to develop, resulting in a well-crystallized pattern at around 800 °C, as seen in Figure II-4. The structure of the polyol sample heated at 800 °C will be discussed in the next paragraph.

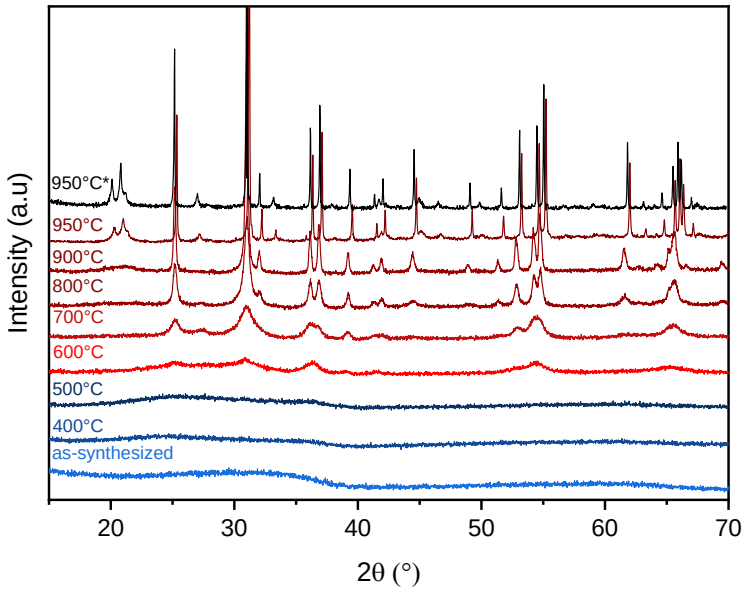

Figure II-4. In-situ *temperature X-Ray diffraction patterns of the polyol sample from as-synthesized to 900 °C. Two XRDPs recorded at room temperature are added for comparison: one after heating the polyol sample at 950 °C (brown line) and one of the ceramic sample synthesized at 950 °C* (black line).*

We added in Figure II-4 two XRDPs recorded at room temperature: one from the ceramic sample synthesized at 950 °C and one from the polyol sample after heating it at 950 °C. We note that, at T = 950 °C, additional reflections, broader than the others, appear on both XRDPs. At T = 900 °C, a bump is observed around 20-22°, which corresponds to the 2θ location of the most intense additional reflections seen at T = 950 °C. These features will be discussed in detail in section 4.

The as-synthesized sample (without any further heat treatment) and the samples heat-treated at 400 °C, 600 °C, and 800 °C were selected to follow some extra characterizations and will be referenced as FWO-RT, FWO-400, FWO-600, and FWO-800, respectively in the upcoming text.

II.2.3.2. Rietveld analysis for Fe_2WO_6 polyol sample at 800 °C using JANA 2006

In order to confirm the presence of a Fe_2WO_6 crystalline phase in the sample synthesized via the polyol mediated route, we decided to perform Le Bail and Rietveld refinements on the sample heat-treated at 800 °C. As we observed in the previous section, this sample already contains well-defined reflections to conduct a structural refinement.

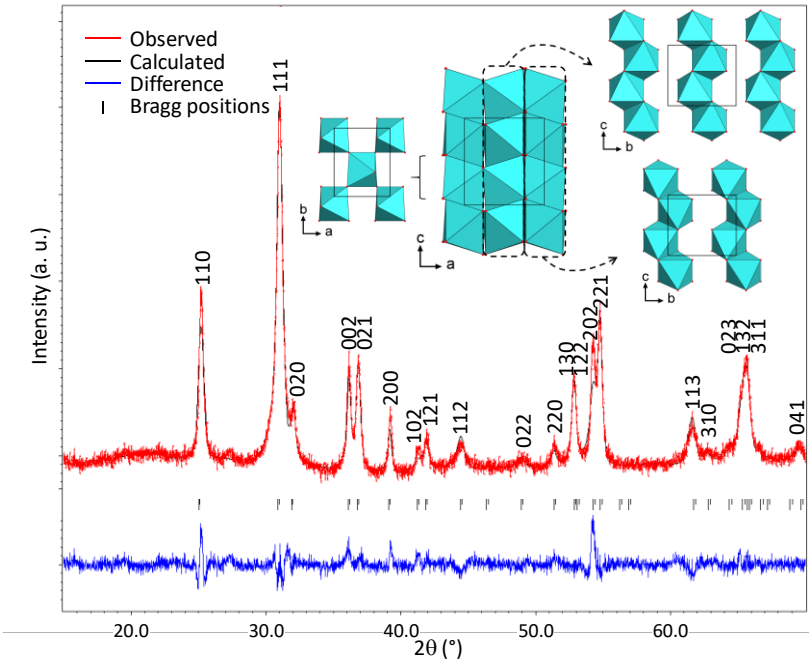

Figure II-5. *Final Rietveld refinement of the XRD pattern for the Fe_2WO_6 polyol sample at 800°C with Cu-Kα1-Kα2 radiation (R(obs) = 3.26 %, GoF = 1.33, wRp = 5.61 %). The inset shows the hypothetical structure of Fe_2WO_6 that can be described as the stacking along the a axis of layers made of zigzag chains of edge-sharing Fe/W octahedra shifted from one layer to another with a (1/2, 1/2, 0) vector. Layers are connected to each other through corner sharing octahedra.*

The reflections observed in the X-ray powder pattern can be indexed into a unit cell of the α-PbO_2 structure ($a_{\alpha\text{-}PbO2}$, $b_{\alpha\text{-}PbO2}$, $c_{\alpha\text{-}PbO2}$; *Pbcn* space group) with *a* axis equal to one-third that of α-Fe_2WO_6, the low-temperature form of Fe_2WO_6 with the columbite structure ($3a_{\alpha\text{-}PbO2}$, $b_{\alpha\text{-}PbO2}$, $c_{\alpha\text{-}PbO2}$; *Pbcn* space group).[26] It is as if the structure adopts the α-PbO_2 structure without

cation ordering and has a single mixed Fe/W site distributed in the unit cell (see Figure II-5). The cell parameters are refined in a *Pbcn* space group with a = 4.5995(15) Å, b = 5.6043(19) Å, c = 4.9718(19) Å.[27] Both Fe and W atoms occupy the same crystallographic site with a 2:1 ratio (see Table II-1). After refining the atomic coordinates and the atomic displacement parameters (ADP), the resulting R-values are R(obs) = 3.26 %, wRp = 5.61 % and GoF = 1.33 indicating a valid structural model. Note that Le Bail refinement using the cell parameters of the columbite structure in the *Pbcn* space group resulted in a worse GoF.

Table II-1. *Atomic coordinates and atomic displacement parameters of Fe_2WO_6 polyol sample at 800°C with* a *= 4.5995(15) Å,* b *= 5.6043(19) Å,* c *= 4.9718(19) Å, V = 128.16(8) Å^3, SG* Pbcn.

Atom	Wyck. pos.	*x*	*y*	*z*	SOF	U_{iso} (Å^2)
Fe1	4*c*	0	0.1654(5)	0.75	0.6667	0.0206(17)
W1	4*c*	0	0.1654(5)	0.75	0.3333	0.0206(17)
O1	8*d*	0.233(3)	0.144(2)	0.427(2)	1	0.012(4)

II.2.3.3. Morphology, surface area and chemical analysis

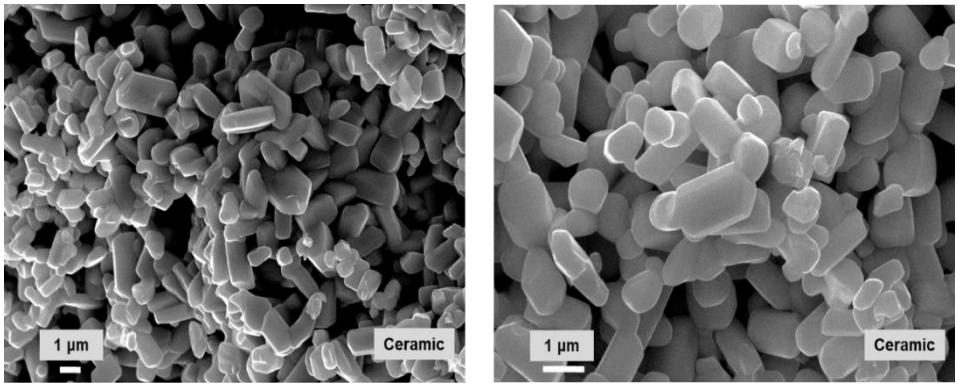

Figure II-6. *Scanning electron microscopy images for the ceramic sample at 950 °C.*

The morphology and chemical analysis of the different materials obtained were characterized by Scanning Electron Microscopy using a Merlin SEM from Carl Zeiss and Energy Dispersive X-ray Spectroscopy with an X-Max detector 50 mm^2 by Oxford Instruments NanoAnalysis installed in the same microscope. The specific surface area of the powders was determined using the BET method (Brunauer-Emmett-Teller) from the 77 K nitrogen adsorption curves with a Quantachrome Nova 4200e equipment (Anton Paar).

Figure II-6 shows the SEM images for the ceramic sample at 950 °C. This sample is composed of well-defined, flat, and smooth surface particles. The average particle size can be found between 0.8-2 μm in agreement with the well-crystallized X-ray diffraction pattern observed in the previous section with very sharp peaks, explaining the uniformity of the surface.

Contrarily to the Fe_2WO_6 synthesized at high temperature, the particles corresponding to the low-temperature polyol-mediated route seem to be completely different. They are more agglomerated with each other with the higher number of defects at the surface and a more significant particle size distribution. Figure II-7 shows the SEM images for the as-synthesized sample, FWO-400, FWO-600, and FWO-800. Neither precise geometry nor form can be detected, which is an attractive feature compared to what can be found in the literature where the reported works have shown the synthesis of nano-sized particles.[8,25]

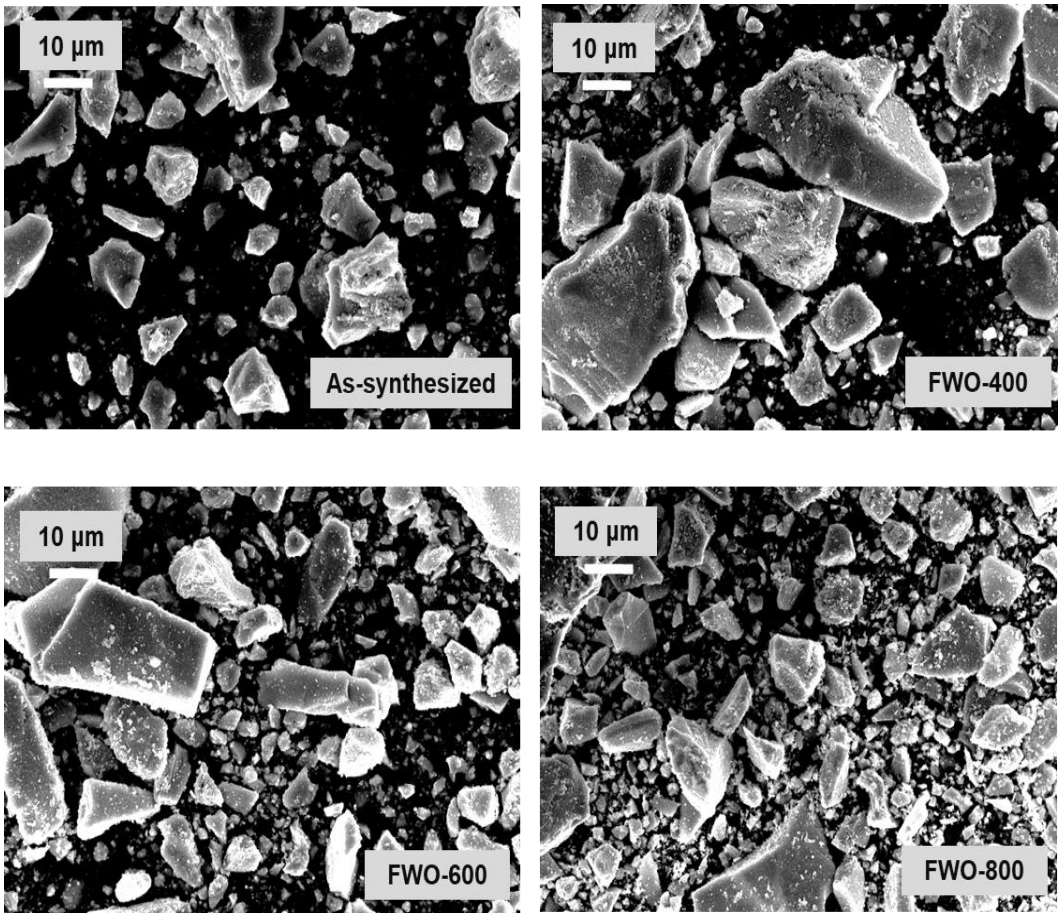

***Figure II-7**. Scanning electron microcopy images for the selected polyol samples: as-synthesized and with different heat treatment: 400°C, 600°C and 800°C.*

All samples kept a Fe/W ratio ~ 2:1 according to the EDX measurements. The specific surface area (SSA) was measured using BET method and as it was expected for the selected polyol samples, the increase in temperature directly impacts the decrease of SSA. The results show 133, 121, 26, and 11 $m^2.g^{-1}$, for FWO-RT, FWO-400, FWO-600, and FWO-800, respectively. Whenever the temperature increases, the particles begin to agglomerate and become more compact, reducing the space, closing and shrinking the open defects on their surface, thus diminishing the SSA. Moreover, the SSA for the ceramic sample was found to be ~2 $m^2.g^{-1}$.

II.2.4. Electrochemical performance of Fe_2WO_6 pseudocapacitive electrode material

II.2.4.1. Electrode preparation and electrochemical setup

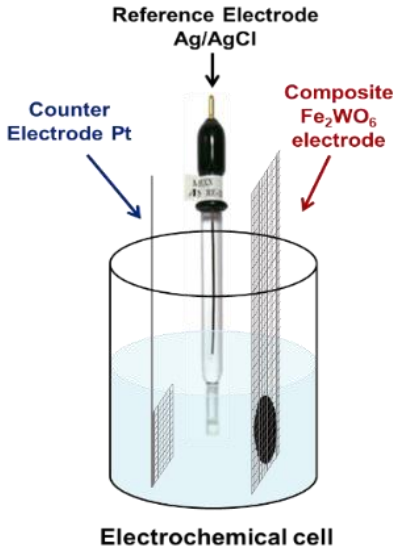

Figure II-8. *Electrochemical cell showing the three-electrode setup.*

The composite electrodes were prepared in agreement with that described by Brousse *et al.*[28] The electrode composition was as follows: Fe_2WO_6 as the active material, conductive carbon (Carbon Black by Superior Graphite, >99%) to improve electronic conductivity, and as the binder to ensure the mechanical strength of the electrode, Polytetrafluoroethylene (PTFE Sigma Aldrich) in the respective weight ratios: 60/30/10. The mixture was suspended in ethanol

and heated up to 60 °C under vigorous stirring until the complete evaporation of ethanol. The remaining black slurry was then cold-rolled until reaching a composite film with a thickness between 100 and 150 µm. After drying at 60 °C to remove the remaining ethanol, 10 or 12 mm diameter disks were cut out and pressed at 900 MPa onto stainless steel or titanium grids, used as current collectors. The mass loading of the prepared electrodes varied from 5 to 10 mg.cm^2, which is an accepted loading for assessing the properties of an electrode material used in electrochemical capacitors.[29]

The electrochemical performance for all the samples was carried out by cyclic voltammetry with a VMP3 galvanostat–potentiostat (from Biologic run under ECLab software). The experiments were conducted using a three-electrode electrochemical setup employing Ag/AgCl (3M NaCl) as the reference electrode and a platinum grid as the counter electrode (see Figure II-8). A neutral 5M $LiNO_3$ aqueous solution was used as the electrolyte, and all the experiments were performed in a [-0.6 V; 0 V] *vs.* Ag/AgCl potential window.

II.2.5. Electrochemical characterization by cyclic voltammetry

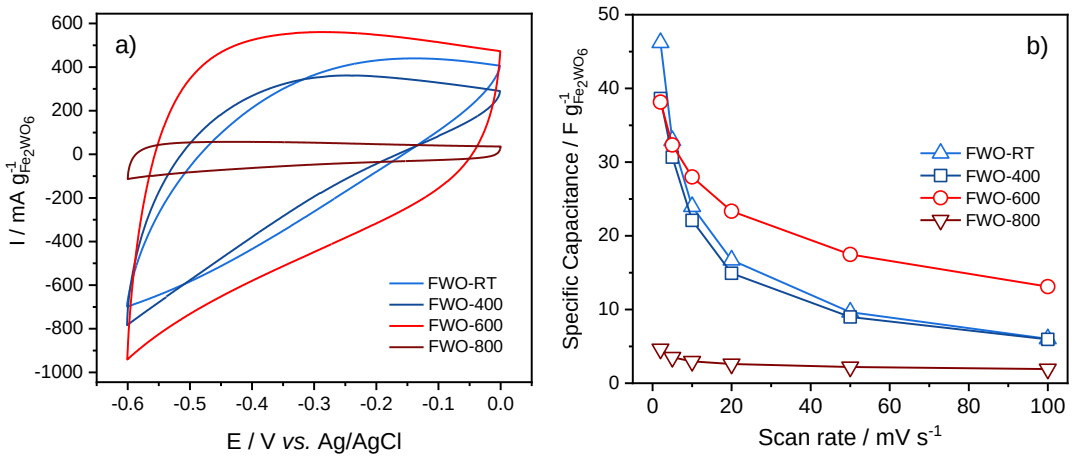

Figure II-9. *a) Cyclic voltammograms at 20 mV.s^{-1} from 0 to −0.6 V vs. Ag/AgCl and b) Evolution of the specific capacitance in F.g^{-1} vs. scan rate in 5M LiNO3 for the selected Fe_2WO_6 samples FWO-RT, FWO-400, FWO-600, and FWO-800.*

Cyclic voltammetry was used to evaluate the electrochemical behavior only for the selected polyol Fe_2WO_6 samples, FWO-RT, FWO-400, FWO-600, and FWO-800. Figure II-9a shows the cyclic voltammogram recorded at 20 mV.s^{-1}. For all samples, no evidence of redox peaks can be observed; thus, we can rule out a faradic response for the electrode materials.

Instead, a distorted rectangular shape is present for all of them but with significant differences. We can notice that the low-temperature samples FWO-RT and FWO-400 present a sort of "rugby ball" shape voltammogram, corresponding to a very resistive composite electrode with a specific capacitance of 17 $F.g^{-1}$ and 15 $F.g^{-1}$, respectively. The high-temperature sample FWO-800 exhibits a more rectangular shape typical of pseudocapacitive oxides[10,30] but with a meager capacitance value (3 $F.g^{-1}$). On the other hand, the sample FWO-600 exhibits a quasi-rectangular shape CV with a specific capacitance of 23 $F.g^{-1}$at 20 $mV.s^{-1}$. This behavior is very similar to that observed for $FeWO_4$ material cycled under similar conditions,[8,13] attributing this performance to the $Fe^{3+/}Fe^{2+}$ redox couple.[14]

Figure II-9b displays specific capacitance values in Farads per gram ($F.g^{-1}$) at different scan rates for all the samples. It is observed that despite a capacitance value of 47 $F.g^{-1}$ for the FWO-RT sample when cycled at 2 $mV.s^{-1}$, a rapid fade occurs while increasing the scan rate. Sample FWO-400 also exhibits a similar behavior while FWO-600 keeps the best performance even at higher rates. For this latter sample, the specific capacitances measured at the different scan rates are within the same range as those measured for $FeWO_4$[5,8]. FWO-600 can reach up to 38 $F.g^{-1}$, corresponding to a volumetric capacitance of 240 $F.cm^{-3}$ when cycled at 2 $mV.s^{-1}$; this value was calculated considering a density of 6.3 $g.cm^{-3}$, measured by helium pycnometry, being comparable to the theoretical value of 6.82 $g.cm^{-3}$ reported by Pinto *et al.*[19]. This attractive density value, comparable to different multicationic oxides, can be exploited to implement this oxide material as a high volumetric capacitance electrode in aqueous-based asymmetric devices.

II.2.5.1. Electrochemical stability

The electrochemical stability of all the samples was then studied over 3000 cycles at 20 $mV.s^{-1}$. Figure II-10 shows that after a slight increase during the first 200 cycles for FWO-600, almost 90 % of capacitance retention can be achieved after 3000 cycles, rarely reported for pseudocapacitive electrodes[31,32]. This slight increase has already been observed in our lab for similar materials. The reason is the impregnation time with the aqueous electrolyte throughout the porosity of the composite electrode. For FWO-400 and FWO-RT samples, a quicker fade in capacitance can be observed with only 65% and 50% capacitance retention, respectively. Finally, the FWO-800 exhibits a stable but very low capacitance upon the 3000 cycles.

A compromise between the crystallinity and the specific surface area (or the particle size) directly impacts the electrochemical performance of the material[8,31] to get better capacitance values associated with both interesting cycling stability and power capability. The low-temperature sample presents the highest SSA (up to 133 $m^2.g^{-1}$) compared to FWO-600 (26 $m^2.g^{-1}$). Nonetheless, this latter sample achieves the best performance among all. When polyol Fe_2WO_6 is heated up at 600 °C, we achieve a relatively high specific surface area to maintain a higher capacity while avoiding a progressive dissolution upon cycling, as observed for the amorphous materials as-prepared or sintered at lower temperatures.

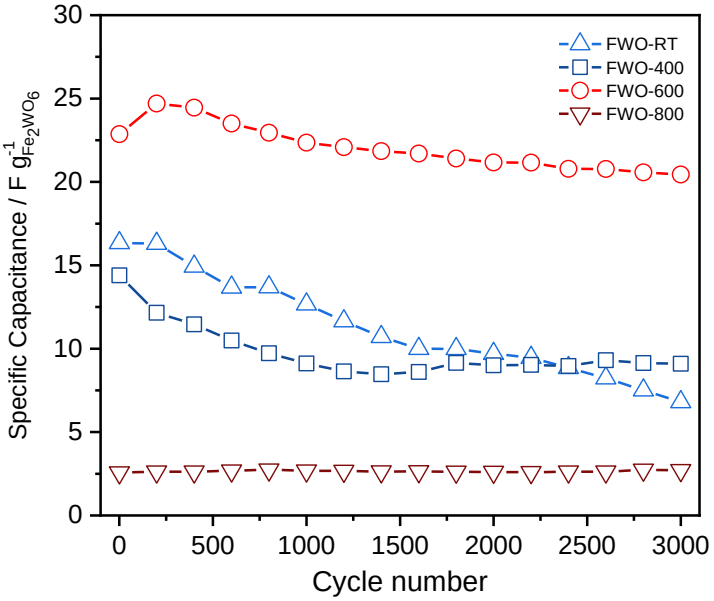

Figure II-10. *Cycling stability up to 3000 cycles at 20 mV.s^{-1} in 5M $LiNO_3$ for the selected Fe_2WO_6 samples.*

The changes occurring upon long-term cycling in pseudocapacitive electrodes are scarcely investigated[31,32]. In order to get further insights into the structural or/and microstructural modifications occurring to the materials upon long-standing cycling, we performed more in-depth analyses. Therefore, the FWO-600 electrode material was specifically selected for such purposes since it exhibits the best electrochemical performance in terms of capacitance, power capability, and cycling stability, as it was presented before. The following section will describe the different approaches and characterization techniques used to elucidate this oxide's stability.

II.3. Cycling Stability of Fe_2WO_6 pseudocapacitive electrode materials

II.3.1. Long cycling stability study

FWO-600 electrode material was submitted to 10,000 cycles (charge/discharge) at a cycling rate of 20 $mV.s^{-1}$. Figure II-11 shows the relative capacitance after the long cycling experiment with the inset presenting the first and last cyclic voltammograms. The remaining capacitance after 10,000 cycles is close to 85%, with a very similar CV shape to the first cycle (inset Figure II-11). No apparent degradation of the electrode nor material dissolution could be observed in the electrochemical cell.

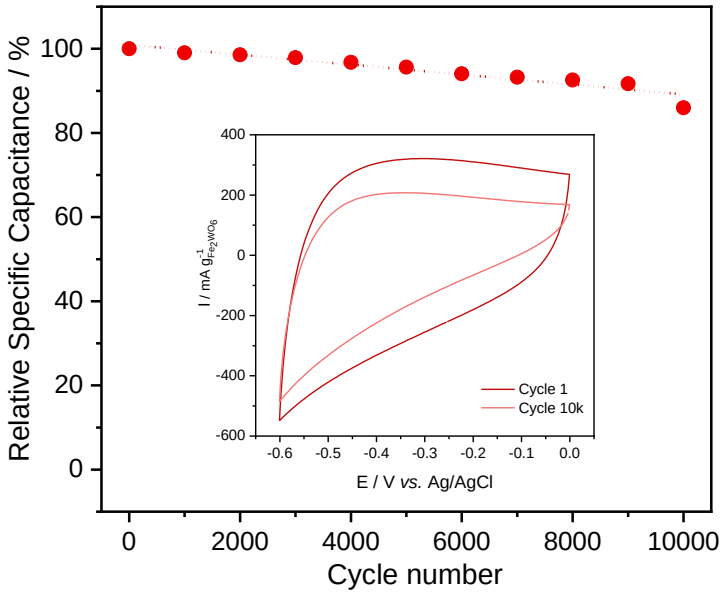

Figure II-11. *Long term cycling stability for FWO-600 sample at 20 $mV.s^{-1}$ in 5M $LiNO_3$. Inset: Cyclic voltammograms at cycle 1 and at cycle 10,000.*

As a comparison, N.L. Wu *et al.*[33] assigned the fade in capacitance of a MnO_2 electrode in aqueous 1M KCl to several factors, including severe surface modifications induced by varying the upper cut-off potential. In order to thoroughly investigate the changes that could occur to Fe_2WO_6 particles after an extended cycling, several electrodes (prior cycling, after 10,000 cycles at 20 $mV.s^{-1}$, and a "blank" electrode soaked in electrolyte but without any

cycling) were cut into small pieces to perform experiments using different characterization techniques on the same material for all the tests.

II.3.1.1. Surface observations by Transmission Electron Microscopy

The study on the effects caused by the long-term cyclability began with the hypothesis of possible changes occurring at the surface of the particles. In order to put on evidence such a proposition, the microstructure, surface, morphology, and particle size modifications were studied with a transmission electron microscope (TEM) ThermoFisher S/TEM Themis G3 at 300 kV point to point resolution: 0.18 nm.

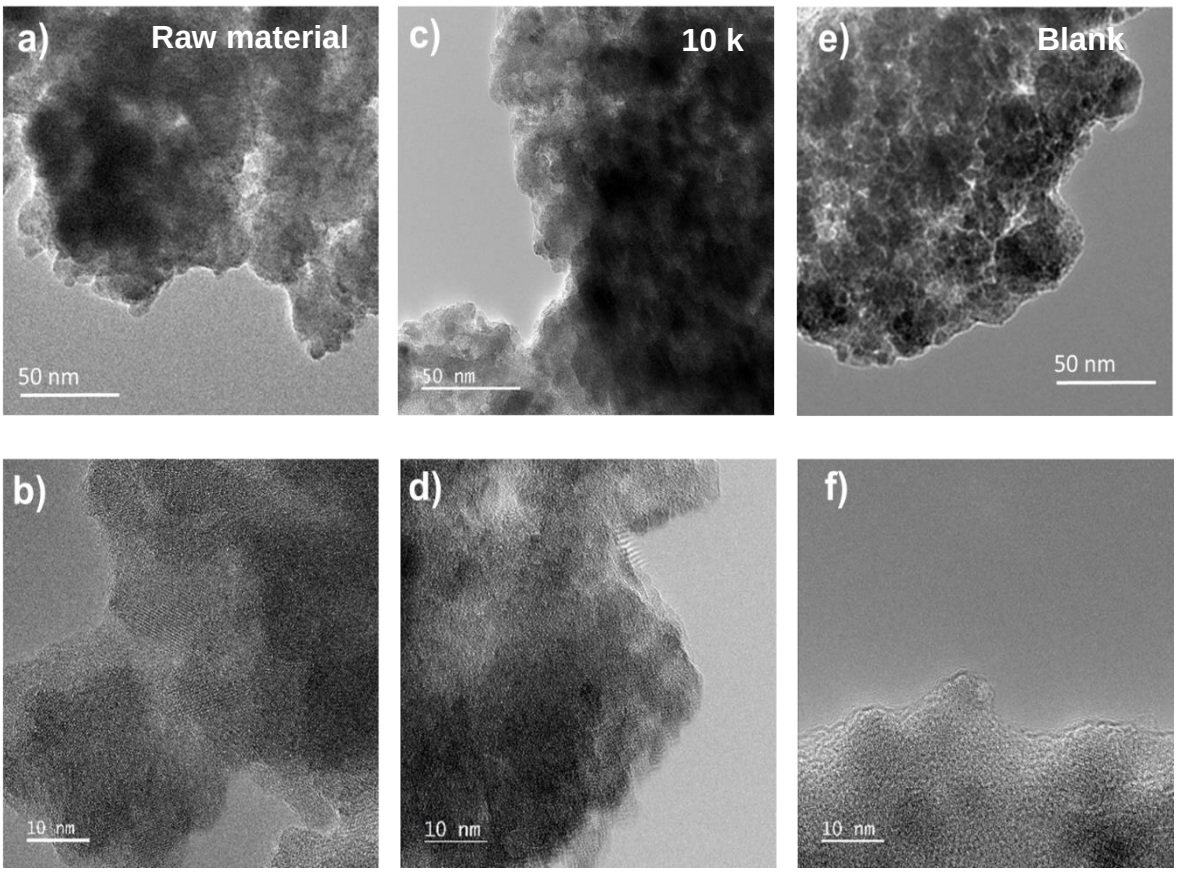

Figure II-12. *TEM images of raw FWO-600 particles (a, b), after 10,000 cycles (c, d) and from the blank electrode soaked in the electrolyte (e, f). Scale bar for figures a, c and e is 50 nm while it is 10 nm for figures (b, d, f).*

As mentioned above, the study was performed by comparing a series of three different electrodes: a piece of dry and non-cycled FWO-600 composite electrode (Electrode film, Figure II-12a and b, FWO-600 electrode cycled 10,000 times (Electrode 10k, Figure II-12c and d) and an FWO-600 electrode that was not cycled but only soaked the electrolyte (Electrode blank, Figure II-12e and f) for the same time as the electrode cycled 10,000 times. At low magnification (Figure II-12a, c and e), all the samples present similar aggregates with an average size close to 100 nm, composed of tiny, irregular-shaped primary particles. From TEM images, it is challenging to claim significant particle size distribution in the different samples. At higher magnification, some small crystalline domains of a few nm can even be observed, without relevant differences between each other. These observations are in good agreement with the broad peaks shown on the XRD patterns (Figure II-4). Interestingly, clear and sharp edges are visible for all samples at the surface of the particles, and no dissolution or formation of extra layers or coatings can be detected, contrary to what has been already reported for MnO_2 after extended cycling.[33] Furthermore, the particles extracted from the "Electrode blank" presented no distinguishable effect. Thus, neither cycling nor electrolyte interaction induces significant and visible changes at the surface of FWO-600 particles.

Microstructural changes do not seem to occur upon cycling or prolonged exposure to the electrolyte, and the slight capacitance fade observed after 10,000 cycles must be investigated with more specific analytical tools that could evidence such modification.

II.3.1.2. Mössbauer Spectroscopy Analysis

Mössbauer spectroscopy is perfectly adapted for the study of Fe-based materials, as it should enable to reveal several modifications of Fe cations in the Fe_2WO_6 structure, such as their oxidation state and environment. This interesting tool can help us in the investigation of the long-term cyclability of the FWO-600 sample.

^{57}Fe Mössbauer spectra were measured in transmission mode with a ^{57}CoRh source. Both the source and the absorber were kept at ambient temperature (294 K) during the measurements. The spectrometer was operated in the constant acceleration mode with a triangular velocity waveform. The velocity scale was calibrated with the magnetically split sextet spectrum of a high-purity α-Fe reference absorber at room temperature. Since the data fitting is not possible using one doublet (one environment), they were fitted with an appropriate

distribution of six Lorentzian profiles representing quadrupole doublets by the least-squares methods using the software PolMoss v2.0.[34,35] In this way, spectral parameters such as the quadrupole splitting (QS), the isomer shift (IS), the linewidth at half maximum (LW) of the different spectral components were determined. Isomer shifts are given relative to the α-Fe.

^{57}Fe spectra were collected at room temperature on the same samples that were used for the TEM observations. Mössbauer spectra of the as-prepared electrode after being soaked in the electrolyte (blank) and after 10,000 cycles (10k) are shown in Figure II-13a. The as-prepared electrode spectrum agrees well with the data reported by Birchall *et al*. for Fe_2WO_6 powder.[36] The fitting was performed with an appropriate distribution of six Lorentzian profiles representing quadrupole doublets by least-squares methods (Figure II-13b).

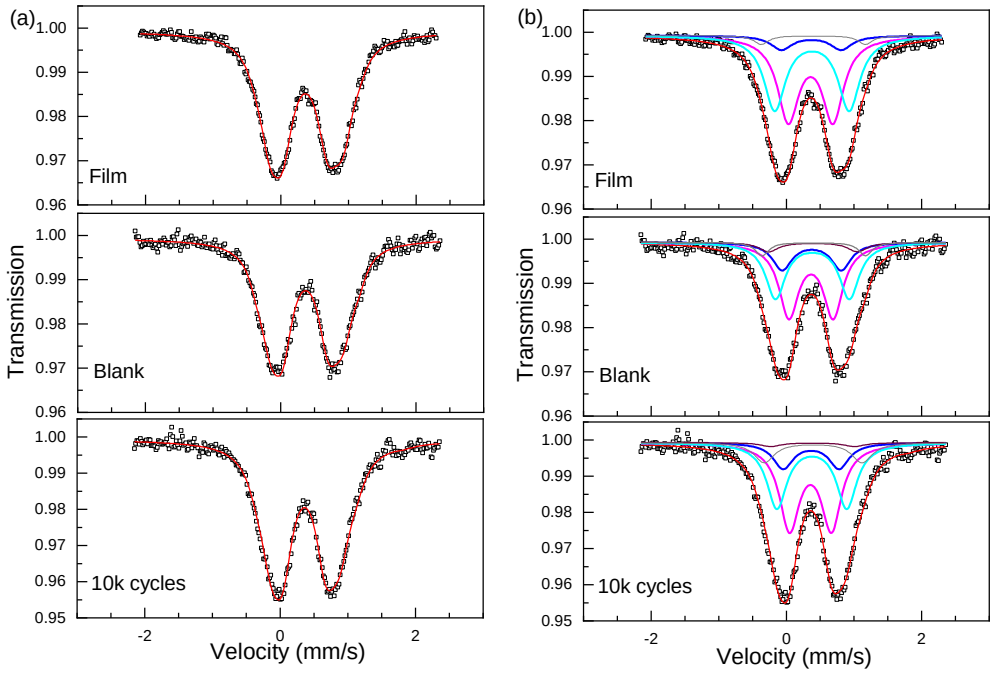

***Figure II-13**. a) Room temperature Mössbauer spectra for non-cycled FWO-600 electrode ("Film"), non-cycled but soaked in electrolyte ("Blank") and cycled electrode after 10,000 cycles at 20 mV.s^{-1} ("10k cycles") and b) Room temperature ^{57}Fe Mössbauer spectra of all samples showing an appropriate distribution of six Lorentzian profiles representing quadrupole doublets by least-squares methods.*

All the iron is in a ferric state and high spin octahedral configuration. The obtained average isomer shifts and quadrupole splitting (given in Table II-2) show that no Fe^{2+} can be detected in all the samples, thus confirming that the low-temperature synthesis of Fe_2WO_6 leads to a pure phase with Fe^{3+}. Moreover, no significant change is observed after 10,000 cycles or

prolonged soaking in the electrolyte, hence discarding any irreversible formation of Fe^{2+} upon cycling or soaking. Very tiny differences can be observed in QS distribution (see Figure II-14), showing a slight increase in the high QS contribution weight (around 1.2 to 1.5 mm/s). This might indicate a possible but meager increase of the iron sites distortion after cycling or soaking in the electrolyte.

Table II-2. *Room temperature ^{57}Fe Mössbauer hyperfine parameters, <IS>, <QS> and <LW> are the average isomer shifts, quadrupole splitting and linewidth, respectively.*

Sample	<IS> (mm/s)	<QS> (mm/s)	<LW> (mm/s)
Film	0.37	0.85	0.38
Blank	0.39	0.84	0.35
10k cycles	0.40	0.79	0.36

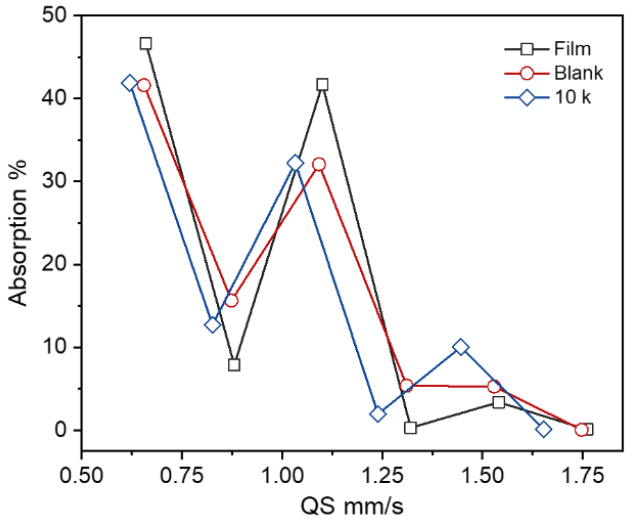

Figure II-14. *QS distribution for the three samples.*

Considering that both accurate TEM observation of the surface for FWO-600 material and Mössbauer spectroscopy experiments performed before, after cycling, and with a soaked electrode without electrochemical activity did not allow us to explain the capacitance fade observed after 10,000 cycles and that no significant change can be observed concerning the surface, morphology and on the Fe atoms environments. Therefore, we decided to use a different approach concerning the magnetic properties of Fe_2WO_6. On this matter, in the interest of better understanding such changes, the same selected electrodes were subjected to the following experiments.

II.3.1.3. Magnetization measurements

The magnetization experiments were performed using a commercial SQUID magnetometer (MPMS-XL7 by Quantum Design) from 5 to 300 K at a field strength of H = 200 Oe. Electrode film, Electrode 10 k, and Electrode blank were measured under the same conditions used by Guskos *et al*.[26] for studying pristine Fe_2WO_6. Each sample was measured on warming two times: once when the sample had been cooled in the absence of a field (zero-field-cooled, ZFC) and once when the sample had been cooled in the measuring field of 200 Oe (field-cooled, FC). Magnetizations of the mixture of conductive carbon black and PTFE binder and of the Fe_2WO_6 polyol powder were also measured separately. The mass magnetization of the mixture of carbon plus PTFE was found to be very small (see Figure II-15), and the data for pristine Fe_2WO_6 were consistent with those published in reference.[26]

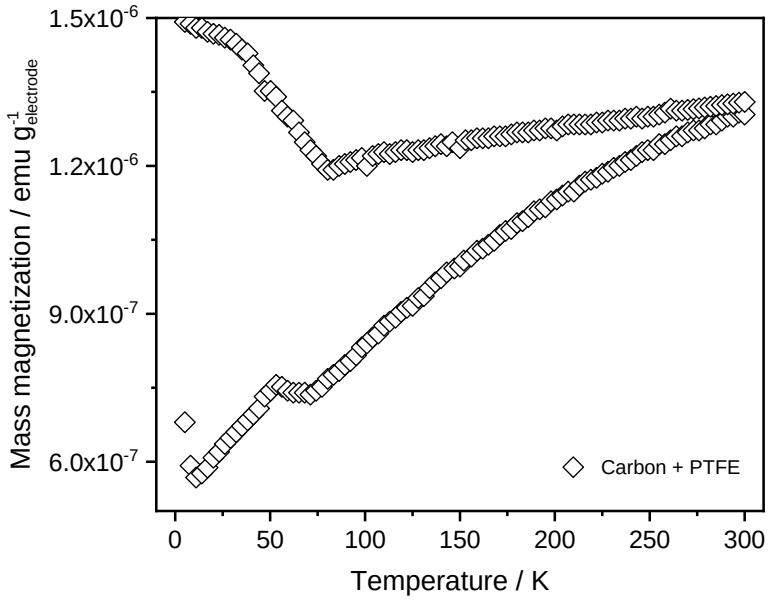

Figure II-15. *T-dependent FC and ZFC mass magnetization @ 200 G for carbon +PTFE. Difference between ZFC and FC data was assumed to arise from minuscule amounts of ferromagnetic impurities.*

Figure II-16 presents the T-dependent FC, and ZFC mass magnetizations for the three electrodes studied. Data for the electrode film and for the electrode blank, which was only soaked in electrolyte but without being cycled, are very similar to those obtained for pristine (film) Fe_2WO_6 in that both the ZFC-FC bifurcation at about 250 K and the ZFC step-like anomaly at about 200 K are clearly visible.[26] As can be seen in Figure II-16, these two latter features, which are a hallmark of crystallized Fe_2WO_6, are still observed in the T-dependent

magnetization of the 10 k cycled electrode. Therefore, our data indicate that neither soaking nor cycling induces a qualitative change in the bulk magnetic behavior of Fe_2WO_6. In other words, the bulk of the oxide powders remains crystallized, and there is no change in the chemical composition of the bulk upon cycling. However, it does not preclude chemical and/or structural changes on the oxide surface as these bulk magnetization measurements do not probe surfaces.

Consequently, the magnetization measurements performed on the different samples indicate no amorphization or modification of the iron cations environment upon cycling. Therefore, the magnetic properties of the Fe_2WO_6 material are not affected by long-term cycling in the 5M $LiNO_3$ aqueous electrolyte**.**

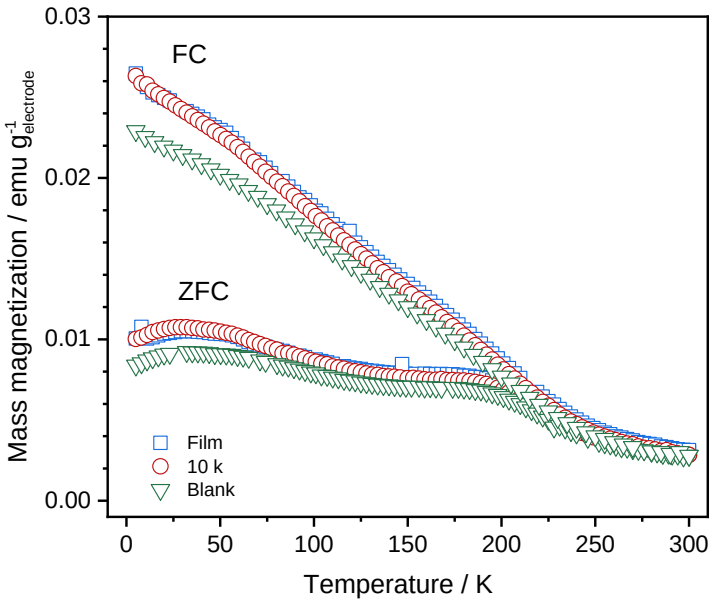

Figure II-16. *T-dependent FC (field-cooled) and ZFC (zero-field-cooled) mass magnetizations for non-cycled "Film", cycled electrode "10 k", and non-cycled but soaked in electrolyte "Blank".*

II.3.2. Preliminary conclusions on cycling stability

Long-term cycling stability in aqueous 5M $LiNO_3$ is presented for Fe_2WO_6 electrode material synthesized by polyol mediated-route and sintered at 600 °C. Such a study intended to enlighten the high stability (only ~ 15 % loss in capacitance after 10,000 cycles) that is not often observed for oxide compounds used in electrochemical capacitors. TEM observations, Mössbauer spectroscopy, and magnetization measurements were further used to correlate the fade in capacitance to microstructural or structural changes. All the experiments demonstrated

that the morphology, crystallographic structure, and magnetic properties were not affected by the electrochemical cycling nor simple prolonged soaking in the electrolyte. No partial dissolution at the surface of the particles nor Fe^{2+} formation could be detected, confirming thus the stability of the material. However, some slight current collector corrosion at the interface with the electrode was indeed observed, which could have been due to some dissolved oxygen in the aqueous electrolyte, hence explaining the capacitance fade after 10,000 cycles.

II.4. Crystallographic evidence of incommensurate modulations in Fe_2WO_6 powder

II.4.1. Introduction

In this section, we will investigate the structure of the high-temperature form of Fe_2WO_6 (referred to as γ-Fe_2WO_6) that was synthesized in our laboratory at T = 950 °C and relate its structure to that of the heat-treated polyol samples at 900 and 950°C discussed in section II.2.3.1.

γ-Fe_2WO_6 is the most studied phase among the three polymorphs α,[37] β[38] and γ[18] mainly because it is relatively simple to synthesize. This material has been studied in many fields for its electrical,[39] dielectric [40] and magnetic[19,41] properties as well as its electrochemical activity, as already discussed in the previous sections. It has been reported that the structure of γ-Fe_2WO_6 adopts the tri-α-PbO_2 structure-type with *b* axis thrice of that of α-PbO_2 ($a_{\alpha\text{-}PbO2}$, $3b_{\alpha\text{-}PbO2}$, $c_{\alpha\text{-}PbO2}$, *Pbcn* space group) with *a* = 4.576(2) Å, *b* = 16.766(5) Å, *c* = 4.967(2) $Å^3$. The structure can be described as the stacking along the *a* axis of layers made of zigzag chains of edge-sharing octahedra[38] (Figure II-17). In a layer, one-third of the zigzag chains contain $Fe1O_6$ octahedra and two-thirds of the chains are composed of alternating $Fe2O_6$ and WO_6 octahedra (Figure II-17b-c. The sequence of cations is identical in the first (x ~ 0) and second (x ~ 1/2) layers, the zigzag chains being translated with a vector (1/2, 1/2, 0) from one layer to another. Layers are connected to each other through corner sharing leading to two kinds of *ab* planes consisting of alternating $Fe1O_6$, $Fe2O_6$ and WO_6 rows of octahedra along the *b* axis (Figure II-17a and d).

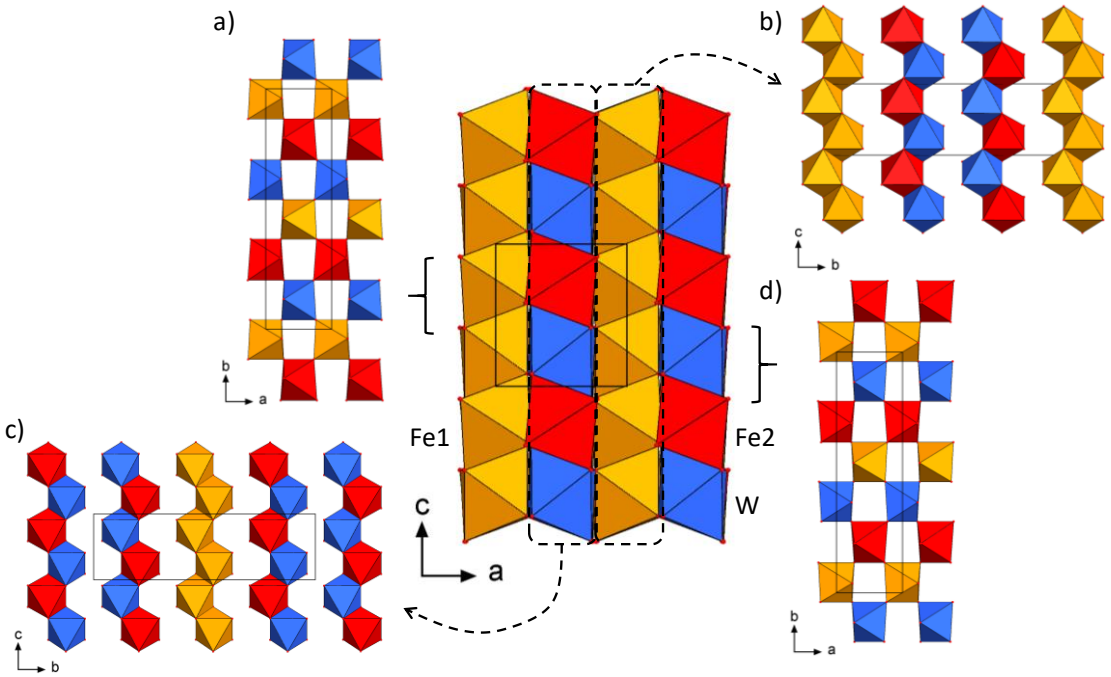

Figure II-17. *Representation of the γ-Fe_2WO_6 structure at room temperature. WO_6, $Fe1O_6$ and $Fe2O_6$ octahedra are displayed in blue, orange and red, respectively.*

The temperature-dependent X-ray diffraction study indicated (see Figure II-4) at 800°C, the formation of a well-crystallized phase whose diffraction peaks were successfully indexed into the cell of the α-PbO_2 structure ($a_{\alpha\text{-}PbO2}$, $b_{\alpha\text{-}PbO2}$, $c_{\alpha\text{-}PbO2}$, *Pbcn* space group). At 900 and 950°C, additional reflections appear corresponding to the tri-α-PbO_2 structure with the remarkable difference that these reflections are broader than the other reflections. For a Fe_2WO_6 sample prepared by the classical ceramic route at 950°C, the same behavior was observed: some diffraction peaks, the same as those of the polyol sample, are broader than others. In order to shed light on this particular phenomenon, the structure of the polyol and ceramic powders at 900 and 950°C has been carefully investigated and reveals that the structure of γ-Fe_2WO_6 is perfectly described using the superspace formalism. In this section, full details on the Rietveld refinement of the high-temperature form of γ-Fe_2WO_6 solved in a 4D space group will be described and an explanation of the physical origin of the reflection broadening will be provided.

II.4.2. Experimental part

II.4.2.1. Synthesis

As already stated in section II.2.2, polycrystalline samples of γ-Fe_2WO_6 were synthesized using the standard solid state reaction. The starting materials Fe_2O_3 (Riedel-de Haën, purity > 95 %) and WO_3 (Sigma-Aldrich, 99.9%) were mixed stoichiometrically and ground in an agate mortar. The powders were annealed at 950 °C for 24 h in air. To study the effect of annealing on peak broadening in Fe_2WO_6 X-Ray powder patterns, several heat treatments of Fe_2WO_6 were performed at 950°C for 24 h with intermediate grinding and XRD recording. Samples of γ-Fe_2WO_6 phase were also prepared by a low-temperature polyol-mediated route[42]. The resulting powders were ground before undergoing two separate heat treatments in air at 900 and 950°C. The powders obtained by solid state reaction or by polyol route are hereafter referred to as ceramic and polyol samples.

II.4.2.2. Powder X-ray diffraction

The XRD pattern (XRDP) of the ceramic samples was recorded in air at room temperature (RT) with a Bruker D8 A25 diffractometer using a Cu-Kα1-Kα2 radiation (λ = 1.54060, 1.54439 Å) and a LynxEye detector in Bragg-Brentano geometry. XRD patterns of the polyol samples were recorded in air at room temperature using a Bruker D8 Advance. Data were collected in the Bragg–Brentano geometry using a Cu-Kα1-Kα2 radiation (λ = 1.54060, 1.54439 Å) and a Vantec detector. XRDPs of the polyol samples were also recorded in air at room temperature (RT) in Bragg-Brentano geometry with a PANalytical X'Pert Pro diffractometer using a Cu-Kα1-Kα2 radiation (λ = 1.540598, 1.5444260 Å) and an X'Celerator detector. Le Bail and Rietveld analyses of the XRD data were performed using JANA2006[27] and the fundamental Cheary-Coelho approach for XRD profile parameters was applied in refinement for each diffractometer[43].

II.4.3. Preliminary structural refinements

The Figure II-18 shows the XRPD performed at room temperature of the ceramic sample prepared at 950 °C and the polyol samples annealed at 900 or 950°C. All peaks can be indexed

in the tri-α-PbO_2 structure-type cell (inset of Figure II-18). At 950°C, the plots of the polyol and ceramic samples show narrower and broader diffraction lines highlighted by black and green *hkl* indices, respectively. It is interesting to note that the narrower diffraction lines have *hkl* indices following the rule: *hkl*, *k* = 3n, with n being an integer. At 900°C, the plot of the polyol sample shows a large bump located around 20-22° corresponding to the 2θ positions of the strongest and broadest reflections in the ceramic plot. We expect that at 900 and 950°C, the structure of the sample is identical but the broad diffraction lines (for instance, 110, 021 and 040) in the 950°C plots are so broad that they appear as a large bump at 900°C and the least intense broad diffraction lines in the 950°C plots (for instance, 111, 041, 150, 022 and 151) do not appear in the 900°C plot.

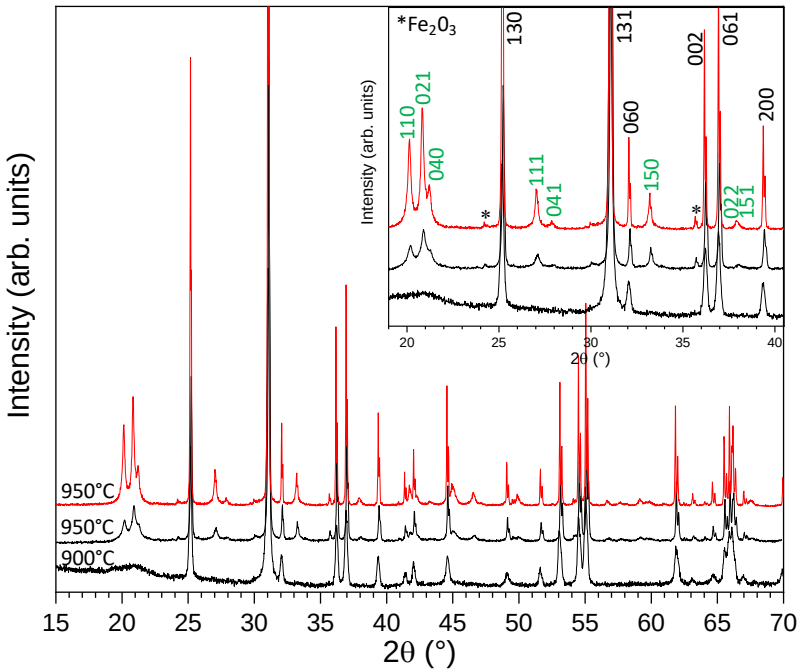

***Figure II-18**. XRPD at room temperature of the ceramic sample synthesized at 950 °C (red) and the polyol (black) samples annealed at 900 or 950°C. The inset shows the* hkl *indexation considering* a = *4.576(2) Å,* b = *16.766(5) Å,* c = *4.967(2) Å cell in a* Pbcn *space group.*

The structure of the ceramic sample was initially refined by the Rietveld method in the *Pbcn* space group using the model of γ-Fe_2WO_6[18,19] with Fe atoms in two 4c sites (0,y,0.25) with y ≈ 0.06, y ≈ 0.72, W atoms in one 4c site (0,y,0.25) with y ≈ 0.39 and O atoms in three 8d sites. The refinement yielded non-positive definite atomic displacement parameters (ADP) for both Fe atoms and two O atoms. In addition, the use of anisotropic size or strain broadening parameters to try to model the broadening of some reflections was not successful. This is related

to the unusual equation governing the *hkl* indices. The broader diffraction lines are the cause of the structural differences between the γ-Fe_2WO_6 sample reported by Senegas *et al.*[18] and the ceramic and polyol samples in the present study. It is interesting to note that $ZnNb_2O_6$, with the columbite structure ($3a_{\alpha\text{-PbO2}}$, $b_{\alpha\text{-PbO2}}$, $c_{\alpha\text{-PbO2}}$) was initially refined in a 3D model[44] but was recently solved in a 4D model.[45] This encouraged us to solve and refine the structure of the ceramic and polyol samples in a 4D model by applying the superspace formalism using JANA2006 software.[27]

II.4.4. Introduction to incommensurate structural refinement

In a 3+n D (n = 1, 2 or 3) spaces, the reciprocal space vectors are usually expressed as $H = ha^* + kb^* + lc^* + mq$ (a^*, b^*, and c^* are the basis vectors of the 3D reciprocal lattice). The modulation vector can be expressed as $q = \alpha\, a^* + \beta\, b^* + \gamma\, c^*$, where α, β, and γ are rational numbers for commensurate cases and irrational for incommensurate cases.

In the present study, the unit cell of γ-Fe_2WO_6 (a = 4.576(2) Å, b = 16.766(5) Å, c = 4.967(2) Å), which corresponds to a cationically ordered α-PbO2 structure, is transformed into a cell without cation ordering, by dividing the parameter b by a factor of three, which leads to $a \approx 4.57$ Å, $b \approx 5.58$ Å and $c \approx 4.96$ Å. All observed XRPD reflections from the ceramic sample fulfilled the reflection conditions for the 4D superspace group *Pbcn*(0β0)000. The main reflections (*hklm*, m = 0) could be indexed on the basis of an orthorhombic unit cell ($a \approx 4.57$ Å, $b \approx 5.58$ Å and $c \approx 4.96$) and the satellite reflections (*hklm*, $m \neq 0$) could be indexed on the basis of an incommensurate modulation vector, q = 0.66872(17) b^*, where b^* is the reciprocal lattice vector. The β component of the modulation vector is close, but significantly different from the 2/3 (≈ 0.66667) rational ratio (difference > 12 σ(β)). Therefore, the structure should a priori be considered as incommensurate, an assumption later on confirmed by the refinements. The structure of γ-Fe_2WO_6 is thus a (3+1)-dimensional incommensurately modulated structure. In the 4D superspace formalism approach, an additional coordinate x_4 can be expressed as $x_4 = t + q \cdot x$, where $x = (x_1, x_2, x_3)$ is the coordinate of physical-space with respect to the lattice and the parameter t $(0 \leq t \leq 1)$ is the distance between a point and physical space.

II.4.5. Refinement of the incommensurately modulated Fe_2WO_6 structure

***Table II-3**. Crystallographic data, details of the data collection and structure refinement of Fe_2WO_6*

Chemical formula	**$Fe_{2.667}W_{1.333}O_8$**
Modulation	Incommensurate
Formula weight (g mol^{-1})	522.01
Crystal system	Orthorhombic
Super space group	*Pbcn*(0β 0)000
Temperature (K)	293
***a* (Å)**	4.57964(3)
***b* (Å)**	5.58662(4)
***c* (Å)**	4.96920(3)
***V* (Å^3)**	127.1355(14)
Modulation wave vector	q = 0.66872(17) *b**
Z	1
D_{calc} (g cm^{-3})	6.818
Radiation type	Cu *K*α
Wavelength (Å) *K*α1, *K*α2, *I (K*α2)/*I (K*α1)	1.5406, 1.54439, 0.5
Diffractometer	Bruker D8 A25
2θ range (°), step scan (°), no. of data pts	10-100, 0.015, 6137
Profile function for main reflections	Pseudo-Voigt
No. of background parameters	12-term Legendre polynomials
No. of reflections (all/obs [I > 3σ(I)])	201/184
No. of main reflections, *m* = 0 (all/obs)	68/63
No. of satellite reflections, *m* ± 1 (all/obs)	133/121
Number of refined parameters	49
***Rp* (%)**	7.92
***wRp* (%)**	11.26
GoF (goodness of fit)	1.33
***R*, *wR* (%) (R_{obs}/R_{all})**	3.81/4.17, 4.42/4.49
***R*, *wR* (%) (R_{obs}/R_{all}) main reflections**	2.55/2.79, 3.13/3.22
***R*, *wR* (%) (R_{obs}/R_{all}) first-order satellites**	5.94/6.45, 5.09/5.15
$\Delta\rho_{max}$ / $\Delta\rho_{min}$ (e Å^{-3})	2.09 / -2.19
Volume fraction Fe_2WO_6/Fe_2O_3	0.962(2)/0.037(2)

The results of the structural refinement are given in Table II-3, and the details of the refined parameters of the final refinement are given in Table II-4**.** Le Bail refinement of the modulated Fe_2WO_6 structure was performed in the *Pbcn*(0 β 0)000 superspace group starting with β = 2/3. The profile of main reflections was successfully described by a pseudo-Voigt function. The Rietveld refinement starts from the $ZnNb_2O_6$ model[45], which is close to that of the α-PbO2 structure, containing the following three atoms. Fe1 and W1 occupy the same site of multiplicity 4 (0,*y*,0.75) with $y \approx 0.16$ and O1 is located in a site of multiplicity 8 (*x*,*y*,*z*) with $x \approx 0.22$, $y \approx 0.11$, and $z \approx 0.41$. The parameters of Fe1 and W1 are restricted to have the same coordinates, modulations and ADP. First, the atomic positions and ADP are refined. A crenel

function, describing the discontinuous occupation of the same site by Fe1 and W1 atoms, is then introduced in the refinement with x_4^0 (Fe1) = x_4^0 (W1) + 0.5 and Δ (Fe1), Δ (W1), according to the Fe_2WO_6 composition, equal to 2/3 and 1/3, respectively. After refinement, the main (*hklm*, *m* = 0) and the satellite reflections of order 1 (*hklm*, m ± 1) are indexed. The refinement was further improved by introducing a displacive modulation function for the Fe1/W1 and O1 atoms and an anisotropic ADP for Fe1/W1 site.

Table II-4 *Atomic coordinates and atomic displacement parameters (Å^2) obtained from the superspace refinement of the incommensurately modulated Fe_2WO_6 structure ((3+1)D group Pbcn(0β 0)000, a = 4.57964(3) Å, b = 5.58662(4) Å, c = 4.96920(3) Å, V = 127.1355(14) Å^3, q = 0.66872(17) b*).*

Atom	**Site multiplicity**	***x***	***y***	***z***	**U_{eq}[1] / U_{iso}**
Fe1/W1	4	0	0.1677(2)	0.75	0.0206(3)[1]
O1	8	0.2235(8)	0.1164(7)	0.4180(7)	0.0115(12)
Atom	U11	U22	U33	U12	U13	U23
Fe1/W1	0.0157(5)	0.0243(5)	0.0217(5)	0	0.0020(10)	0

Parameters of the occupational wave using crenel function (x_4^0 and Δ are the center and the width of the wave along the x_4 axis, respectively).

Atom	x_4^0	Δ
Fe1	0.7594(8)	0.6667
W1	0.2594(8)	0.3333

Amplitudes of the displacive modulation function

Atom	**xcos1**	**ycos1**	**zcos1**	**xsin1**	**ysin1**	**zsin1**
Fe1/W1	0	0.0016(4)	0	0	-0.0044(5)	0
O1	-0.0336(17)	-0.0136(15)	-0.001(3)	-0.010(2)	0.010(3)	0.0144(15)

At this stage, the profile fitting of the satellite reflections is not satisfactory because the refinement does not take into account their broadening. A method, based on a line-broadening model, proposed by Leineweber & Petrıcek in 2007[46] designed for incommensurately modulated structures and successfully used in similar cases[47,48] was then applied. The refinement of the values of the twelve *S*'$_{hklm}$ coefficients, describing the line-broadening in case of orthorhombic symmetry, leads to three *S*'$_{hklm}$ coefficient values, *S*'$_{2002}$, *S*'$_{2002}$ and *S*'$_{0022}$, significantly higher than the other *S*'$_{hklm}$ coefficients, whose values are set to 0. The refinement leads to a significant improvement in the reliability factors, and the broadening of the satellite reflections is now correctly described (see the final Rietveld refinement plot displayed in Figure II-19). Refining the β-value, by adding a single refined parameter, led to significantly lower R-values compared to those obtained with the commensurate model. A small amount of Fe_2O_3 phase (< 4 vol. %) is present in the ceramic sample. Refinement tests considering the formula $Fe^{3+}_{2-2x}W^{6+}_{1+x}O_6$ with an equation linking Δ(Fe1) and Δ(W1) surprisingly resulted in an Fe-rich

composition, which is the opposite of what is targeted. This test composition was abandoned and the stoichiometric composition Fe_2WO_6 was reapplied and considered as the final formula. Figure II-20a-f shows the occupational and positional modulations of Fe1, W1 and O1 atoms along the x_4 axis. Table II-5 gives the selected interatomic distances in the Fe_2WO_6 ceramic sample and Figure II-21 represents the detailed distributions of the Fe–O and W–O distances. The distances of the Fe-O and W-O bonds in the incommensurately modulated Fe_2WO_6 structure are in the range of standard values.

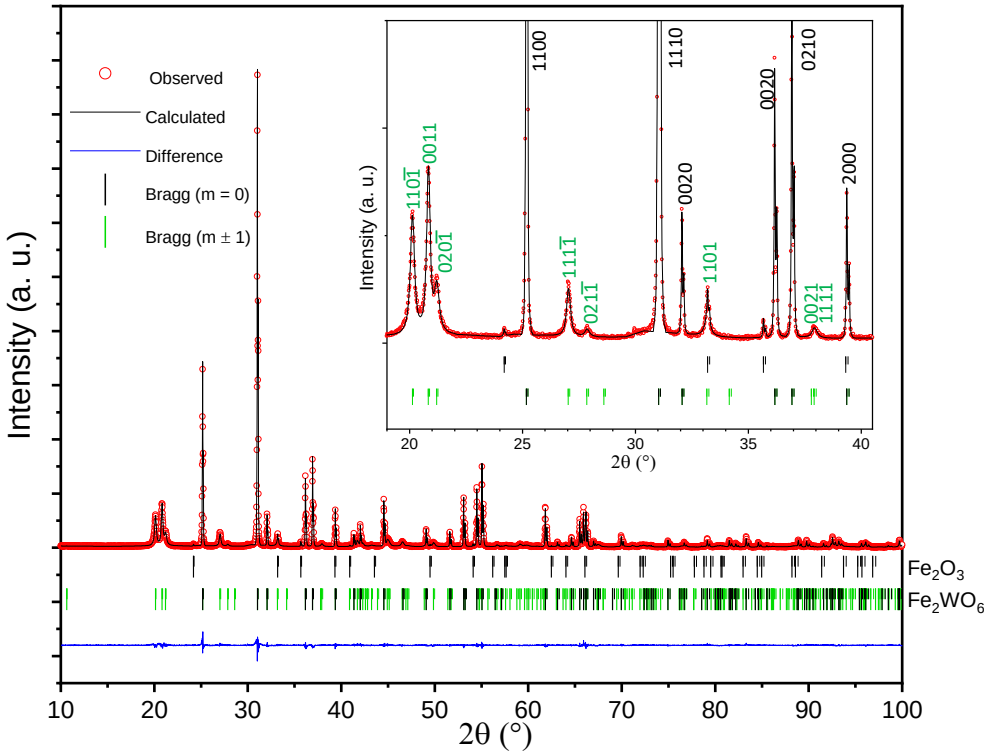

Figure II-19. *Final Rietveld refinement plot of the XRD data at RT of the Fe_2WO_6 ceramic sample with Cu-Kα1-Kα2 radiation. The inset shows a portion of the pattern with indexation of the main and satellite reflections. Long and short ticks correspond to Kα1 and Kα2, respectively.*

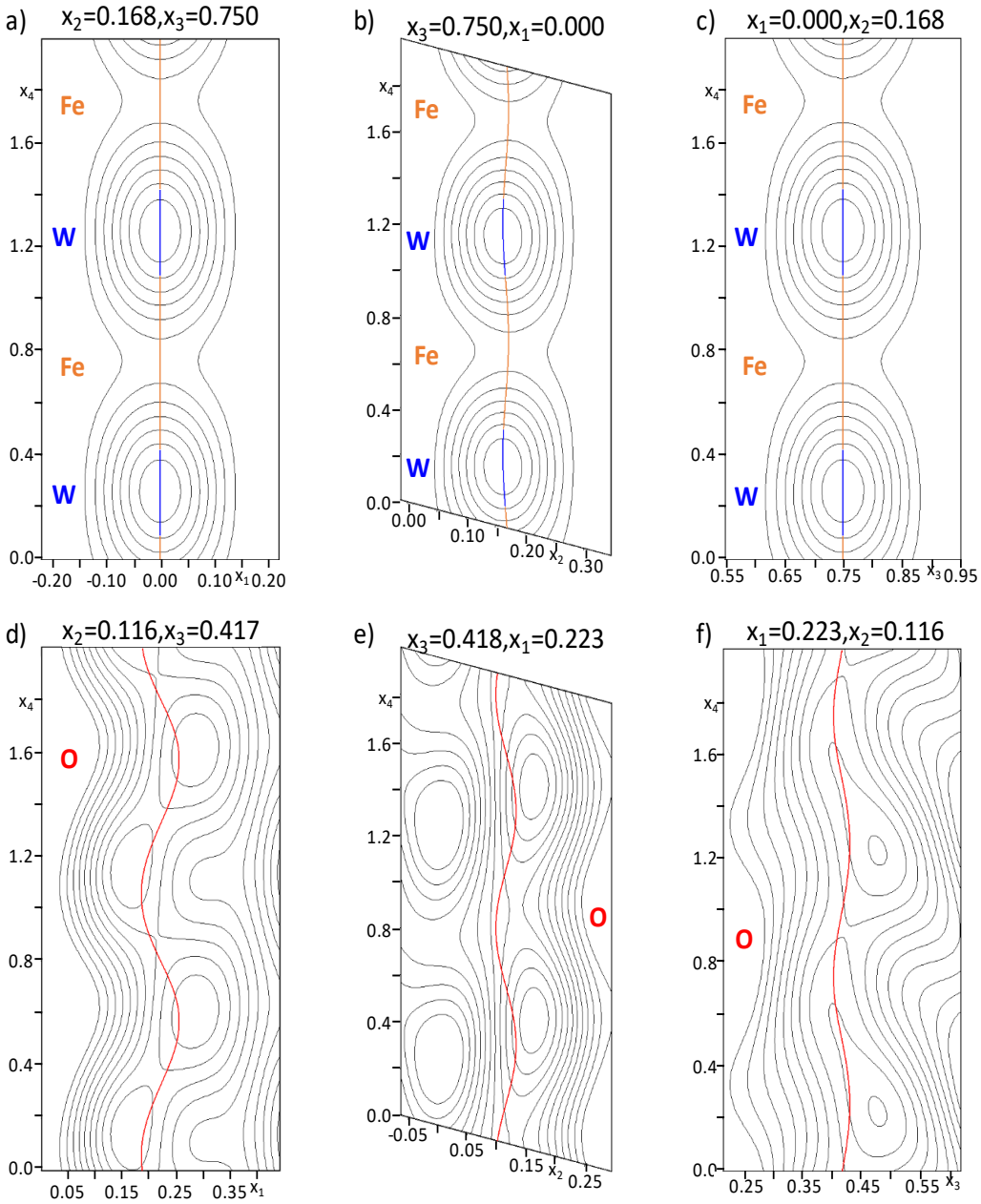

Figure II-20. *De Wolff x_1–x_4, x_2–x_4 and x_3–x_4 sections showing the occupational and positional modulations of Fe, W and O in Fe_2WO_6 ceramic sample as a function of the internal x_4 axis calculated in the vicinity of the atomic position (x_1 = x, x_2 = y, x_3 = z). The central colored lines correspond to the calculated atomic positions (orange—Fe; blue—W; red—O).*

Table II-5. *Selected interatomic distances (Å) and bond valence sums (BVS) in the modulated structure of Fe_2WO_6 ceramic sample.*

	Average	Minimum	Maximum
Fe1-O1	2.012(11)	1.873(13)	2.084(13)
Fe1-O1^{ii}	1.993(11)	1.839(13)	2.076(13)
Fe1-O1^{iii}	2.012(11)	1.873(13)	2.084(13)
Fe1-O1^{iv}	1.993(11)	1.839(13)	2.076(13)
Fe1-O1^{v}	2.131(12)	1.973(14)	2.224(14)

Fe1-O1^{vi}	2.131(12)	1.973(14)	2.224(14)
W1-O1	1.876(10)	1.846(12)	1.953(12)
W1-O1^{ii}	1.834(11)	1.803(13)	1.907(13)
W1-O1^{iii}	1.876(10)	1.846(12)	1.953(12)
W1-O1^{iv}	1.834(11)	1.803(13)	1.907(13)
W1-O1^{v}	1.936(11)	1.906(13)	2.001(13)
W1-O1^{vi}	1.936(11)	1.906(13)	2.001(13)
BVS Fe1	2.9016(15)	2.329(11)	3.965(11)
BVS W1	6.573(8)	5.781(11)	7.026(11)
BVS O1	2.0625(17)	1.669(11)	2.444(11)

Symmetry codes: (ii) $-x_1+1/2, -x_2+1/2, x_3+1/2, -x_4$; (iii) $-x_1, x_2, -x_3+3/2, x_4$; (iv) $x_1-1/2, -x_2+1/2, -x_3+1, -x_4$; (v) $-x_1, -x_2, -x_3+1, -x4$; (vi) $x_1, -x_2, x_3+1/2, -x_4$.

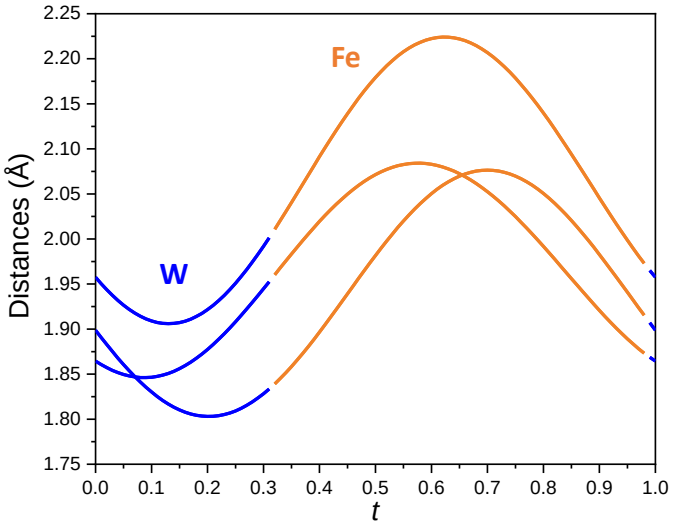

Figure II-21. *Evolution of W–O and Fe–O distances versus the internal parameter* t *of the* Fe_2WO_6 *ceramic sample.*

II.4.5.1. Crystallite size of the ordered domains in Fe_2WO_6 samples

For the XRDP of the ceramic sample, we are in the special case where, first, the line broadening occurs only for the satellite reflections, as the main reflections are narrow and, second, only the first-order (i.e. $m \pm 1$) satellite reflections are present on the pattern.[46–48] Therefore, variations in the q vector are mainly responsible for the broadening of the satellites observed in the experiment.[46] This result confirms the use of an incommensurate structural model to solve and refine the XRD plot of the Fe_2WO_6 ceramic powder.

The values of the refined parameters S'_{2002}, S'_{2002} and S'_{0022} could be related to the anisotropic size of the ordered domains in the Fe_2WO_6 samples.[46] The effective crystallite size

D_x along the three crystallographic directions could thus be calculated[48] for the ceramic sample. The same calculations were carried out for the polyol samples heated to 900 or 950°C after performing similar Rietveld refinements. For those refinements, the β component of the modulation vector is, as for the ceramic sample, significantly different from the 2/3 (≈ 0.66667) rational ratio (difference > 6 σ(β) and 4 σ(β) for 950°C and 900°C polyol samples, respectively).

The results are summarized in Table II-6. We observe that the β component deviates more from the rational value 2/3 in the polyol samples compared to the ceramic and conclude that the synthesis route has strong influence on this value. As expected, the effective crystallite sizes are highest for the ceramic sample, ranging from 200 to 500 Å, and lowest for the polyol sample heated to 900°C, ranging from 16 to 45 Å. The ceramic phase was then heat-treated at 950°C, with intermediate grinding and XRPD, for a total of 100 h. The results show a continuous decrease in *S*' values associated with a continuous increase in domain size. The phase, ceramic or polyol annealed at 900 or 950°C, does not consist of one single domain but is composed from small, differently oriented domains. The limited size of these domains leads to a size-broadening of the satellite reflections. However, the main reflections are not broadened, because the basic structure of the differently oriented domains diffracts coherently. In later stages of annealing, the coarsening of the initially small ordered domains leads to a narrowing of the satellite reflections and an increase in the size of the domains.

Table II-6. *Peak profile parameters S'HKL2 for line broadening of satellite reflections and effective size Dx along the three crystallographic directions of Fe_2WO_6 ceramic sample heated at 950°C and polyol samples heated at 900 or 950°C. For each incommensurately modulated structure, the value of β in $q = \beta b^*$ is given.*

	Ceramic 950°C	**Polyol 950°C**	**Polyol 900°C**
β	0.66872(17)	0.6705(6)	0.697(7)
S'2002 (°/Å²)²	13.34(9)	37.1(5)	3166(37)
S'0202 (°/Å²)²	14.91(12)	31.7(5)	277(11)
S'0022 (°/Å²)²	3.03(8)	16.8(3)	1586(21)
$\boldsymbol{D_{x\|\|a^*_{orth}}}$**(Å)**	≈ 251	≈ 151	≈ 16
$\boldsymbol{D_{x\|\|b^*_{orth}}}$**(Å)**	≈ 195	≈ 134	≈ 45
$\boldsymbol{D_{x\|\|c^*_{orth}}}$**(Å)**	≈ 486	≈ 207	≈ 21

The Figure II-22 shows the 3D structure of the Fe_2WO_6 ceramic sample as a function of the internal t ($0 \leq t \leq 1$) parameter. When the parameter t varies from 0 to 1 values, the occupational modulations change the nature of the cations in the MO_6 octahedra and these are associated with the positional modulations that change the distances of the Fe-O and W-O bonds. When the M-O bond distances increase, the cation type changes from W to Fe and when

the M-O bond distances decrease, the cation type changes from Fe to W, in agreement with the Shannon ionic radii.[49] In general, the cell is composed of one W cation and three Fe cations and there are few values of t for which two Fe atoms and two W atoms are present at the same time. This leads, by adding cell compositions at each t, to the final formula Fe_2WO_6. The modulated structure is significantly different from the reported γ-Fe_2WO_6 in which Fe and W atoms are ordered in zigzag chains of edge-sharing octahedra (Figure II-17).[18] This new structural description may help to better understand the properties of future research dealing with this material or similar compounds, especially with regards to the reported electrochemical properties.

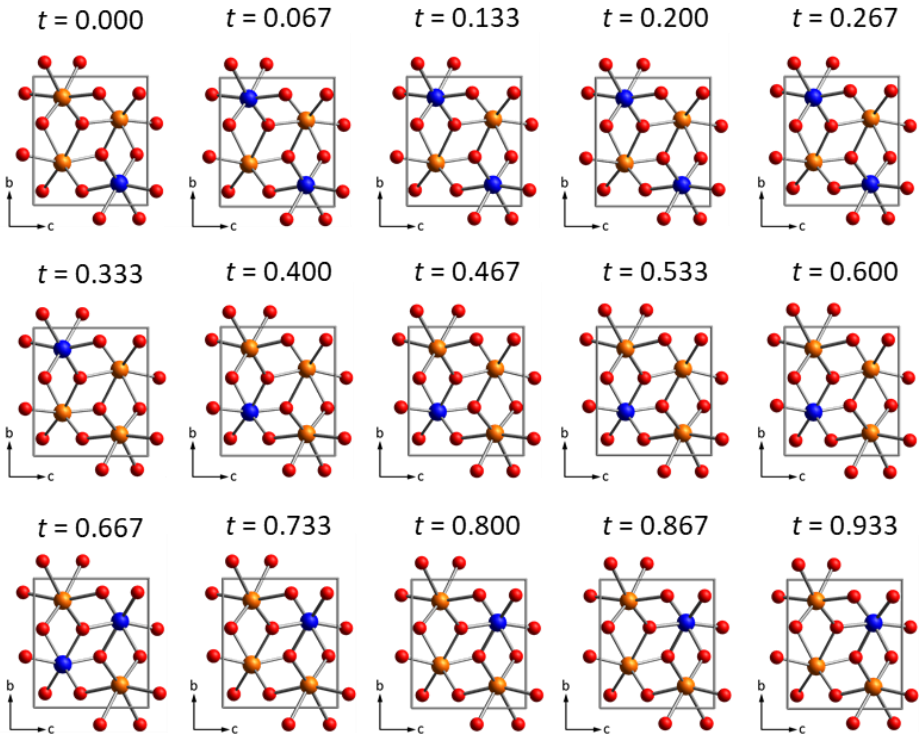

Figure II-22. *3D structure of the Fe_2WO_6 ceramic sample as a function of parameter t(orange: Fe; blue: W; red: O).*

II.4.5.2. Preliminary conclusions on Fe_2WO_6 powder with incommensurate modulations

For the first time, we solved the powder structure of a promising material, Fe_2WO_6, prepared by two different synthesis methods and annealed at 900 or 950 °C. The phases exhibit an incommensurately modulated structure and crystallize in (3 + 1)-D Pbcn(0 0.66872(17) 0)000 superspace group. The variation of the q value of the modulation vector broadens the satellite reflections compared to the main reflections, which remain narrow. This broadening is related to the small size of the ordered domains.

II.5. Conclusions – Chapter II

This chapter presents an electrochemical and crystallographic study for the multicationic compound iron tungsten oxide in its form of Fe_2WO_6. As for the moment of writing this manuscript, we report for the first time this low-temperature s (220 °C) synthesis method for the synthesis of such an oxide. The amorphous as-synthesized powder recovered was further annealed in air at different temperatures, showing the evolution of the crystallization starting at 600 °C, leading to a well-crystallized material at 800 °C. Simultaneously, the specific surface area decreased upon increasing the temperature. The electrochemical performance and cycling stability of selected Fe_2WO_6 powders were then investigated as negative electrode materials in an electrochemical capacitor using a 5M $LiNO_3$ aqueous electrolyte. We succeeded in achieving the best performance for the sample annealed at 600 °C (FWO-600), which at the same time exhibited the most prolonged cycling stability, not very studied for such oxide materials. A specific and volumetric capacitance of 38 $F.g^{-1}$ and 240 $F.cm^{-3}$ were obtained when cycled at 2 $mV.s^{-1}$, respectively, and a quasi-rectangular shape corresponding to a typical pseudocapacitive signature was depicted, showing many similarities with the previously studied $FeWO_4$.

As FWO-600 presented such an exciting behavior at long-term stability (up to 10,000 cycles at 20 $mV.s^{-1}$) study was performed for FWO-600 with only ~15% loss in capacitance. TEM observations, Mössbauer spectroscopy, and magnetization measurements were further used to correlate the fade in capacitance to microstructural or structural changes. All the experiments demonstrated that the morphology, crystallographic structure, and magnetic properties were not affected by the electrochemical cycling nor simple prolonged soaking in the electrolyte. No partial dissolution at the surface of the particles nor Fe^{2+} formation could be detected, confirming thus the stability of the material. However, some slight corrosion of the current collector at the interface with the electrode was noticed, which could be due to dissolved oxygen in the aqueous electrolyte, hence explaining the capacitance fade after 10,000 cycles.

Therefore, Fe_2WO_6 material represents another option of a multicationic oxide exhibiting very interesting pseudocapacitive performance in density, volumetric capacitance, and long-term cycling behavior.

On the other hand, the crystallographic study established a relationship between the structure and synthesis methods having a strong influence on the incommensurate modulation

vector *q* and, by extension, on the size of the ordered domains. This study provided a better understanding of the crystal structure of A_2BO_6-type polycrystalline compounds, which may be beneficial for future research to determine the structure-property relationship of analogous compounds.

These results have brought new highlights about the mechanism ruling the stability of multicationic oxides upon electrochemical cycling. Adjusting different parameters such as the crystallinity, microstructure or specific surface area of the electrode material could lead to optimized electrochemical properties of oxide materials used in aqueous-based electrochemical capacitors.

II.6. References – Chapter II

1. Trasatti, S. & Buzzanca, G. Ruthenium dioxide: A new interesting electrode material. Solid state structure and electrochemical behaviour. *J. Electroanal. Chem. Interf. Electrochem.* **29**, A1–A5 (1971).
2. Lee, H. Y. & Goodenough, J. B. Supercapacitor Behavior with KCl Electrolyte. *J. Solid State Chem.* **144**, 220–223 (1999).
3. Toupin, M., Brousse, T. & Bélanger, D. Influence of Microstucture on the Charge Storage Properties of Chemically Synthesized Manganese Dioxide. *Chem. Mater.* **14**, 3946–3952 (2002).
4. Wu, N.-L. Nanocrystalline oxide supercapacitors. *Mater. Chem. Phys.* 6 (2002).
5. Crosnier, O. *et al.* Polycationic oxides as potential electrode materials for aqueous-based electrochemical capacitors. *Curr Opin Electrochem* **9**, 87–94 (2018).
6. Kuo, S.-L. & Wu, N.-L. Electrochemical Capacitor of MnFe2O4 with NaCl Electrolyte. *Electrochem. Solid-State Lett.* **8**, A495 (2005).
7. Abdollahifar, M. *et al.* High-performance carbon-coated ZnMn2O4 nanocrystallite supercapacitors with tailored microstructures enabled by a novel solution combustion method. *J. Power Sources* **378**, 90–97 (2018).
8. Goubard-Bretesché, N., Crosnier, O., Payen, C., Favier, F. & Brousse, T. Nanocrystalline FeWO4 as a pseudocapacitive electrode material for high volumetric energy density supercapacitors operated in an aqueous electrolyte. *Electrochem. commun.* **57**, 61–64 (2015).
9. Kuo, S.-L., Lee, J.-F. & Wu, N.-L. Study on Pseudocapacitance Mechanism of Aqueous MnFe2O4 Supercapacitor. *J. Electrochem. Soc.* **154**, A34 (2007).
10. Augustyn, V., Simon, P. & Dunn, B. Pseudocapacitive oxide materials for high-rate electrochemical energy storage. *Energy Environ. Sci.* **7**, 1597 (2014).
11. Simon, P., Brousse, T. & Favier, F. *Supercapacitors Based on Carbon or Pseudocapacitive Materials*. (John Wiley & Sons, Inc., 2017). doi:10.1002/9781119007333.
12. Lannelongue, P. *et al.* Investigation of Ba0.5Sr0.5CoxFe1-xO3-δ as a pseudocapacitive electrode material with high volumetric capacitance. *Electrochim. Acta* **271**, 677–684 (2018).
13. Goubard-Bretesché, N., Crosnier, O., Buvat, G., Favier, F. & Brousse, T. Electrochemical study of aqueous asymmetric FeWO 4 /MnO 2 supercapacitor. *J. Power Sources* **326**, 695–701 (2016).
14. Goubard-Bretesché, N. *et al.* Unveiling Pseudocapacitive Charge Storage Behavior in FeWO4 Electrode Material by Operando X-Ray Absorption Spectroscopy. *Small* **16**, 2002855 (2020).
15. Kendrick, E., Świątek, A. & Barker, J. Synthesis and characterisation of iron tungstate anode materials. *J. Power Sources* **189**, 611–615 (2009).
16. Rawal, S. B., Ojha, D. P., Sung, S. D. & Lee, W. I. Fe2WO6/TiO2, an efficient visible-light photocatalyst driven by hole-transport mechanism. *Catal. Commun.* **56**, 55–59 (2014).

17. Abdi, F. F., Chemseddine, A., Berglund, S. P. & van de Krol, R. Assessing the Suitability of Iron Tungstate (Fe2WO6) as a Photoelectrode Material for Water Oxidation. *J. Phys. Chem. C.* **121**, 153–160 (2017).

18. Senegas, J. & Galy, J. L'oxyde double Fe2WO6. I. Structure cristalline et filiation structurale. *J. Solid State Chem.* **10**, 5–11 (1974).

19. Pinto, H., Melamud, M. & Shaked, H. Magnetic structure of Fe2WO6, a neutron diffraction study. *Acta Crystallogr., Sect. A.* **33**, 663–667 (1977).

20. Walczak, J., Rychiowska-Himmel, I. & Tabero, P. Iron(III) tungstate and its modifications. *J. Mater. Sci.* **27**, 3680–3684 (1992).

21. Fievet, F., Lagier, J. P., Blin, B., Beaudoin, B. & Figlarz, M. Homogeneous and heterogeneous nucleations in the polyol process for the preparation of micron and submicron size metal particles. *Solid State Ion.* **32–33**, 198–205 (1989).

22. Viau, G., Fiévet-Vincent, F. & Fiévet, F. Monodisperse iron-based particles: precipitation in liquid polyols. *J. Mater. Chem.* **6**, 1047–1053 (1996).

23. Trenque, I., Mornet, S., Duguet, E. & Gaudon, M. New Insights into Crystallite Size and Cell Parameters Correlation for ZnO Nanoparticles Obtained from Polyol-Mediated Synthesis. *Inorg. Chem.* **52**, 12811–12817 (2013).

24. Dong, H., Chen, Y.-C. & Feldmann, C. Polyol synthesis of nanoparticles: status and options regarding metals, oxides, chalcogenides, and non-metal elements. *Green Chem.* **17**, 4107–4132 (2015).

25. Ungelenk, J., Speldrich, M., Dronskowski, R. & Feldmann, C. Polyol-mediated low-temperature synthesis of crystalline tungstate nanoparticles MWO4 (M = Mn, Fe, Co, Ni, Cu, Zn). *Solid State Sci.* **31**, 62–69 (2014).

26. Guskos, N. *et al.* Magnetic and EPR Studies of α-, β-, and γ-Fe2WO6 Phases at Low Temperatures. *J. Solid State Chem.* **120**, 216–222 (1995).

27. Petříček, V., Dušek, M. & Palatinus, L. Crystallographic Computing System JANA2006: General features. *Z. Kristallogr. Krist.* **229**, 345–352 (2014).

28. Brousse, T. *et al.* Long-term cycling behavior of asymmetric activated carbon/MnO2 aqueous electrochemical supercapacitor. *J. Power Sources* **173**, 633–641 (2007).

29. Gogotsi, Y. & Simon, P. True Performance Metrics in Electrochemical Energy Storage. *Science* **334**, 917–918 (2011).

30. Brousse, T., Bélanger, D. & Long, J. W. To Be or Not To Be Pseudocapacitive? *J. Electrochem. Soc.* **162**, A5185–A5189 (2015).

31. Ghodbane, O., Ataherian, F., Wu, N.-L. & Favier, F. In situ crystallographic investigations of charge storage mechanisms in MnO2-based electrochemical capacitors. *Journal of Power Sources* **206**, 454–462 (2012).

32. Hsieh, Y.-C., Lee, K.-T., Lin, Y.-P., Wu, N.-L. & Donne, S. W. Investigation on capacity fading of aqueous MnO2·nH2O electrochemical capacitor. *J. Power Sources* **177**, 660–664 (2008).

33. Ataherian, F. & Wu, N.-L. Long-Term Charge/Discharge Cycling Stability of MnO2 Aqueous Supercapacitor under Positive Polarization. *J. Electrochem. Soc.* **158**, A422 (2011).

34. Grosse, G. *PC-Mos II, Version 1.0 Manual and Program Documentation.* (1993).

35. Tyczyński, P. *et al.* Performance of Maraging Steel Sleeves Produced by SLM with Subsequent Age Hardening. *Materials* **13**, 3408 (2020).

36. Birchall, T., Hallett, C., Vaillancourt, A. & Ruebenbauer, K. A study of iron–tungsten oxides and iron–chromium–tungsten oxides. *Can. J. Chem.* **66**, 698–702 (1988).

37. Parant, C. & Bernier, J. C. *C R Acad Sc* **276**, 495–497 (1973).

38. Caubergh, S. *et al.* Original Network of Zigzag Chains in the β Polymorph of Fe_2WO_6: Crystal Structure and Magnetic Ordering. *Inorg. Chem.* **59**, 9798–9806 (2020).

39. Guskos, N. *et al.* Electrical transport and EPR properties of the α, β, and γ phases of Fe2WO6. *Phys. Rev. B* **60**, 7687–7690 (1999).

40. Panja, S. N., Kumar, J., Harnagea, L., Nigam, A. K. & Nair, S. γ -Fe2WO6 – A magnetodielectric with disordered magnetic and electronic ground states. *J. Magn. Magn.* **466**, 354–358 (2018).

41. Pak, J.-J., Bahgat, M. & Paek, M.-K. Synthesis of nanocrystalline Fe–W composite through hydrogen reduction of thermally synthesized iron tungstate, Fe2WO6. *J. Alloys Compd.* 7 (2009).

42. Espinosa-Angeles, J. C. *et al.* Investigating the Cycling Stability of Fe2WO6 Pseudocapacitive Electrode Materials. *Nanomaterials* **11**, 1405 (2021).

43. Cheary, R. W. & Coelho, A. A. Axial Divergence in a Conventional X-ray Powder Diffractometer. I. Theoretical Foundations. *J. Appl. Crystallogr.* **31**, 851–861 (1998).

44. Waburg, M. & Müller-Buschbaum, Hk. ZnTa2O6, ein neuer Vertreter des tri-α-PbO2-Typs (mit ergänzenden Daten über ZnNb2O6). *Z. Anorg. Allg. Chem.* **508**, 55–60 (1984).

45. Zhao, D. *et al.* Structure modulation, band structure, density of states and luminescent properties of columbite-type ZnNb2O6. *CrystEngComm* **18**, 2929–2936 (2016).

46. Leineweber, A. & Petricek, V. Microstrain-like diffraction-line broadening as exhibited by incommensurate phases in powder diffraction patterns. *J. Appl. Crystallogr.* **40**, 1027–1034 (2007).

47. Arakcheeva, A. *et al.* KSm(MoO(4))(2), an incommensurately modulated and partially disordered scheelite-like structure. *Acta Crystallogr., Sect. B.* **64**, 160—171 (2008).

48. Leineweber, A. Incommensurately modulated LT″-Ni1+δSn (δ=0.60, 0.63): Rietveld refinement, line-broadening analysis and structural relation with LT- and LT′-Ni1+δSn. *J. Solid State Chem.* **182**, 1846–1855 (2009).

49. Shannon, R. D. Revised effective ionic radii and systematic studies of interatomic distances in halides and chalcogenides. *Acta Crystallogr. A* . **32**, 751–767 (1976)

Chapter III: Chapter III: Electrochemical study of hexagonal tungsten bronzes (HTB): A_xWO_3 (A = Li, Na, and K) as electrode materials for fast energy storage devices

III.1. Introduction

In Chapter, I**,** tungsten oxide, WO_3, was introduced. The different polymorphs such as the γ-WO_3 phase or the hydrated layered compounds WO_3•$2H_2O$ and WO_3•H_2O were described. Nonetheless, little has been done regarding the hexagonal tungsten bronze phases. Indeed, compared to the other polymorphs, only a few studies have been performed in the field of energy storage systems, especially in devices operating with water-based electrolytes. Our group, therefore, decided to investigate these materials and contribute to the understanding and application of such specific phases.

In this chapter, an extensive study on the hexagonal tungsten bronzes (HTBs) with the general formula A_xWO_3 ($0 < x < 0.33$, and A=Li, Na or K) will be presented.

In section II, the HTBs will be introduced, describing their history and some of their structural features. Moreover, the classic synthesis methods will be detailed to pave the way to hydrothermal synthesis used in this work. The importance of the different salts and cations used to obtain the proper phase will be highlighted in this part.

In section III, the study will focus mainly on understanding the role of the cations inside the crystal structure and how they will affect the growth and morphology of the particles. A thorough crystallographic study will be presented to enlighten such interesting features among these phases. In addition, thermal, chemical, and morphological characterizations will be exhibited.

The fourth section will be focused on the electrochemical properties of these materials. Different aqueous-based electrolytes will be used to understand how the nature of these electrolytes plays a role in the electrochemical behavior of the phase. The cation in the electrolyte, concentration, and pH will be evaluated and compared to shed some light on the understanding of the charge storage mechanism.

Furthermore, in the fifth and last section, the study will be dedicated to the classic organic-based electrolyte. An organic *vs.* aqueous-based electrolyte will be compared, the differences between them and the preference for aqueous systems will be discussed.

III.2. Hexagonal tungsten bronzes (HTB)

III.2.1. Introduction

The tungsten bronzes are a widely studied family of compounds with the general formula A_xWO_3, where A can be an alkali metal and x is between 0 and 0.33. The name bronze comes from the synthesis first reported in 1824 when Wöhler[1] passed a flow of dry hydrogen over sodium tungstate while heating it. He observed the growth of yellow crystals with a metallic aspect. These materials were named bronzes because of their brightness characteristic.

The study of the tungsten bronzes continued with Magnéli in the 1950s. He was interested in defining the composition and crystal structure of the phases already reported[2]. At that time, there were already some reports by Hägg[3] on alkaline tungsten bronzes with different symmetries and compositions. These studies led to Magnéli's famous publication in *Nature* in 1952[4], where he described for the first time the six-membered rings of WO_6 octahedra arrangement for the tungsten bronzes as shown in Figure III-1. The general formula for such compounds is M_xWO_3 with M=K, Rb, or Cs and an approximate content of x ~ 0.3.

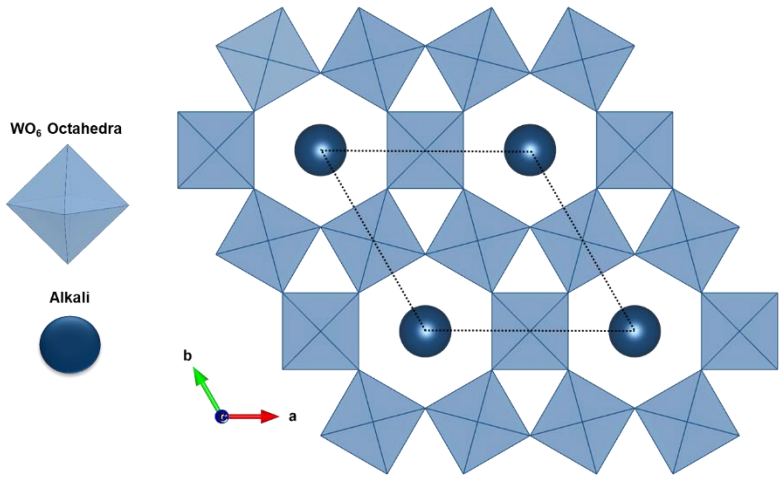

Figure III-1. *Structure of the hexagonal tungsten bronze showing the formation of the six-membered ring WO_6 octahedra.*

This study has contributed to the further investigations of potassium, rubidium, and cesium HTB phases obtained by reducing acid mixtures of tungsten trioxide and tungstates of

the respective alkalis. The structure was elucidated using single-crystal Weissenberg photographs confirming the general formula M_xWO_3, with a theoretical upper limit of *x* of 1/3 and a lattice formed by layers consisting of WO_6 octahedra, containing the alkali atoms distributed in the interstices between layers.[5]

Building on the contributions of Magnéli *et al.*[5], Dickens and Whittingham in the late 1960's examined these materials adopting different symmetries.[6] They attributed three general characteristics to describe tungsten bronzes:

1) if the value of *x* in M_xWO_3 decreases, the symmetry of the structure will decrease.
2) the final structure will depend considerably on the ionic radius of M, and
3) all the bronze structures are based on WO_6 octahedra linked together by sharing their corners.

They all agreed that the WO_3 structure is a distorted version of that of ReO_3[7] (see Figure III-2). In the case of Na_xWO_3, when the value of *x* is between 0.3 and 0.95, it should crystallize in a cubic structure. If sodium content decreases, then the lattice symmetry will also decrease from cubic to tetragonal (I and II, the nomenclature for the tetragonal phases is that of Hägg and Magnéli)[6] until the distorted monoclinic phase of WO_3 is observed. On the other hand, if the alkali content is ≤ 0.05, an orthorhombic structure is formed. This relationship between the different phases can be better observed in Figure III-3.

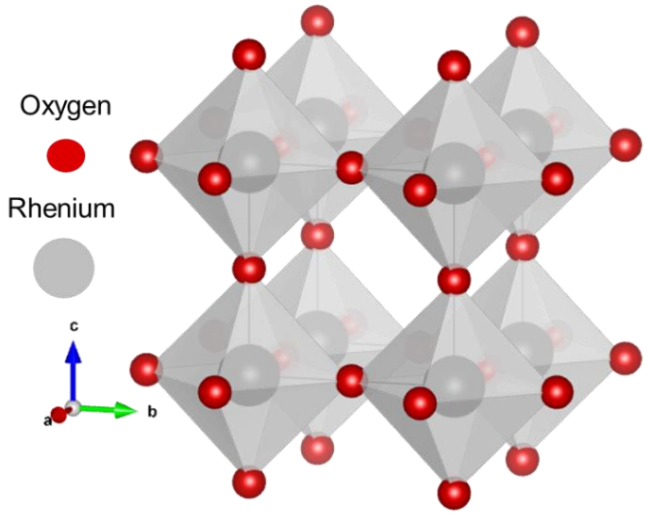

Figure III-2. *ReO_3 structure.*

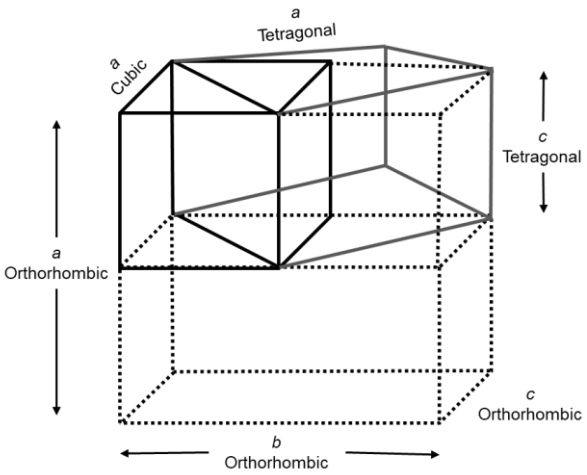

Figure III-3. *Relationship between the phases: cubic, tetragonal II, and orthorhombic.*[6]

Such a relationship involves the amount of alkali within the bronze structure and the role of the synthesis, primarily temperature, as stated by Ribnik, Post, and Banks.[8] Later, the discussion resumed with the assumption that the size of the cavities available in each HTB phase will tend to host different types of cations. The radii of the sites available for occupation are in cubic, 0.96 Å, tetragonal I, 0.96 Å and 1.29 Å, hexagonal, 1.63 Å. Thus, the smaller cations such as Li^+ (0.60 Å) and Na^+ (0.95 Å) will form cubic structures, while in the case of K^+ (1.33 Å), Rb^+ (1.48 Å), and Cs^+ (1.69 Å), will form hexagonal bronzes. Thereby, a new relationship concerning the amount of alkali-metal was presented as in Figure III-4.[6,8] Indeed, this previous approach was not entirely accurate and will be modified as, as discussed later in the chapter.

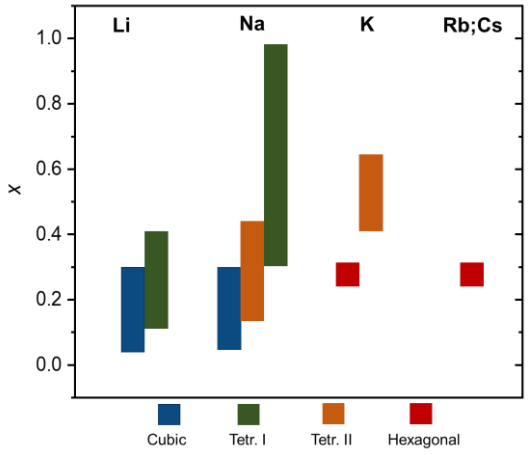

Figure III-4. *Relationship between crystal structure and composition for the alkali tungsten bronzes.*[6,8]

The studies of tungsten phases led to the notice that other families of bronzes can be formed. Similar compounds of molybdenum,[9,10] vanadium,[11] niobium,[12] and titanium[12,13] have been prepared, showing structural properties comparable to those found with tungsten. The term "bronze" can therefore be applied more generally to compounds with the formula $M'_x M''_yO_z$, where M'' is a transition metal, M''_yO_z is its highest binary oxide, M' an alkali or other metal, and *x* can take a value from 0 to 1. Conventional approaches for the synthesis of these compounds will be described below.

III.2.2. Classic synthesis methods

A) Vapor phase reaction: this process is appropriate when the metal used is volatile at high temperature and can be easily manipulated at room temperatures. In this case, the crystals of the bronze are deposited on a cold finger projecting into the reaction container. An example is that reported by Sienko for the synthesis of Tl_xWO_3.[14]

$$xTl_{(g)} + WO_{3\,(g)} = \ Tl_xWO_{3(s)} \qquad \text{Eq. III-1}$$

B) Electrolytic reduction: in this procedure, molten mixtures of tungstate and tungstic oxide are mixed with platinum or tungsten electrodes. Then the crystals grow at the cathode while oxygen is released at the anode. A disadvantage of this technique is the adjustment of the right experimental conditions. This technique has been used not only for tungsten bronzes but for molybdenum bronzes as well.[9]

C) Solid-state reaction: this is a classical synthesis route and the most versatile procedure. Reactant powders are finely ground and heated in *vacuum* to react at different temperatures.[8, 15–19]

$$\frac{x}{2}Na_2WO_4 + \frac{3-2x}{3}WO_3 + \frac{x}{6}W \rightarrow Na_xWO_3\ (at\ 850°C) \qquad \text{Eq. III-2}$$

III.2.3. A new alternative for tungsten oxide preparation: the hydrothermal synthesis

Over the years, there has been considerable interest in WO_3, especially the metastable hexagonal phase. As stated before, the most common route to obtain this compound was high temperature in vacuum or another inert/reducing atmosphere. However, with the development of soft chemistry or "Chimie douce",[20,21] new strategies for synthesizing hybrid and nanomaterials were designed.[22–25] This includes the studies on topochemical reactions, intercalation chemistry, ion-exchange reactions, use of fluxes, sol-gel synthesis, and hydrothermal synthesis.[26] The latter is characterized for inducing a chemical reaction in a closed media where the precursors will react with the solvent (water) at a specific temperature that is higher than the boiling temperature of the corresponding solvent used.[27–30]

Hydrothermal synthesis was first developed for the crystal growth of functional materials and expanded its applications to synthesize new metastable inorganic and hybrid materials.[31–33] To produce these phases, it is necessary to consider chemical and thermodynamical features such as the physicochemical properties of the solvent. They can control the concentration of chemical species and change the kinetics of the reaction. Moreover, they can change the coordination of the solvated species leading to unique structures. The solubility of the reactants and the pH of the solution can impact the composition, the stabilization of specific phases, and a possible effect on the morphology and particle size of the desired materials.

Additionally, temperature and pressure will play an important role. Temperature can influence the kinetics, solubility, and stability of the reactants. With pressure, thermal stability can be enlarged, enhancing chemical reactivity and reaction kinetics and producing denser structures.[30]

With the development of this technology, it has been possible to synthesize a new tungsten trioxide hydrated, $WO_3 \bullet 1/3H_2O$, reported for the first time by Gerand *et al.*[34,35] They used a gel of tungstic acid prepared by the sodium tungstate and hydrochloric acid mixture, placed in a hydrothermal autoclave for 20 h at 120 °C. They claimed that dehydration of this compound led to the formation of pure hexagonal WO_3 (h-WO_3). Further in this chapter, whether or not pure, pristine h-WO_3 can be obtained without the need for alkali cations or water molecules within the lattice will be addressed.

A few years later, Whittingham *et al.*[36] studied the sodium tungstate phases. They used the hydrothermal synthesis already mentioned, analyzing the influence of pH from 1.5 to 4.5. All their syntheses were performed at 155 °C for 3 days of reaction. They reported that when the pH is kept between 3.5 and 4.5, the synthesis leads to a cubic pyrochlore-type lattice compared to the hexagonal phase obtained only when the pH is below 2.5. This study showed how pH could impact the arrangement of the same group of atoms, changing the crystal structure and the morphology of the final particles. They also suggested for the first time the possibility of having water inside the crystal structure. A few years later, this hypothesis was confirmed when they performed a powder neutron diffraction experiment and Rietveld analysis.[37,38] The refinement showed, for the general formula $Na_xWO_{3+x/2}\bullet_yH_2O$, that the oxygen or water atoms are located in the hexagonal cavities, between the layers of the hexagonal rings. On the other hand, sodium atoms can be found at the center of the hexagonal window, in the middle of the hexagonal rings (see Figure III-5).

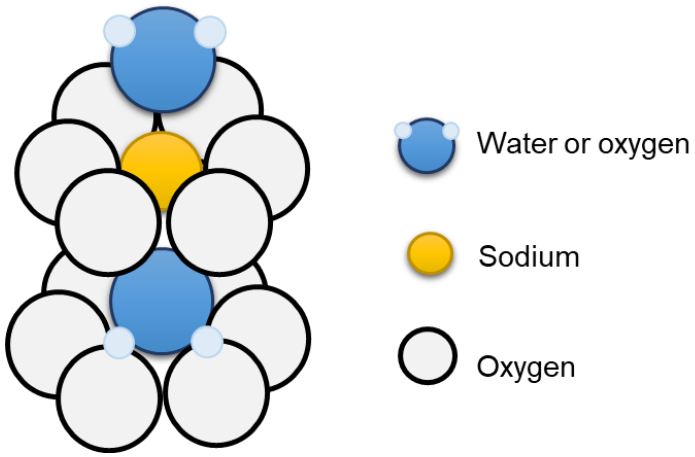

Figure III-5. *Hexagonal tungsten bronze showing sodium atom located in the hexagonal window surrounded by six oxygen atoms and water molecules located in the cavity between the two layers.*[37,38]

As aforementioned, hexagonal tungsten bronzes (HTB) continue to fascinate the scientific community because of their structural properties and the different synthetic approaches that can be used to obtain such phases.[39,40] Thus, in the next section, the experimental procedures followed to synthesize HTBs will be described.

III.2.4. Synthesis of hexagonal tungsten bronzes A_xWO_3 (A= Li, Na and K)

The synthesis followed to produce the HTBs of Li, Na, and K is based on several reports from different authors. They discussed various parameters and conditions that will affect the outcome of the HTB phases. They considered the precursor for tungsten, the pH and the type of acid used, the media, and the type and amount of salt added. Moreover, temperature and time of reaction will also influence the growth of the proper phase, which will impact the morphology of the particles and the crystal structure.[41–45] The description of the synthesis is presented below.

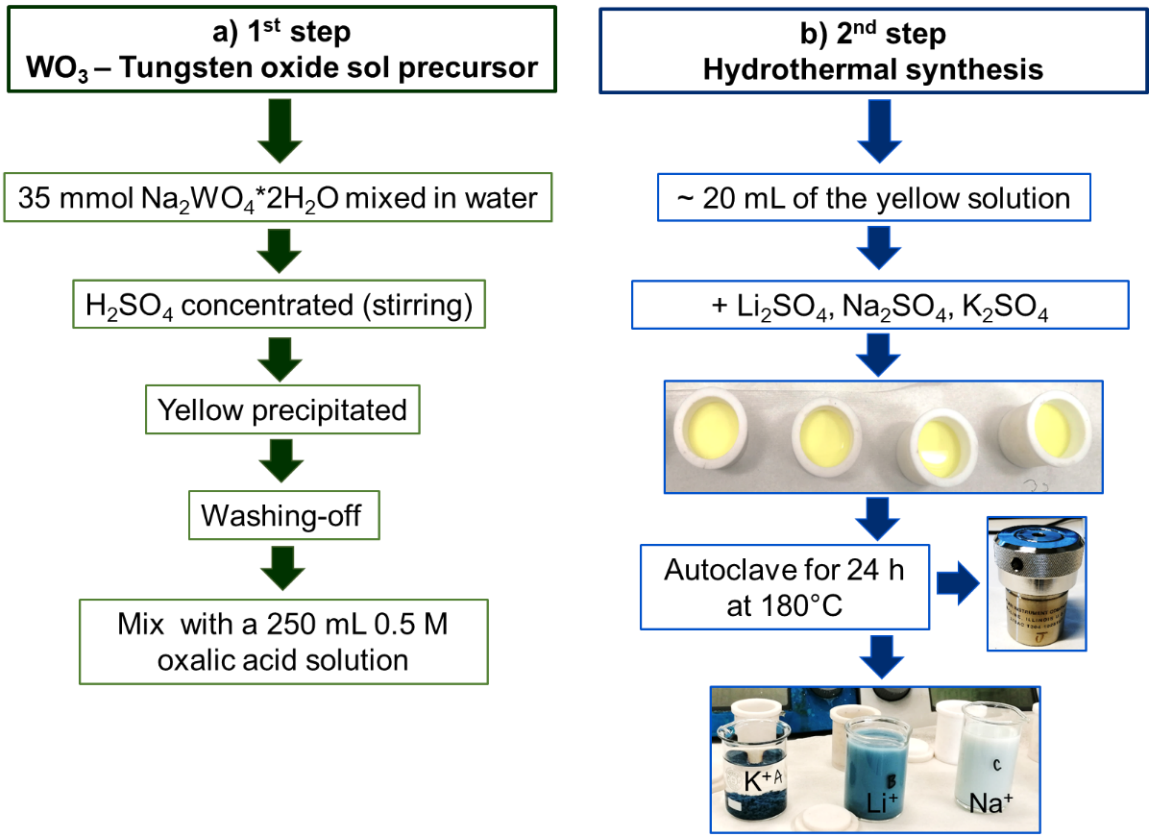

Figure III-6. *Synthesis of the hexagonal tungsten bronzes by hydrothermal route.*

The synthesis of the HTB is divided into two steps. First, 35 mmol of sodium tungstate hydrate (Na_2WO_4•$2H_2O$) (Sigma Aldrich) is mixed with ~150 mL of deionized water. Then, ~15 mL of concentrated H_2SO_4 (Alfa Aesar) is added dropwise under stirring until a uniform yellow precipitated is formed. This mixture is left under stirring overnight to ensure all the precipitation of the WO_3 sol. After 24 h, the sol is washed off with more deionized water to

remove all the extra acidic solution. Once the supernatant is no longer acidic, we can stop the washing, and the sol can be mixed with a solution of 0.5 M oxalic acid (see Figure III-6a) Secondly, the Teflon-lined vessel is placed ~20 mL of the yellow solution with oxalic acid. Then, 2 g of lithium sulfate monohydrate (Alfa Aesar) $Li_2SO_4•H_2O$, 3 g of sodium sulfate Na_2SO_4 (Sigma Aldrich), or 1 g of potassium sulfate K_2SO_4 (Sigma Aldrich) are added depending on the final phase of HTB to be prepared. The vessels are sealed and placed in their respective autoclaves and then transported to an oven where they are left for 24 h at 180 °C, where the hydrothermal reaction occurs (see Figure III-6b).

To compare the formation of the HTB with other WO_3 phases, an extra "blank" sample was synthesized. Before adding the respective salt, only ~20 mL of the yellow WO_3 sol was placed in an autoclave for the hydrothermal reaction.

After the reaction is completed and the autoclaves are cooled, a blueish precipitate is obtained, indicating the achievement of the desired HTB phase, which did not occur for the blank sample that gave a yellow powder. Then, the mixtures are washed off with deionized water several times to remove additional side products and then left to dry ~60-80 °C in air.

III.3. Structural and physicochemical characterizations of hexagonal tungsten bronzes

III.3.1. Introduction

As aforementioned, hexagonal tungsten bronzes are formed by a rigid tungsten-oxygen framework built up of layers containing corner-shared WO_6 octahedra arranged in six-membered rings. The layers are stacked along the [00l] direction, resulting in one-dimensional tunnels, as shown in Figure III-7. The preparation of hexagonal tungsten bronzes in alkali metals leads to the formation of compounds that show structural differences. These are, for example, a different order of the atoms occupying the tunnels, the presence or absence of water molecules, and the formation of regular or distorted tungsten octahedra.

First, a discussion about the prepared blank sample will be presented to verify that the cation involved in the synthesis does affect the structure of the final compound. This blank will be compared to the γ-WO_3 of a commercial brand (Alfa Aesar).

Afterwards, the chemical analysis of the HTBs will be presented, with emphasis on the determination of the water content. The latter will be used to provide helpful information for structural refinement of X-ray diffraction patterns and to elucidate the crystal structure of each material.

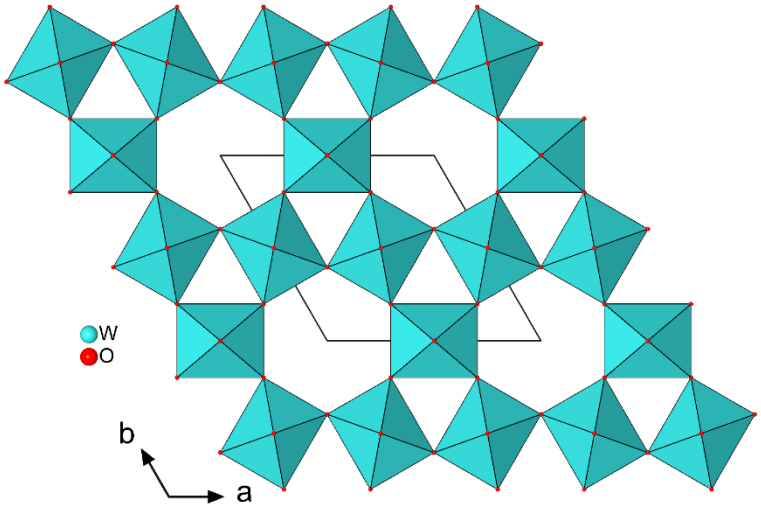

Figure III-7. *Structure of hexagonal tungsten bronze WO_3.*

Before refinement, a small review of the structural parameters of WO_3 with similar compositions reported in the literature will be presented. This study will help to compare or to refute some of those parameters. Then, the results of the structural refinement for HTBs with Li^+, Na^+, and K^+ will be presented, and the structures will be described.

III.3.2. γ-WO_3: Cations are important

In section III.2, the synthesis of the HTBs was described. The synthesis of a "blank" sample was also mentioned. Such a blank sample consisted of taking only the yellow solution and transferring it to the autoclave for the hydrothermal synthesis to occur without adding salt. Without cations for the reaction to occur, the outcome should be a traditional γ-WO_3 phase with a distorted ReO_3 structure. Figure III-8 shows the X-ray diffraction patterns for the "blank" sample as-synthesized and the commercial γ-WO_3 (Alfa Aesar) comparison. Both correspond to JCDPS 01-072-1465[46] in the database. The blank sample shows extra reflections that can explain the differences in particle morphology, as observed in Figure III-8a and b for the as-synthesized sample, and Figure III-8c and d, for the commercial sample. The main differences

between the particles are in their size and morphology. An advantage of the hydrothermal synthesis, even in the absence of cations, is the slightly smaller and better-defined particles than the commercial compound.

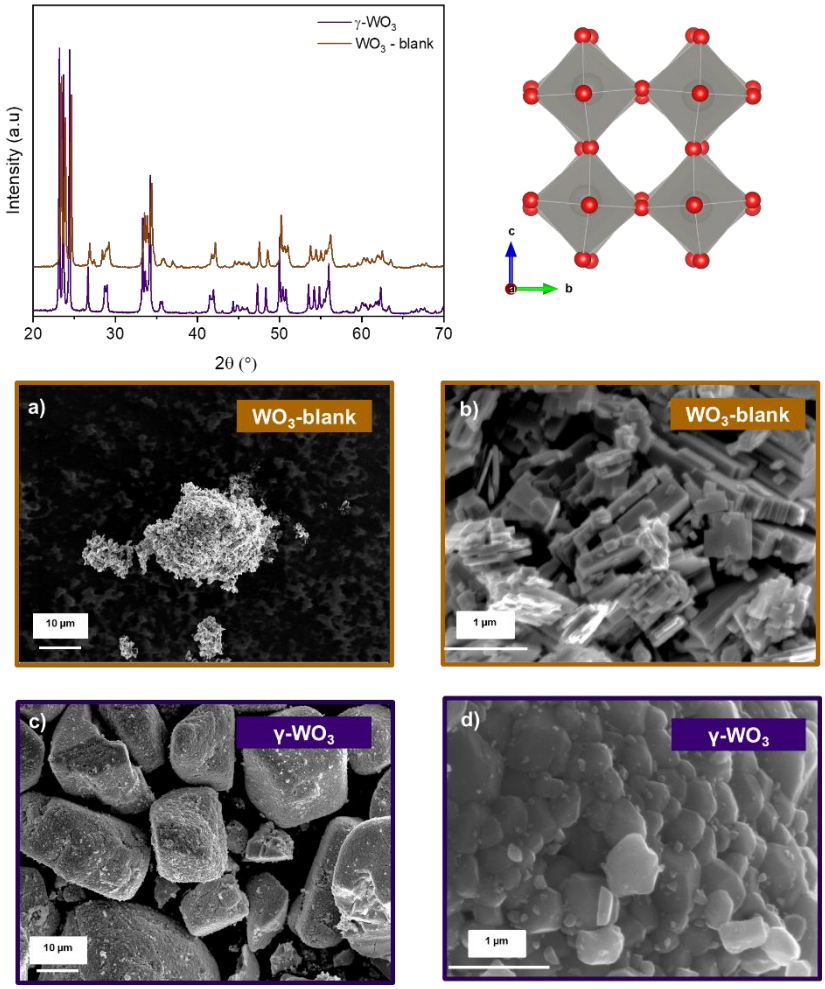

Figure III-8. *X-ray diffraction pattern, crystal structure and SEM imaged for both γ-WO3: blank and reference sample.*

These adopted structures will influence their electrochemical behavior, as observed in Figure III-9. Both WO_3 blank as-synthesized and commercial γ-WO_3 show poor performance when cycling in aqueous 5 M $LiNO_3$ at 2 $mV.s^{-1}$, with 6 and 5 $C.g^{-1}$, respectively.

This first result encouraged us to propose two hypotheses: 1) the salt and, more importantly, the cations used in the synthesis impact the growth and formation of the desired phase. And 2) the hexagonal tungsten bronze structure will exhibit improved electrochemical performance due to the arrangement of its hexagonal windows and hexagonal cavities. Thus, it

allows faster intercalation of cations from the water-based electrolyte. The studies and results carried out to investigate these hypotheses are presented in the following section.

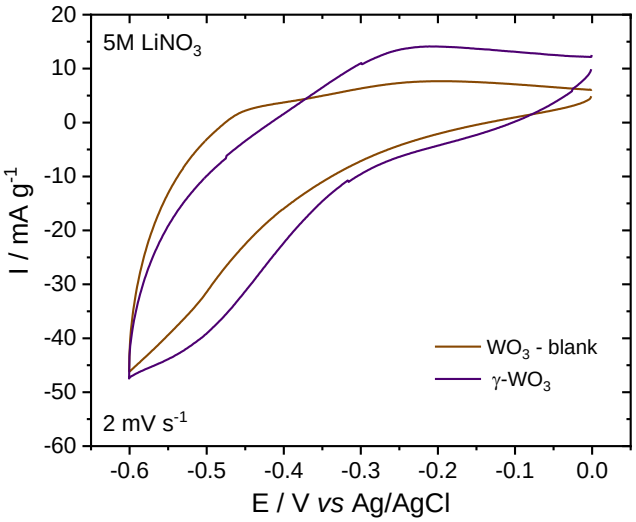

Figure III-9. *Cyclic voltammogram at 2 mV.s-1 of the WO3 blank and commercial γ-WO3 in aqueous 5 M LiNO3.*

III.3.3. Chemical and thermal analysis of HTB

III.3.3.1. Chemical compositions of HTB

EDX analysis was performed to determine the chemical composition for the HTBs of Na and K in a Scanning Electron Microscopy using a Merlin SEM from Carl Zeiss with an X-Max detector 50 mm2 by Oxford Instruments NanoAnalysis. These results revealed that Na HTB and K HTB contain about 0.28 and 0.33 moles of sodium and potassium, respectively. According to previous reports, this number of cations inside the HTBs was expected, where x is found to be $0 < x \leq 0.33$. For the Li compound, EDX analysis did not detect the presence of lithium due to its low atomic number. However, chemical analysis carried out by inductively coupled plasma optical emission spectrometry (ICP-OES), using a Thermo Scientific iCAP 6300 emission spectrometer for analyzing major elements, was able to determine the Li content. Using this technique, we confirmed the presence of Li in this compound with about 0.16 moles per W atom. Compared to the Na and K phases, this smaller amount is expected due to the size

of Li, being much smaller than the other cations. For this reason, it is more difficult to be held within the lattice of the HTBs.

In summary, through these techniques, the identification and the amount of the cation inside the structures of the HTBs were determined.

III.3.3.2. Thermal analysis of HTB

Thermogravimetric analyses (TGA) were performed in a thermal analyzer NETZSCH STA 449 F3. The analyses were carried out under air for the three bronze materials, Li, Na, and K. A mass loss ~ 3 to 4% from the beginning of the experiment to about 350°C was determined for the Li and Na HTBs (see Figure III-10).

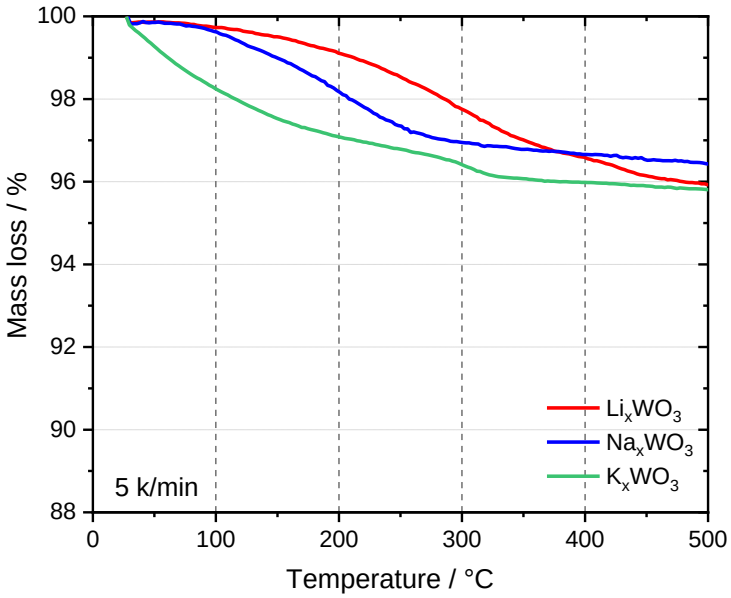

Figure III-10. *TGA analyses of hexagonal tungsten bronzes.*

It is interesting to note that the beginning of the mass loss for the Li and Na compounds is around 100°C while for the K HTB, mass loss begins at room temperature. Therefore, it is likely that some of the mass loss observed for the K compound is water adsorbed only on the surface. The total mass loss after 350°C was estimated to be about ~3.0% for Li and Na HTBs, and 4.0% for K compound. These mass losses result in ~0.4, ~0.44, and ~0.55 of moles of H_2O released after 350 °C, as indicated in Table III-1.

Table III-1. *TGA mass loss and number of H_2O molecules.*

HTB	% Total mass loss	~ H_2O moles
Li_xWO_3	~3.0	~0.4
$Na_{0.28}WO_3$	~3.5	~0.5
$K_{0.33}WO_3$	~4.0	~0.5

Additionally, Figure III-11 compares the HTBs *vs.* the hydrated WO_3 phase reported by Augustyn's group.[47] In the case of the hydrated phase, the loss of water at particular stages is evident. Whereas in the case of the HTBs, the water is gradually lost until achieving a step after 350 °C. In conclusion, through the TGA study, the presence of water molecules in the HTBs was confirmed. Moreover, this information will be helpful for the structural refinement presented next.

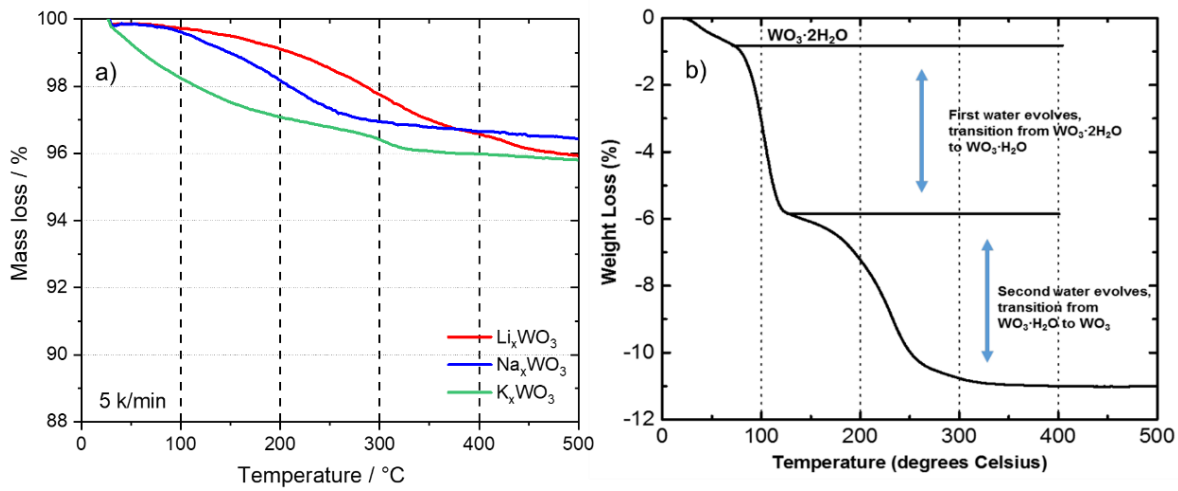

Figure III-11. *TGAs for a) HTBs study reported in this thesis and b) TGA for a hydrated WO_3 phase reported by Augustyn et.al.*[47].

III.3.4. Structure of the Hexagonal Tungsten Bronzes

III.3.4.1. A brief review of the compounds listed in the ICSD database

In the database, two WO_3 compounds that crystallize in hexagonal symmetry can be found (see Table III-2). It is interesting to note that, in the 1979 study, the authors solved the structure in an average cell (V = 179.84 Å^3).[34] Transmission electron microscopy analysis of

WO_3 particles showed additional diffraction spots imposing a doubling of the *c*-parameter. The 1992 study presented a model crystallizing in a cell with a doubled *c*-parameter in the $P6_3/mcm$ space group corresponding to the "large" cell of the 1979 study.[48] Note also that there is no hydrated WO_3 compound in the database crystallizing in a hexagonal symmetry.

Table III-2. *WO_3 compounds crystalizing in the hexagonal symmetry.*

Compound	Space group	Cell parameters	Reference
WO_3	P6/mmm	*a* = 7.298(2) Å, *c* = 3.899(2) Å V = 179.84 Å^3	34
WO_3	$P6_3/mcm$	*a* = 7.3244(6) Å, *c* = 7.6628(5) Å V = 356.01 Å^3	48

For the Li compound, there is no lithium-containing tungsten bronze with a hexagonal structure in the database. There is only one tungsten bronze crystallizing in the P6/mmm space group containing sodium in the ICSD database for Na compounds. This compound is hydrated; its formula is $Na_{0.17}WO_{3.085}\bullet(H_2O)_{0.17}$, and its structure was determined by neutron diffraction[37]. The cell parameters are *a* = 7.331(1) Å, *c* = 3.891(6) Å and V = 181.10 Å^3. The authors mention that the chemical analysis of the compound gives the composition $Na_{0.24}WO_{3.12}\bullet 0.5H_2O$. The difference in water content between refinement and chemical analysis is due to the water adsorbed on the surface. Table III-3 gives the Wyckoff positions as well and the atomic coordinates of the atoms contained in the cell.

Table III-3. *Atomic coordinates in $Na_{0.17}WO_{3.085}\bullet(H_2O)_{0.17}$ compound.[37]*

	Wyck. pos.	x	y	z	SOF
W	3f	0.5	0	0	1
O1	3g	0.5	0	0.5	1
O2	6l	0.2120(3)	2x	0	1
O3	2e	0	0	0.415(6)	0.382
H	12o	0.065(4)	2x	0.302(6)	0.085
Na	1a	0	0	0	0.51

The atoms W, O1, and O2 form the rigid framework composed of WO_6 octahedra arranged in six-membered rings giving the formula WO_3 (see Figure III-7). The O3 and Na atoms are disordered along the *c*-axis with partial occupancy characterized by the Site Occupation Factor (SOF). Some hydrogen atoms are bonded to O3 atoms to form water molecules.

For the potassium phase, there are several tungsten bronzes with hexagonal structures in the database (Table III-4). They all crystallize in hexagonal symmetry with a doubled *c* parameter compared to the cell of $Na_{0.17}WO_{3.085}\bullet(H_2O)_{0.17}$. It should be noted that, among the

compounds listed, two propose the space groups $P6_3$ and $P6_322$. However, the diffractograms of the potassium tungsten bronze reported in this thesis show the presence of a *c*-glide plane and consequently, only the structural model of the publications whose compounds adopt the space group $P6_3/mcm$ is taken into consideration for structure resolution.

The structural models differ from each other in the occupied sites and the filling of these sites. Table III-5 summarizes the occupied sites and SOFs for the atoms contained in the cell of the four compounds 1-4 listed in Table III-4.

Table III-4. *K_xWO_3 compounds crystalizing in the hexagonal symmetry.*

Compound	N°	Space group	Cell parameters	Reference
$\mathbf{K_{0.26}W^{5.7+}O_3}$	-	$P6_3$	*a* = 7.389(1) Å, *c* = 7.508(2) Å V = 355.00 Å^3	49
$\mathbf{K_{0.3}W^{5.7+}O_3}$	-	$P6_322$	*a* = 7.3867(3) Å, *c* = 7.5199(3) Å V = 355.34 Å^3	50
$\mathbf{K_{0.183}W^{5.8+}O_3}$	1	$P6_3/mcm$	*a* = 7.3835(3) Å, *c* = 7.5007(4) Å V = 354.13 Å^3	51
$\mathbf{K_{0.333}W_{0.944}^{6+}O_3}$	2	$P6_3/mcm$	*a* =7.3110(35) Å, *c* = 7.64943(31) Å V = 354.09 Å^3	52
$\mathbf{K_{0.179}W^{5.8+}O_3}$	3	$P6_3/mcm$	*a* = 7.380(9) Å, *c* = 7.492(7) Å V = 353.38 Å^3	53
$\mathbf{K_{0.33}W^{5.67+}O_3}$	4	$P6_3/mcm$	*a* = 7.3742(5) Å, *c* = 7.5169(5) Å V = 354.00 Å^3	54

The W, O1, and O2 atoms form the rigid WO_3 framework (see Figure III-7). Whatever the study considered, the tungsten atoms occupy the same 6g site with a total occupation for the syntheses carried out under reducing conditions (compounds 1, 3, and 4) or partial occupation, in the case of the syntheses, carried out under oxidizing conditions (compound 2). Moreover, the oxidation state of tungsten varies between 5.67 and 6^+ depending on the experimental conditions used. Concerning the O1 oxygen atoms, the studies suggest either a total occupation of the 6f site or a half occupation of the 12k site. All the studies propose the same model for the O2 oxygen atoms which occupy the 12j site. Finally, for the potassium atoms, the studies diverge: some suggest a total or partial occupation of the 2b site or a partial occupation of the 4e site.

Contrary to the sodium compound, there are no oxygen atoms along the *c* axis, and only potassium atoms occupy this axis. In addition, the tungsten atoms are slightly off-center in the WO_6 octahedra, characterized by an x-coordinate slightly different from 0.5. Finally, the WO_6 octahedra are more distorted than those found in the Na compound due to a y-coordinate of O2 atoms slightly different from twice the value of x (y ~ 2x).

The solution of the powder structures of the Li, Na, and K hexagonal tungsten bronzes will be presented and discussed next, considering all reports mentioned above.

***Table III-5**. Summary of atomic coordinates in K_xWO_3 compounds adopting $P6_3/mcm$ space group.*

	Wyck. pos.	**x**	**y**	**z**	**SOF**	**Compound**
W	6g	x ~ 0.47	0	1/4	1	1, 3, 4
	6g	x ~ 0.49	0	1/4	0.944	2
O1	6f	0.5	0	0	1	3, 4
	12k	x ~ 0.47	0	z ~ 0.01	0.5	1, 2
O2	12j	x ~ 0.20	y (~ 2x)	1/4	1	1, 2, 3, 4
K	2b	0	0	0	1	4
	2b	0	0	0	~ 0.55	1, 3
	4e	0	0	z ~ 0.04	0.5	2

III.3.4.2. Refinement analyses of the structures of Li, Na and K HTB

The XRD patterns (XRDP) of the HTB synthesized were recorded in air at room temperature (RT) with a Bruker D8 Advance diffractometer using a Cu-Kα1 radiation (λ = 1.54060 Å) and a LynxEye detector in Bragg-Brentano geometry. The structures of the Li, Na, and K hexagonal tungsten bronzes were refined using the JANA2006 program.[55]

III.3.4.2.1. $Li_{0.167}WO_{3.083}•(H_2O)_{0.25}$

The lithium tungsten bronze compound crystallizes in the same space group P6/mmm as WO_3[34] with cell parameters *a* = 7.3335(3) Å, *c* = 3.86285(17) Å (see Figure III-12). The cell volume 179.913(12) $Å^3$ is close to the cell volume of WO_3, V = 179.84(14) $Å^3$.

The structural refinement of the Li HTB from the X-ray powder pattern started with the structural model of WO_3 containing the following three atoms: W in 3f (0.5,0,0), O1 in 3g (0.5,0,0.5), and O2 in 6l (x,2x,0) with x ~ 0.21. After refinement of atomic positions and atomic displacement parameters (ADP), Fourier difference maps (see Figure III-13) indicated a large

electron density (charge = 4.97) in the 2e (0,0,z) site with z ~ 0.30 (position named "max1"). An atom occupying max1 is too close to another atom occupying max1 (dmax1-max1 = 1.51 Å); the maximum occupancy of max1 is then 0.5. The 2e site occupied by oxygen atoms (= O3) is introduced in the refinement with half-occupancy. As the ADP of O3 resulted negative, this one is fixed at 0.01, and the site occupation factor of O3 is fixed at its maximum, *i.e.*, 0.5. The TGA analysis showed a mass loss of about 3% of the compound from room temperature to 350°C, corresponding to about 0.3 moles of H_2O. Note that the Fourier difference maps did not allow locating the hydrogen atoms. We assume that some of the previously introduced O3 atoms contribute to the water in the structure. In addition, the ICP-OES chemical analysis confirmed 0.16 moles of Li in the compound. Fourier difference maps indicated some electron density located at the 2d Wyckoff position (1/3,2/3,1/2) with M-O distances about 2 Å. Thus, the 2d site occupied by Li atoms is introduced into the refinement with an occupancy of 1/4 and an ADP set at 0.01. Finally, the ADP of W atoms is switched to anisotropy.

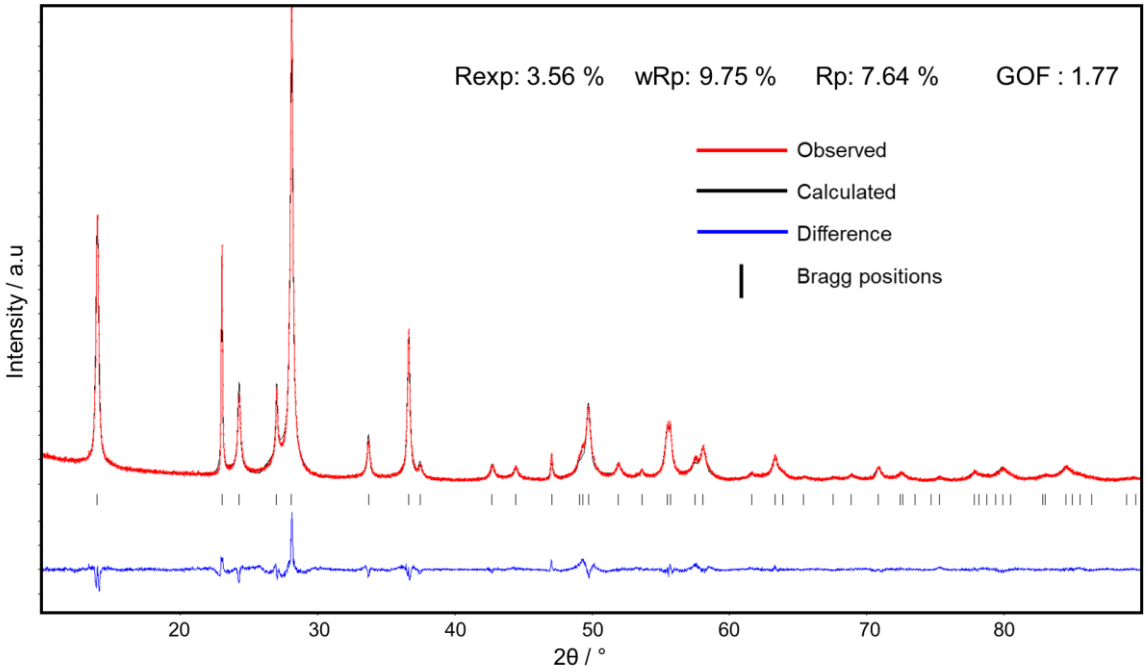

Figure III-12. *Rietveld refinement of* $Li_{0.167}WO_{3.083}(H_2O)_{0.25}$.

The structural refinement of the Li HTB from the X-ray powder pattern started with the structural model of WO_3 containing the following three atoms: W in 3f (0.5,0,0), O1 in 3g (0.5,0,0.5), and O2 in 6l (x,2x,0) with x ~ 0.21. After refinement of atomic positions and atomic displacement parameters (ADP), Fourier difference maps (see Figure III-13) indicated a large electron density (charge = 4.97) in the 2e (0,0,z) site with z ~ 0.30 (position named "max1").

An atom occupying max1 is too close to another atom occupying max1 (dmax1-max1 = 1.51 Å); the maximum occupancy of max1 is then 0.5. The 2e site occupied by oxygen atoms (= O3) is introduced in the refinement with half-occupancy. As the ADP of O3 resulted negative, this one is fixed at 0.01, and the site occupation factor of O3 is fixed at its maximum, *i.e.*, 0.5. The TGA analysis showed a mass loss of about 3% of the compound from room temperature to 350°C, corresponding to about 0.3 moles of H_2O. Note that the Fourier difference maps did not allow locating the hydrogen atoms. We assume that some of the previously introduced O3 atoms contribute to the water in the structure. In addition, the ICP-OES chemical analysis confirmed 0.16 moles of Li in the compound. Fourier difference maps indicated some electron density located at the 2d Wyckoff position (1/3,2/3,1/2) with M-O distances about 2 Å. Thus, the 2d site occupied by Li atoms is introduced into the refinement with an occupancy of 1/4 and an ADP set at 0.01. Finally, the ADP of W atoms is switched to anisotropy.

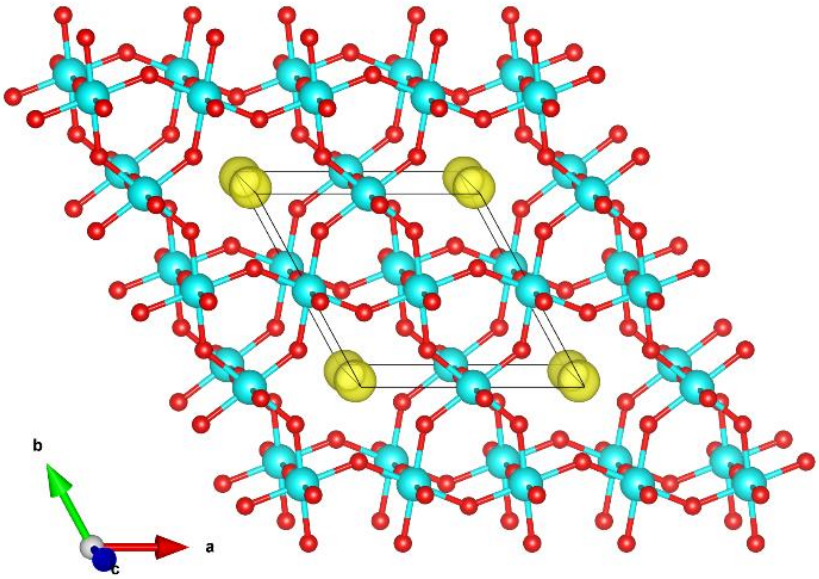

Figure III-13. *Electronic density at 2e (0,0,z) with z ~ 0.30 (max1) obtained after refining the WO_3 model and Fourier differences calculation.*

The formula obtained is $Li_{0.167}WO_{3.333}$ or $Li_{0.167}WO_{3.083}(H_2O)_{0.25}$, taking into account the water molecules in the structure. As with the Na analog,[37] not all the O3 oxygen atoms in the hexagonal cavity are water molecules. To balance the lithium charge, approximately 0.083 oxygen ions must be present. The final atomic coordinates and ADPs are given in Table **III-6**. Figure III-12 shows the observed and calculated diffractograms and their difference and indicates the final reliability factors obtained. Note that a preferred orientation along the [001] direction was introduced during the refinement due to the elongated shape of the rod-shaped

particles obtained after synthesis and an anisotropic size broadening treated by spherical harmonics of order 4[56] were introduced during the refinement. Moreover, considering the fundamental parameters of the powder X-Ray diffractometer, the crystallite size and lattice strain were obtained, being 54.2(8) nm and 0.379(8), respectively.

Table III-6. *Atomic coordinates of* $Li_{0.167}WO_{3.333}$ *compound with a = 7.3335(3) Å, c = 3.86285(17) Å, V = 179.913(12) Å^3, SG P6/mmm.*

Atom	Wyck. pos.	x	y	z	SOF	U_{eq}* / U_{iso} (Å^2)
W1	3f	0.5	0	0	1	0.0287(10)*
O1	3g	0.5	0	0.5	1	0.018(5)
O2	6l	0.1975(6)	0.3950(11)	0	1	0.020(4)
O3	2e	0	0	0.323(8)	0.5	0.01
Li1	2d	0.3333	0.6667	0.5	0.25	0.01

The structure of the lithium hexagonal tungsten bronze can be described by layers of corner-shared WO_6 octahedra arranged in six-membered rings giving rise to one-dimensional tunnels along the *c* axis, as shown in Figure III-14.

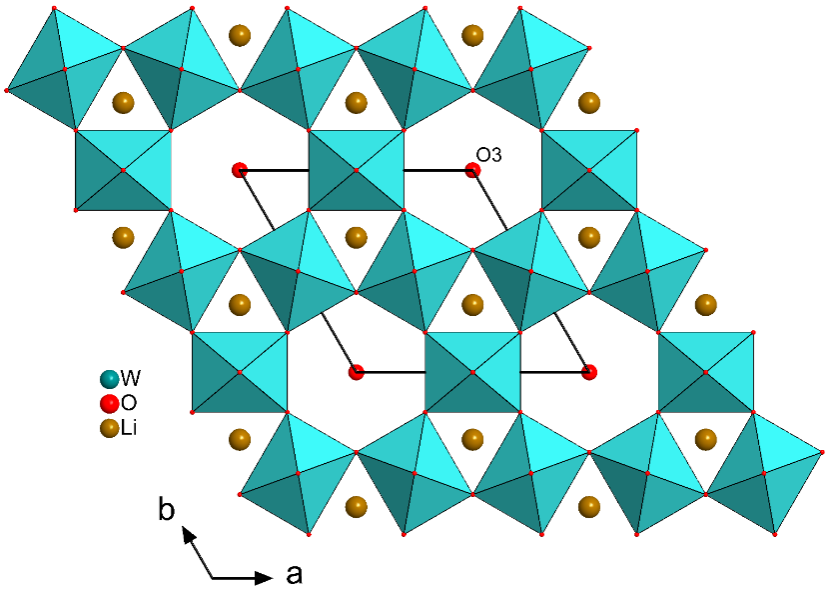

Figure III-14. *Structure of* $Li_{0.167}WO_{3.333}$ *compound.*

The small tunnels formed by WO_6 octahedra arranged in the three-membered ring are 25% filled with lithium atoms (see Figure III-14 and Figure III-15a). The O3 atoms are in the hexagonal cavity and disordered along the *c* axis (see Figure III-15c). The lithium atoms occupy

polyhedra with Li-O distances ranging from 2.117 to 2.590 Å (Figure III-15a). To explain this unusual Li environment, the assumption that the Li site is split into two sites along the *c* axis was made. This leads to two positions, occupied at 1/8, whose environment is a distorted octahedron (see Figure III-15b). Due to the small amount of Li atoms, such split sites could not be detected by Fourier difference maps. Comparable distorted LiO_6 octahedra are observed in other compounds (Li_4WO_5,[57] $LiNbWO_6$[58]). In this case, the Li-W distances would be shorter (d(Li-W) = 2.621 Å versus 2.866 Å in the un-split Li site model). However, similar short distances are encountered in some Li-W-O compounds (d(Li-W) = 2.494 Å as in $Li_5W_2O_7$).[59]

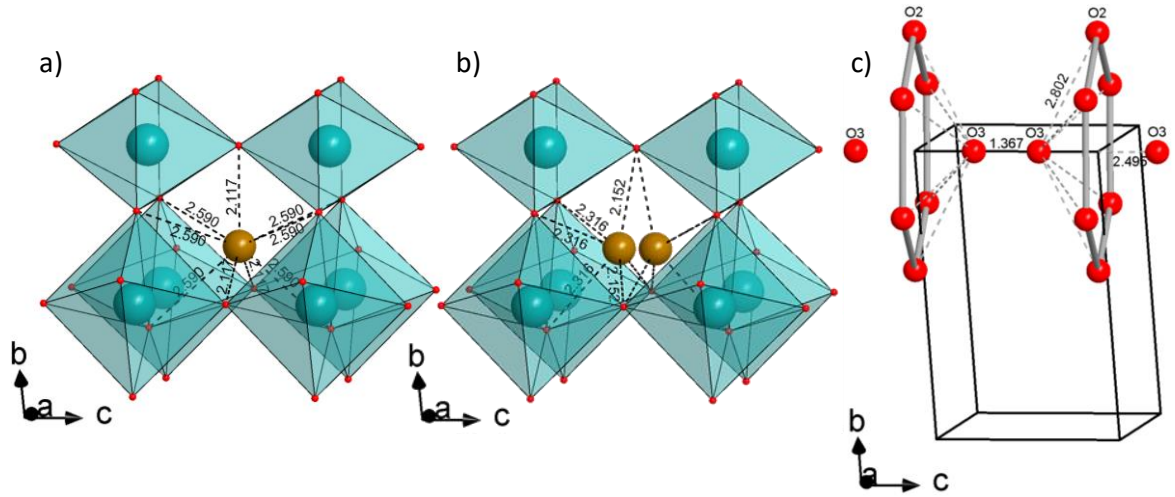

Figure III-15. *a) Li-O distances in the un-split Li site model and b) in the split Li site model, and c) O3 atoms in the hexagonal cavity along the c-axis and O-O distances (Distances in Angstroms).*

III.3.4.2.2. $Na_{0.278}WO_{3.139}\bullet(H_2O)_{0.083}$.

The X-ray diffraction pattern for the Na HTB indicates that it crystallizes in the P6/mmm space group with cell parameters of *a* = 7.32401(13) Å, *c* = 3.90018(8) Å, and a cell volume of V = 181.181(6) $Å^3$, as shown in Figure III-16.

The refinement started with the structural model of WO_3 with the following three sites: W in 3f (0.5,0,0), O1 in 3g (0.5,0,0.5) and O2 in 6l (x,2x,0) with x ~ 0.21. EDX analysis indicated 0.28 moles of Na in this compound. Therefore, it is necessary to introduce it in the refinement as well as the oxygen atoms which come to compensate the charge of the sodium atoms and also those brought by the water molecules. After refinement of the atomic positions and ADPs, the Fourier difference maps (Figure III-17) indicate two peaks with high electron

density in 1b (0,0,0.5) (charge 5.57, position named max1) and 2e (0,0,z) with z ~ 0.19 (charge 5.08, position named max2).

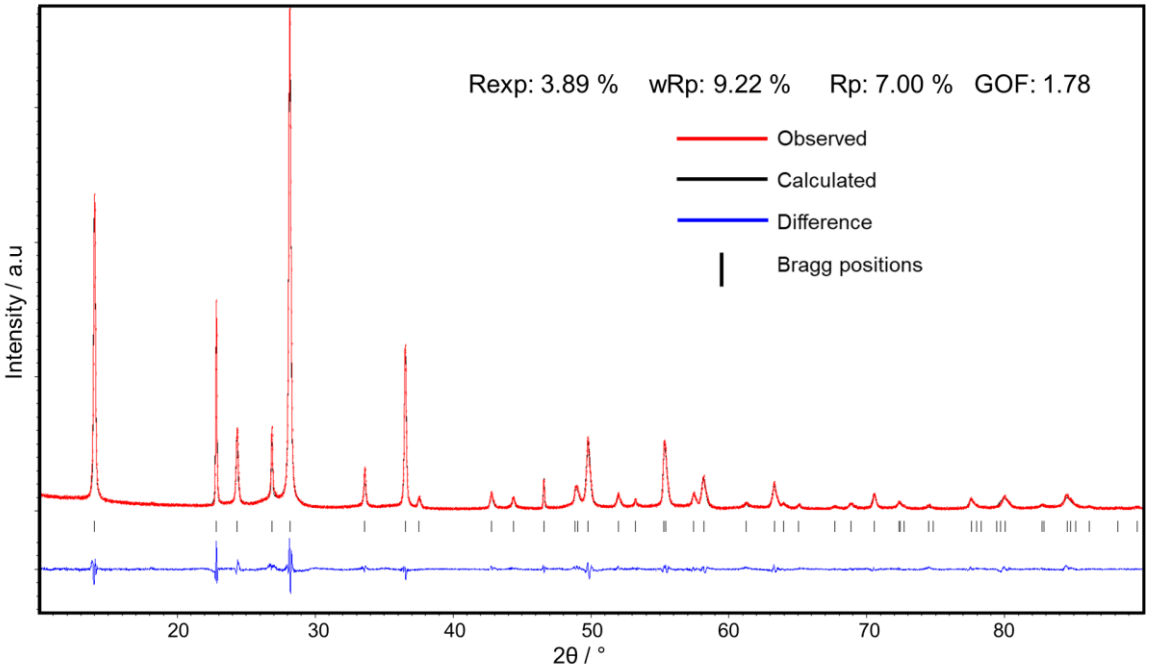

Figure III-16. *Rietveld refinement of* $Na_{0.278}WO_{3.139}\bullet(H_2O)_{0.083}$.

An atom occupying max1 is 1.22 Å away from an atom occupying the max2 site, which is too short a distance for both sites to be occupied simultaneously. Therefore, the maximum occupancies of max1 and max2 are 0.5. Max1 has a higher electron density than max2; it is assumed that max1 is occupied by Na atoms, and max2 is occupied by O atoms. Then, both max1 (= Na1) and max2 (= O3) are introduced in the refinement with half occupancy. After refinement, the ADP of Na1 is positive, and that of O3 is negative. At this stage, the formula of the compound is $Na_{0.167}WO_{3.333}$.

As mentioned above, the literature has reported $Na_{0.17}WO_{3.085}\bullet(H_2O)_{0.17}$,[37] with Na and O atoms found disordered along the *c* axis. It is somewhat possible to consider a mixed Na/O site if Na-O, O-O and Na-Na distances are acceptable. Thus, some Na atoms (= Na2) are placed in the same site as O3 atoms with identical atomic coordinates and ADPs (Table III-7). After refinement, all ADPs are positive, and the formula obtained is $Na_{0.278}\bullet WO_{3.222}$. By introducing a mixed Na/O site, the number of Na moles is thus very close to that determined by EDX analysis.

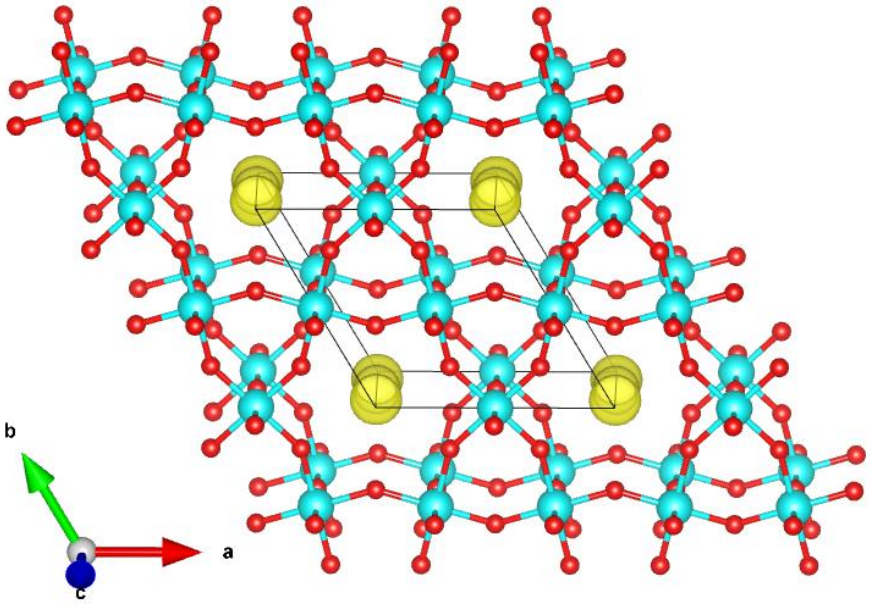

Figure III-17. *Electronic density at 1b (0,0,0.5) (max1) and 2e (0,0,z) with z ~ 0.19 (max2) obtained after refining the WO_3 model and performing Fourier differences calculation.*

As for the Li compound, the hydrogen atoms could not be located by Fourier difference calculations. However, if the charge of some O3 atoms compensates for the charge of Na atoms, the remaining oxygen atoms are used to form water molecules. In that case, the formula of the compound is $Na_{0.278}WO_{3.139}\bullet(H_2O)_{0.083}$. The TGA analysis showed a mass loss of about 4% between room temperature and 350°C, corresponding to about 0.5 moles of H_2O. Also, as for the compound reported in the literature, there is a discrepancy between chemical analysis and refinement that probably comes from water adsorbed at the surface, thus explaining the higher water content determined by TGA than by Rietveld refinement.

Table III-7. *Atomic coordinates of $Na_{0.278}WO_{3.222}$ compound with a = 7.32401(13) Å, c = 3.90018(8) Å, V = 181.181(6) Å3, SG P6/mmm.*

Atom	Wyck. pos.	x	y	z	SOF	U_{eq}* / U_{iso} (Å^2)
W1	3f	0.5	0	0	1	0.0345(7)*
O1	3g	0.5	0	0.5	1	0.027(4)
O2	6l	0.2114(4)	0.4228(8)	0	1	0.014(3)
Na1	1b	0	0	0.5	0.5	0.016(8)
O3	2e	0	0	0.1868	0.333	0.037(9)
Na2	2e	0	0	0.1868	0.167	0.037(9)

Finally, after introducing a preferred orientation along the [001] direction due to the elongated shape of the rod-like particles obtained after synthesis and an anisotropic strain broadening treated by Stephens mode[60] in the refinement, the final reliability factors are given in Figure III-16. The crystallite size and lattice strain determined by performing a refinement considering the fundamental parameters of the powder diffractometer are 102(2) nm and 0.296(4), respectively.

The structure of the Na HTB can be described by layers of corner-shared WO_6 octahedra arranged in six-membered rings giving rise to one-dimensional tunnels along the *c* axis, as shown in Figure III-18a. The W-O distances in WO_6 octahedra range from 1.895(8) to 1.95009(8) Å (Figure III-18b).

The structure differs from that published in 1992,[37] which proposed a model with Na occupying site 1a (0,0,0) and O3 occupying site 2e (0,0,z) with z = 0.41. The sodium atoms are in the transition-metal plane, in the hexagonal window surrounded by a ring of six oxygen atoms and water molecules are in the hexagonal cavity (Figure III-19a). In contrast to the literature data, for the present compound, the sodium atoms are located in the center of the hexagonal cavity of anions between the layers of the transition-metal atoms. The O3/Na2 mixed sites are in the hexagonal cavity and disordered along the c axis (Figure III-19b). Considering the site occupancy, the Na-O and O-O distances range from 2.443 to 3.316 Å and 2.443 to 2.779 Å, respectively. The Na1-Na2 d

istance is about 2.679 Å. All these distances are acceptable and exist in other compounds.

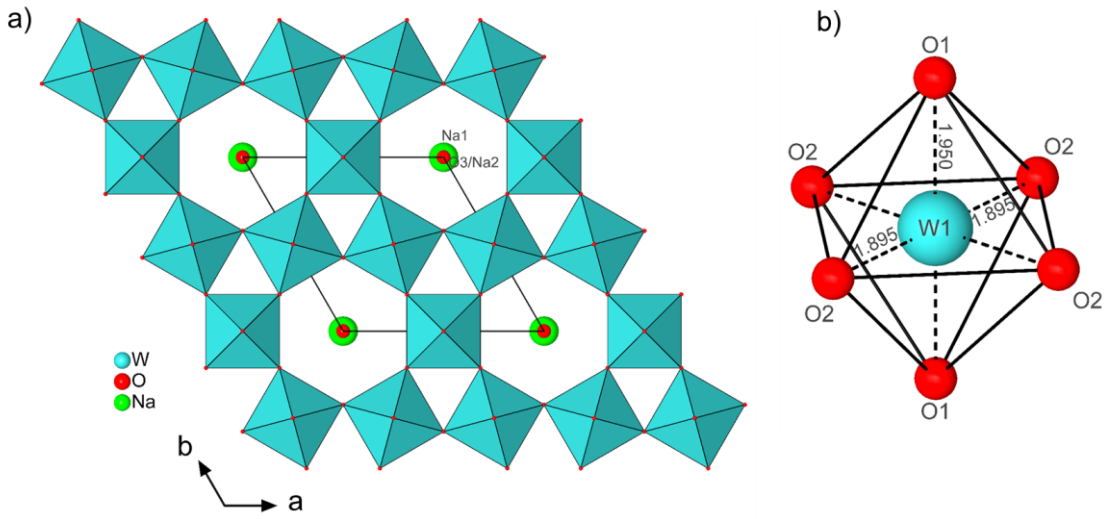

***Figure III-18**. a) Structure of $Na_{0.278}WO_{3.222}$ compound and b) WO_6 octahedra with W-O (distances in Angstroms).*

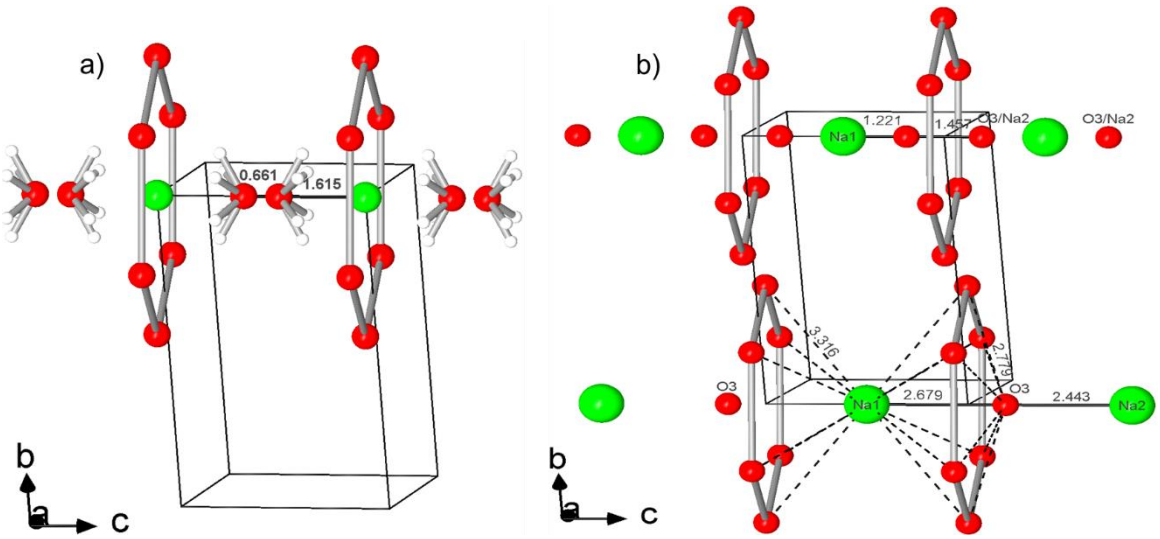

Figure III-19. *Atom positions along the c-axis of hexagonal tungsten bronze in the structure of a) $Na_{0.17}WO_{3.085}(H_2O)_{0.17}$ according to literature data and b) $Na_{0.278}WO_{3.222}$ according to the present results. Atom positions at the top of the cell, without considering the site occupancy and at the bottom, proposition of atom positions considering the site occupancy (Distances in Angstroms).*

III.3.4.2.3. $K_{0.33}WO_3$

The X-ray diffraction pattern for the K HTB indicated that it crystallizes in the space group $P6_3/mcm$ with cell parameters a = 7.3169(8) Å, c = 7.6198(10) Å, and a cell volume of V = 353.28(7) $Å^3$, as shown in Figure III-20.

The refinement began from the WO_3 structural model of the $K_{0.179}WO_3$ and $K_{0.33}WO_3$ compounds (3 and 4 in Table III-4) with the following three sites: W in 6g (x,0,1/4) with x ~ 0.5, O1 in 6f (1/2,0,0) and O2 in 12j (x,y,1/4) with x ~ 0.2, y ~ 0.4. EDX analysis confirmed the presence of about 0.33 moles of K in the compound. After refinement of atomic positions and ADPs, Fourier difference maps indicate a peak with the highest electron density in 4e (0,0,z) with z ~ 0.12 (charge 1.70) corresponding to K atoms.

The K atoms that simultaneously occupy the 4e site are at a distance of 1.34 Å from each other, which is too close. The maximum occupancy of K atoms is therefore 0.5. The K atoms are then introduced in the refinement in the 4e site with half occupancy. The SOF refinement of the K atoms leads to an increase in the SOF and, for this reason, the SOF was set to 0.5. Moreover, TGA analysis indicated a mass loss. However, the shape of the curve suggested the water was probably adsorbed on the surface and not present structurally. Therefore, the formula obtained is $K_{0.33}WO_3$, and the oxidation state of W is 5.67^+.

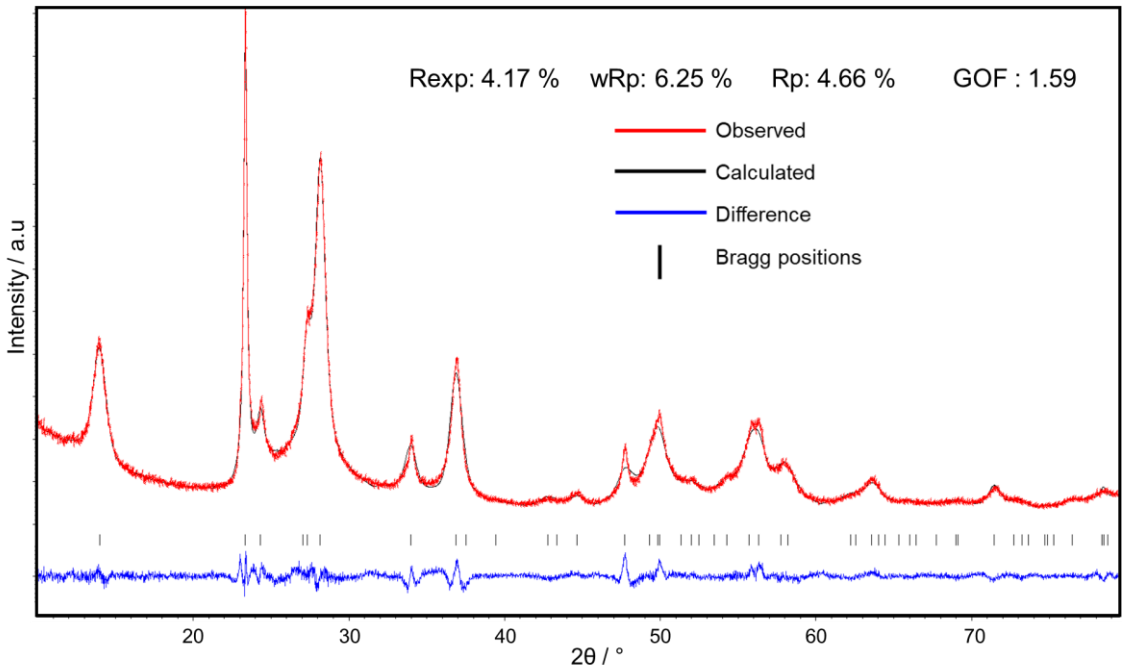

Figure III-20. *Rietveld refinement of $K_{0.33}WO_3$.*

The final reliability factors are given in Figure III-20. The atomic coordinates and ADPs of all atoms are provided in Table III-8. In contrast to Li and Na compounds, no preferred orientation was introduced during the refinement. An anisotropic size broadening, treated by spherical harmonics of order 2,[56] was considered in the refinement. The crystallite size and lattice strain determined by performing a refinement taking into account the fundamental parameters of the powder diffractometer are 18.2(3) nm and 0.62(3), respectively.

Table III-8. *Atomic coordinates of $K_{0.33}WO_3$ compound with a = 7.3169(8) Å, c = 7.6198(10) Å, V = 353.28(7) Å^3, SG P63/mcm.*

Atom	Wyck. pos.	x	y	z	SOF	U_{iso} (Å^2)
W1	6g	0.505(2)	0	1/4	1	0.0522(12)
O1	6f	1/2	0	0	1	0.016(7)
O2	12j	0.210(12)	0.3997(18)	1/4	1	0.015(7)
K1	4e	0	0	0.088(2)	0.5	0.089(9)

The final structure is similar to that of $K_{0.179}WO_3$ and $K_{0.33}WO_3$ compounds (3 and 4 in Table III-4) except that the K atoms occupy half of the 4e site instead of the 2b site (0,0,0). Similar to the Li and Na HTBs, the potassium structure can be described by layers of corner-shared WO_6 octahedra arranged in six-membered rings giving rise to one-dimensional tunnels along the *c* axis (Figure III-21a).

In contrast to the Li and Na compounds, the *c* parameter is doubled, and the K atoms are located in the hexagonal cavity and disordered along the *c* axis (see Figure III-21b). The WO_6 octahedra are slightly more distorted than those of Li and Na HTBs, with W-O distances ranging from 1.84(7) to 2.03(7) Å (Figure III-22). Another difference between Li and Na compounds is the oxidation state of tungsten. The absence of oxygen in the hexagonal cavity implies that the formal oxidation state of tungsten is below 6^+.

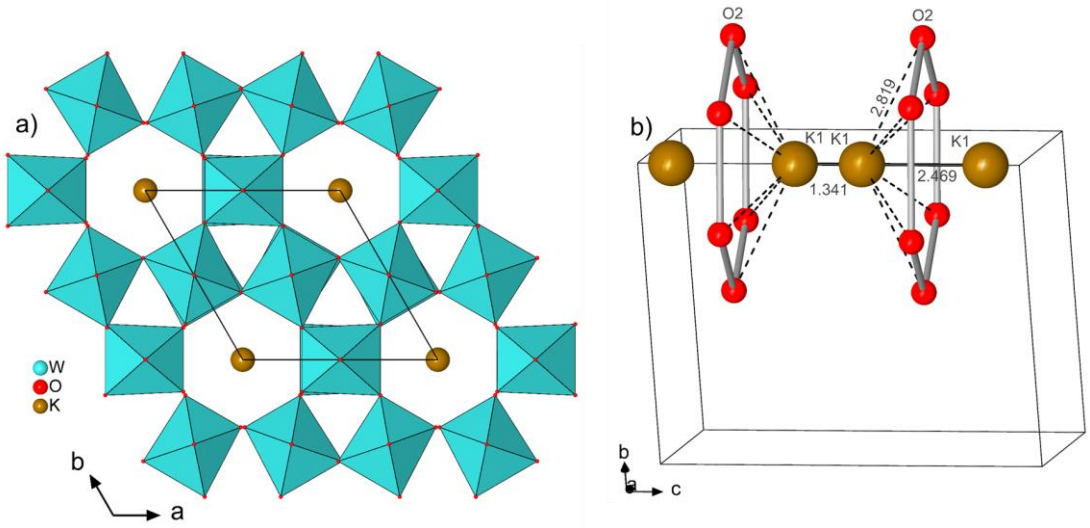

***Figure III-21**. a) Structure of $K_{0.33}WO_3$ compound and b) K atoms in the hexagonal cavity along the c-axis (K-K distances in Angstroms).*

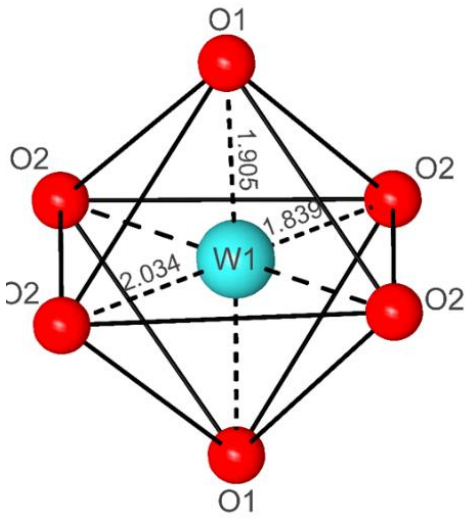

***Figure III-22.** WO_6 octahedra with W-O (distances in Angstroms).*

III.3.4.2.4. Preliminary conclusions on the structural refinement

As mentioned previously, the Rietveld refinement for Li HTB considers the results obtained from the ICP-OES experiment, revealing the presence of Li in the structure. The final formula with water determined from the TGA is $Li_{0.167}WO_{3.083}(H_2O)_{0.25}$. In addition, a new model of atomic arrangement along the *c* axis is proposed for Na HTB, whose resulting formula is $Na_{0.278}WO_{3.139}(H_2O)_{0.083}$. This model, different from the previously published one, is consistent in terms of Na-Na, Na-O, and O-O distances and shows good agreement with the Na amount determined by EDX analysis. In contrast to the Li and Na HTBs, the $K_{0.33}WO_3$ compound exhibits a doubled *c* parameter and more distorted WO_6 octahedra structure. Nonetheless, the structure is similar to the $K_{0.33}WO_3$ reported by Lee *et al.*[54], except that the K atoms occupy a less symmetric site (4e) with a z coordinate that can be refined.

The most important difference between these three synthesized phases is the deviation of the Li and Na compounds from the normal stoichiometry of the M_xWO_3 tungsten bronze, which results from the presence of oxygen in the hexagonal cavity. Unlike the "classical" tungsten bronzes, which are reduced compounds like the K compound, the Li and Na phases are fully oxidized, the formal oxidation state of tungsten being its highest valence, *i.e.*, VI^+.

III.3.5. Morphology and surface characterization

The morphology and shape of the HTB synthesized were characterized by Scanning Electron Microscopy using a Merlin SEM from Carl Zeiss and Transmission Electron Microscopy with a ThermoFisher S/TEM Themis G3 at 300 kV point to point resolution: 0.18 nm. The specific surface area of the powders was determined using the BET method (Brunauer-Emmett-Teller) from the 77 K nitrogen adsorption curves with a Quantachrome Nova 4200e equipment.

III.3.5.1. Growth mechanism and morphology

The hydrothermal route followed for the successful synthesis of Li, Na, and K HTBs was described in section III.2.4. This synthesis begins with the precipitation of the WO3 yellow

sol using a variation of the tungstic acids method proposed by Freedman[61]. The mixing of the sol with oxalic acid ensures a soft, reducing environment. Afterwards, hydrothermal synthesis takes place. The addition of sulfate salts serves to obtain the desired compound. Moreover, the insertion of cations inside the structure serves to direct and control the shape of the particles, as already seen in the literature.[41–45] Figure III-23 illustrates how the formation mechanism of the rod/wire morphology occurs.

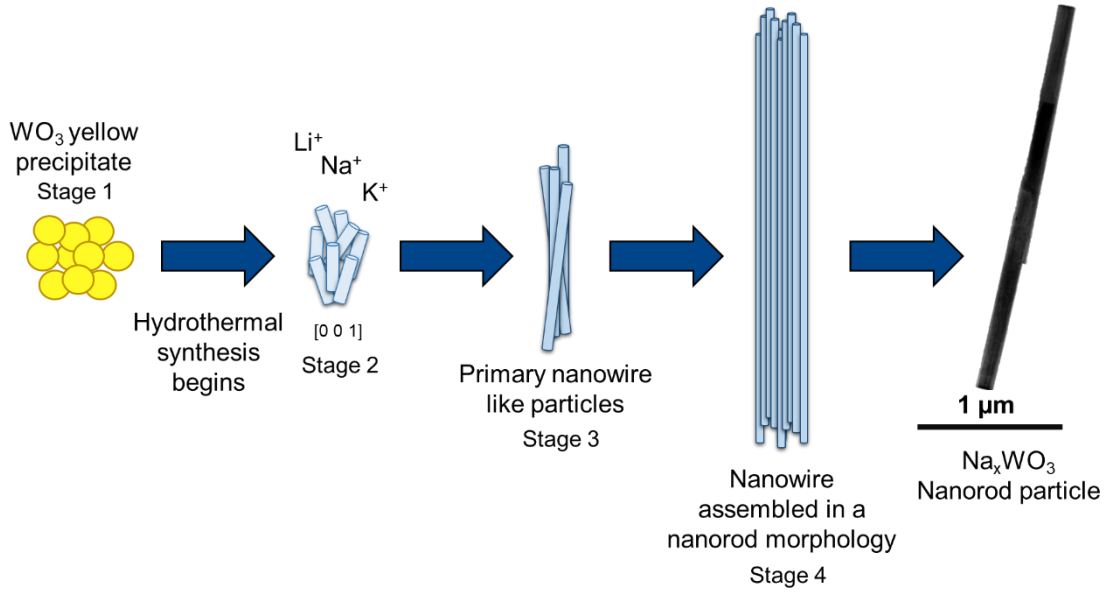

Figure III-23. *General growth mechanism for the hexagonal tungsten bronzes.*

The three cations Li^+, Na^+, and K^+ together with SO_4^{2-} will promote the growth in the [001] direction. However, the larger the cation is, the longer and thinner the particles will be. This shape is observed in the SEM pictures shown in Figure III-24. Li HTB particles are defined by the third stage in the growth mechanism scheme (see Figure III-23). The primary nanowire or nanorod shape is present, but the growth does not go far. They stack on top of each other with spikes and agglomerate, as shown in Figure III-24a, b, and c.

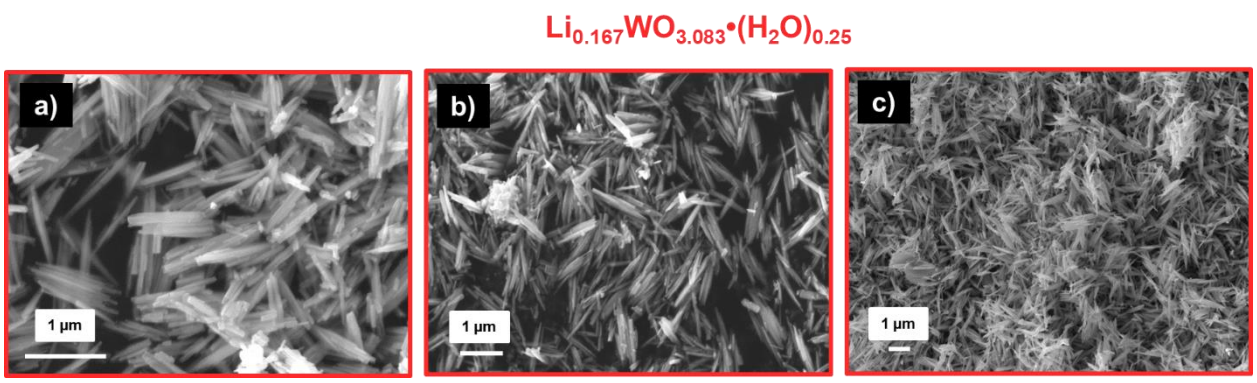

Figure III-24. *SEM images for Li HTB.*

When Na^+ is present, the growth mechanism advances to stage four, where the primary nanowire-like particles are assembled in a larger nanorod shape-like particle. This effect is seen in Figure III-25a, b, and c, the shape of the Na HTB is better defined, and the surface seems smoother than for Li HBT. The bundle formed by the nanorods is less likely to be agglomerated together.

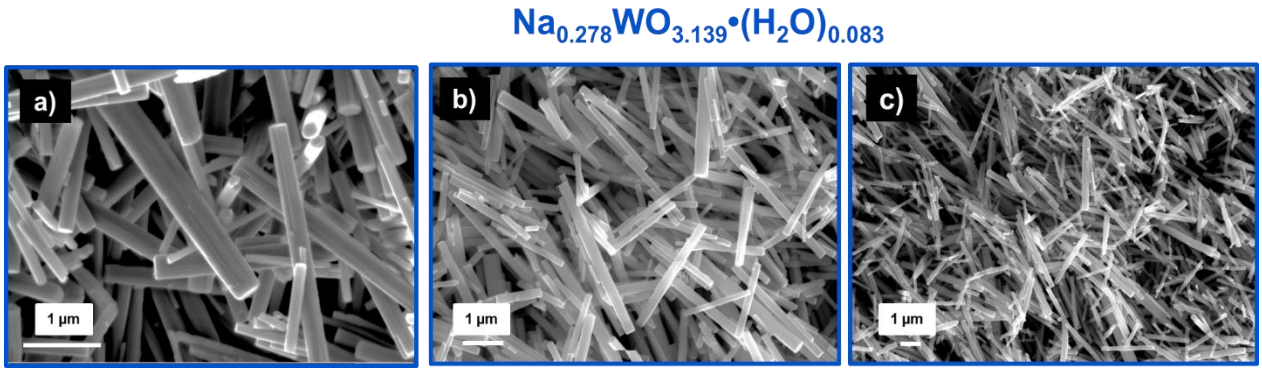

Figure III-25. *SEM images for Na HTB.*

On the other hand, for K HTB, the mechanism is the same as for Na. However, in this case, the primary nanowire particles do not stack on top of each other as much. They keep growing thinner along the *c* direction. This growth makes the particles more easily agglomerate than Na and Li HTBs, as displayed in Figure III-26a, b, and c.

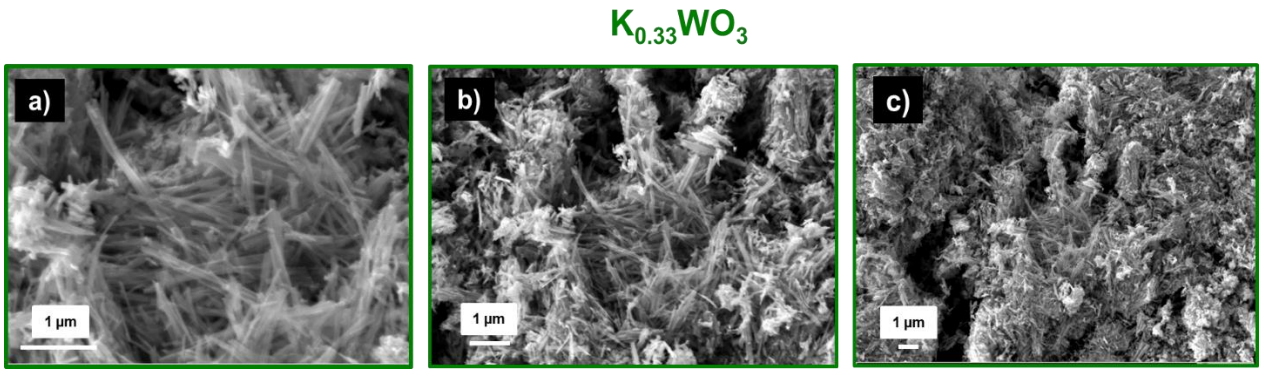

Figure III-26. *SEM images for K HTB.*

Figure III-27 shows the TEM images obtained. They illustrate more clearly what has been aforementioned. It shows the assembly of the primary wire particles into a more extensive nanorod-like morphology for the cases of Li and Na HTB (Figure III-27a, b, d, and e). As mentioned earlier, in the case of K HTB, the nanowire-like particles are much thinner and smaller in diameter (Figure III-27g and h). In the zoom-in (Figure III-27c, f, and h), the growth along the *c* direction can be confirmed as we observed the *ab* plane from above. Moreover, the

inset shows the corresponding indexed electron diffraction patterns for each HTB. Unfortunately, the alignment of the nanorods along the tunnels [001] was not possible.

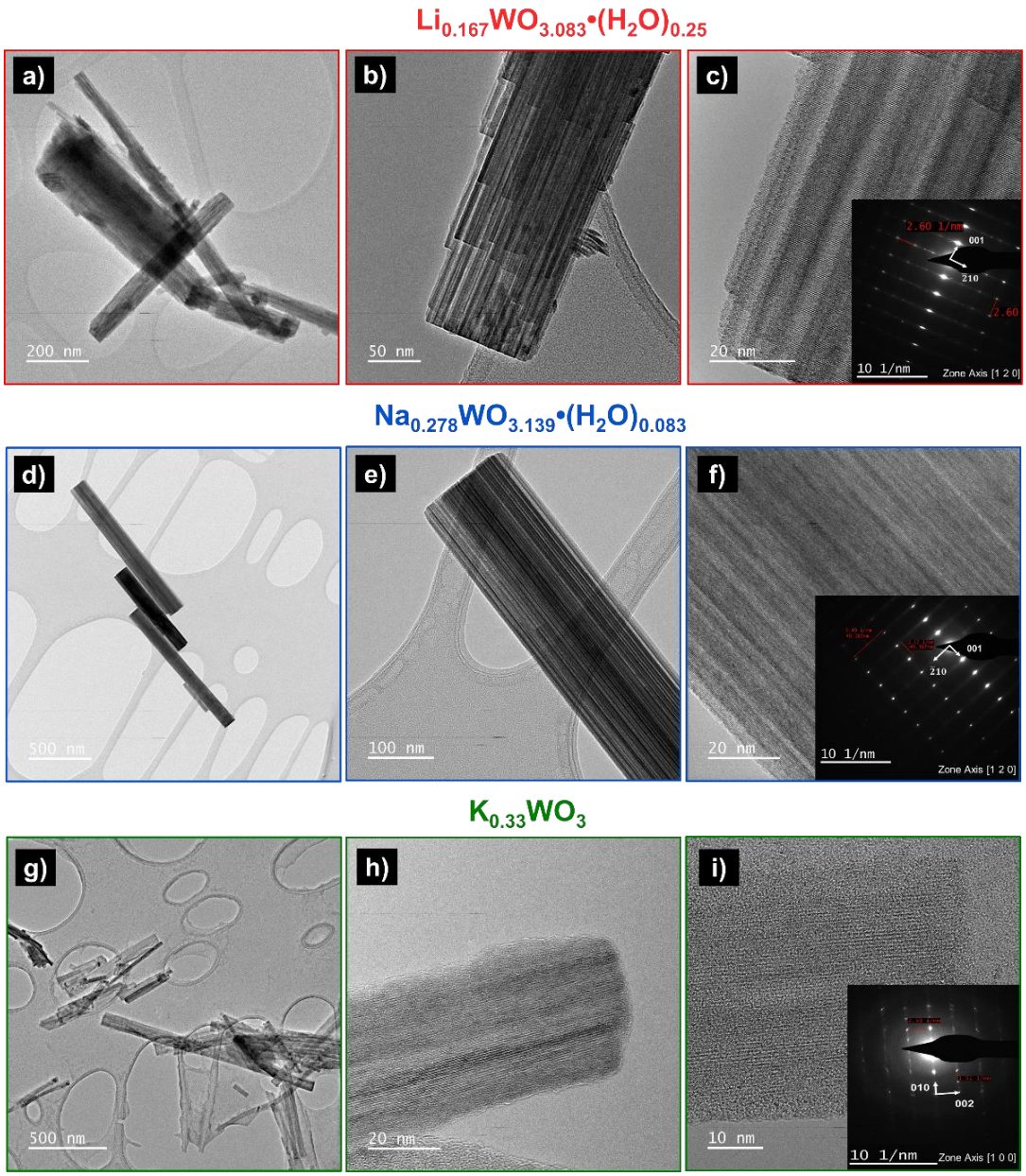

Figure III-27. *TEM images for the HTB. a), b), and c) showing the Li compound, d), e), and f) the Na compound and g) h) and i) the K compound.*

III.3.5.2. Surface area

The BET specific surface area in $m^2\ g^{-1}$ (SSA) was measured according to N_2 adsorption for the three HTBs. It is observed that potassium HTB has the highest SSA, probably due to the

longer and thinner nanowires that form the bronze compound. Since the particles are mainly elongated, they may have a more exposed surface area, as shown by the BET (Table III-9). On the other hand, for the cases of Li and Na HTB, the nanorod shape looks pretty similar, being more uniform and smoother for the Na bronze. Despite these differences, the SSA does not seem to change much, as shown in Table III-9.

Table III-9. *BET specific surface area for the hexagonal tungsten bronzes.*

Hexagonal tungsten bronze	**BET Specific Surface Area ($m^2\ g^{-1}$)**
$Li_{0.167}WO_{3.083}•(H_2O)_{0.25}$	~ 12
$Na_{0.278}WO_{3.139}•(H_2O)_{0.083}$	~ 12
$K_{0.33}WO_3$	~ 55

III.3.6. Preliminary conclusions on structural and morphological study of Li, Na and K HTBs

This section presents the structural and physicochemical characterization of the hexagonal tungsten bronzes of Li, Na, and K. We have shown that the synthesis directly impacts the structural arrangement of the HTBs. In addition, we have confirmed the presence of structural water for Li and Na compounds but not for K HTB.

The growth of the particles in nanorods/nanowires type morphology is explained by the size of the cation involved in the synthesis. The larger the cation, *i.e.*, K^+, the thinner the wires will be. On the other hand, the smaller the cation, *i.e.*, Li^+, the broader and sharper the rods are. In the case of Na, the particles acquired a much higher uniformity, as shown by SEM and TEM images. Nonetheless, Li and Na HTB present the same SSA in comparison with K HTB.

In conclusion, the structural arrangement, the morphology of the particles, and the SSA could impact the electrochemical behavior of the hexagonal tungsten bronzes. The following section provides an in-depth discussion on this topic

III.4. Electrochemical study on hexagonal tungsten bronzes A_xWO_3

III.4.1. Introduction

The reversible intercalation of alkali metals in tungsten oxides involves a charge transfer mechanism. This property was reported in the study of WO_3 thin films by Green *et al.*[62,63] They passed a small amount of current through a colorless WO_3 cathode resulting in the formation of a deep blue color resulting from the formation of a tungsten bronze phase.[62]

The chemical intercalation of alkali metal into different polymorphs of tungsten oxides was studied by Cheng *et al.*[64,65] They stated a maximum uptake of 0.26 moles of Na per W and 0.3 moles of K per W in the hexagonal WO_3 phase reacting sodium and potassium benzophenones in tetrahydrofuran, respectively. These are the final formulas: $Na_{0.26}WO_3$ and $K_{0.26}WO_3$. On the other hand, lithium uptake gave a maximum content of $Li_{2.0}WO_3$ compared to the monoclinic phase with the uptake of $Li_{0.67}WO_3$ when mixing the tungsten oxide with n-butyl lithium in hexane.

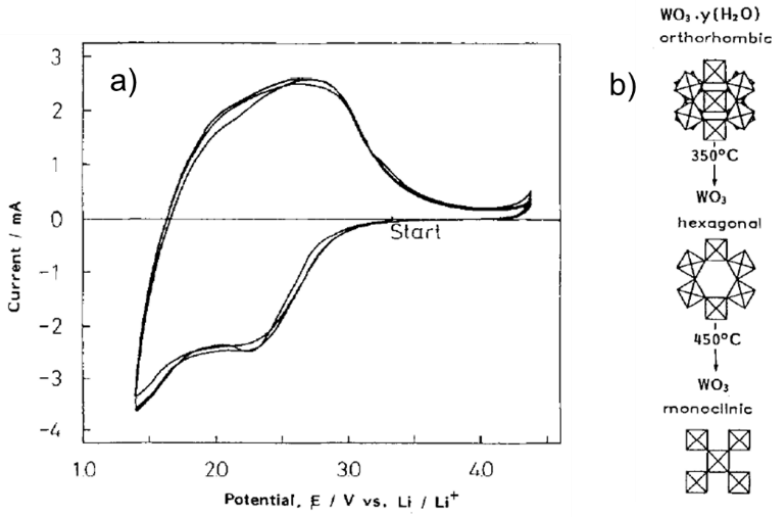

Figure III-28. *a) Cyclic voltammogram for WO_3 electrode in 1 M $LiClO_4$ in PC. And b) Structural relationship of WO_3 polymorphs.*[69]

The electrochemical intercalation of alkali cations was later investigated by Kumagai *et al.*[66–69] They studied the hexagonal WO_3 phase obtained after the heat treatment of the orthorhombic hydrated phase at 350 °C (Figure III-28b). They studied the reversible electrochemical intercalation of Li^+ with $LiClO_4$ in propylene-carbonate (PC) electrolyte (see

Eq. III-3) accommodating 1.9 Li^+ in the lattice of h-WO_3. The cyclic voltammogram showing faradaic response due to the Li intercalation is depicted in Figure III-28a.

$$h - WO_3 + xLi^+ + xe^- \leftrightarrow Li_xWO_3 \qquad \text{Eq. III-3}$$

A few years later, Augustyn's group investigated the hydrated monoclinic phase of WO_3[47] (see Figure III-29a, and b). They studied the transition from a battery-like to a pseudocapacitive behavior observed in the electrochemical response in 0.5M H_2SO_4 electrolyte (Figure III-29c, and d). They reported a much higher increase in capacity in the hydrated phase at higher rates than the non-hydrated phase. Such a reported behavior was attributed to the fast and reversible intercalation of protons coming from the aqueous electrolyte.

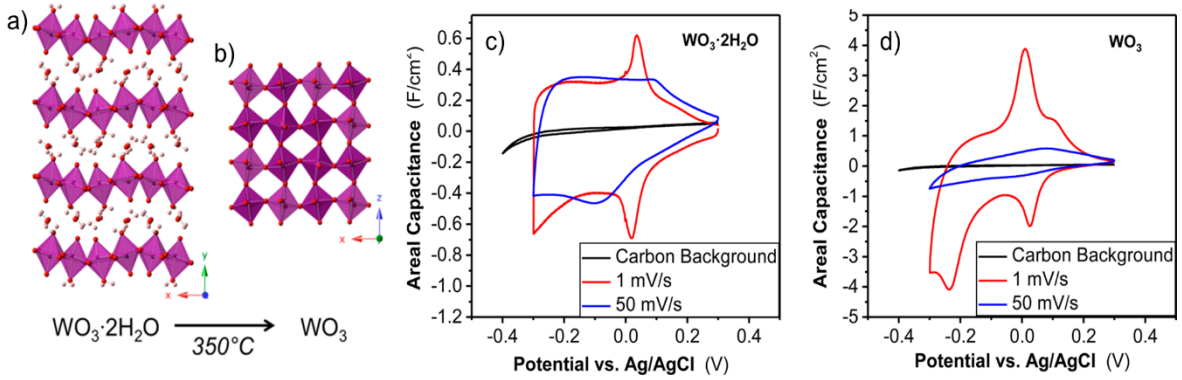

Figure III-29. *Crystallographic structures of (a) monoclinic WO_3•$2H_2O$ and (b) monoclinic γ-WO_3. And Cyclic voltammograms at 1 and 50 mV s^{-1} in 0.5 M H_2SO_4 of c) WO_3•$2H_2O$ and d) γ-WO_3.*[47]

The studies mentioned above performed in the different polymorphs of tungsten oxide encouraged the present work. In the past sections, a full investigation of the structure of the HTBs was presented, demonstrating a particular structural arrangement differing from the ones reported in the literature. In this way, a thorough investigation of the electrochemical behavior of the hexagonal tungsten bronzes in aqueous and organic electrolytes will be presented in the following sections.

III.4.2. Electrode preparation and electrochemical set-up

The HTB materials are assembled as composite electrodes[70] and pressed-in stainless steel grids as described in Chapter II, Section II.1.3.1. The active material is mixed with conductive carbon (Carbon Black by Superior Graphite, >99%) to improve electronic conductivity and as the binder, to ensure the mechanical strength of the electrode, Polytetrafluoroethylene (PTFE Sigma Aldrich) in the respective weight ratios of 60/30/10. The mass loading of the prepared electrodes varied from ~5 to ~10 $mg.cm^{-2}$. [71]

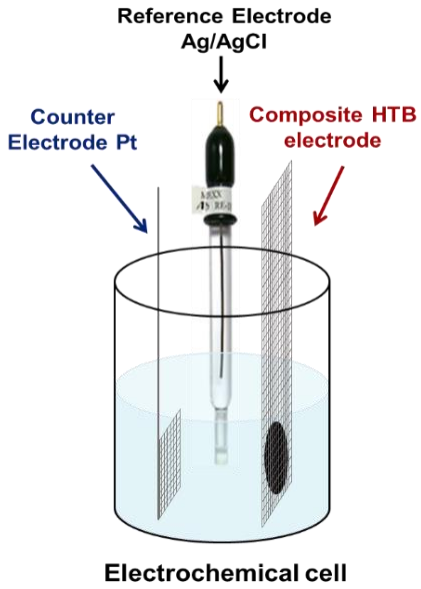

***Figure III-30**. Electrochemical cell showing the three-electrode setup.*

The electrochemical performance for all the samples was carried out by cyclic voltammetry with a VMP3 galvanostat–potentiostat (from Biologic run under ECLab software). The experiments are conducted using a three-electrode electrochemical setup with Ag/AgCl (3M NaCl) as the reference electrode and a platinum grid as the counter electrode (see Figure III-30). The HTBs will be tested in different neutral and acidic aqueous electrolytes to study their stability and performance depending on the nature, pH, and concentration of the electrolyte. All the experiments were performed in a [-0.6 V; 0 V] *vs*. Ag/AgCl potential window and [-0.3 V; 0.3 V] *vs*. Ag/AgCl for lower pH tests.

III.4.3. Electrochemical study of HTB in aqueous 5M $LiNO_3$

III.4.3.1. Li Hexagonal Tungsten Bronze

In section III.3.2, an initial electrochemical study for the γ-WO_3 phase was presented, both blank and commercial reference. A weak electrochemical activity was observed with poorly reversible faradaic behavior when the electrode is cycled at 2 $mV.s^{-1}$ from -0.6 V to 0.0 V *vs.* Ag/AgCl in 5M $LiNO_3$. Moreover, no reports have been presented in the literature under such cycling conditions for tungsten bronzes.

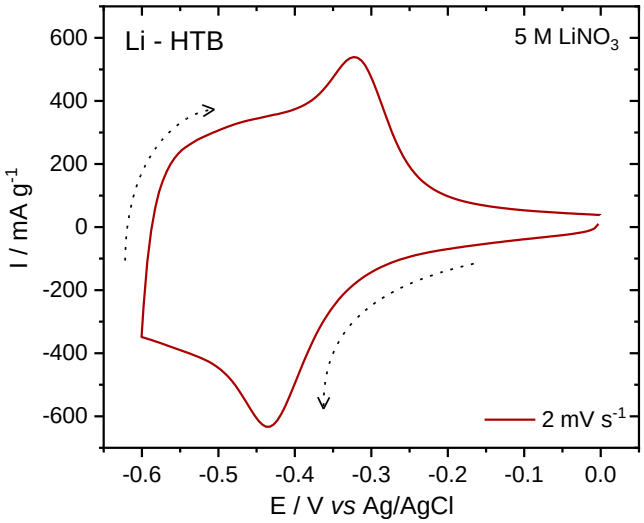

Figure III-31. *Cyclic voltammogram of Li HTB at 2 $mV.s^{-1}$ in 5M $LiNO_3$.*

In Figure III-31, the CV of the Li HTB is presented. The shape of the CV is a clear representation of a faradaic-like behavior. As the sweep moves to a more negative potential, a faradaic peak upon reduction at -0.43 V *vs.* Ag/AgCl is observed. Then, as the sweep moves back, a peak upon oxidation at -0.32 V *vs.* Ag/AgCl appears. Furthermore, a quasi-rectangular shape can be noticed when the sweep moves from reduction to oxidation through a small region in the CV.

Both peaks are most likely related to a Li^+ intercalation mechanism coming out from the aqueous $LiNO_3$ electrolyte and into the structure of the material. The slight quasi-rectangular shape described must involve two surface mechanisms: a contribution of

pseudocapacitive-like behavior caused by fast redox reactions happening at the surface and the second contribution of purely electrostatic charges being adsorbed at the same surface.

Such an observed behavior expanded the exciting features of these compounds. The HTBs have already been studied because of their appealing electrochromic and electrochemical properties. However, all of them are being investigated only in organic media. In the CV presented in Figure III-31, at a sweep rate of 2 $mV.s^{-1}$ a maximum specific capacity of ~71 $C.g^{-1}$ is achieved; this corresponds to a charge/discharge rate of 10 min., which is a much faster phenomenon compared to the charge/discharge rates previously reported for the related compounds.[67]

Considering the total theoretical capacity extracted when 1 e^- is being transferred is about 404 $C.g^{-1}$, as shown in Eq. III-3. Therefore, the number of Li intercalated corresponding to the capacity extracted for $Li_{0.167}WO_{3.333}$ (Li HTB) at 2 $mV.s^{-1}$ is ~0.175, see Eq. III-4.

$$Li_{0.167}WO_{3.333} + 0.175\,Li^+ + 0.175\,e^- \leftrightarrow Li_{0.342}WO_{3.333} \qquad \text{Eq. III-4}$$

The Li HTB could accommodate more Li^+ inside than the one reported here, as previous studies have shown with a "similar" hexagonal structure. [48,67,69]However, to maintain the structure's stability, a maximum of 0.33 cations can be intercalated. On the other hand, the water occupying the 2d site, in the hexagonal cavity between two layers of hexagonal rings, might be a vital feature responsible for how the intercalation of Li+ takes place. Moreover, the Li+ solvation shell may be another essential feature to consider, whether Li^+ cations are completely desolvated or if water molecules accompany them.

Figure III-32a shows the CVs corresponding to the evolution of the scan rate from 2 $mV.s^{-1}$ to 100 $mV.s^{-1}$. The CVs show the faradaic response fading when reaching higher sweep rates. At 20 $mV.s^{-1}$ a broader anodic peak is still visible, but it is no longer observed, and the CV shows a more resistive shape. Such a behavior can be explained kinetically, meaning that the cations in the electrolyte do not have enough time to be inserted or absorbed at the surface of the material. At higher rates, a surface capacitive (non-limited by diffusion) process takes over. Moreover, whenever the scan rate goes even higher, the shape of the CV gets even more resistive, showing the total loss of the interesting intercalation feature depicted for Li HTB.

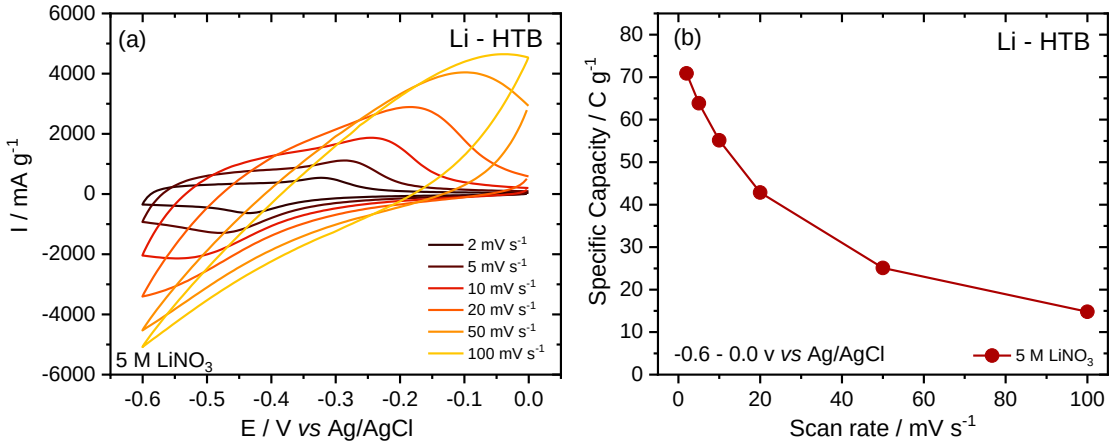

***Figure III-32**. (a) Cyclic voltammograms of the respective scan rates and (b) evolution of the capacity in C.g^{-1} vs. the scan rate.*

Additionally, Figure III-32b shows the evolution of the capacity *vs.* the scan rate. Li HTB reaches above 40 C.g^{-1} at 20 mV.s^{-1}, translated to a charge/discharge rate of only 1 min. These preliminary results shed light on the possibility of applying such materials for fast energy storage devices in aqueous systems.

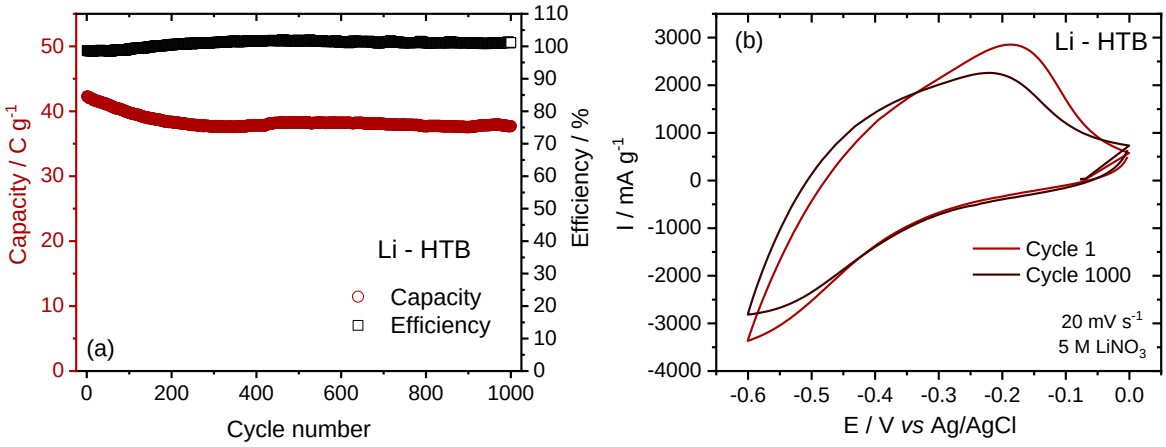

***Figure III-33.** (a) Specific capacity in C.g^{-1} and efficiency vs. cycle number. And (b) Cyclic voltammograms at 20 mV.s^{-1}showing the cycle 1 and cycle 1000.*

Figure III-33a shows the stability of the Li HTB at 20 mV.s^{-1} over 1000 cycles. During the first couple of hundred cycles, there is a slight drop in the capacity that remains very stable even after 500 cycles. As aforementioned, at 20 mV.s^{-1} it is still possible to appreciate a specific faradaic response in the material. Figure III-33b shows the CVs of cycle 1 *vs.* cycle 1000, where

the slight capacity loss is observed, although the shape remains unchanged, being slightly resistive with the broad anodic peak still present.

Taking into consideration a capacity of ~40 $C.g^{-1}$ extracted at 20 $mV.s^{-1}$, then a 0.1 e^- are being exchanged, as seen in Eq. III-5. Even though 1000 cycles do not seem like long cycling, this preliminary result gives an insight into the electrochemical stability of this bronze phase in a neutral aqueous medium.

$$Li_{0.167}WO_{3.333} + 0.1Li^+ + 0.1e^- \leftrightarrow Li_{0.267}WO_{3.333} \qquad \text{Eq. III-5}$$

III.4.3.2. Na Hexagonal Tungsten Bronze

In section III.3, the structure and morphology of the HTBs were described. It was mentioned that Li and Na HTBs present a similar structure, both with structural water inside the lattice occupying the sites available between the hexagonal rings' layers (or hexagonal cavities). Nonetheless, with slightly different morphology and with different cations arrangement. Figure III-34 shows the CV at 2 $mV.s^{-1}$ for the Na HTB. It exhibits a similar faradaic response as in the case of Li HTB. Such behavior is due to Li^+ cations begin intercalated into the available sites of the nanorods.

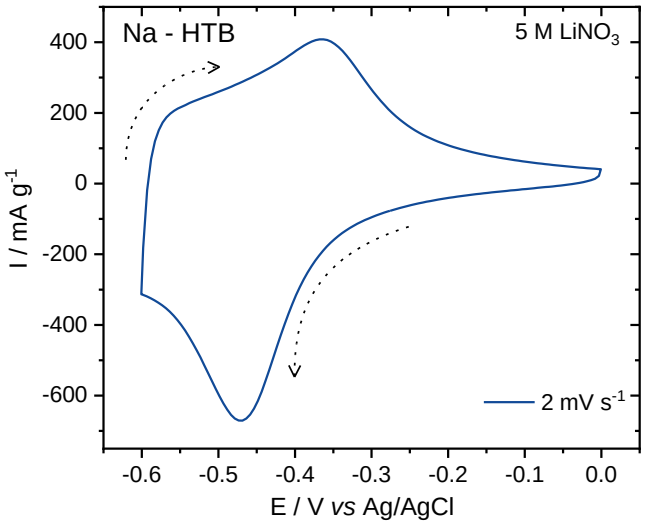

***Figure III-34**. Cyclic voltammogram of Na HTB at 2 $mV.s^{-1}$ in 5 M $LiNO_3$.*

The CV shows a cathodic peak at ~-0.47 V and an anodic peak at ~ -0.36 V *vs.* Ag/AgCl. These redox peaks support the hypothesis that Li^+ cations coming out from the electrolyte

interact with the host material. Moreover, as observed in Li HTB, a quasi-rectangular shape can be noticed through a small region of the CV when the sweep moves from -0.6 V to higher potential values. Because of these many resemblances to the Li bronzes, in this case, for the Na HTB, we should expect both contributions for the charge storage, a pseudocapacitive behavior, plus an intercalation mechanism.

The total theoretical capacity for Na HTB is about 399 $C.g^{-1}$, for one electron exchanged. The capacity obtained at 2 $mV.s^{-1}$ is about 63 $C.g^{-1}$, which corresponds to 0.158 e^- being transferred, see Eq. III-6.

$$Na_{0.278}WO_{3.139} + 0.158\,Li^+ + 0.158\,e^- \leftrightarrow Li_{0.158}Na_{0.278}WO_{3.139} \qquad \text{Eq. III-6}$$

Figure III-35a, and b show the CVs at different scan rates and the evolution of specific capacity *vs*. scan rate. The capacity reached at 2 $mV.s^{-1}$ is slightly lower than for the case of Li HTB. The CVs in the Figure III-35a exhibit a very similar behavior as the Li bronze. After 20 $mV.s^{-1}$ the CV becomes more resistive, even though it still shows a broader peak in the oxidation sweep.

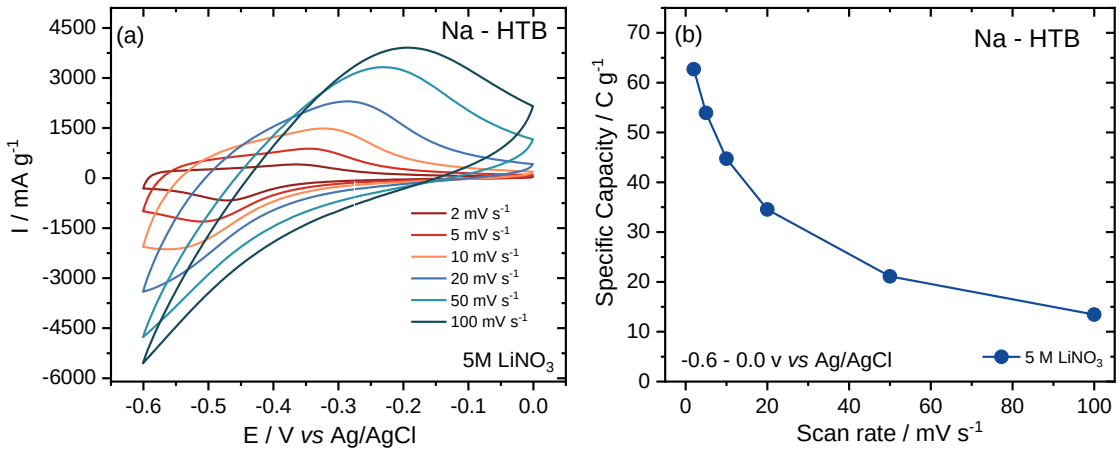

Figure III-35. *(a) Evolution of the capacity in $C.g^{-1}$ vs. the scan rate and (b) Cyclic voltammograms of the respective scan rates.*

In Figure III-36, the stability of up to 1000 cycles for the Na HTB is presented. Figure III-36a shows that a minor increment in the capacity is observed around the first hundreds of cycles. This effect might be causes by 1) the impregnation of the electrolyte in the composite electrode, as already seen in previous experiments in our lab, and 2) some reorganization of the

cations making room for more Li^+ to be inserted into the structure. Considering a capacity of ~40 C.g^{-1} extracted at 20 mV.s^{-1}, then a 0.1 e$^-$ are being exchanged, as seen in Eq. III-7.

$$Na_{0.278}WO_{3.139} + 0.1\,Li^+ + 0.1\,e^- \leftrightarrow Li_{0.1}Na_{0.278}WO_{3.139} \qquad \text{Eq. III-7}$$

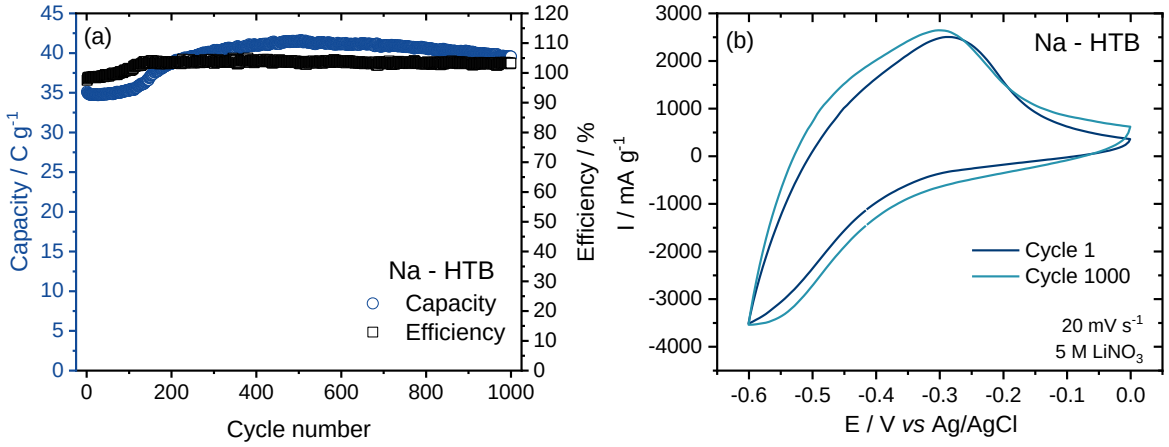

Figure III-36. *(a) Cyclic voltammograms at 20 mV.s^{-1}showing the cycle 1 and cycle 1000, and (b) Specific capacity in C.g^{-1} and efficiency vs. cycle number.*

III.4.3.3. K Hexagonal Tungsten Bronze

The K HTB presented an entirely different behavior to the one already observed for Li and Na HTBs. Two significant disparities exhibited in the K HTB structure are the double of the *c* parameter and the more distorted tungsten octahedra in the crystal structure. A priori, according to the thermal analysis and the structural refinement, no structural water between the hexagonal ring layers can be detected, and only K atoms can be located in that position. Other differences are the longer and thinner nanowire-like particles agglomerated into a bundle of bigger particles with higher SSA and the lower crystallite size. All of these differences could explain such a distinct electrochemical response.

Figure III-37 displays the CV at 2 mV.s^{-1} for the K HTB in 5M $LiNO_3$. It is very quickly appreciated that the CV's shape does not resemble those shown in the previous Li and Na HTBs. The potassium compound presents a resistive quasi-rectangular shape CV with a lack of faradaic response (no redox peaks). Such a behavior could be comparable to materials exhibiting a purely electric double layer (EDL) mechanism, *i.e.*, activated carbons with significant SSA or materials with a pseudocapacitive response, as discussed in chapter II**.**

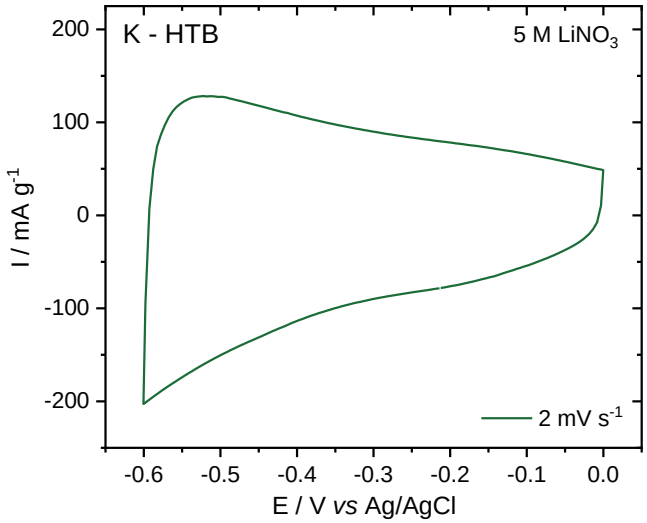

Figure III-37. *Cyclic voltammogram of K HTB at 2 mV.s^{-1} in 5M $LiNO_3$.*

The total theoretical capacity for K HTB is about 394 C.g^{-1}, for one electron exchanged. The capacity obtained at 2 mV.s^{-1} is about 29.5 C.g^{-1}, which corresponds to only 0.075 e$^-$ being transferred (see Eq. III-8).

$$K_{0.33}WO_3 + 0.075\,Li^+ + 0.075\,e^- \leftrightarrow Li_{0.075}K_{0.333}WO_3 \qquad \text{Eq. III-8}$$

Like Li and Na HTBs, a similar electrochemical response caused by the Li^+ intercalation was expected. However, this was not the case. The agglomerated nanowires could affect the way cations are being adsorbed at the surface, hence refusing the viability for Li^+ to go into the structure. K cations and the absence of structural water may also prevent the Li^+ pathway towards the host material, bringing a fascinating discussion concerning the structural and morphological features of K HTB being reflected directly in its electrochemical performance.

Figure III-38a and b show the CVs at different scan rates and the capacity *vs.* scan rate evolution, respectively. All of them maintained the quasi-rectangular shape at higher rates without showing any faradaic response. It is observed, as s for the previous HTBs, that the resistivity increase as the scan rate increases. At 20 mV.s^{-1}, the capacity extracted is about 19 C.g^{-1} that corresponds to ~0.049 e$^-$ being exchanged in the reaction, as seen in Eq. III-9.

$$K_{0.33}WO_3 + 0.049\,Li^+ + 0.049\,e^- \leftrightarrow Li_{0.049}K_{0.333}WO_3 \qquad \text{Eq. III-9}$$

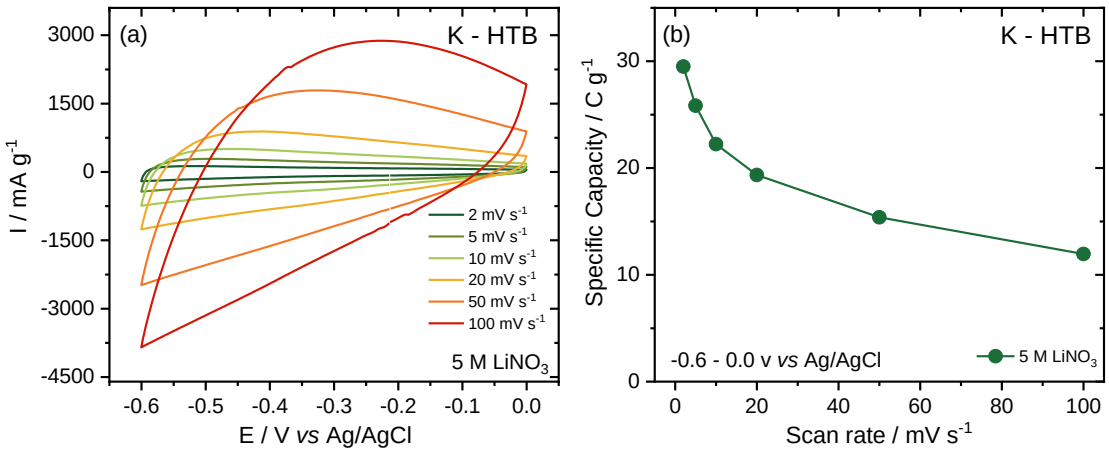

***Figure III-38**. a) Cyclic voltammograms at different scan rates and b) Evolution of the capacity in C.g^{-1} vs. scan rates.*

In Figure III-39a, the stability study at 20 mV.s^{-1} is presented. During the first tens of cycles, a decrease in the capacity is visible. The capacity remains stable after the 100th cycle up to the 1000th, and Figure III-39b shows the CVs at 20 mV.s^{-1}, before and after cycling, with not large differences between each other.

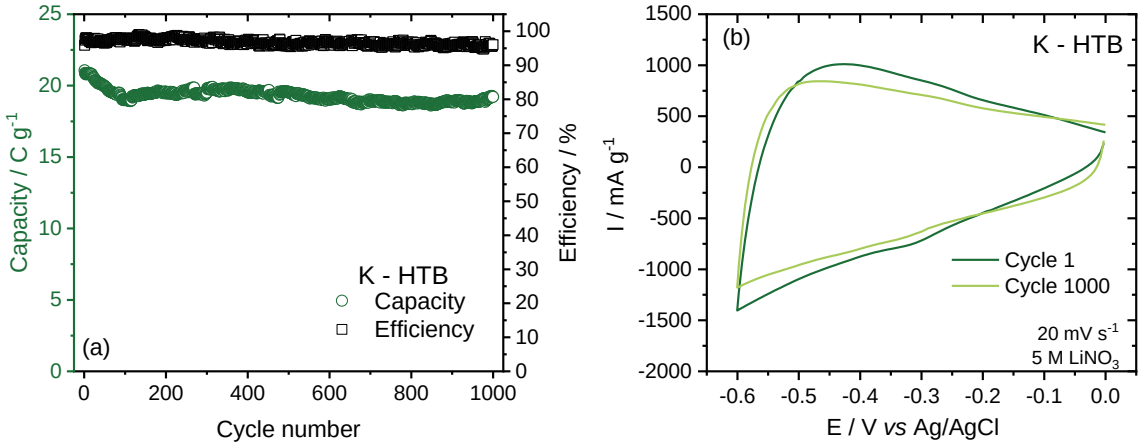

***Figure III-39.** a) Specific capacity in C.g^{-1} and efficiency vs. cycle number and b) cyclic voltammograms at 20 mV.s^{-1} showing the cycle 1 and cycle 1000.*

III.4.3.4. HTBs electrochemical behavior comparison in 5M $LiNO_3$

Figure III-40a and b, and Table III-10 summarize the electrochemical behavior of the hexagonal tungsten bronzes of Li, Na, and K. The CVs show the enormous difference between

the faradaic response of the Li and Na HTB *vs.* the pseudocapacitive response of the K HTB. As aforementioned, such a discrepancy in the behavior between these phases was not expected. Li and Na HBTs are similar compared to the K compound. Consequently, both structural and morphological properties have an impact on how the electrochemical response is taking place. Figure III-40b shows the performance in capacity *vs.* the scan rate. Although Li and Na are very close, structural-wise, the first one exhibits the higher capacity in $C.g^{-1}$, including at a high rate. Moreover, the faradaic response in the Li phase illustrates a more defined faradaic response caused by the intercalation of Li^+ into the lattice of the material.

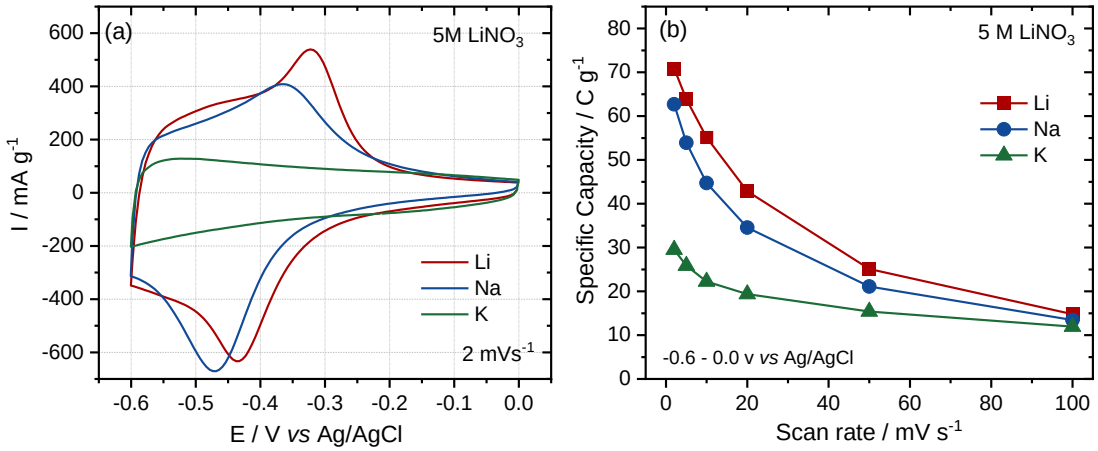

Figure III-40. *a) Cyclic voltammograms at 2 $mV.s^{-1}$ comparing the three HTBs and b) Capacity vs. scan rate comparing the HTBs in $LiNO_3$ 5M.*

Table III-10*. Capacity comparison for the HTBs.*

Hexagonal Tungsten Bronze	**Specific capacity in $C.g^{-1}$ at 2 $mV.s^{-1}$ (~10 min charge/discharge time)**
Li	71
Na	63
K	29.5

A more detailed study about the charge storage mechanism and how the faradaic and pseudocapacitive mechanism takes place will be presented in chapter IV.

III.4.4. HTBs electrochemical behavior in different aqueous electrolytes

In the previous section, the electrochemical study in 5M LiNO3 was shown. This section will discuss the nature of the aqueous electrolyte and its impact on the electrochemical response on the HTBs. The cation in the media will interact differently depending on the alkali host in the compound structure. It will help prove what type of cations are more likely to be intercalated into the lattice. All the electrolytes used are summarized in Table III-11. They all keep 1 M concentration for the respective A+ cation (A=Li^+, Na^+, and K^+) in the solution.

Table III-11. *Aqueous electrolytes with a pH ~7.*

Electrolyte	Concentration
Li_2SO_4	0.5 M
Na_2SO_4	0.5 M
K_2SO_4	0.5 M
$LiNO_3$	1 M

The CVs at 2 $mV.s^{-1}$ comparing the three HTBs in the selected electrolytes are shown in Figure III-41. 0.5 M Na_2SO_4 (see Figure III-41b) shows a kind of small bump at lower potential upon oxidation sweep, for the Li and Na HTBs at -0.47 V and -0.52 V *vs.* Ag/AgCl, respectively. This effect may indicate a small intercalation of Na^+ into the material. Nonetheless, it cannot be conclusive. For the case of the K HTB, the quasi-rectangular shape is observed, meaning no intercalation of Na^+. This particular shape of the potassium compound kept repeating for the other aqueous electrolytes. In 0.5 M K_2SO_4, 0.5 M Li_2SO_4, and 1.0 M $LiNO_3$, the response is very similar for K HTB, a rectangular shape CV with a low performance (Figure III-41a, c, and d).

0.5 M K_2SO_4 electrolyte was the exception for the Li and Na HTBs, showing an irregular CV. Hence, K^+ cations are less likely to be adsorbed for these bronzes than the K HTB, which has the higher SSA. On the other hand, electrolytes containing Li follow the same electrochemical response (Figure III-41a and d). 0.5 M Li_2SO_4 and 1.0 M $LiNO_3$ exhibit a small peak upon oxidation sweep. In the case of Li HTB, it is located at about -0.41 V *vs.* Ag/AgCl, for both Li electrolytes. For Na HTB, the same peaks are located at -0.4 V and -0.41 V *vs.* Ag/AgCl, for 0.5 M Li_2SO_4 and 1.0 M $LiNO_3$, respectively. Thus, confirming the hypothesis that Li+ is more likely to be inserted into the lattice of Li and Na HTBs. Both the structural arrangement and morphology of the nanorods-like particles favor such a mechanism.

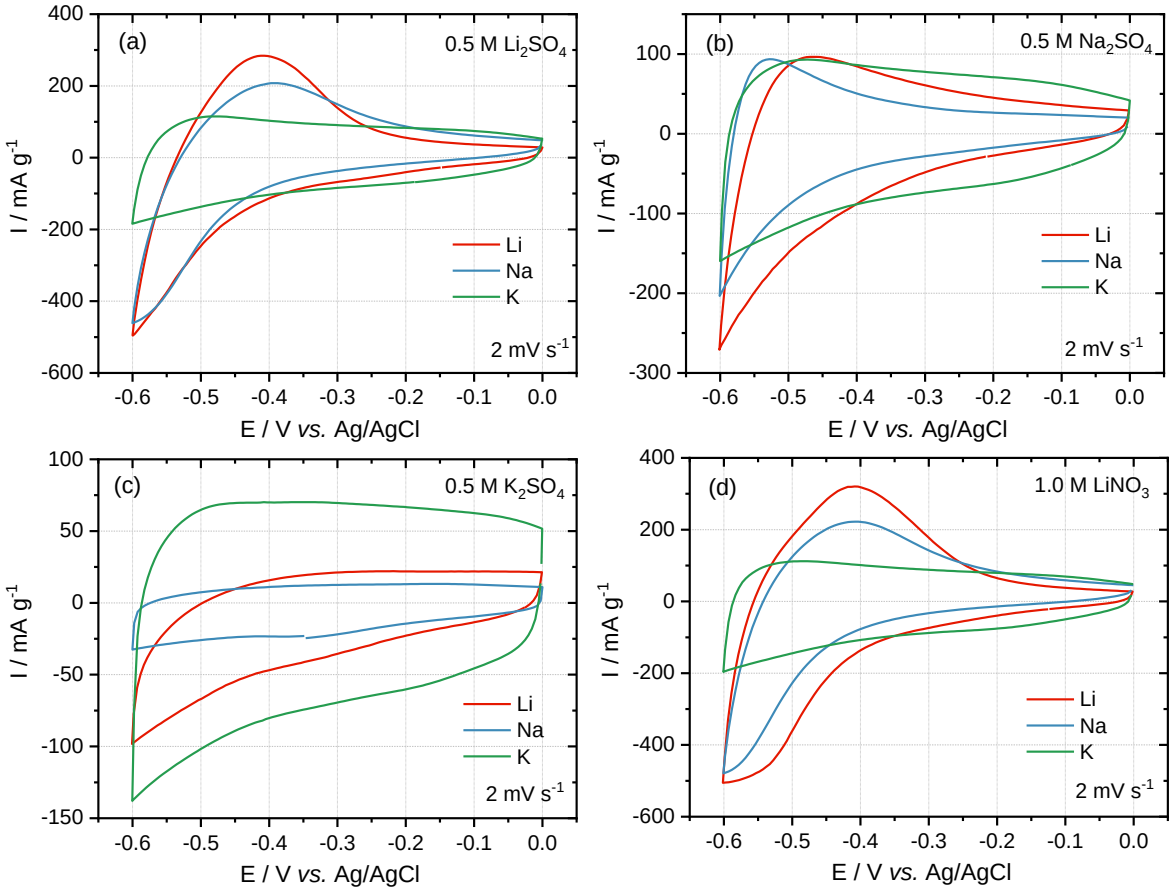

Figure III-41. *Cyclic voltammograms at 2 mV.s^{-1} for a) 0.5 M Li_2SO_4, b) 0.5 M Na_2SO_4, c) 0.5 M K_2SO_4 and d) 1.0 M $LiNO_3$, aqueous electrolytes.*

The CVs above reflect what is shown in Figure III-42, where the K HTB is better in 0.5 M Na_2SO_4 and 0.5 M K_2SO_4, being the opposite in 0.5 M Li_2SO_4 and 1.0 M $LiNO_3$. Thus, demonstrating how the electrolyte's nature and concentration may have an important effect on the electrochemical response of the hexagonal tungsten bronzes. Moreover, a study performed in carbon materials, such as graphene has evidenced the "ion sieving effect",[72] which is related to the size of the cation in the electrolyte *vs.* the size of the pores of the material. For the case of the HTBs, a close relationship can be made. The effective ionic radii[73] for desolvated Li^+, Na^+, and K^+ are 0.76 Å, 1.02 Å, and 1.38 Å, respectively. Li^+ being the smallest one, can have easier access into the HTBs, shown by the faradaic responses observed. Following Li^+ is Na^+, with a similar trend but with less impact. And finally, K^+, which does not present any intercalation activity in the materials. However, it must be mentioned the ion sieving effect described before explains only the behavior for Li and Na HTBs. Whereas the K HTB, does not follow the same trend and only presents a capacitive like behavior in all the electrolytes (see Table III-12).

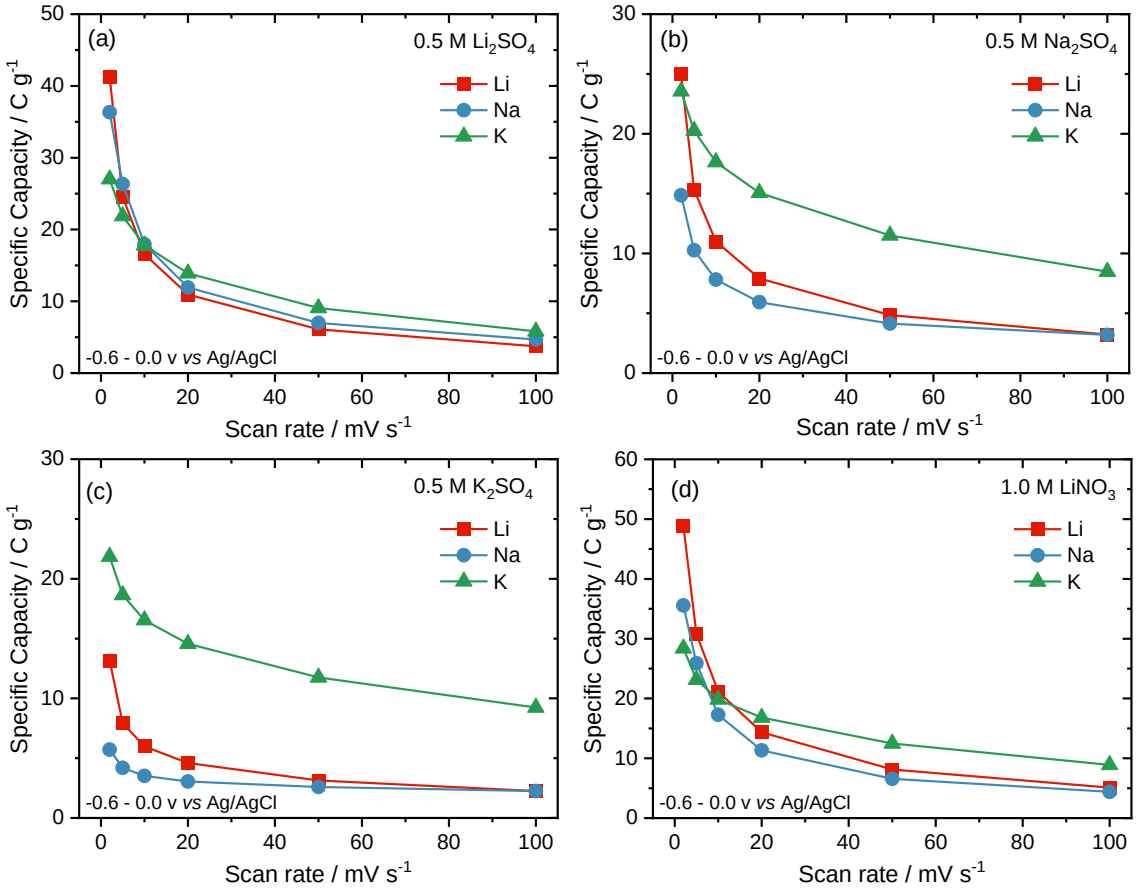

Figure III-42. *Performance of the three bronzes in the different aqueous electrolytes, capacity vs. scan rate in a) 0.5 M Li_2SO_4, b) 0.5 M Na_2SO_4, C) 0.5 M K_2SO_4 and d) 1.0 M $LiNO_3$.*

Table III-12. *Specific capacity comparison in different aqueous electrolytes.*

HTBs	**Specific capacity in C.g^{-1} at 2 mV.s^{-1}**			
	1 M $LiNO_3$	0.5 M Li_2SO_4	0.5 M Na_2SO_4	0.5 M K_2SO_4
Li	49	41	25	13
Na	36	36	15	6
K	28	27	24	22

In the case of 0.5 M K_2SO_4 electrolyte, a particular data treatment was followed, showing a capacitive response for the three HTBs. The current, normalized by the mass of active material shown in Figure III-41c, was normalized *vs.* the specific surface area of each material. The goal is to visualize how the SSA, surface-exposed, will contribute to the adsorption of the ions from the electrolyte. Thus, Figure III-43 compares both CVs in mA.g^{-1} and in µA.cm^{-2}, respectively.

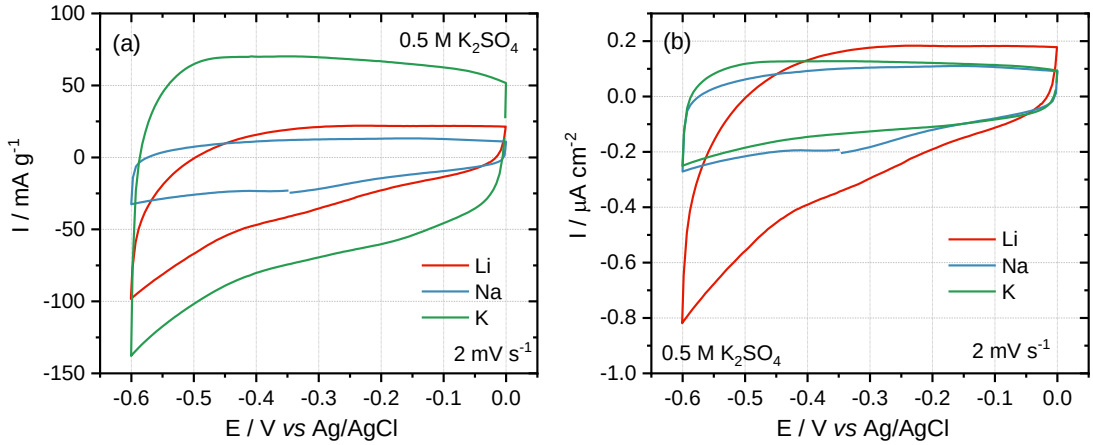

Figure III-43. *Cyclic voltammograms at 2 mV.s^{-1} for 0.5 M K_2SO_4 comparing a) normalized current with mass of active material and b) normalized current with mass of active material and the SSA*

Figure III-43b demonstrates that the electrochemical response for the Na and K HTB in 0.5 M K_2SO_4 electrolyte is very similar, considering the pure electrostatic adsorption of ions at the surface. On the other hand, Li HTB presents a higher value of current upon reduction, which may be related to possible K^+ interaction. However, such a mechanism not be optimal and is indeed a non-reversible process. Moreover, the normalized capacitance was calculated at 2 mV.s^{-1}. It shows that despite the capacitive-like behavior of the CV, the reported values (see Table III-13) are higher than the ones reported for CDCs (carbide-derived-carbons) with SSA higher than 1000 m^2.g^{-1}, around 10-15 µF.cm^{-2}.[74–76] However, one must not take these values lightly since different metals present capacitance values very close to those reported here, as previously shown by Trasatti.[77] Therefore, the capacitance obtained by the SSA will most likely correspond only to a double layer contribution.

Table III-13. *Normalized capacitance for the HTBs in 0.5 M K_2SO_4 at 2 mV.s^{-1}.*

HTB	Normalized capacitance in µF.cm^{-2}
Li	108
Na	50
K	40

The nature of the electrolyte impacting the electrochemical behavior has been presented. it was noticed that the electrolyte concentration seems to play a different role in the response. Therefore, in the following section, electrochemical tests for Li and Na HTBs with LiNO3 at different concentrations will be presented to get a broader understanding of this parameter in the electrochemical study of these materials.

III.4.5. HTB electrochemical behavior in different $LiNO_3$ concentrations *vs.* Water-In-Salt electrolyte

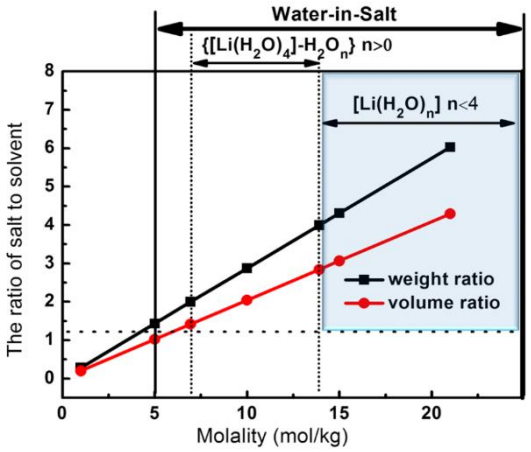

Figure III-44. *The weight and volume ratio of LiTFSI to H_2O change with increasing the molality of LiTFSI in H_2O*[78].

In this section, the study of Li and Na HTBs in different $LiNO_3$ concentrations will be presented. The study will shed light on the differences observed in the past sections in the CVs of 1 M and 5M $LiNO_3$. Additionally, the so-called "water-in-salt" electrolyte will be used as a comparison. These are highly concentrated electrolytes, where the salt outnumbers the solvent both weight and volume-wise (see Figure III-44). In these systems, the average number of water molecules available to solvate an ion is much lower than the regular solvation numbers for lower concentrated electrolytes. Hence, this feature will impact the interfacial interactions between the electrolyte and the surface of the electrodes.[78,79]

LiTFSI (Lithium bis (trifluoromethanesulfonyl) imide) with a concentration of 21 m (moles of solute per kilograms of solvent) will be used along with 1 M $LiNO_3$ (LNO 1M), 5 M $LiNO_3$ (LNO 5M), and 10 M $LiNO_3$ (LNO 10M).

III.4.5.1. The case of Li HTB and Na HTB

Figure III-45a and b shows the cyclic voltammograms for the different $LiNO_3$ concentrations and LiTFSI 21 m for Li HTB and Na HTB, respectively. The shift in the faradaic

response (redox peaks) towards higher potentials can be easily noticed when the concentration of Li^+ increases for both HTBs materials.

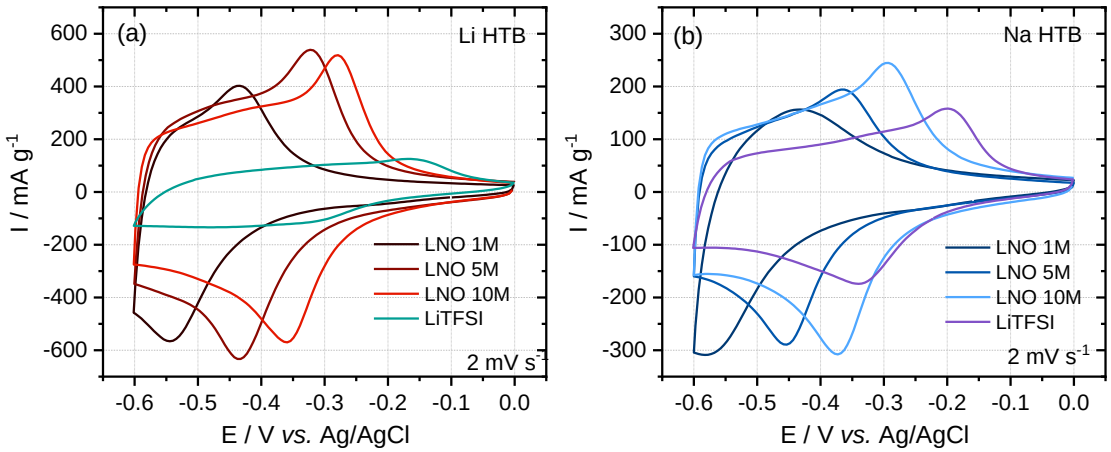

Figure III-45. *Cyclic voltammograms with different $LiNO_3$ concentrations and Water-In-Salt LiTFSI 21 m a) Li HTB and b) Na HTB.*

In the case of the Li HTB in water-in-salt electrolytes, such a shift is not that obvious compared to Na HTB. This is explained as a result the aging of electrode used to carry out the test. Nevertheless, a clear trend related to the concentration and the potential is observed. Figure III-46a and b display ΔE (difference between peaks potentials, cathodic and anodic) and $E_{1/2}$, half wave potential (measured by taking the average of the difference between the potential values of anodic and cathodic peaks), *vs.* the concentration of electrolyte, for each phase.

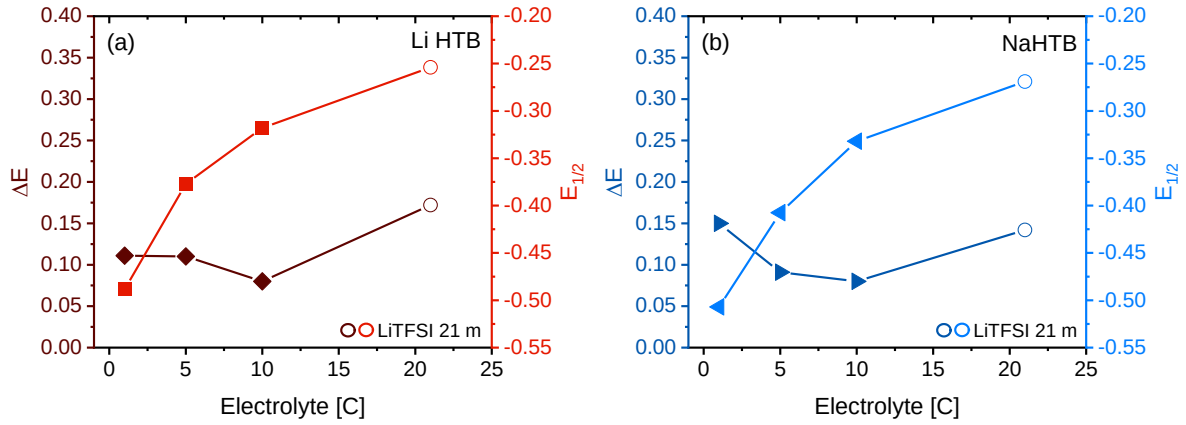

Figure III-46. *ΔE and $E_{1/2}$ vs. electrolyte concentration for (a) Li HTB and (b) for Na HTB.*

Figure III-46 shows how the $E_{1/2}$ moves towards more positive potential values and ΔE shrinks as the concentration increases. These changes upon the increase of concentration are

caused by the lowering of the energy required for the Li^+ cations to be intercalated into the lattice of the materials. Hence, facilitating the intercalation, making it even more reversible[78].

In order to explain this relationship, the number of water moles per Li^+ moles in each electrolyte tested was determined. It provides an idea of how many waters surround one mol of Li^+ cation and if there are enough molecules available to form the respective hydration shells fully.

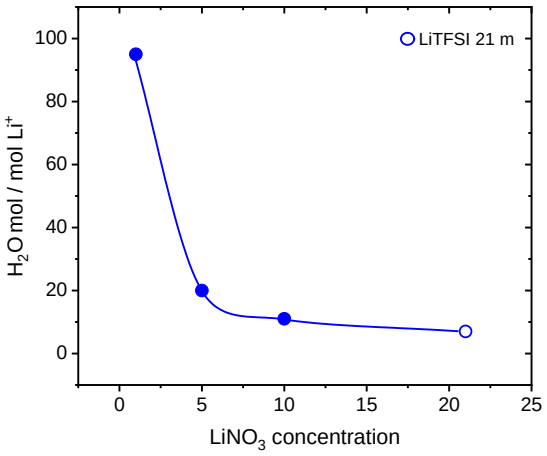

Figure III-47. *Ratio of moles of per moles of Li^+ cations vs. electrolyte concentration*

Figure III-47 shows how the ratio of moles of H_2O per moles of Li^+ cations decreases as the concentration increases, as expected. The vast difference between the LNO 1M *vs.* LNO 5M, ~75 moles of H2O per of 1 mole of Li+ is noticeable. Above 5M, the difference is not that large, ~11 and ~ 7 moles of H_2O per 1mole of Li^+ for LNO 10M and LiTFSI 21 m, respectively. Furthermore, the half wave-potential was plotted *vs.* the ratio of moles of H_2O per moles of Li^+. Thus, confirming that the water surrounding the Li^+ cations plays an important role whenever the Li^+ is intercalated into Li and Na HTBs (see Figure III-48).

Less water is available for the Li^+, consequently less water can form the respective hydration shells (~6 for the first shell).[80–82] For this reason, a decrease in the solvation energy will make it easier to desolvate Li^+ to be intercalated in the hexagonal tungsten bronzes. Subsequently, the potential at which the Li^+ intercalation takes place is higher when the ratio H_2O/Li^+ decreases.

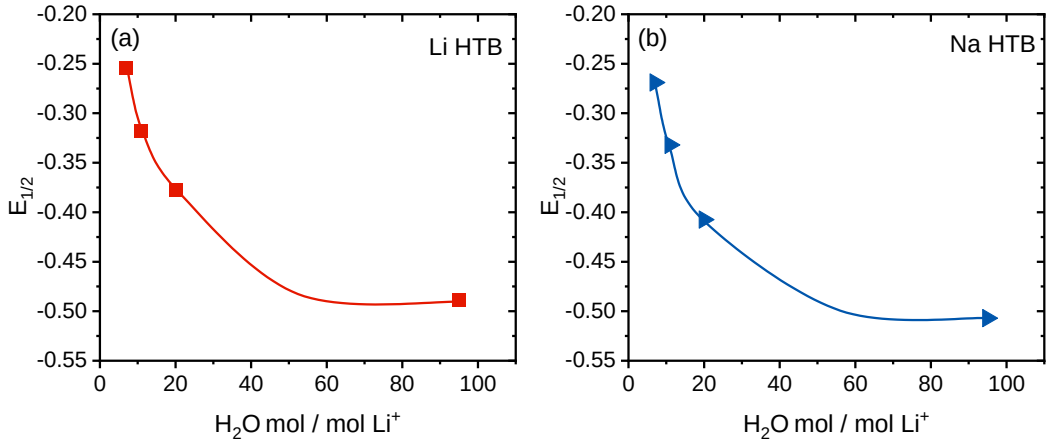

Figure III-48. *Half wave potential $E_{1/2}$ vs. moles of H_2O per mol of Li^+ cations. a) for Li HTB and b) for Na HTB.*

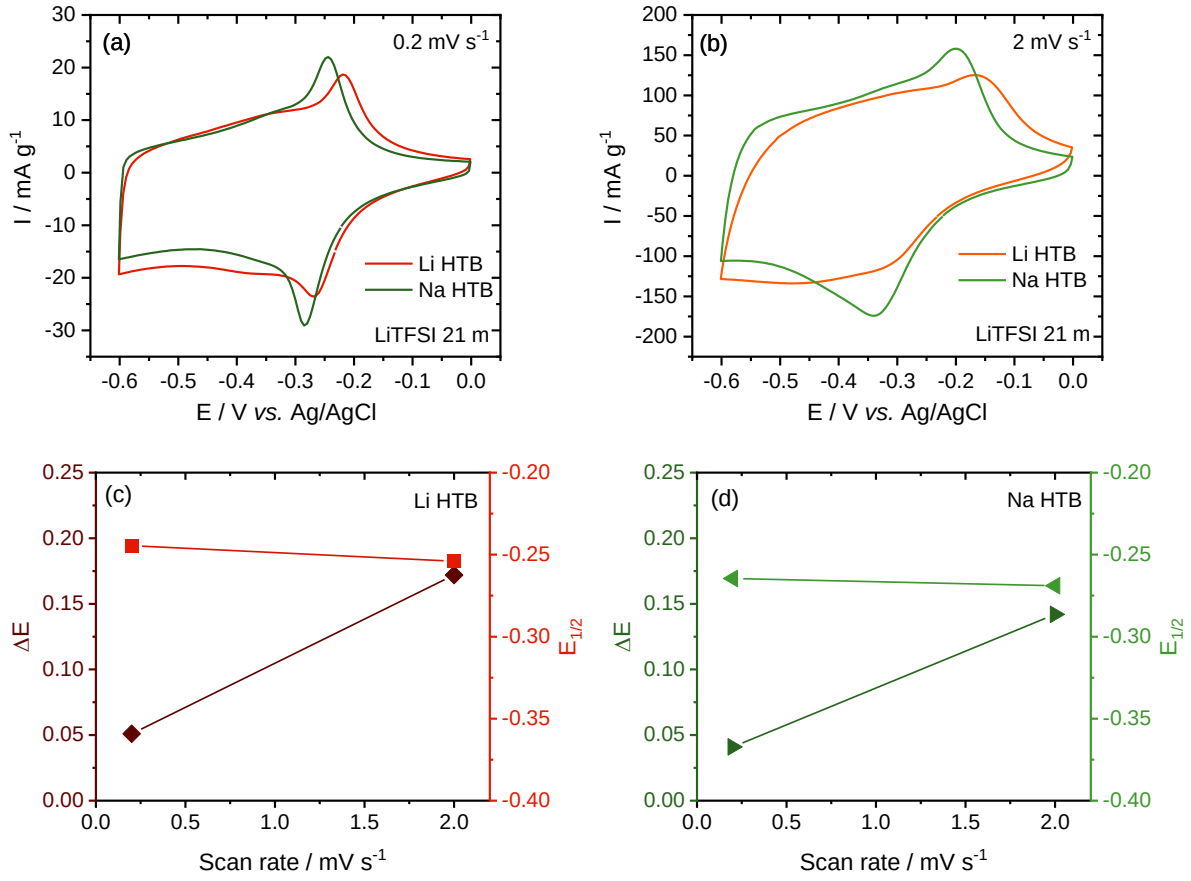

Figure III-49. *Cyclic voltammogram for Li HBT and Na HTB in Water-In-Salt electrolyte (LiTFSI) at a) 0.2 mV.s^{-1} and b) 2 mV.s^{-1}* and, *c) and d) ΔE and $E_{1/2}$ vs. scan rate for Li and Na HTB respectively.*

Finally, to conclude the study using Water-In-Salt electrolyte, CVs at 0.2 mV.s^{-1} and at 2 mV.s^{-1} for both Li HTB and Na HTB were performed. Figure III-49 shows the respective CVs

and plots indicating the ΔE and $E_{1/2}$ *vs.* the respective scan rate (see Figure III-49c and d). As expected, the sweep rate increase will be reflected in the increase in the ΔE, peaks more separated. On the other hand, $E_{1/2}$ should not change, and virtually no variation for the Li HTB and Na HTB is observed.

III.4.6. HTB electrochemical behavior in aqueous 5 M $LiNO_3$ electrolyte at different pH

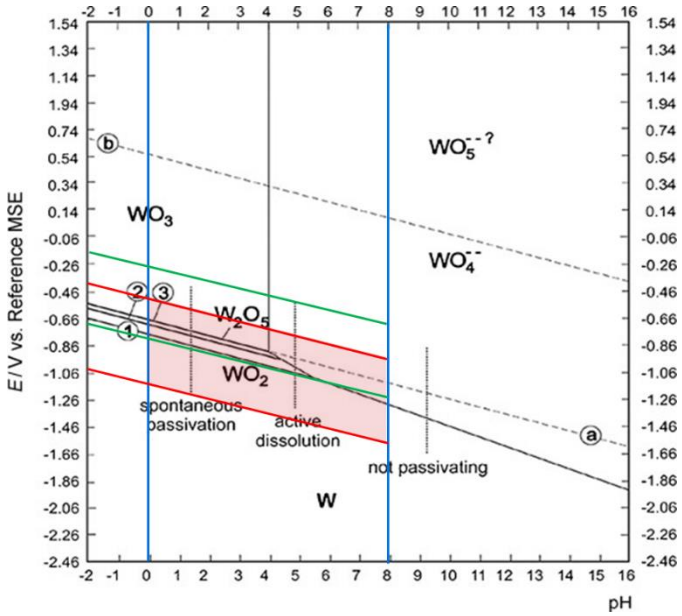

Figure III-50. *Pourbaix diagram for W (25 °C, [$WO4^{2-}$ 10^{-6} mol.L^{-1}). Line (a) shows the reduction equilibrium of water $E_{0,a}$=-0.0591 V x pH at a H_2 or O_2 pressure of 1 bar. Line (b) shows the oxidation equilibrium of water $E_{0,b}$=1.228 V – 0.0591 x pH.*[83,84] *Green lines showing the stability zone for -0.3 – 0.3V vs. Ag/AgCl and red lines the stability zone for -0.6-0.0 V vs. Ag/AgCl, potential windows.*

Several authors have reported the electrochemical properties of different WO_3 polymorphs in acidic electrolytes.[47,85,86] The work presented in this thesis focuses only on studying the hexagonal bronze phases of A_xWO_3 in mild aqueous conditions: aqueous electrolytes with a pH of around 7. Nevertheless, the Pourbaix diagram contains the species in equilibrium in an aqueous electrolyte dominated by various pH-dependent half-cell reactions. By looking at it (see Figure III-50), the question about how the electrochemical behavior of HTBs would change with the variation of the pH was asked. Therefore, several experiments

were performed in 5 M $LiNO_3$ with different pH: 0.0, 2.0, and 7.0. The pH was adjusted with 0.1 M HNO_3.

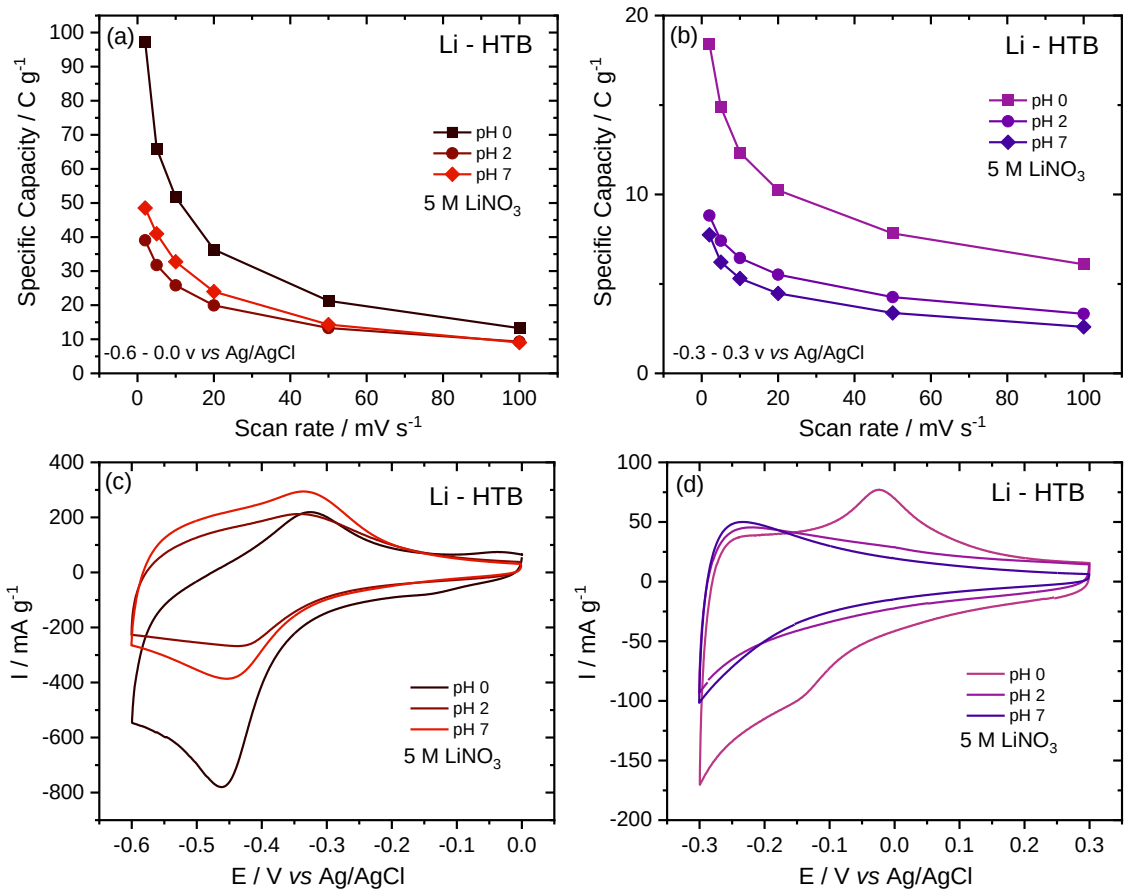

Figure III-51. *Li HTB study in 5M $LiNO_3$ at pH=0.0, pH=2.0 and pH=7.0 in between -0.6 – 0.0 V and -0.3 – 0.3 V vs. Ag/AgCl. a) and b) showing the capacity vs. scan rate and c) and d) the respective CVs.*

Figure III-51 and Figure III-52 show the results for the Li and Na HTB, respectively. These two phases follow the same behavior upon pH change. It can be noticed right away a substantial irreversible capacity in a low pH (~0.0) when cycled from -0.6 – 0.0 V *vs.* Ag/AgCl. Probably due to multiple protons being multiple protons being intercalated without the possibility of getting out, as observed in the very weak anodic peak at ~ 0.3 V *vs.* Ag/AgCl, for both HTBs. If the potential window is shifted now towards more positive potentials, *i.e.*, -0.3 – 0.3 V *vs.* Ag/AgCl, and as indicated in the Pourbaix (see Figure III-50) diagram, the stability of WO_3 will be enhanced. In this more positive potential window, the aforementioned anodic peak is found at ~-0.02 V *vs.* Ag/AgCl, for both HTBs, implicating then some proton deintercalation.

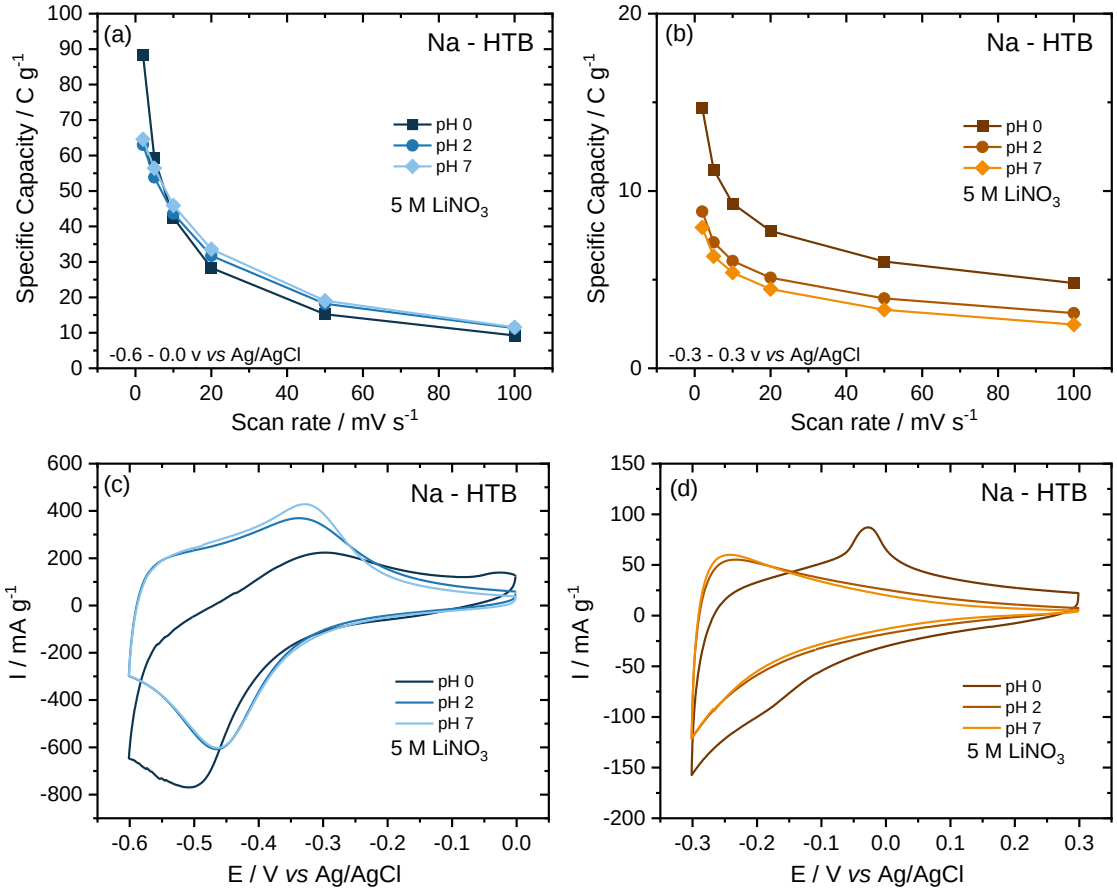

Figure III-52. *Na HTB study in 5M $LiNO_3$ at pH=0.0, pH=2.0 and pH=7.0 in between -0.6 – 0.0 V and -0.3 – 0.3 V vs. Ag/AgCl. a) and b) showing the capacity vs. scan rate and c) and d) the respective CVs.*

At a pH of 2, the already seen "standard" CV shape for the Li and Na HTBs appears. The CV shows the reversible faradaic response from -0.6 – 0.0 V *vs.* Ag/AgCl. A similar shape is maintained when compared to a pH of 7, and a slight increase in capacity is observed. On the other hand, when the test was carried out at a potential window of -0.3 – 0.3 V *vs.* Ag/AgCl, a meager response was obtained for pH 2 and 7.

Such behavior is equally observed for both Li and Na HTBs. It can be explained as follows: Firstly, when the experiment is conducted at lower values of potential (-0.6 – 0.0 V *vs.* Ag/AgCl), and the pH is set at 2, proton intercalation becomes negligible compared to Li^+ activity towards the HTBs, as seen in the CVs of pH 0 *vs.* pH 2. Moreover, there is not any significant improvement being observed when the pH is set back at 7. As initially tested in the previous sections, the performance gets slightly better for both Li and Na HTBs.

Secondly, if the potential window is set from -0.3 – 0.3 V *vs.* Ag/AgCl, a very weak response is obtained for the three pH tests, as seen in Figure III-51b, d, and Figure III-52b and d, which means that in order for the Li^+ cations to be inserted into the host material, the range of the potential window has to be set towards lower values of potentials.

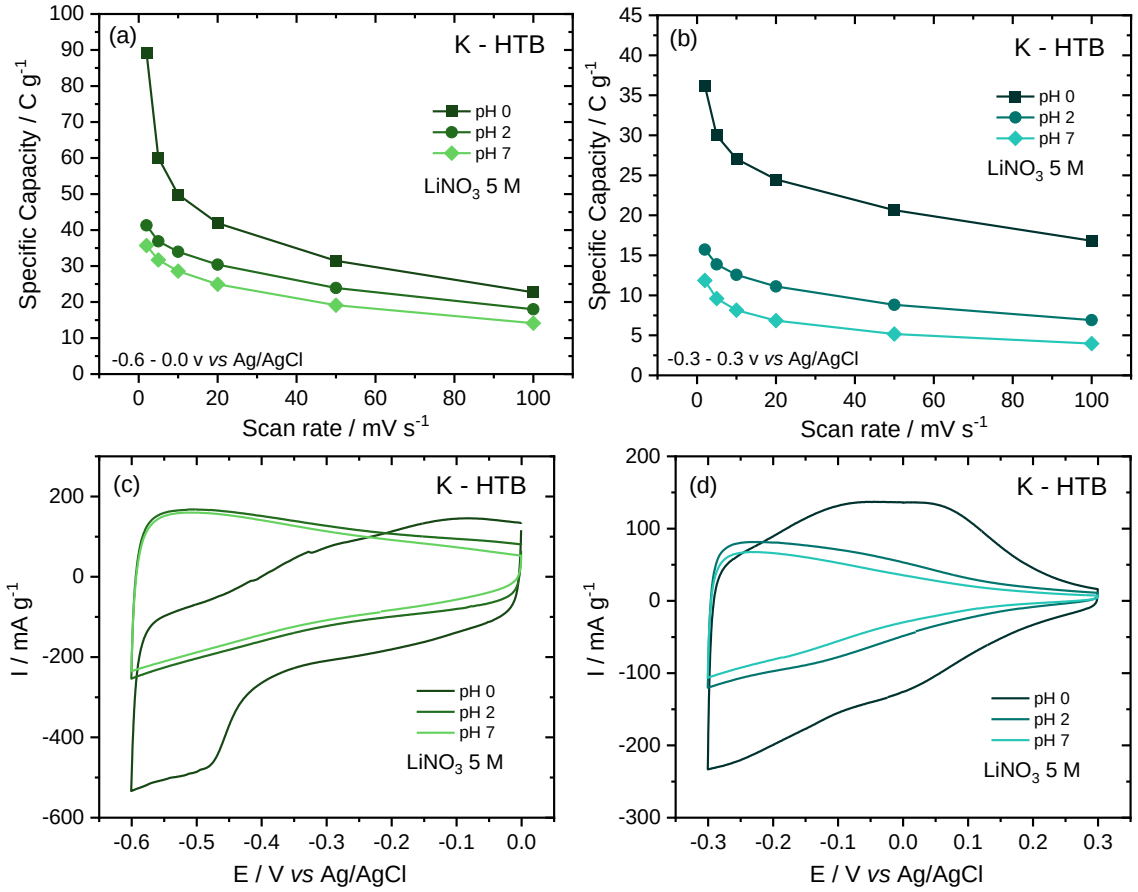

Figure III-53. *K HTB study in 5M $LiNO_3$ at pH=0.0, pH=2.0 and pH=7.0 in between -0.6 – 0.0 V and -0.3 – 0.3 V vs. Ag/AgCl. a) and b) showing the capacity vs. scan rate and c) and d) the respective CVs.*

In the case of K HTB, significant differences can be remarked when cycled in the same previous conditions (see Figure III-53). In previous sections, the performance of K HTB has shown no Li^+ intercalation into the material, due to the clear absence of the faradaic peaks (see Figure III-37 in neutral pH, in section III.4.3.3). However, whenever the K HTB is tested at a pH of 0, the CV shows the same irreversible proton intercalation at lower values of potentials, as seen in Li and Na HTBs. In addition, improved performance at more positive potentials is observed, comparable to the hydrated phase of WO_3 reported by Augustyn *et al.*[47,85] In contrast,

K HTB in 5M $LiNO_3$ at pH 2 and 7 follows the same behavior as Li and Na HTBs. A very similar response at lower values of potentials and weak response at positive potentials.

Table III-14 summarizes the specific capacity at 2 $mV.s^{-1}$ for the three bronzes at a pH of 0, 2, and 7. As mentioned above, the improvement in the capacity upon reduction at a pH of 0 is caused by the irreversible intercalation of H^+ in the material.

Table III-14. *Summary comparing the specific capacity at 2 $mV.s^{-1}$ for the three HTBs at pH 0, 2 and 7.*

HTBs	pH 0	pH 2	pH 7
Li	97	39	49
Na	88	63	65
K	89	41	36

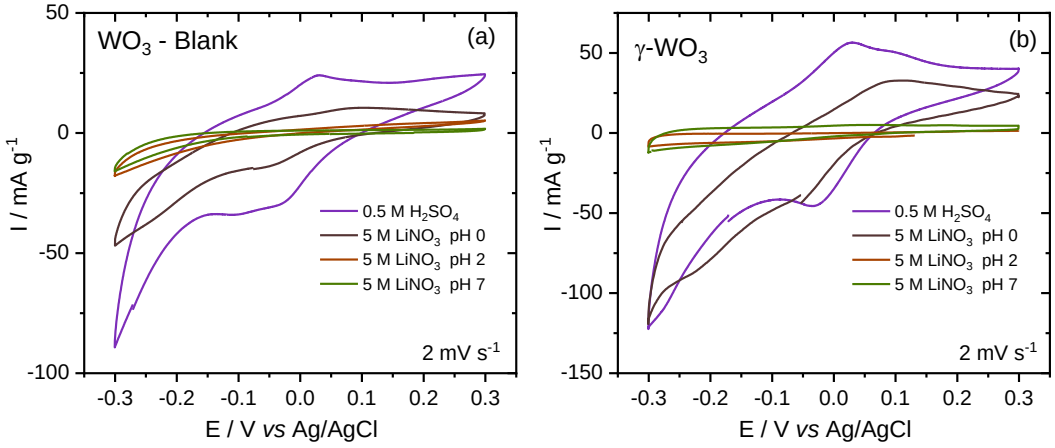

Figure III-54. *Cyclic voltammograms for a) WO_3-blank and b) γ-WO_3 in 5 M $LiNO_3$ pH 0, pH 2, pH 7 and 0.5 M H_2SO_4.*

Furthermore, a comparison in the same set of electrolytes was performed for the monoclinic phase WO_3. In section III.3.2 (see Figure III-9), a glimpse of the electrochemical performance in 5 M $LiNO_3$ of WO_3-blank *vs.* the γ-WO_3 (as-synthesized) was presented. Both materials showed inferior performance, in agreement with what was expected of these specific structural arrangements. In this part, the study will be complemented by comparing the different pH of 5 $LiNO_3$ and with 0.5 M H_2SO_4. Figure III-54 presents the CV for both materials in all the electrolytes mentioned. A priori, no faradaic response is observed for any pH in 5 M $LiNO_3$, for both WO_3-blank and γ-WO_3. The trend mentioned above is followed for pH 2 and pH 7,

with very similar CV shapes. In contrast, pH 0 follows the irreversible proton activity at lower values of potentials, as seen for the HTBs.

On the other hand, the CV in sulfuric acid moderately shows a faradaic response with weak redox peaks observed for both WO_3-blank and γ-WO_3. It must be mentioned that the shape of the CV is not entirely uniform nor symmetric.

Finally, to conclude this study, an electrochemical test of the HTBs in acidic media was conducted in a potential window from -0.3 – 0.3 V *vs.* Ag/AgCl. Figure III-55a and b shows the results obtained. Astonishingly, the performance of the HTBs, Li, Na, and K in 0.5 M H_2SO_4 is far more significant than WO_3 reference phases. Both Li and Na clearly show the faradaic response due to the H^+ (or H_3O^+) intercalation into the material. One defined cathodic peak is depicted at a ~ 0.045 V and -0.084 V *vs.* Ag/AgCl for both Li and Na HTBs. On the other hand, two defined peaks are presented in the reverse sweep: at ~ -0.16 V and 0.114 V, for Li HTB; and -0.16 V and 0.076, for Na HTB. Thus, it demonstrates the capability of the Li and Na HTBs capability to store H^+ (or H3O$^+$) in their structures.

In contrast, K HTB shows the quasi-rectangular shape, typical for this compound. However, in this acidic media, a slight faradaic response can be depicted in a big a significant bump at ~-0.097 V and ~ -0.013 V *vs.* Ag/AgCl in a cathodic and anodic sweep, respectively. It suggests that protons are preferred to be intercalated in this host material compared to Li+, Na+, and K+, as previously exhibited.

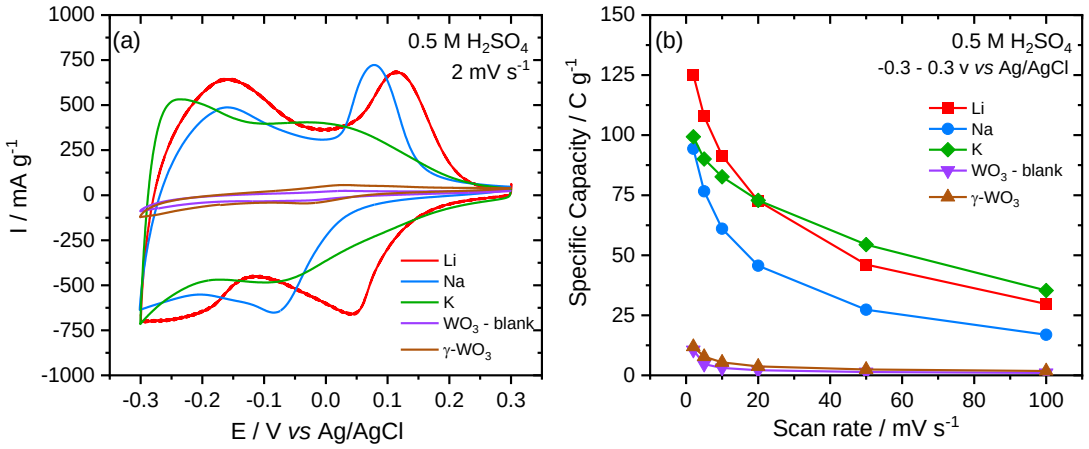

Figure III-55. *a) Cyclic voltammograms at 2 mV.s^{-1} and b) capacity vs. scan rate comparing the electrochemical behavior of the HTBs vs. the references of WO_3 in 0.5 M H_2SO_4.*

This experiment in acidic electrolyte shed light on how fully proton intercalation takes place in the HTBs of Li, Na, and K. As it is depicted in Eq. III-10, Eq. III-11, and, Eq. III-12, due to the small size of H^+, more protons can be inserted into the HTBs structures, regardless of the cation already located inside. In addition, HTBs show a remarkable response when compared to the traditional γ phase of WO_3. Moreover, the CV shape obtained differs from the one already reported by Augustyn's group for the hydrated phase of WO_3[47], highlighting the structural differences between the polymorphs.

$$Li_{0.167}WO_{3.333} + 0.37\,Li^+ + 0.37\,e^- \leftrightarrow H_{0.37}Li_{0.167}WO_{3.333} \qquad \text{Eq. III-10}$$

$$Na_{0.278}WO_{3.139} + 0.24\,Li^+ + 0.24\,e^- \leftrightarrow H_{0.24}Na_{0.278}WO_{3.139} \qquad \text{Eq. III-11}$$

$$K_{0.33}WO_3 + 0.25\,Li^+ + 0.25\,e^- \leftrightarrow H_{0.25}K_{0.333}WO_3 \qquad \text{Eq. III-12}$$

III.4.7. Role and importance of Li^+ in aqueous electrolytes

As previously established, Li^+ is an essential element of the charge storage mechanism for the hexagonal tungsten bronzes when used as electrode materials for energy storage devices operating in aqueous electrolytes. It has been demonstrated how the concentration and the ratio between Li^+ and H_2O molecules make it easier, or not, for the intercalation process to take place. In order to evaluate this vital role of Li^+ and the counter anion in their performance, an electrochemical experiment using sodium nitrate and potassium nitrate with the same concentration as $LiNO_3$ (5 M) was carried out.

Figure III-56a and b show the CVs for the electrolytes described. As reported in section III.4.4 of this chapter, neither Na^+ nor K^+ showed any intercalation activity into the HTBs. This statement is reaffirmed when the bronzes are tested in 5M $NaNO_3$ and 5M KNO_3. The CV shapes and the capacity values obtained are not comparable when the HTBs are cycled in aqueous lithium-based electrolytes. Li and Na HTB show the lowest performance in both $NaNO_3$ and KNO_3, compared to the K HTB, where the "quasi-rectangular" shape is maintained. A disclaimer has to be made concerning the K electrolyte, as it was very saturated, and re-crystallization took place while cycling. Thus an uneven and distorted CV is observed.

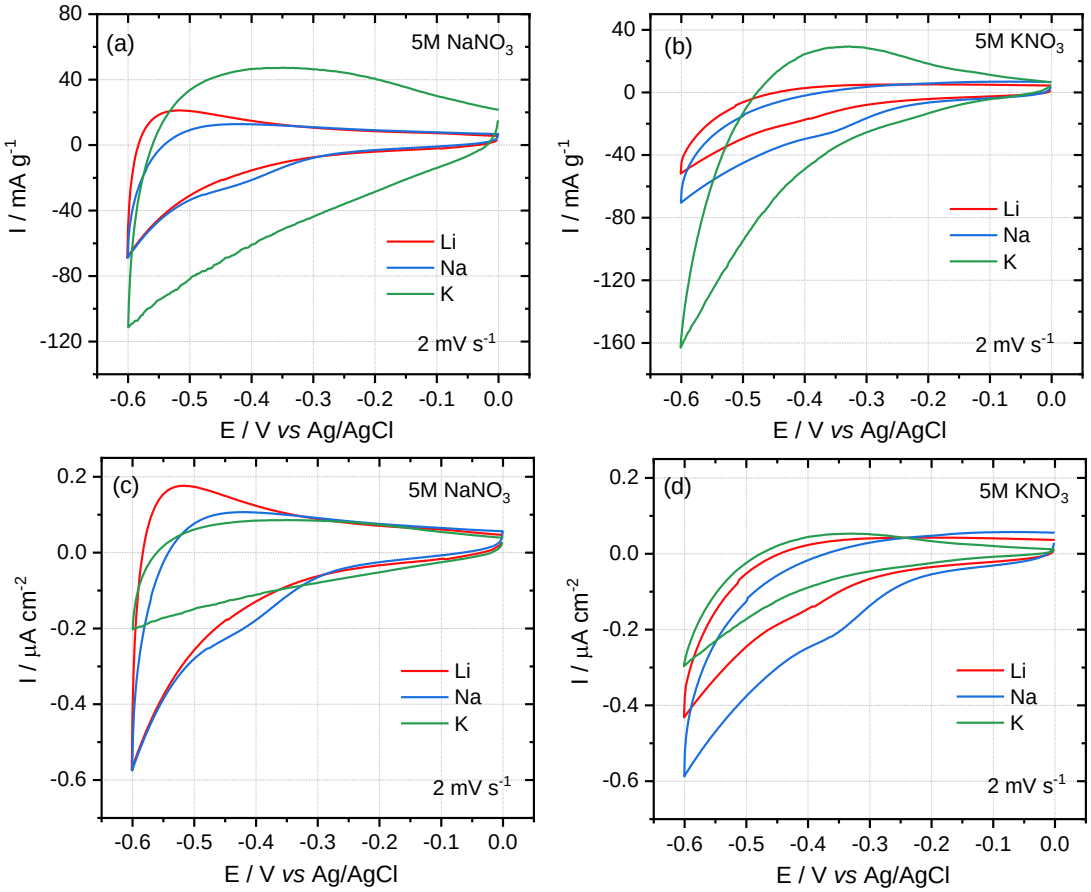

Figure III-56. *Cyclic voltammograms at 2 mV.s^{-1} of the HTBs tested in aqueous a) 5M $NaNO_3$ and b) 5M KNO_3, c) and d) show the normalized current by the SSS in the respective electrolytes.*

Since the significant contribution to the charge storage seems to be "capacitive" because of the shape of the CVs, a normalization of the current over the SSA was made, as previously seen in section III.4.4 in the case of K_2SO_4 electrolyte, see Figure III-56c and d. Table III-15 summarizes the respective capacities in C.g^{-1} *vs.* capacitance in µF.cm^{-2}. It is worth mentioning that the values reported in µF.cm^{-2} may be due to a pure electric double layer behavior with no charge transfer taking place, faradaic or pseudocapacitive.[74,77]

Table III-15. *Comparison of capacity in C.g^{-1} vs. µF.cm^{-2} in 5M $NaNO_3$ and 5M KNO_3.*

HTBs	**Capacity and Capacitance**			
	5 M $NaNO_3$		05 M KNO_3	
	C.g^{-1}	µF.cm^{-2}	C.g^{-1}	µF.cm^{-2}
Li	4.7	65	4.5	63
Na	5.4	75	9.5	132
K	15	45	17	52

Furthermore, to underline the effect of Li^+ in the electrolyte, a test using 2.5 M $NaNO_3$ and 2.5 M KNO_3 with different $LiNO_3$ concentrations was performed. This experiment will follow the change from zero faradaic activity, in the absence of Li^+, *i.e.*, only 2.5 M KNO_3, *versus* the electrolyte containing Li^+ at different concentrations, see Figure III-57.

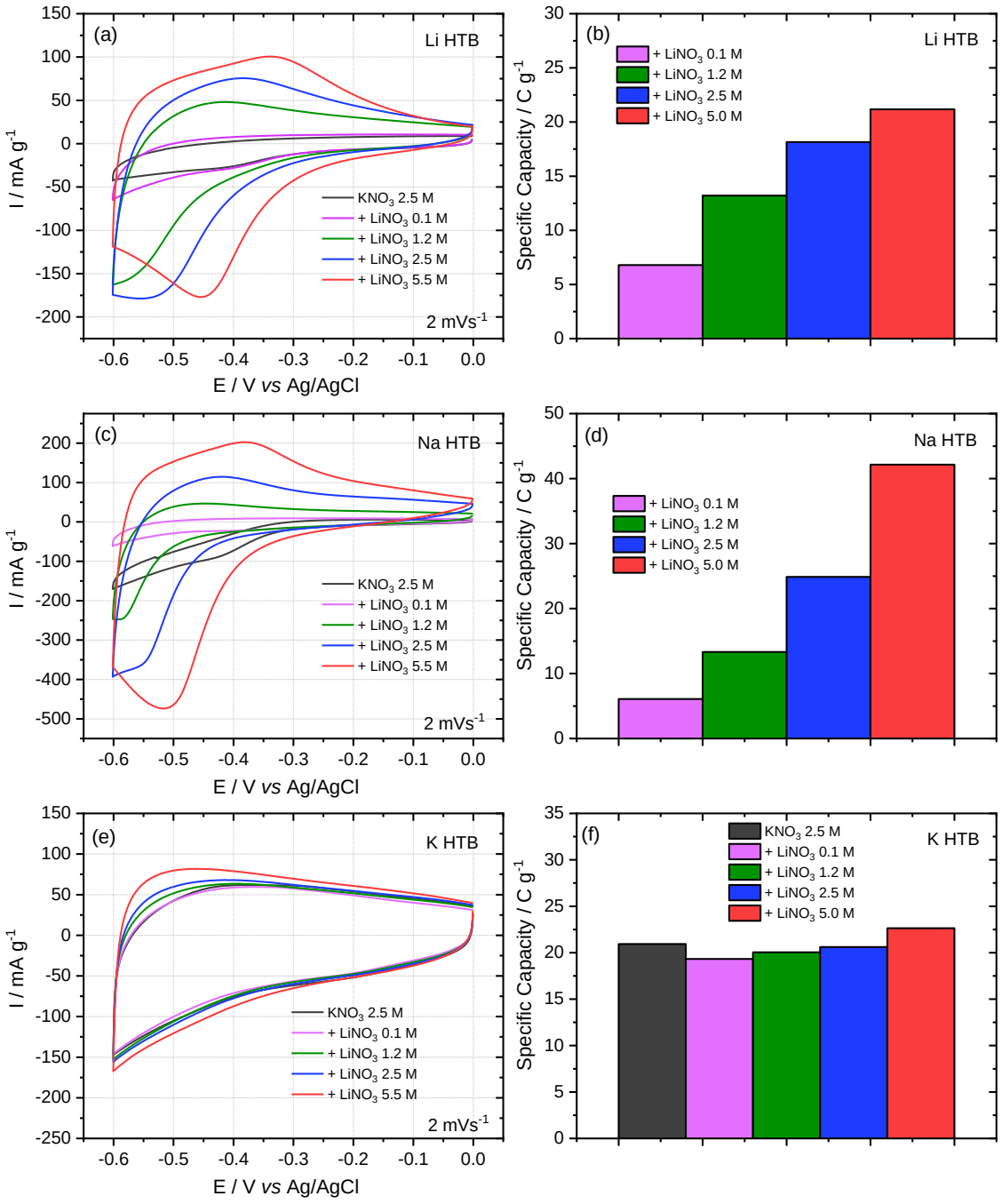

Figure III-57. *Cyclic voltammograms for the HTBs when tested in KNO_3 2.5 M plus different $LiNO_3$ concentrations, a), c) and e). And the respective performances shown in b), d) and f).*

These results highlight how the amount of Li^+/H_2O influences the shape of the CV, regardless of the presence of both K^+ and NO_3^- ions, coming from KNO_3. In the case of Li and Na HTBs, the intercalation mechanism is observed very easily. When $LiNO_3$ reaches 1.2 M concentration, the shape of the CV begins to change until reaching a 5 M concentration; in this point, the usual observed faradaic shape is ultimately manifested (see Figure III-57a and c).

On the other hand, the classic quasi-rectangular shape for the K HTB is seen even with 2.5 M KNO_3 electrolyte with no Li^+. The results showed very close capacity values for all the electrolytes tested, including the maximum Li^+ concentration, supporting the fact that no faradaic response occurs in the K HTB and that the charge storage mechanism is due to capacitive and to a less extend pseudocapacitive contributions.

III.4.8. Preliminary conclusions on the study of hexagonal tungsten bronzes in aqueous electrolytes

There is a relationship between the crystallographic structure of the HTBs and the electrochemical performance. Li and Na phases present similar structural features as well as very similar electrochemical signatures. On the other hand, K HTB shows utterly different behavior. For both Li and Na HTBs, there is clear evidence of the intercalation of Li^+ into the structure shown by the faradaic redox peaks observed. Whereas for the K HTB, the charge storage mechanism, with an evident absence of any faradaic response, most likely only concerns a double layer or a pseudocapacitive mechanism. Further investigations and additional information on that subject will be given in the next chapter. Furthermore, the vital role of the ratio of Li^+/H_2O was evidenced when both Li and Na HTBs were tested in different concentrations of aqueous $LiNO_3$, in addition to the water-in-salt electrolyte test.

III.5. Electrochemical study in organic electrolytes

At the beginning of this section, the electrochemical properties of different phases of WO_3 were introduced. This included the pioneer study by Kumagai *et.al.*[69] They showed the electrochemical intercalation of Li^+ (using $LiClO_4$ in PC) into what they called hexagonal structure of WO_3. This specific phase draws attention due to the absence of alkali cations and

water inside the structure. The synthesis of a pure hexagonal phase in such conditions is questionable. Nevertheless, the interesting electrochemical signature presented by Kumagai encouraged the intention of studying the HTBs reported in this thesis in organic media. Moreover, to compare such behavior to the aqueous systems previously reported.

III.5.1.1. Cyclic voltammetry of Li and Na HTBs at different potential windows

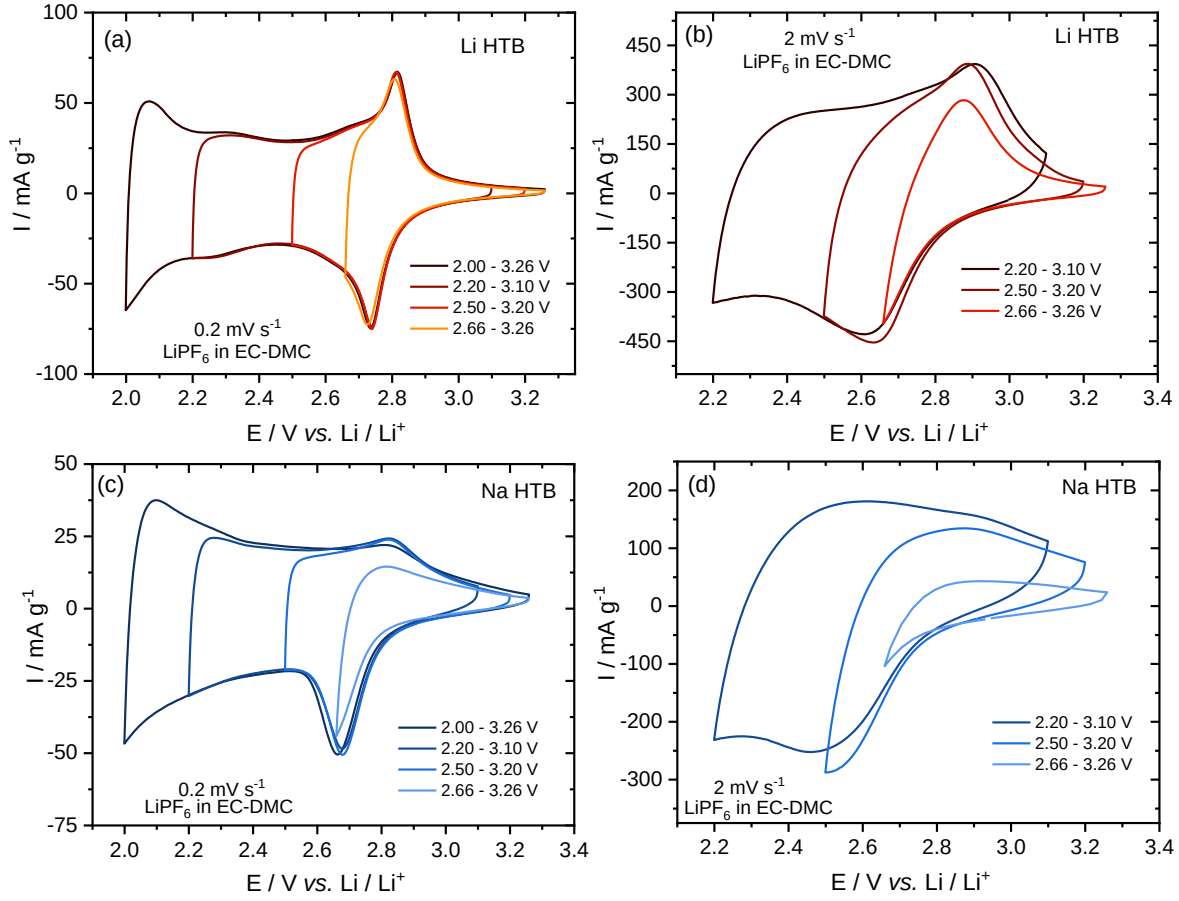

Figure III-58. *Cyclic voltammograms in different potential windows for Li HTB a) 0.2 mV.s^{-1} and b) 2.0 mV.s^{-1} and for Na HTB c) 0.2 mV.s^{-1} and d) 2.0 mV.s^{-1}.*

All the experiments were conducted in the standard electrolyte LP30, 1 M $LiPF_6$ in EC-DMC (50/50 v/v) (lithium hexafluorophosphate in ethylene carbonate and dimethyl carbonate). The first tests consisted in finding the adequate potential window where the faradaic activity could be observable; thus, the Li and Na materials were selected to carry out these experiments. The test started running CVs at 0.2 mV.s^{-1} in four potential windows 2.0-3.26 V, 2.2-3.1 V, 2.5-

3.2 V and 2.66-3.26 *vs.* Li/Li^+ to be compared to 2.0 $mV.s^{-1}$ scan rate in 2.2-3.1 V, 2.5-3.2 V and 2.66-3.26 *vs.* Li/Li^+, as seen Figure III-58.

The faradaic response is located at ~2.73 and 2.81 V *vs.* Li/Li^+ for cathodic and anodic peaks, respectively, in the Li HTB compound (Figure III-58a). In the case of Na HTB, the response is depicted at ~2.67 and 2.82 V *vs.* Li/Li^+ for both cathodic and anodic peaks, respectively. It is worth mentioning the shift towards higher potentials of the HTBs reported here compared to the study of Kumagai *et al.*[69], where broader peaks are presented in ~2.4 V and ~2.6 V *vs.* Li/Li^+.

Once the potential window is extended towards more negative potentials, no more peaks can be depicted before ~2.0 V *vs.* Li/Li^+, where the sweep stopped. Hence, a shorter potential window was selected for further tests. In contrast, when the scan rate increases, a distortion of the CV is observed, compared to the low scan rate CV. Thus, this may indicate a kinetic dependence on the scan rate. Moreover, this will be more important in aqueous systems. Such a comparison will be presented further in this section.

III.5.1.2. HTBs in organic media

As previously mentioned, an evaluation of different potential windows was performed. A cyclic voltammetry test was performed at 0.1 $mV.s^{-1}$ for over 100 cycles between 2.5 and 3.1 V *vs.* Li/Li^+, where the faradaic activity is more evident. These experiments will help understand how the material behaves in an organic electrolyte at a low sweep rate. Such results are shown in Figure III-59.

Both Li and Na HTBs present the expected faradaic response. Furthermore, the remarkable stability of up to 100 cycles at such a slow rate is observed. Li HTB shows a slight decrease in the capacity compared to the sodium compound, which increases the performance. This could be associated with an activation process occurring before the system achieves its maximum performance. This difference is evidenced in the CV at cycle 100^{th} *vs.* the 1^{st} cycle, see Figure III-59c.

Unsurprisingly, the K HTB exhibited the same CV form as in an aqueous system, a classic quasi-rectangular shape with no visible faradaic contributions. Moreover, it shows a more considerable capacity loss after 100 cycles when compared to the previous HTBs. A

summary of the respective capacities in the 1st cycle *vs.* the 100th cycle and the capacity retention in % is shown in Table III-16.

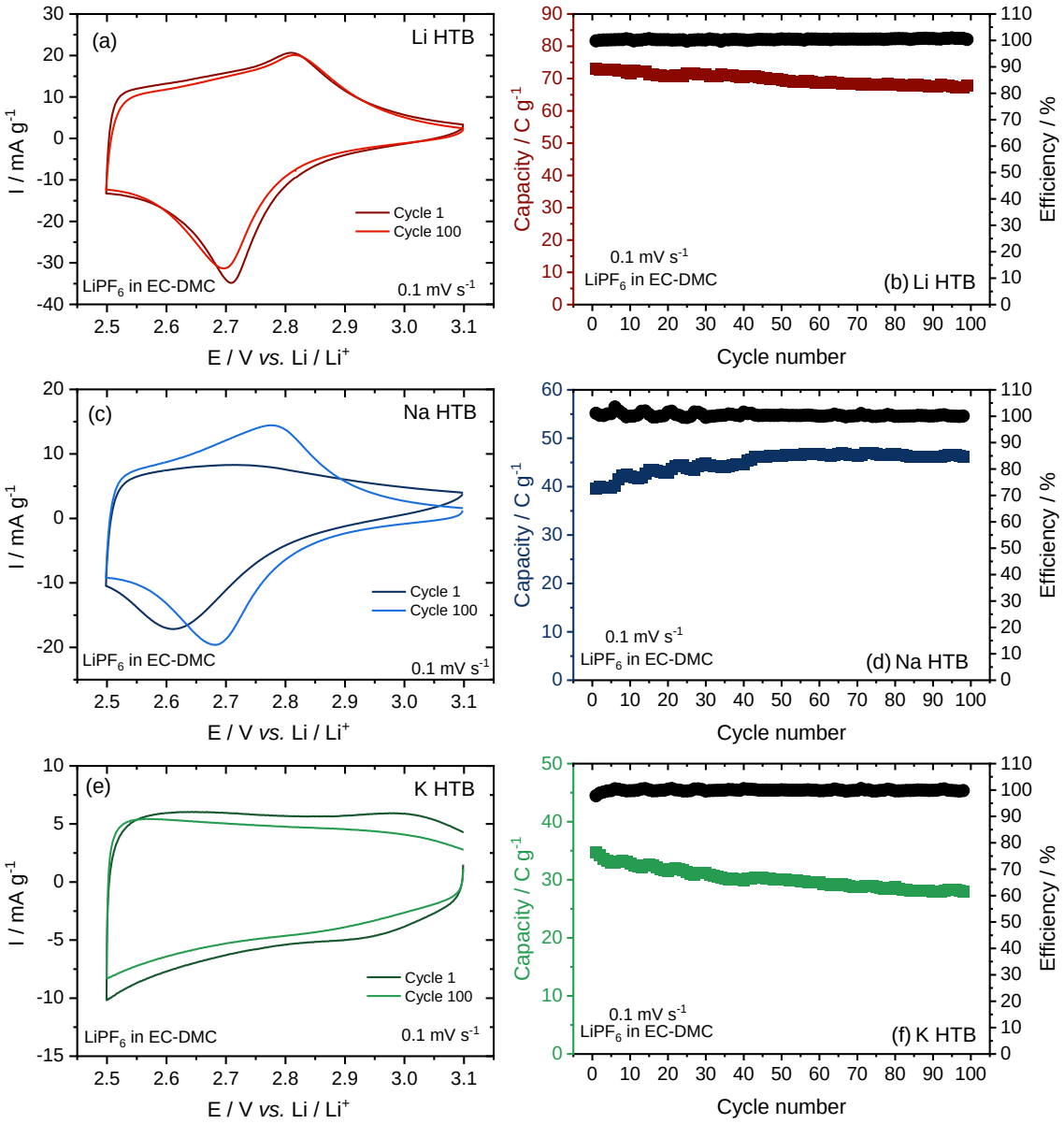

Figure III-59. *Cyclic voltammograms at 0.1 mV.s^{-1} showing cycle 1 and cycle 100 for a) Li, c) Na and e) K HTB. And efficiency vs. cycle number in b), d) and f), respectively.*

Table III-16. *Capacity of the HTBs in organic electrolyte.*

HTB	**Capacity in C.g^{-1}**		**Capacity retention in %**
	Cycle 1	Cycle 100	
Li	73	68	~ 93 %
Na	40	46	~ 115 %
K	35	28	~ 80 %

Furthermore, it should be noted that the values of capacity presented for the three materials at 0.1 $mV.s^{-1}$ are very close to the ones reported in aqueous 5 M $LiNO_3$ at a much larger rate (2 $mV.s^{-1}$). A comparison of the two systems will be presented later in the next section.

III.5.1.3. Organic *vs.* Aqueous systems

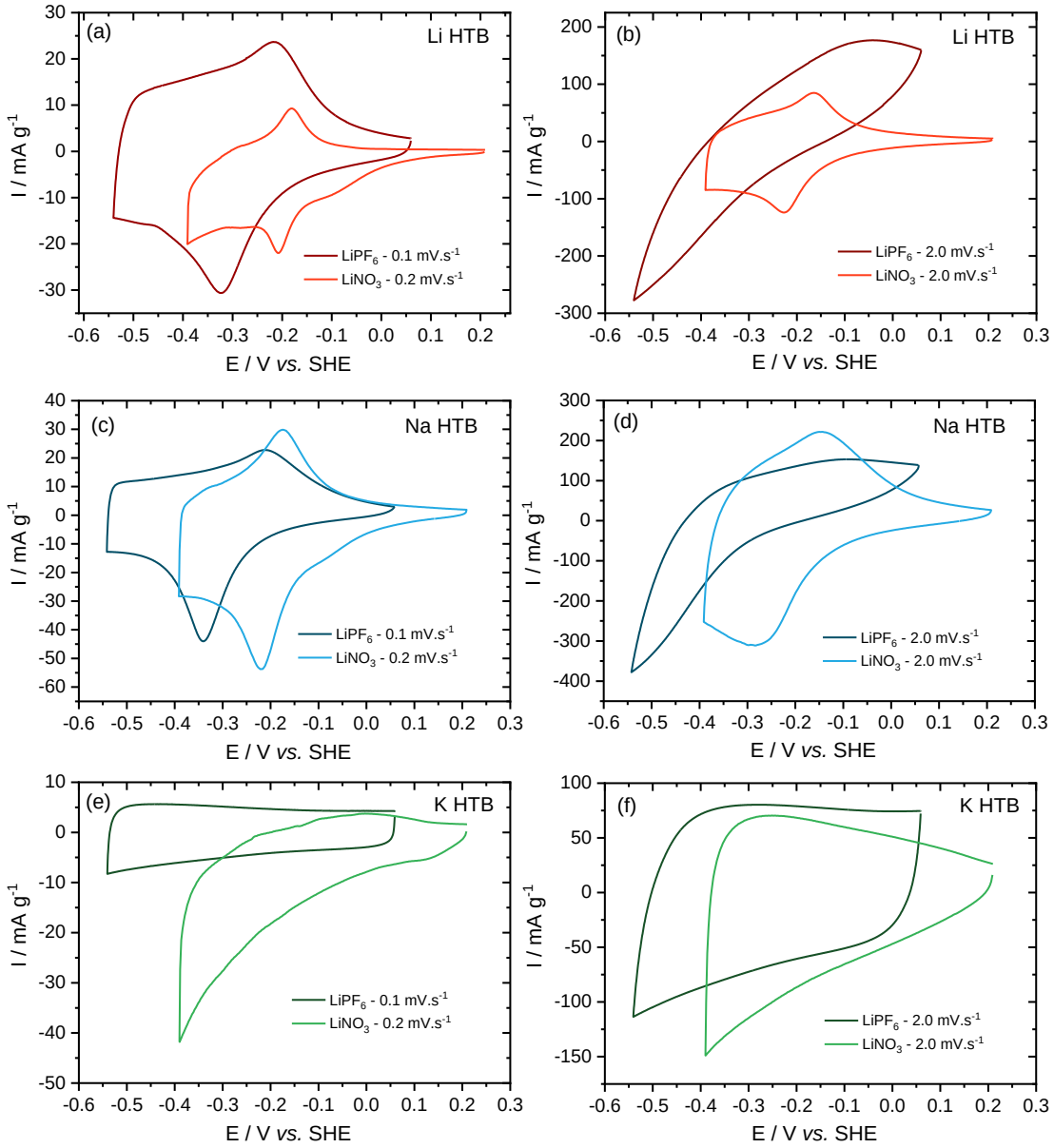

Figure III-60. *Cyclic voltammograms comparing the performance of the HTBs in organic vs. aqueous electrolytes at different sweep rates, a) and b) Li HTB, c) and d) Na HTB, and e) and f) K HTB.*

The electrochemical performance of the Li, Na, and K hexagonal tungsten bronzes, both in aqueous and organic systems, have been previously described and discussed in this chapter. This section will present a comparison between aqueous 5M LiNO3 and 1M LiPF6 in EC-DMC. This will help to continue the investigation and understanding of how Li^+ cations in the electrolyte interact with the HTBs depending on the surrounding media.

Figure III-60 displays the CVs at 0.1 $mV.s^{-1}$, 0.2 $mV.s^{-1}$ and 2.0 $mV.s^{-1}$ in the corresponding electrolytes. All the CVs have been re-plotted *vs.* Standard Hydrogen Electrode to have a full comparison and highlight the position of the faradaic responses in each experiment. Unfortunately, the experiments at 0.1 $mV.s^{-1}$ in aqueous electrolyte were not performed.

First of all, a shift towards lower potentials is presented in organic electrolyte *vs.* aqueous at a meager scan rate, 0.1 $mV.s^{-1}$, compared to 0.2 $mV.s^{-1}$ in aqueous. As aforementioned, water molecules in the electrolyte somehow are involved in the intercalation mechanism of the Li^+, reducing thus the amount of energy necessary for that specific process to take place. The lack of water in organic electrolytes changes how the intercalation occurs, being substantially visible at higher rates. The CVs at 2.0 $mV.s^{-1}$ shows how, in the organic media, the classic shape of the faradaic behavior is completely lost compared to the case of water-base electrolytes where the cathodic and anodic peaks are undisturbed. All of these changes are visible for the Li and Na HTBs.

On the other hand, the K compound presents an entirely different behavior. It performs very poorly at a low scan rate in aqueous media, showing a very resistive and very uneven CV. In the case of organic media at 0.1 $mV.s^{-1}$, the quasi-rectangular shape will be maintained. On the contrary, the behavior is nearly identical at higher rates with very similar CVs and close values of capacity. This brings more evidence about the EDL behavior of this compound, where possibly no faradaic activity is occurring.

III.6. Conclusions – Chapter III

In this chapter, the hexagonal tungsten bronzes of Li, Na, and K were introduced. The low-temperature "hydrothermal synthesis" specifically adapted for these phases was presented. In this method, the role of the cation size was evidenced by the different structural and morphological arrangements obtained for each HTB. Moreover, we demonstrated important crystallographic features deferring from those already reported in the literature. This study adds to the literature and contributes to the enrichment and better understanding of this subject.

Afterwards, the electrochemical performance of the HTBs was investigated in different aqueous electrolytes, which is the central area of interest of this thesis. Moreover, the classic LP30 organic electrolyte was used as a comparison and to prove differences. We shed light on the exciting performance mainly for the Li and Na HTBs, depicting a faradaic signature originated by the Li^+ intercalation of the electrolyte.

We demonstrated that the cation size in the electrolyte and the number of water surrounding the cations impact the intercalation mechanism. Moreover, the different electrochemical behavior for the K HTB was evidence, where no faradaic signature was observed.

In conclusion, we have proposed different mechanisms to explain such exciting and different behaviors for each HTBs. However, in-depth studies using more powerful techniques are necessary to better understand how the charge transfer is taking place and differentiate the intermediating contributions. These further studies will be presented in chapter 4.

III.7. References – Chapter III

1. Wöhler, F. Ueber das Wolfram. *Ann. Phys. phys. Chem.* **78**, 345–358 (1824).
2. Magnéli, A. *et al.* Contribution to the Knowledge of the Alkali Tungsten Bronzes. *Acta Chem. Scand.* **5**, 372–378 (1951).
3. Hägg, G. The Spinels and the Cubic Sodium-Tungsten Bronzes as New Examples of Structures with Vacant Lattice Points. *Nature* **135**, 874–874 (1935).
4. Magnéli, A. Tungsten Bronzes containing Six-membered Rings of WO_6 Octahedra. *Nature* **169**, 791–792 (1952).
5. Magnéli, A., Virtanen, A., Olsen, J. & Sörensen, N. A. Studies on the Hexagonal Tungsten Bronzes of Potassium, Rubidium, and Cesium. *Acta Chem. Scand.* **7**, 315–324 (1953).
6. Dickens, P. G. & Whittingham, M. S. The tungsten bronzes and related compounds. *Q. Rev., Chem. Soc.* **22**, 30 (1968).
7. Magnéli, A. Some aspects of the crystal chemistry of oxygen compounds of molybdenum and tungsten containing structural elements of ReO_3 or perovskite type. *J. inorg. nucl.* **2**, 330–339 (1956).
8. Ribnick, A. S., Post, B. & Banks, E. Phase Transitions in Sodium Tungsten Bronzes. in *Nonstoichiometric Compounds* vol. 39 246–253 J. Am. Chem. Soc., (1963).
9. Wold, A., Kunnmann, W., Arnott, R. J. & Ferretti, A. Preparation and Properties of Sodium and Potassium Molybdenum Bronze Crystals. *Inorg. Chem.* **3**, 545–547 (1964).
10. Bither, T. A., Gillson, J. L. & Young, H. S. Synthesis of Molybdenum and Tungsten Bronzes at High Pressure. *Inorg. Chem.* **5**, 1559–1562 (1966).
11. Hagenmuller, P. Les bronzes oxygénés. *Prog. Solid. State Ch.* **5**, 71–144 (1971).
12. Ridgley, D. & Ward, R. The Preparation of a Strontium-Niobium Bronze with the Perovskite Structure. *J. Am. Chem. Soc.* **77**, 6132–6136 (1955).
13. Andersson, S. & Wadsley, A. D. The structures of $Na_2Ti_6O_{13}$ and $Rb_2Ti_6O_{13}$ and the alkali metal titanates. *Acta Crystallogr.***15**, 194–201 (1962).
14. Sienko, M. J. Thallium-Tungsten Bronze: A Solid State Defect Structure. *J. Am. Chem. Soc.* **81**, 5556–5559 (1959).
15. Conroy, L. E. & Yokokawa, T. The Preparation and Properties of a Barium Tungsten Bronze. *Inorg. Chem.* **4**, 994–996 (1965).
16. Hussain, A. Phase Analyses of Potassium, Rubidium and Cesium Tungsten Bronzes. *Acta Chem. Scand.* **A32**, 479–484 (1978).
17. Hussain, A., Kihlborg, L. & Klug, A. The transformation between hexagonal potassium tungsten bronze and polytungstate. *J. Solid State Chem.* **25**, 189–195 (1978).
18. Pye, M. F. & Dickens, P. G. A structural study of the hexagonal potassium tungsten bronze, K0.26WO3. *Mater. Res. Bull.* **14**, 1397–1402 (1979).
19. Sharma, R. Bronzoid phases in the pseudo-binary system $A_xNb_xW_{1-x}O_3$ with A = K and Cs. *Mater. Res. Bull.* **20**, 1373–1381 (1985).

20. Livage, J. Chimie douce: from shake-and-bake processing to wet chemistry. *New J. Chem.* **25**, 1–1 (2001).

21. Sanchez, C. *et al.* "Chimie douce": A land of opportunities for the designed construction of functional inorganic and hybrid organic-inorganic nanomaterials. *Comptes Rendus Chimie* **13**, 3–39 (2010).

22. Livage, J., Henry, M. & Sanchez, C. Sol-gel chemistry of transition metal oxides. *Prog. Solid. State Ch.* **18**, 259–341 (1988).

23. Zha, J. & Roggendorf, H. Sol–gel science, the physics and chemistry of sol–gel processing, Ed. by C. J. Brinker and G. W. Scherer, Academic Press, Boston 1990, xiv, 908 pp., bound—ISBN 0-12-134970-5. *Advanced Materials* **3**, 522–522 (1991).

24. Judeinstein, P. & Sanchez, C. Hybrid organic–inorganic materials: a land of multidisciplinarity. *J. Mater. Chem.* **6**, 511–525 (1996).

25. Sanchez, C., Ribot, F., Rozes, L. & Alonso, B. Design of Hybrid Organic-Inorganic Nanocomposites Synthesized Via Sol-Gel Chemistry. *Mol. Cryst. Liq. Cryst*. **354**, 143–158 (2000).

26. Soft Chemistry Routes. in *Essentials of Inorganic Materials Synthesis* 57–95 (John Wiley & Sons, Inc, 2015). doi:10.1002/9781118892671.ch10.

27. Rabenau, A. The Role of Hydrothermal Synthesis in Preparative Chemistry. *Angew. Chem. Int. Ed. Engl.* **24**, 1026–1040 (1985).

28. Eugster, H. P. Minerals in hot water. *American Mineralogist* **71**, 655–673 (1986).

29. Byrappa, K. & Yoshimura, M. *Handbook of hydrothermal technology: a technology for crystal growth and materials processing*. (Noyes Publications, 2001).

30. Demazeau, G. Review. Solvothermal Processes: Definition, Key Factors Governing the Involved Chemical Reactions and New Trends. *Z. Naturforsch. B.* **65**, 999–1006 (2010).

31. Li, Y. J. & Whittingham, M. S. Hydrothermal synthesis of new metastable phases: preparation and intercalation of a new layered titanium phosphate. *Solid State Ion.* **63–65**, 391–395 (1993).

32. Katz, E. & Willner, I. Integrated Nanoparticle–Biomolecule Hybrid Systems: Synthesis, Properties, and Applications. *Angew. Chem. Int. Ed.* **43**, 6042–6108 (2004).

33. Rao, C. N. R., Cheetham, A. K. & Thirumurugan, A. Hybrid inorganic–organic materials: a new family in condensed matter physics. *J. Phys.: Condens. Matter* **20**, 083202 (2008).

34. Gerand, B., Nowogrocki, G., Guenot, J. & Figlarz, M. Structural study of a new hexagonal form of tungsten trioxide. *J. Solid State Chem.* **29**, 429–434 (1979).

35. Gerand, B., Nowogrocki, G. & Figlarz, M. A new tungsten trioxide hydrate, WO_3*1/3H_2O: Preparation, characterization, and crystallographic study. *J. Solid State Chem.* **38**, 312–320 (1981).

36. Reis, K. P., Ramanan, A. & Whittingham, M. S. Hydrothermal synthesis of sodium tungstates. *Chem. Mater.* **2**, 219–221 (1990).

37. Reis, K. P., Prince, E. & Whittingham, M. S. Rietveld analysis of sodium tungstate hydrate $Na_xWO_{3+x/2}$•yH_2O, which has the hexagonal tungsten bronze structure. *Chem. Mater.* **4**, 307–312 (1992).

38. Reis, K. P., Ramanan, A. & Whittingham, M. S. Synthesis of novel compounds with the pyrochlore and hexagonal tungsten bronze structures. *J. Solid State Chem.* **96**, 31–47 (1992).

39. Bartha, L., Kiss, A. B. & Szalay, T. Chemistry of tungsten oxide bronzes. *Int J Refract Hard Met.* **13**, 77–91 (1995).

40. Gotić, M., Ivanda, M., Popović, S. & Musić, S. Synthesis of tungsten trioxide hydrates and their structural properties. *Mater. Sci. Eng. B.* **77**, 193–201 (2000).

41. Gu, Z. *et al.* A Simple Hydrothermal Method for the Large-Scale Synthesis of Single-Crystal Potassium Tungsten Bronze Nanowires. *Chem. Eur. J* **12**, 7717–7723 (2006).

42. Wang, J., Khoo, E., Lee, P. S. & Ma, J. Synthesis, Assembly, and Electrochromic Properties of Uniform Crystalline WO_3 Nanorods. *J. Phys. Chem. C* **112**, 14306–14312 (2008).

43. Gao, T. & Jelle, B. P. Visible-Light-Driven Photochromism of Hexagonal Sodium Tungsten Bronze Nanorods. *J. Phys. Chem. C* **117**, 13753–13761 (2013).

44. Miao, B. *et al.* Large scale hydrothermal synthesis of monodisperse hexagonal WO_3 nanowire and the growth mechanism. *Mater. Lett.* **147**, 12–15 (2015).

45. Gao, T. & Jelle, B. P. Electrochromism of hexagonal sodium tungsten bronze nanorods. *Sol. Energy Mater Sol. Cells.* **177**, 3–8 (2018).

46. Loopstra, B. O. & Rietveld, H. M. Further refinement of the structure of WO_3. *Acta Crystallogr. B* **25**, 1420–1421 (1969).

47. Mitchell, J. B., Lo, W. C., Genc, A., LeBeau, J. & Augustyn, V. Transition from Battery to Pseudocapacitor Behavior via Structural Water in Tungsten Oxide. *Chem. Mater.* **29**, 3928–3937 (2017).

48. Oi, J., Kishimoto, A., Kudo, T. & Hiratani, M. Hexagonal tungsten trioxide obtained from peroxo-polytungstate and reversible lithium electro-intercalation into its framework. *J. Solid State Chem.* **96**, 13–19 (1992).

49. Schultz, A. J., Horiuchi, H. & Krause, H. B. Time-of-flight single-crystal neutron and X-ray diffraction study of $K_{0.26}WO_3$. *Acta Crystallogr. C* **42**, 641–644 (1986).

50. Rahman, Md. S., Murshed, M. M., Baabe, D. & Gesing, T. M. Tantalum and vanadium substitution in hexagonal $K_{0.3}WO_3$ bronze: synthesis and characterization. *Z. Kristallogr. Krist.* **231**, 11–21 (2015).

51. Kihlborg, L. & Hussain, A. Alkali metal location and tungsten off-center displacement in hexagonal potassium and cesium tungsten bronzes. *Mater. Res. Bull.* **14**, 667–674 (1979).

52. Kudo, T., Oi, J., Kishimoto, A. & Hiratani, M. Three kinds of framework structures of corner-sharing WO_6 octahedra derived from peroxo-polytungstates as a precursor. *Mater. Res. Bull.* **26**, 779–787 (1991).

53. Chen, R. *et al.* Charge Density Wave and Crystal Structure of K_xWO_3 (x=0.20 and 0.22) Prepared by Hybrid Microwave Method. *J. Low Temp. Phys.* **188**, 1–10 (2017).

54. Lee, J.-S., Liu, H.-C., Peng, G.-D. & Tseng, Y. Facile synthesis and structure characterization of hexagonal tungsten bronzes crystals. *J. Cryst. Growth* **465**, 27–33 (2017).

55. Petříček, V., Dušek, M. & Palatinus, L. Crystallographic Computing System JANA2006: General features. *Z. Kristallogr. Krist.* **229**, 345–352 (2014).

56. Järvinen, M. Application of symmetrized harmonics expansion to correction of the preferred orientation effect. *J. Appl. Crystallogr.* **26**, 525–531 (1993).

57. Hoffmann, R. & Hoppe, R. Zwei neue Ordnungs-Varianten des NaCl-Typs: Li_4MoO_5 und Li_4WO_5. *Z. Anorg. Allg. Chem.* **573**, 157–169 (1989).

58. Fourquet, J. L., Le Bail, A. & Gillet, P. A. $LiNbWO_6$: Crystal structure of its two allotropic forms. *Mater. Res. Bull.* **23**, 1163–1170 (1988).

59. Pralong, V. *et al.* Electrochemical Synthesis of a Lithium-Rich Rock-Salt-Type Oxide $Li_5W_2O_7$ with Reversible Deintercalation Properties. *Inorg. Chem.* **53**, 522–527 (2014).

60. Stephens, P. W. Phenomenological model of anisotropic peak broadening in powder diffraction. *J. Appl. Crystallogr.* **32**, 281–289 (1999).

61. Freedman, M. L. The Tungstic Acids. *J. Am. Chem. Soc.* **81**, 3834–3839 (1959).

62. Green, M., Smith, W. C. & Weiner, J. A. A thin film electrochromic display based on the tungsten bronzes. *Thin Solid Films* **38**, 89–100 (1976).

63. Green, M. Atom motion in tungsten bronze thin films. *Thin Solid Films* **50**, 145–150 (1978).

64. Cheng, K. H. & Whittingham, S. Lithium incorporation in tungsten oxides. *Solid State Ion.* **1**, 151–161 (1980).

65. Cheng, K. H., Jacobson, A. J. & Whittingham, M. S. Hexagonal tungsten trioxide and its intercalation chemistry. *Solid State Ion.* **5**, 355–358 (1981).

66. Kumagai, N., Kumagai, N. & Tanno, K. Electrochemical and structural characteristics of tungstic acids as cathode materials for lithium batteries. *Appl. Phys. A* **49**, 83–89 (1989).

67. Kumagai, N., Matsuura, Y., Kumagai, N. & Tanno, K. Kinetic and Structural Studies of the Electrochemical Insertion of Lithium into Hexagonal-type $_x(A_2O)\bullet WO_3$ (. *J. Electrochem. Soc.* **139**, 3553–3558 (1992).

68. Pereira-Ramos, J.-P. Electrochemical properties of cathodic materials synthesized by low-temperature techniques. *J. Power Sources* **54**, 120–126 (1995).

69. Kumagai, N., Kumagai, N., Umetzu, Y., Tanno, K. & Pereira-Ramos, J. P. Synthesis of hexagonal form of tungsten trioxide and electrochemical lithium insertion into the trioxide. *Solid State Ion.* **86–88**, 1443–1449 (1996).

70. Brousse, T. *et al.* Long-term cycling behavior of asymmetric activated carbon/MnO_2 aqueous electrochemical supercapacitor. *J. Power Sources* **173**, 633–641 (2007).

71. Gogotsi, Y. & Simon, P. True Performance Metrics in Electrochemical Energy Storage. *Science* **334**, 917–918 (2011).

72. Banda, H. *et al.* Ion Sieving Effects in Chemically Tuned Pillared Graphene Materials for Electrochemical Capacitors. *Chem. Mater.* **30**, 3040–3047 (2018).

73. Shannon, R. D. Revised effective ionic radii and systematic studies of interatomic distances in halides and chalcogenides. *Acta Crystallogr. A* . **32**, 751–767 (1976).

74. Chmiola, J. Anomalous Increase in Carbon Capacitance at Pore Sizes Less Than 1 Nanometer. *Science* **313**, 1760–1763 (2006).

75. Largeot, C. *et al.* Relation between the ion size and pore size for an electric double-layer capacitor. *J. Am. Chem. Soc.* **130**, 2730–2731 (2008).

76. Jäckel, N., Simon, P., Gogotsi, Y. & Presser, V. Increase in Capacitance by Subnanometer Pores in Carbon. *ACS Energy Lett.* **1**, 1262–1265 (2016).

77. Trasatti, S. Effect of the nature of the metal on the dielectric properties of polar liquids at the interface with electrodes. A phenomenological approach. *J. Electroanal. Chem.* **123**, 121–139 (1981).

78. Suo, L. *et al.* 'Water-in-salt' electrolyte enables high-voltage aqueous lithium-ion chemistries. *Science* **350**, 938–943 (2015).

79. Chen, M., Feng, G. & Qiao, R. Water-in-salt electrolytes: An interfacial perspective. *Curr Opin Colloid Interface Sci.* **47**, 99–110 (2020).

80. Ohtaki, Hitoshi. & Radnai, Tamas. Structure and dynamics of hydrated ions. *Chem. Rev.* **93**, 1157–1204 (1993).

81. Rempe, S. B. *et al.* The Hydration Number of Li^+ in Liquid Water. *J. Am. Chem. Soc.* **122**, 966–967 (2000).

82. Marcus, Y. Effect of Ions on the Structure of Water: Structure Making and Breaking. *Chem. Rev.* **109**, 1346–1370 (2009).

83. Zhu, T., Chong, M. N. & Chan, E. S. Nanostructured Tungsten Trioxide Thin Films Synthesized for Photoelectrocatalytic Water Oxidation: A review. *ChemSusChem* **7**, 2974–2997 (2014).

84. Shinde, P. A. & Jun, S. C. Review on Recent Progress in the Development of Tungsten Oxide Based Electrodes for Electrochemical Energy Storage. *ChemSusChem* **13**, 11–38 (2020).

85. Mitchell, J. B. *et al.* Confined Interlayer Water Promotes Structural Stability for High-Rate Electrochemical Proton Intercalation in Tungsten Oxide Hydrates. *ACS Energy Lett.* **4**, 2805–2812 (2019).

86. Wang, R. *et al.* Fast Proton Insertion in Layered $H_2W_2O_7$ via Selective Etching of an Aurivillius Phase. *Adv. Energy Mater.* **11**, 2003335 (2020).

Chapter IV: Revealing the charge storage mechanism of the Hexagonal Tungsten Bronzes: Electrochemical, In situ and Operando approaches

IV.1. Introduction

In the previous chapter, the hexagonal tungsten bronzes phases were introduced. The synthesis, the crystallographic structure, and the electrochemical behavior in water-based and organic electrolytes were described and discussed. At the end of the chapter, it was stated that a further and in-depth study had to be followed for a better understanding of the charge storage mechanism of such compounds. In this chapter, such a study will be presented to shed light to understand the phenomena taking place at the electrode/electrolyte interface and inside the material.

A kinetic electrochemical study will be presented in the second section of this chapter. It will intend to separate the charge storage mechanism into diffusion-controlled and surface capacitive processes. Thus, a first idea of how the charge is distributed in the HTBs in aqueous media will be given.

In the third section, the unique technique of EQCM (Electrochemical Quartz Crystal Microbalance) will be described. With this technique, whether or not Li^+ cations are intercalated and how this process takes place in water-based electrolytes will be discussed and finally answered.

In section four, an *in situ* X-ray diffraction study will be presented. Unfortunately, the study will be performed in an organic-based electrolyte. However, this will not prevent us from obtaining exciting information about such phenomena. The difference between the three HTBs will be once again remarked.

Finally, synchrotron *operando* X-ray absorption spectroscopy will be discussed in the last section. This powerful technique will give important information on how tungsten is directly related to the electrochemical behavior of the HTBs, as is expected. Furthermore, this study will help to finalize the understanding of the charge storage mechanism of the hexagonal tungsten bronzes proposed in this thesis.

IV.2. Charge storage mechanism: Surface capacitive *vs.* Diffusion controlled processes

IV.2.1. Introduction: Deconvolution charge storage methods

Electrochemical analytical methods have been applied to distinguish the different contributions in charge storage in oxide materials. Trasatti, a pioneer scientist studying such phenomena, proposed an attractive model to explain the events happening at the surface of RuO_2.[1] This material is remarkably distinctive because of its pseudocapacitive behavior. To elucidate such a mechanism, Trasatti presented the idea of separating the total charge (q_T) in q_i, inner charge with the less accessible surface and q_s, the outer charge and the more accessible surfaces,[2] see Eq. IV-1.

$$q_T = q_i + q_s \qquad \text{Eq. IV-1}$$

Additionally, he stated that the inner charge q_i changes linearly with the square root of the potential scan rate $\upsilon^{-1/2}$ (representing a diffusion-controlled process). On the other hand, the outer surface charge q_s is independent of the scan rate υ (a non-diffusion-controlled process). Therefore, it can be obtained from the intercept of the plot of the Eq. IV-2.

$$(\upsilon) = const * \upsilon^{-\frac{1}{2}} + q_s \qquad \text{Eq. IV-2}$$

Where q(υ) is the total charge, simultaneously, if the scan rate decreases, both inner and outer charges are accessible. Hence, the total q_T can be determined when υ = 0 with the following equation, and q_i can be calculated:

$$\frac{1}{q(\upsilon)} = const * \upsilon^{-\frac{1}{2}} + \frac{1}{q_T} \qquad \text{Eq. IV-3}$$

In a different approach, considering that the current, at a specific value of potential, changes with the scan rate (υ), follows the relationship presented in Eq. IV-4.

$$i\,(V) = a\,\nu^b \qquad \text{Eq. IV-4}$$

Where *a* and *b* are adjustable constants and *b*-value gives information about what type of process dominates the current measured. If the *b*-value is equal to 0.5, this implies a

diffusion-limited process. In contrast, if *b* is equal to 1, it is a capacitive process that dominates the charge storage.[3]

However, the latter relationship is not totally conclusive. Nevertheless, it can give a first view of the processes involved in the studied system. Therefore, based on the reports by Conway *et al.*[4,5], Dunn *et al.*[6] proposed a new method. They investigated further the peak current (i_p) changing with scan rate (υ): for a surface process, i_p increases linearly with υ, and for a diffusion-controlled process i_p changes with $\upsilon^{1/2}$.

This connection helped Dunn to propose the power-law equation, see Eq. IV-5, defining the deconvolution into a capacitive contribution (when the current changes with υ) and a diffusion-limited contribution (when the current changes with $\upsilon^{1/2}$).

$$i(v) = k_1 v + k_2 v^{\frac{1}{2}} \qquad \text{Eq. IV-5}$$

Where *i* is the current (A), and υ is the scan rate ($V.s^{-1}$), k_1 and k_2 are two proportionality constants calculated when the equation is applied and plotted.

In this section, the last two approaches will be used to understand how the charge is stored in the hexagonal tungsten bronzes (HTBs). All the different contributions have to be considered. Moreover, they will shed some light on the dominant charge storage mechanism on these materials.

IV.2.2. Screen-printed electrode setup

In order to minimize the ohmic losses and the shift of redox potentials, a lower mass loading will be preferred compared to the composite electrodes presented in Chapter III. For this reason, screen-printed electrodes acquired from DropSens©[7] will be used as substrates to deposit the respective slurry of HTBs. Further, the electrochemical tests will be carried out.

Figure IV-1 presents the modified setup for these experiments. Firstly, a slurry containing 75 wt.% of active material (HTB) was mixed with 15 wt.% of carbon (Superior Graphite) and 10 wt.% of PVDF (polyvinylidene fluoride, 7 wt.% in NMP). The slurry was mixed until achieving a homogenous appearance. Afterwards, it was taken into a micropipette and dipped onto the surface of the screen-printed electrode until it reached a uniform coating.

After, the electrode was left to dry at 60 °C overnight before performing the experiments achieving an average mass loading of 1.5 mg.cm^{-2}.

Moreover, the use of a small amount of conductive carbon was needed in order to get the desired CV shape. Without the carbon addition, the electrochemical behavior of the CV was very resistive. The electrochemical cell was then assembled using the screen-printed as WE, a Pt grid as CE, and as RE Ag/AgCl. This setup proved to be the most convenient to perform the experiment.

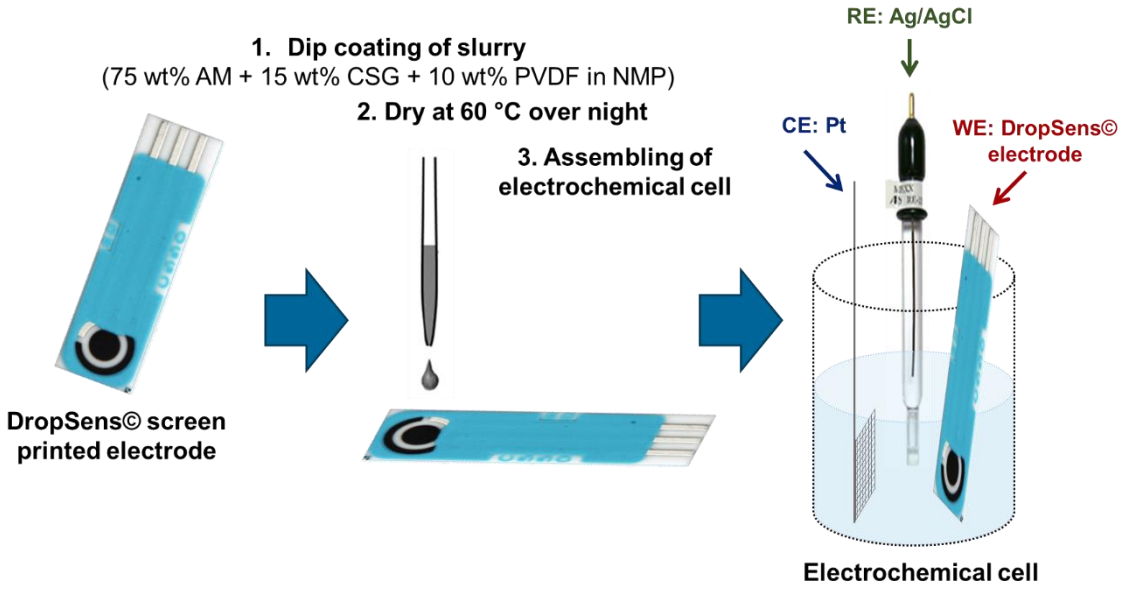

Figure IV-1. *Schematic of setup adapted for these experiments.*

IV.2.3. Electrochemical results and calculations

Figure IV-2 shows the preliminary electrochemical response for the three materials. The CV at 1.0 mV. s^{-1} in 5 M $LiNO_3$ shows the already well-known faradaic signature for both Li and Na HTBs. It is essential to mention the difference in performance observed, being more significant for Na than Li HTB. In contrast, K HTB shows a low performance with a very resistive shape compared to its counterpart materials. Therefore, the calculations were not wholly reliable. The results will be presented only for the Li and Na HTBs.

The first approach used was the determination of the *b*-value. As aforementioned, its value will give a first idea about the contributions involved in the current. For its calculation, the maximum current at the cathodic and anodic peaks was taken as a function of the scan rate,

see Eq. IV-4 above. Figure IV-3a and c display the CVs for the Li and HTB at different scan rates. We can easily observe the evolution of the current when increasing the sweep rate. Moreover, the faradaic responses for both materials are much better defined, up to 15 $mV.s^{-1}$. Figure IV-3b and d show the plots of the log(*i*) *vs.* log(*υ*) where the linear fitting helps to provide *b*-value.

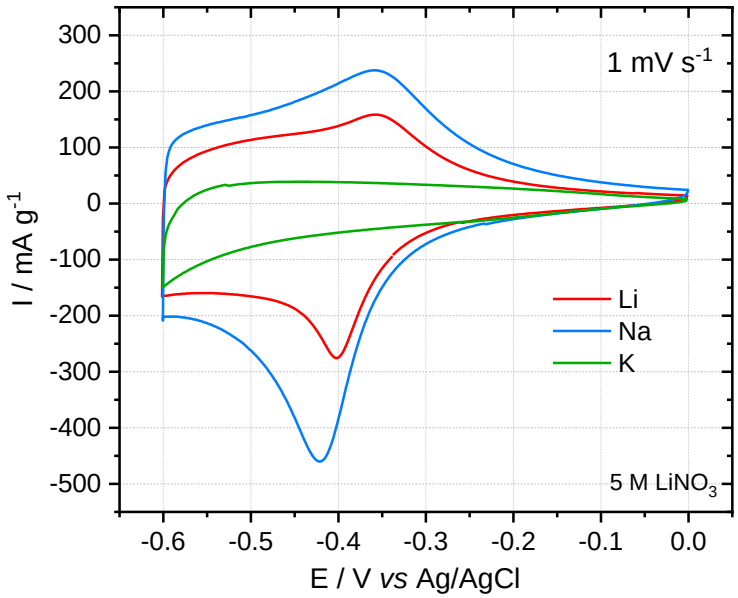

Figure IV-2. *Cyclic voltammogram for the HTBs at 1.0 $mV.s^{-1}$.*

Table IV-1 summarizes the *b*-value from the cathodic and anodic peaks for Li and Na HTBs. In the case of Li HTB, the value is ~0.76 and ~0.79, cathodic and anodic, respectively. Furthermore, for Na HTBs, the values are 0.82 and 0.82, cathodic and anodic, respectively. All the values are found between 0.5 (diffusion-controlled) and 1.0 (non-diffusion control), which is not very conclusive. It could be argued that both contributions dominate the charge storage mechanism for the Li and Na HTBs.

Table IV-1*. b-value.*

	***b*-value**	
HTB	**Cathodic**	**Anodic**
Li	0.79	0.76
Na	0.83	0.82

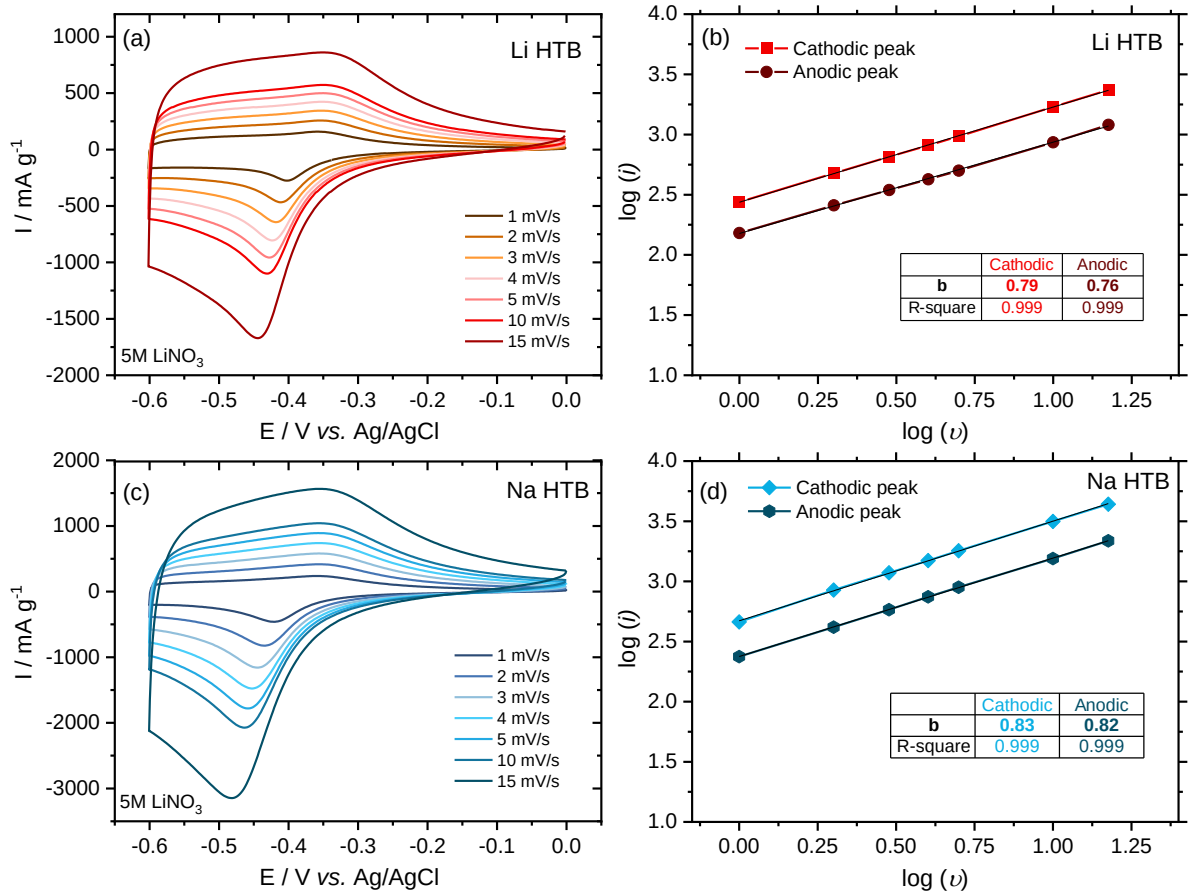

Figure IV-3. *a) and c) Cyclic voltammograms at different sweep rates for Li and HTBs and b) and d) log(i) vs.log(υ) indicating the b-value obtained.*

The second approach followed was the one of Dunn *et al.*[6], as stated in Eq. IV-5. With the determination of both constants, k_1, and k_2, the estimation of surface capacitive and diffusion-controlled contributions can be determined for each value of scan rate. Figure IV-4 shows the linear fitting for the respective HTBs analysis.

Once the calculation and the respective k_1 and k_2 constants were obtained, the contributions for the total charge storage are displayed in Figure IV-5. First, the increase of the surface capacitive contribution upon sweep rate is immediately noted. In contrast, the diffusion-controlled contribution predominates at lesser sweep rates. This effect is expected considering that there is not enough time for the Li^+ to go into the structure at a higher rate. Secondly, both cathodic and anodic elements of the CV follow the same trend as described before.

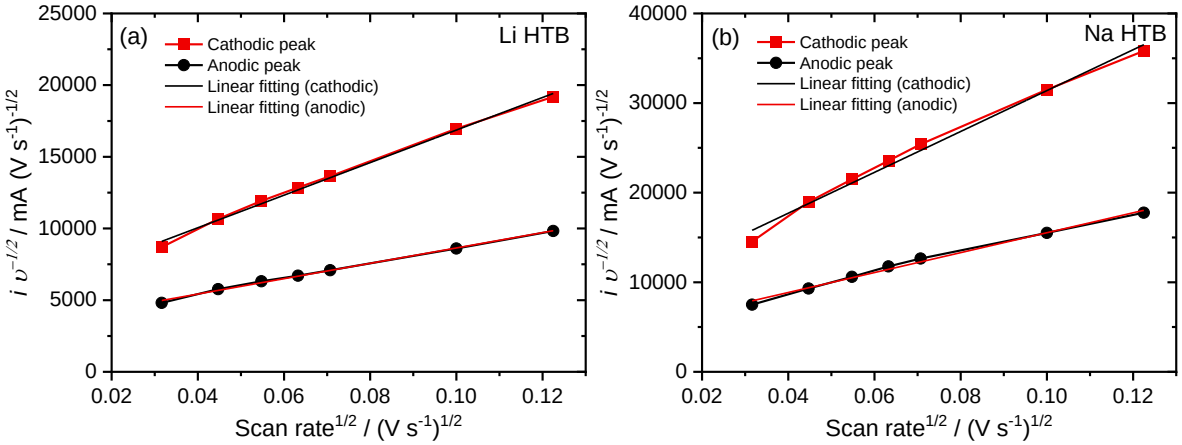

Figure IV-4. *Linear fitting using the* ***Erreur ! Source du renvoi introuvable.*** *to analyze cathodic and anodic peaks of the Li and Na HTBs CVs, sweep rates from 1-15 mV.s^{-1}.*

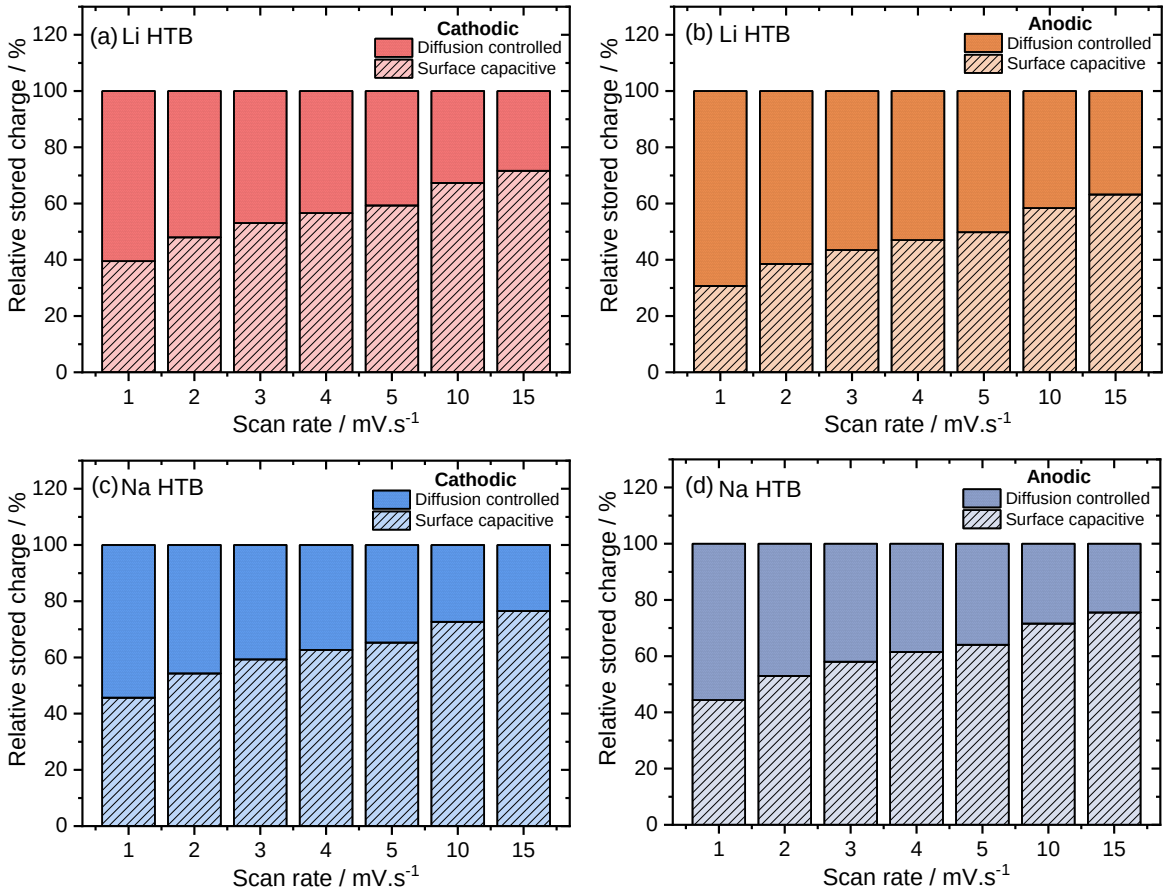

Figure IV-5. *Charge storage contribution for both Li and Na HTBs, showing both cathodic and anodic parts.*

Furthermore, it must be mentioned that the surface capacitive contribution includes both pure electric double-layer (EDL) and pseudocapacitive components. This statement should not

be taken lightly since the shape of the CV does show a quasi-rectangular shape, being more visible at lower potentials and a lower sweep rate, as seen in Figure IV-2.

Finally, this electrochemical analysis gives a first approach on how the charge storage mechanism for the HTBs occurs. In the following sections, special techniques will be presented to shed some light on the topic.

IV.3. Electrochemical Quartz Crystal Micro Balance (EQCM)

In this section, the in situ EQCM technique will be employed to monitor the electrode/electrolyte interface. Moreover, this will contribute to a better understanding of the charge storage mechanism and how the Li^+ intercalation process occurs. All the tests and calculations were performed by Dr. Hui Shao at the CIRIMAT (Centre Interuniversitaire de Recherche et d'Ingénierie des Matériaux) in Toulouse, France; in collaboration with Prof. Patrice Simon and Dr. Pierre-Louis Taberna.

IV.3.1. EQCM in energy storage systems

The Electrochemical Quartz Crystal Microbalance (EQCM) is an experimental technique that enables the *operando* monitoring of the electrochemical reaction occurring at the electrode/electrolyte interface caused by a gravimetric alteration. Such variations at the interface will cause a shift in the quartz resonance frequency (Δf) used as working electrode (WE). Sauerbrey's equation Eq. IV-6 states that this change will be proportional to the mass change (Δm).[8,9] C_f represents the sensitivity factor of the crystal and is calculated by the electro-deposition of Cu on the quartz and using 0.1 M $CuSO_4$ in 1 M of H_2SO_4. Faraday's law is then used to obtain the amount of Cu deposited.

$$\Delta m = -C_f \, \Delta f \qquad \text{Eq. IV-6}$$

Thanks to this particular feature, EQCM has resulted in a unique technique to study the behavior of ions adsorption and solvent molecules in porous carbonaceous materials used in EDL capacitors.[10–14] EQCM explained the enhancement of capacitance in sub-nanometer

porous carbons thanks to the partial ion desolvation.[15] This effect was later confirmed by the partial loss of the solvation shell of solvated Li^+ in aprotic propylene carbonate at the moment of entering the pores.[11] Furthermore, the number of solvent molecules accompanying the ion at the moment of the electro-adsorption was determined.[12]

Wan-Yu Tsai *et al.*[13,16] studied the ion dynamics of the ionic liquid EMI-TFSI electrolyte in carbide-derived carbon (CDC), both neat and solvated, highlighting the different behaviors observed for CDC with 1 nm pore between EMI^+ and $TFSI^-$ adsorption. Figure IV-6 (showing the result for neat EMI-TFSI) displays how the electro-adsorption of the ions occurs depending on the electrode's polarization. During negative charging, only EMI^+ cation adsorption is observed. In contrast, a region of ion exchange is found at positive charging when polarization is low. However, when a higher positive polarization is applied, $TFSI^-$ anions become the significant species, thus balancing the charge.[13,16]

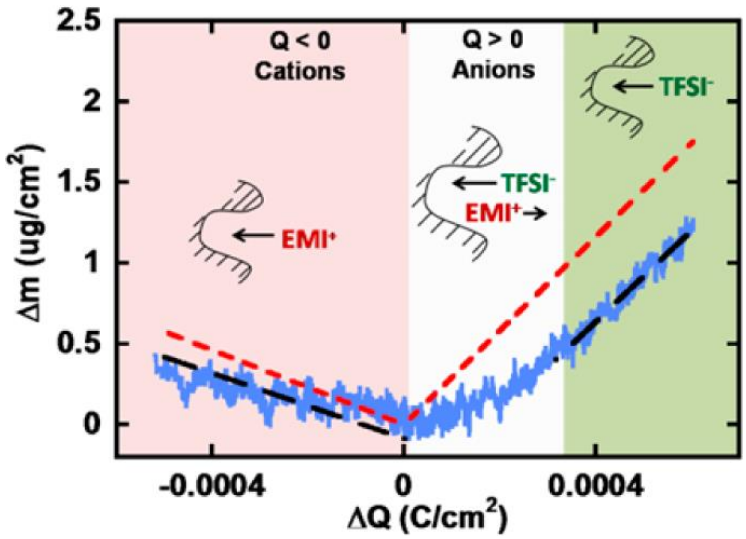

***Figure IV-6**. Electrode mass change vs. charge during the polarization of CDC-1 nm in neat EMI-TFSI: Blue solid lines are measured mass change (EQCM), red dashed lines are the theoretical mass change of neat ions calculated from Faraday's law. The black dashed line shows the linear fitting of the measured mass change.*[13]

Afterwards, a similar study was performed in an aqueous electrolyte by Yin-Chyng Wu *et al.*[17] in TiC-CDC with 0.67 nm pore size in 0.1 M K_2SO_4. They studied the dynamics of K^+ cations and SO_4^{2-} anions during electrode polarization. They estimated the number of water molecules accompanying each ion during electro-adsorption.

Figure IV-7 shows their findings. The most interesting considerations to keep in mind are: 1) they divided the CV into four different zones depending on the cation/anion adsorption/desorption upon polarization, taking as a reference the pzc (potential of zero charge, which refers to a potential at which surface net charge of the electrode is null) and 2) by using Faraday's equation, average molecular weights of cations or anions were estimated taking into consideration that the difference between versus bare ions was exclusively due to water molecules surrounding them. The hydration numbers were 5.3 and 0.9 for potassium ions (K^+) and sulfate ions (SO_4^{2-}) in carbon micropores. Thus, suggesting a partial ion desolvation taking place, in less magnitude for potassium than for sulfate anion.[17]

Other materials investigated by EQCM were the MXenes phases of $Ti_3C_2T_x$ in acidic electrolytes. Hui Shao *et al.* hypothesized that the intercalation of H_3O^+ and/or H^+ or deintercalation of SO_4^{2-} were responsible for the charging mechanism.

The same team carried out the following experiment: A CV with MXene-coated gold quartz crystal as the working electrode in 3 M H_2SO_4 electrolyte at 10 $mV.s^{-1}$ scan rate. The results are shown in Figure IV-8. They found that the change in mass at negative polarization corresponds to a molecular weight of 14 $g.mol^{-1}$. Thus, attributing the intercalation to the hydronium cation H_3O^+, with a molecular weight of 19 $g.mol^{-1}$. The transportation of the cations explains the difference through the confined water in the material.[18,19]

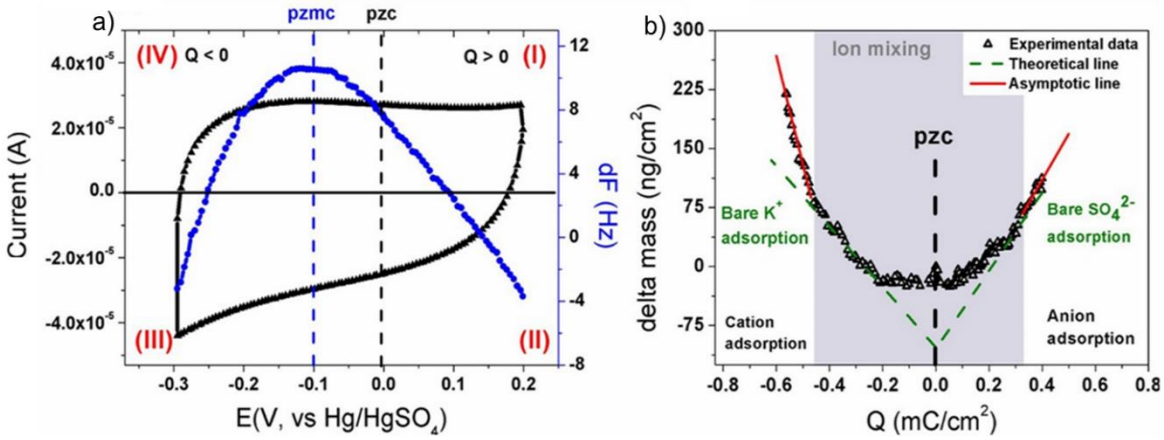

Figure IV-7. *CV and EQCM frequency response of CDC-0.7 nm carbon electrode in 0.1M K_2SO_4 aqueous electrolyte at 10 $mV{\cdot}s^{-1}$. (b) Electrode mass change vs. charge during the polarization of CDC-0.7 nm in 0.1M K_2SO_4 aqueous electrolyte. Black solid marks are measured mass change (EQCM), green dashed lines are the theoretical mass change of neat ions. The solid red line shows the linear fitting of measured mass change.*[17]

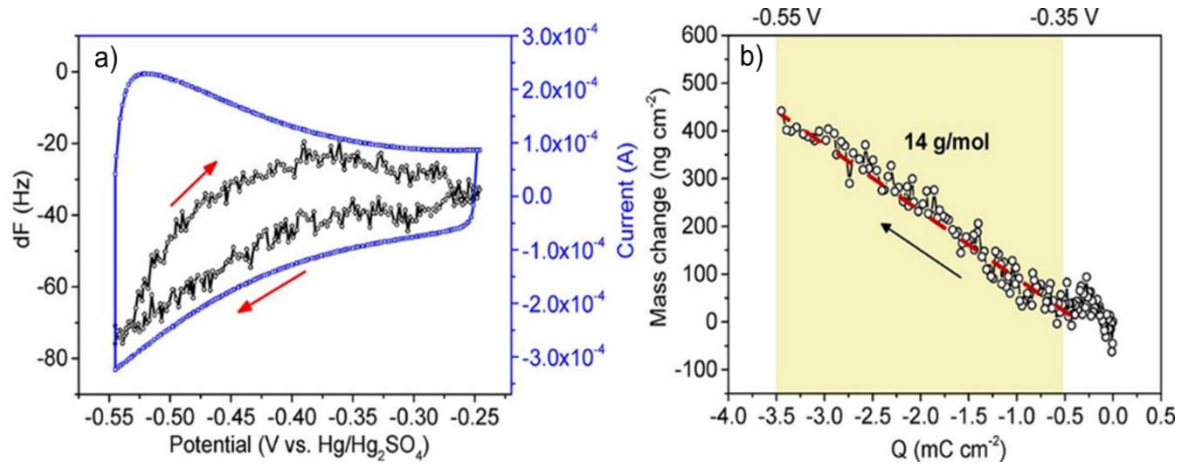

Figure IV-8. *a) CV profile and EQCM frequency response and b) electrode mass change versus charge during the polarization of P-MXene on a gold substrate in 3 M H_2SO_4 recorded at 10 mV s^{-1}, with reference electrode of Hg/Hg_2SO_4.*[18]

The previous reports performed in aqueous electrolytes will help understand how the HTBs behave towards the possible Li^+ intercalation. Above all, it will demonstrate whether Li^+ ions go inside by themselves or surrounded by water molecules.

IV.3.2. EQCM experimental setup

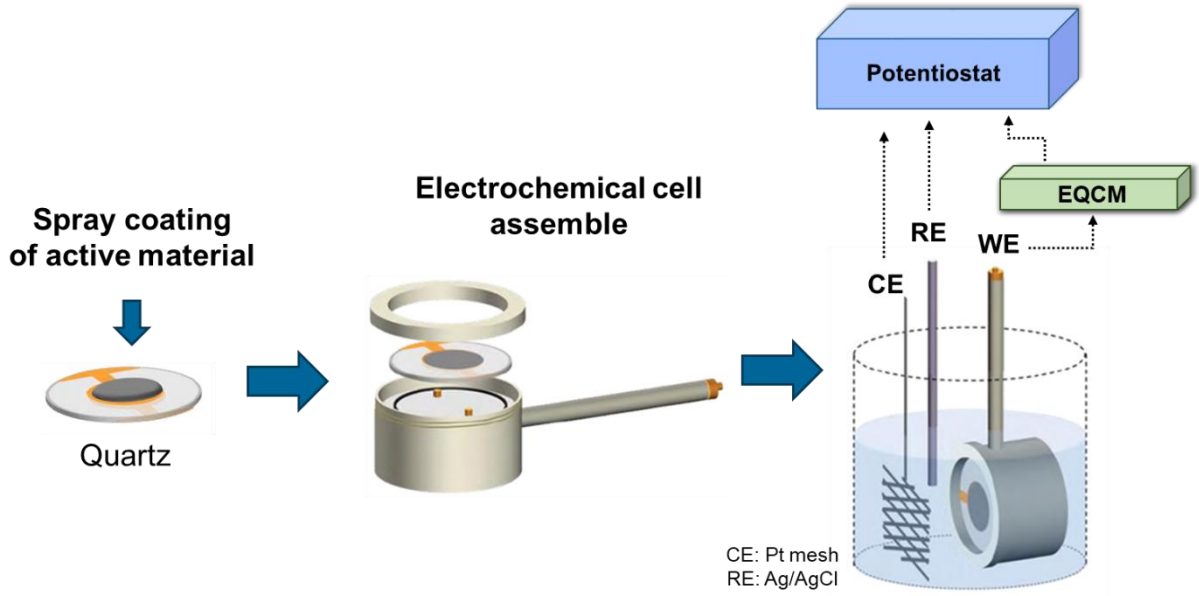

Figure IV-9. *Schematic of EQCM setup, adapted from reference 16.*

The setup of the EQCM is described next: BioLogic 1-in.-diameter Ti-coated quartz crystals (oscillating frequency, f0, 5 MHz) were coated by spray coating with a slurry containing 70 wt.% of active material HTBs powder, 15 wt.% carbon black, and 15 wt.% of polyvinylidene fluoride (PVDF) in N-Methyl-2-pyrrolidone (NMP), as the binder. The coated quartz crystal was placed on a PTFE holder (working electrode) facing the reference electrode (Ag/AgCl). A Pt wire was employed as a counter electrode, thus assembling the traditional three-electrode setup (see Figure IV-9). The tests were performed in 5 M and saturated $LiNO_3$ as electrolytes. All the EQCM electrochemical measurements were carried out by a Maxtek RQCM system combined with Autolab PGSTAT101 for simultaneous EQCM and electrochemical measurements acquisitions.

IV.3.3. EQCM analysis for Li and Na HTBs

Figure IV-10a shows the homogenous coated quartz used to perform the experiments. Moreover, Figure IV-10b shows a first cyclic voltammetry experiment at 10 $mV.s^{-1}$ in 5M $LiNO_3$, comparing the bare quartz *vs.* the coated quartz. It shows the standard electrochemical signature for the Li HTB, explicitly displaying a faradaic response, which will be essential for understanding the phenomena occurring at the surface of the electrode studied.

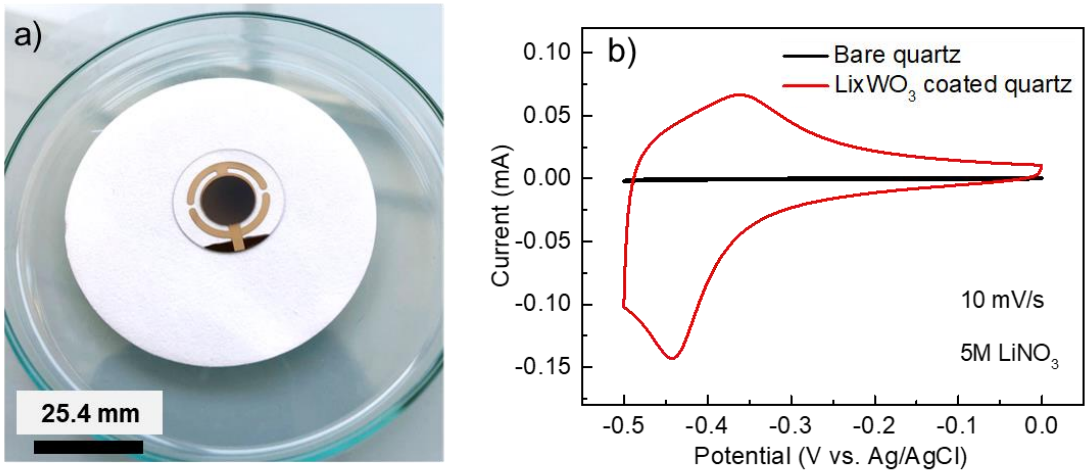

Figure IV-10. *a) Homogeneously coated quartz and b) CV of bare quartz vs.CV of coated quartz with Li HTB in 5M $LiNO_3$ at 10 $mV.s^{-1}$.*

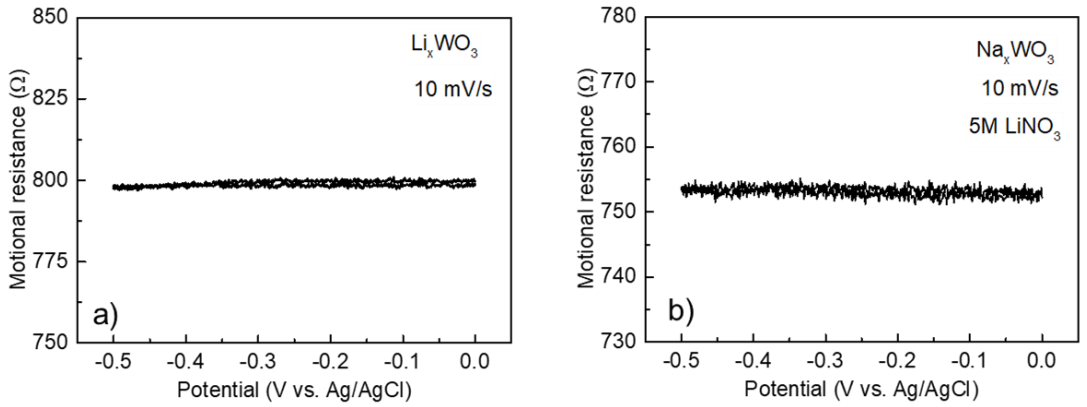

Figure IV-11. *Change of the motional resistance of Li and Na HTBs on a Ti substrate in 5 M $LiNO_3$ at 10 $mV.s^{-1}$.*

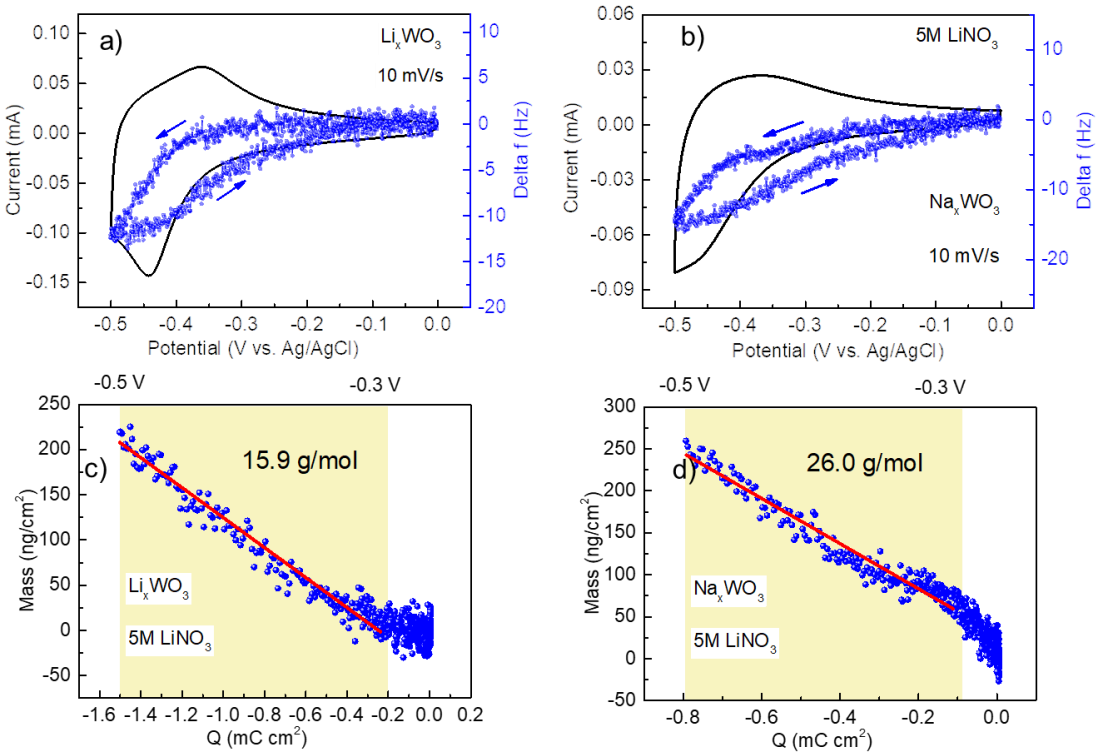

Figure IV-12. *EQCM measurements: (a) and (b) CV profile and EQCM frequency response for Li and Na HTB, respectively; (c) and (d) electrode mass change versus charge during the polarization in 5 M $LiNO_3$ recorded at 10 $mV.s^{-1}$ vs. Ag/AgCl as reference electrode.*

The results obtained out of the EQCM measurements are shown next. A motional resistance test was performed before the EQCM experiment indicating negligible dissipation changes (see Figure IV-11). Thus, Sauerbrey's equation (Eq. IV-6) can fit the gravimetric

model. Figure IV-12a and b display the CV profile and frequency response of Li and Na HTB at 10 $mV.s^{-1}$, respectively, where the arrows indicate the scan direction.

From -0.3 to -0.5 V (*vs.* Ag/AgCl), an increase of mass is observed, which most likely corresponds to the intercalation of ions into the hexagonal windows and cavities of the HTBs and ions adsorption on the electrode surface. In Figure IV-12c and d, the approximately linear increase of mass versus accumulated charged is noted; see the orange area. Following Faraday's law, the average molecular weight per charge (z=1) is calculated to be 15.9 $g.mol^{-1}$ and 26 $g.mol^{-1}$, respectively, for Li and Na HTB. Such values correspond to one mole of Li accompanied by 0.5 moles of H_2O (Li^+•0.5 H_2O) for the Li compound. In the case of Na HTB, one mole of Li^+ is accompanied by 1.1 moles of H_2O (Li^+•1.1 H_2O). Therefore, it is conclusive that Li^+ are not being intercalated by themselves but with H_2O surrounding them.

Furthermore, as aforementioned in Chapter III, section III.4.5., there is a relationship between electrolyte concentration and the number of moles of H_2O per Li^+. For that reason, an extra EQCM measurement was performed in saturated $LiNO_3$. The motional resistance test before the EQCM experiment indicated negligible dissipation changes, as observed in the previous experiment (see Figure IV-13).

Figure IV-14a and b show the CV profile and frequency response of Li and Na HTB at 10 $mV.s^{-1}$, respectively, in the saturated electrolyte. Figure IV-16c and d show the approximately linear increase of mass versus accumulated charged; see the orange area. A similar calculation was performed to determine the average molecular weight per charge (z=1). The values were: about 0.7 moles of H_2O (Li^+•0.7 H_2O) for the Li compound and about 1.3 moles of H_2O (Li^+•1.3 H_2O) for the Na HTB.

Whenever the electrolyte concentration increases, the water molecules available to form the entire hydration shell of Li decreases. Thus, possibly less water in bulk may influence the desolvation process at the electrode interface. Table IV-2 summarizes the results shown for both 5 M and saturated $LiNO_3$.

Table IV-2. *Moles of water surrounding Li^+ in the intercalation mechanism.*

HTB	5 M $LiNO_3$	Saturated $LiNO_3$
Li	0.5	0.7
Na	1.1	1.3

As mentioned in chapter III, section III.4.5., a shift towards higher potential values (*vs.* Ag/AgCl) was described for the higher $LiNO_3$ concentration. This implies a decrease in the energy required for the Li^+ to go into the structure. As expected, such a shift is observed for the

CVs shown in Figure IV-12 and Figure IV-14. However, the ratio of water accompanying Li^+ does not seem to change much whenever the concentration increases. This slight change could be due to the different slopes taken for the molecular weight calculation, meaning that a limit for water surrounding and accompanying Li^+ cations at the moment of intercalation is reached before the saturation of $LiNO_3$.

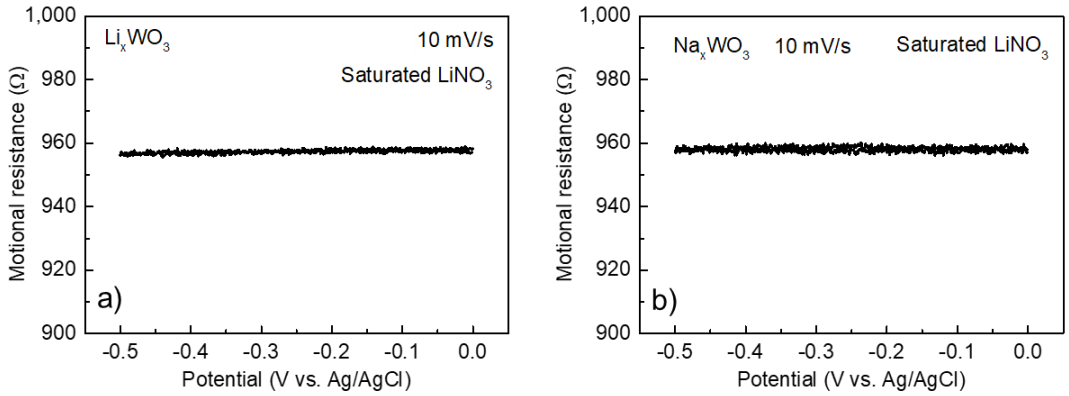

Figure IV-13. *Change of the motional resistance of Li and Na HTBs on a Ti substrate in saturated $LiNO_3$ at 10 $mV.s^{-1}$.*

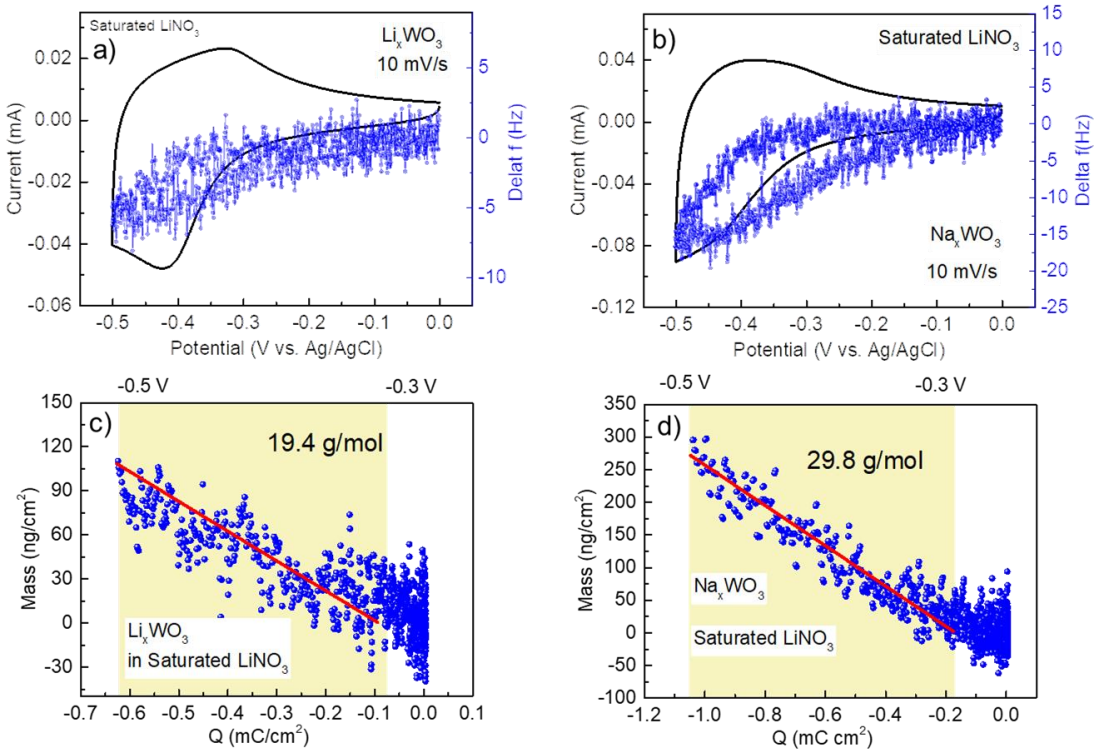

Figure IV-14. *EQCM measurements: (a) and (b) CV profile and EQCM frequency response for Li and Na HTB, respectively; (c) and (d) electrode mass change versus charge during the polarization in saturated $LiNO_3$ recorded at 10 $mV.s^{-1}$ vs. Ag/AgCl as the reference electrode.*

As a preliminary conclusion, we confirm that the Li^+ intercalation occurs at the electrode/electrolyte interphase for the Li and Na HTBs. Moreover, Li^+ must be accompanied by water to facilitate the intercalation and deintercalation into the lattice. The possible structural changes the Li^+ intercalation caused into the crystal structure will be discussed next.

IV.4. *In situ* X-ray diffraction

IV.4.1. In situ X-ray diffraction in energy storage systems

In situ X-ray diffraction (XRD) has been used for more than 20 years as a powerful tool to study electrode materials in energy storage systems.[20] There are different types of mechanisms coinciding. Either a single-phase reaction or multi-phase process can take place. Therefore, to follow the evolution and structural changes due to the polarization of the electrode, *in situ* XRD offers a unique alternative to track both the potential where the phase transition is occurring and the identification of these phases. Moreover, the unit-cell contraction and expansion can be determined. Thanks to this technique, structural changes in materials like $LiCoO_2$,[21] $LiFePO_4$,[22] $Li_3V_2(PO_4)_3$,[23] $LiVPO_4F$[24], $Na_3(VO)_2(PO_4)_2$[25] have been reported as an example.

The compounds above correspond to battery-like materials where the charge/discharge times are much longer than 1 hour, and multi-phase reactions are predominant. Moreover, nowadays, *in situ* and *operando* XRD investigations can be performed in materials presenting fast intercalation or a pseudocapacitive mechanism as the ones reported by Augustyn, Gogotsi, and Simon.[26–28]

In situ XRD has demonstrated a fluctuating expansion/shrinkage phenomenon during charge and discharge, in the case of the well-known 2D titanium carbide ($Ti_3C_2T_x$ MXene phase), as reported by Mu *et al.*[29] and displayed in Figure IV-15. This study exhibits the intercalation charge storage mechanism of $Ti_3C_2T_x$ in an acidic electrolyte.

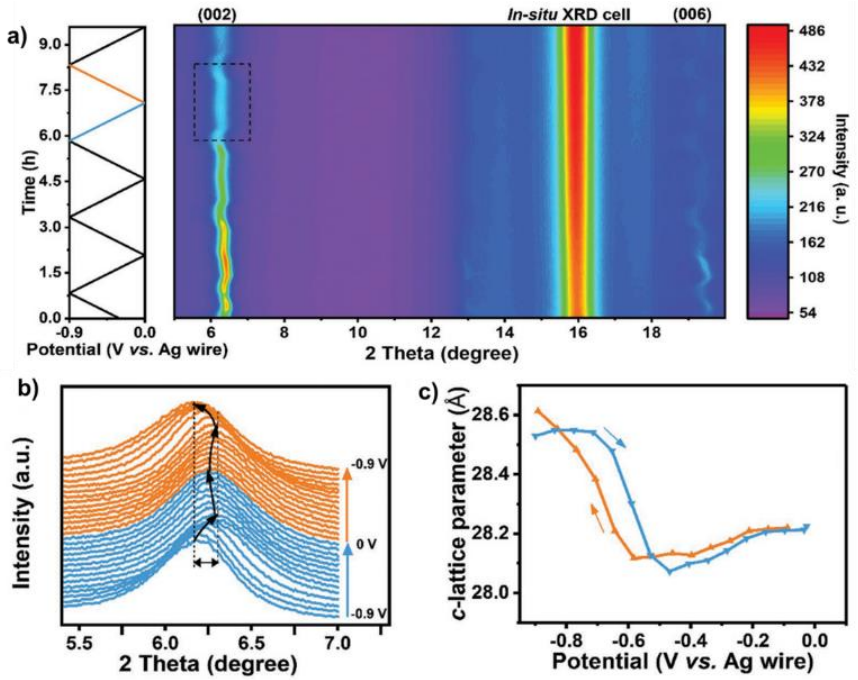

Figure IV-15. *a, b) In situ XRD patterns during the electrochemical cycle. c) Change of the c-lattice parameter with potential.*

Augustyn's group[30] investigated, by *operando* synchrotron XRD, the layered hydrated structure of $WO_3 \bullet H_2O$ carrying out fast proton intercalation, causing a phase transformation from the layered phase to a more symmetric orthorhombic structure (see Figure IV-16). Such structural changes were presented at a low scan rate (1.0 $mV.s^{-1}$) and impressively at the higher sweep of 100 $mV.s^{-1}$.

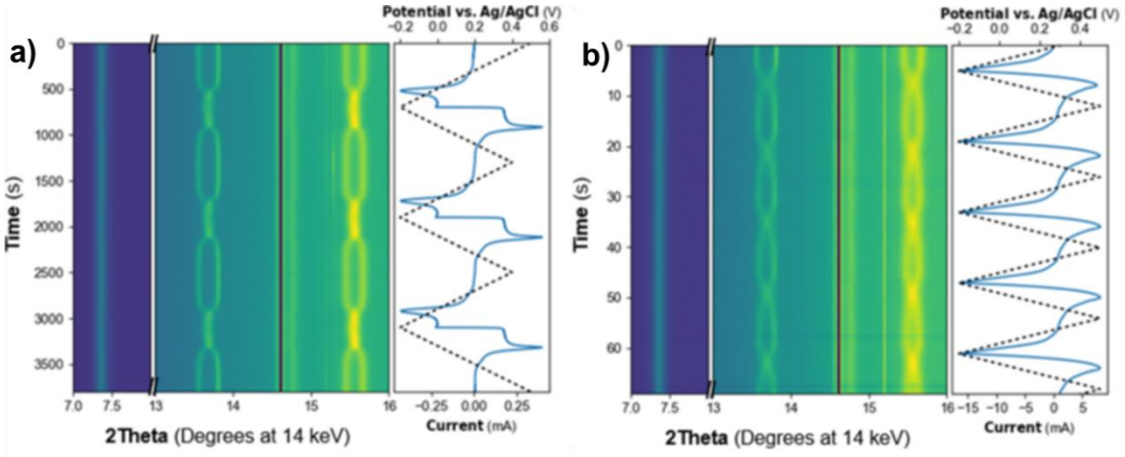

Figure IV-16. *Operando XRD of electrochemically-induced phase transformations in $WO_3 \bullet 2H_2O$. Synchrotron XRD color maps of $WO_3 \bullet 2H_2O$ as a function of electrochemical cycling at a) 1 $mV.s^{-1}$ and b) 100 $mV.s^{-1}$.*[30]

IV.4.2. In situ cell and setup

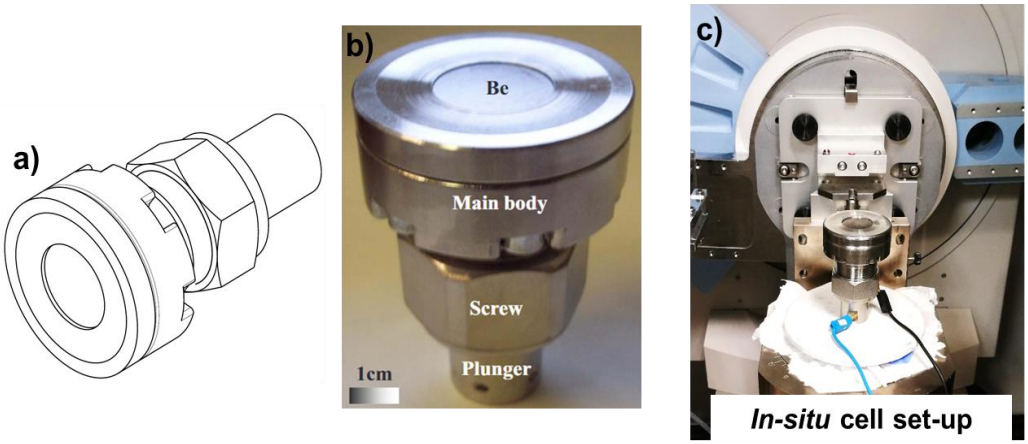

Figure IV-17. *In situ X-ray diffraction cell. a) diagram of the cell, b) cell indicating the parts, and c) the cell setup inside the diffractometer.*

Figure IV-17a, b, and c represent the modified Swagelok cell as an *in situ* cell, the cell itself, and the setup inside the diffractometer, respectively. The upper part of the cell is composed of a stiff, outer ring of diameter 5 cm and a hole of 2 cm behind which a metallic beryllium window (thickness of 200 μm and diameter 4 cm) is placed. A self-standing electrode, usually prepared for electrochemical analyses (see chapter II, section II.2.3.1.), was placed behind the Be window, which acts as a metallic current collector. This part of the cell was attached to the main body, and sealing was achieved with a rubber o-ring in contact with the Be window by tightening with six stainless steel screws. A cylindrical plunger with a disk of Li metal is used as the "negative" part of the cell. A spring was used to properly adjust the mechanical pressure within the cell. The incident X-ray beam penetrates through the Be window of the upper part and hits the positive electrode.

Unfortunately, the cell design mentioned above works only for experiments in organic electrolytes. In order to have a better comparison for the results observed in aqueous systems, the main view of this thesis, a special design would have been necessary. However, we did not have access to that particular setup.

The *in situ* cell was then assembled inside an argon-filled glove-box (MBraun) with less than one ppm of O_2 and H_2O, using a glassy fiber separator (Whatman GF/D, thickness 670 μm) soaked with 1 mol L^{-1} $LiPF_6$ in EC:DMC (vol. 1:1, 99.9% battery grade, Solvionic, H_2O < 20 ppm, 10.3 mS cm^{-1} at 20 °C).

IV.4.3. In situ X-ray diffraction study

The experiments were performed in HTBs composite electrodes with a diameter of 14 mm and a mass loading of about 5-10 $mg.cm^{-2}$. A GCPL technique was used, with Table IV-3 summarizing the corresponding current densities applied for each HTB. Such low values of current densities were desired to approximate the charge/discharge times to those presented in the cyclic voltammetry experiments from Chapter III - Section 5. Every 15 min of applied current was followed by 30 min of XRD acquisition between 10 and 40° in 2θ and a scan step of 0.0167° using a PANalytical X'Pert Pro diffractometer (by Malvern Panalytical) with an X'Celerator detector and Cu-Kα1-Kα2 (λ = 1.54060, 1.54439 Å) radiation. The acceleration voltage and current were 40 kV and 40 mA, respectively. Next, the results of the *in situ* XRD will be discussed.

Table IV-3. *Current density applied for in situ experiments.*

HTBs	**Current density in $mA.g^{-1}$**
Li	12
Na	12
K	6

IV.4.3.1. Li HTB

Figure IV-18 presents the charge/discharge *vs*. the XRD patterns taken at each value of resting potentials. The experiment begins with the Li^+ intercalation into the lattice of the Li HTB when the potential goes from ~3.0 V to 2.5 V *vs.* Li/Li^+. Straight away, a shift of the primary reflections at ~14°, 23.3°, 24.4°, and 28.3° can be observed. These correspond to *100, 001, 110,* and *200 hkl*. Figure IV-19 shows a color map picture where the shift can be more visible.

The capacity obtained after the 1st discharge is about 70 $C.g^{-1}$ and is kept constant along the four cycles studied. This agrees with the one obtained in the organic electrolyte experiment described in chapter III, section 5. Furthermore, Figure IV-20a shows a zoom-in of the *100,* and Figure IV-20b shows a zoom of *001, 110,* and *200 hkl*. This indicates a shrinking along the *c* plane and expansion along the *ab* plane. This shrinking and expansion of the lattice corresponds to the Li^+ cations being intercalated in and deintercalated out of the lattice of the Li HTB. Additionally, as there are no peaks disappearing or new peaks appearing, we can confirm no

second phase evolving upon cycling, as observed in the case of the hydrated phase of $WO_3 \bullet H_2O$.[30]

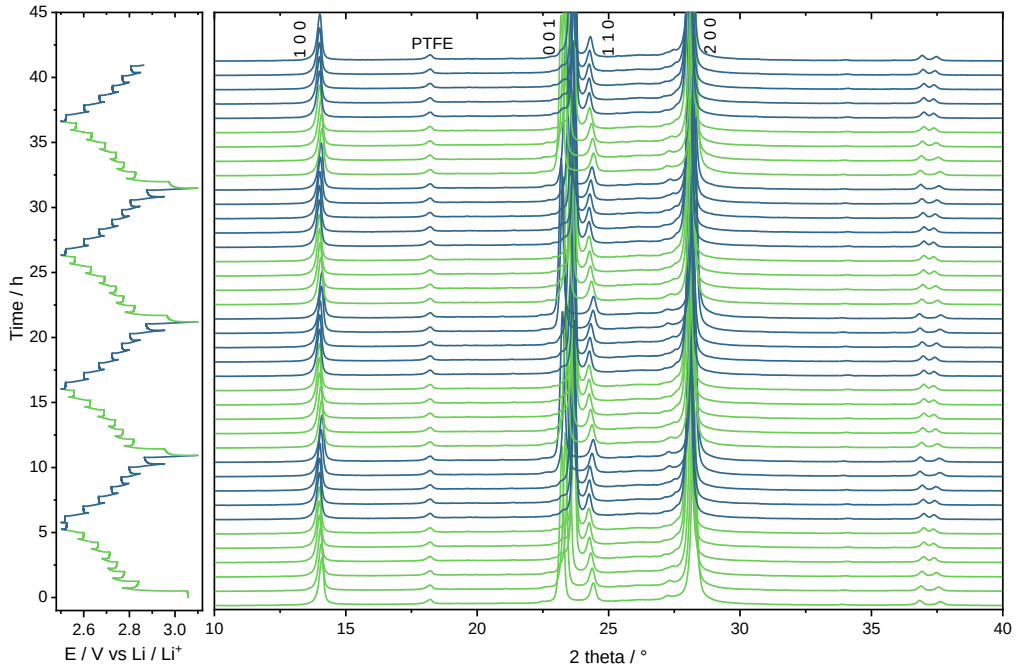

***Figure IV-18**. Charge and discharge curves for Li HTB in $LiPF_6$ in EC-DMC and XRD pattern from 10-40° in 2θ.*

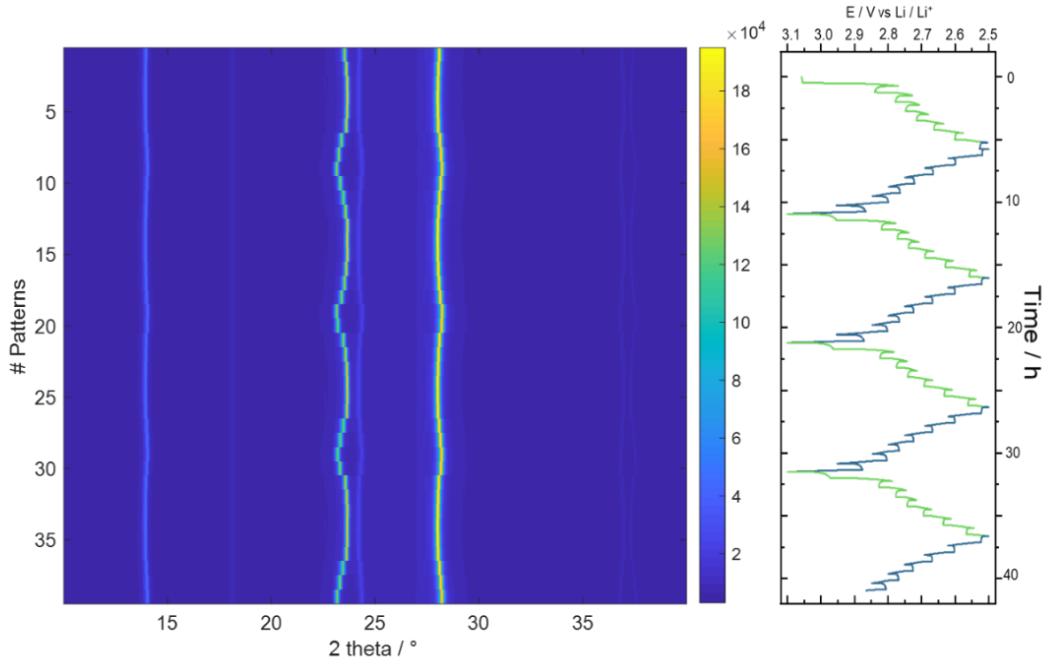

***Figure IV-19.** Color map showing the shift of the peaks upon cycling and charge and discharge curves for Li HTB.*

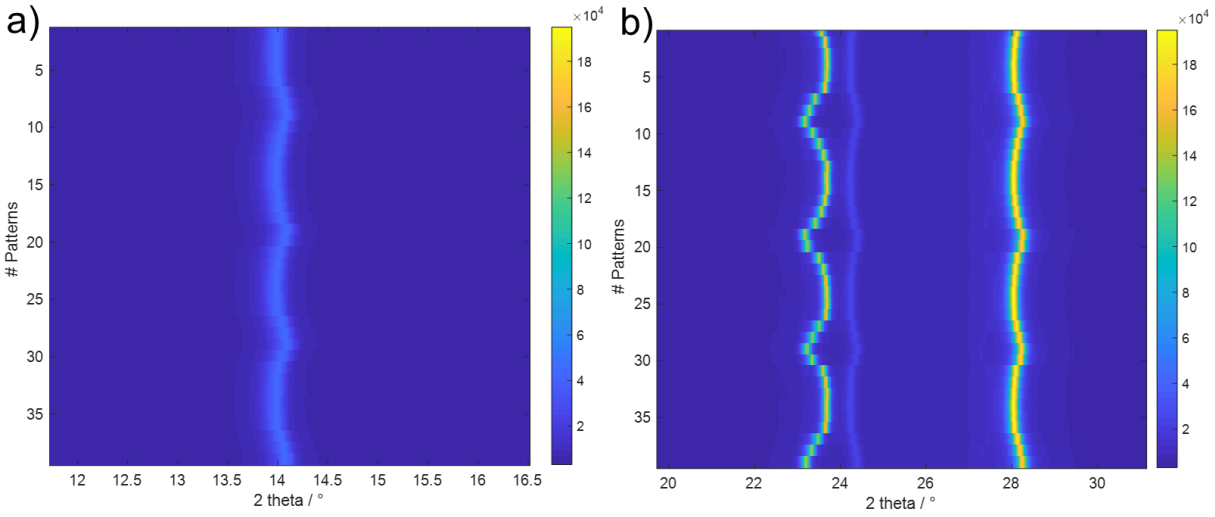

Figure IV-20. *Zoom-in of the a) 100, b) 001, 110, and 200, main reflections shown in the in situ XRD for Li HTB.*

The hexagonal structure (Chapter III – Figure III-7) shows plenty of possible sites where Li^+ cations could be located, for example, at both the hexagonal and trigonal tunnels formed. This means that the Li^+ intercalation most likely comes from the *c* direction, from the pointy side in the nanorod-like Li HTB particles (Chapter III – Figure III-23). In addition, Figure IV-21 shows the evolution of the *c* and *a* parameters, where the expansion and the shrinking are more evident. It is notable how the structure comes back to its initial state, meaning that no significant volume expansion occurs caused by the intercalation and deintercalation of Li^+.

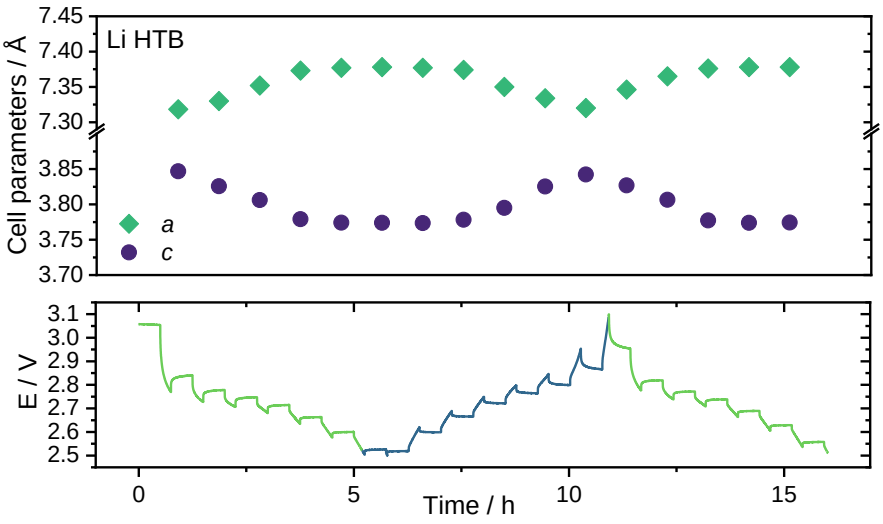

Figure IV-21. *Evolution of the refined cell parameters upon cycling of Li HTB in P6/mmm space group.*

IV.4.3.2. Na HTB

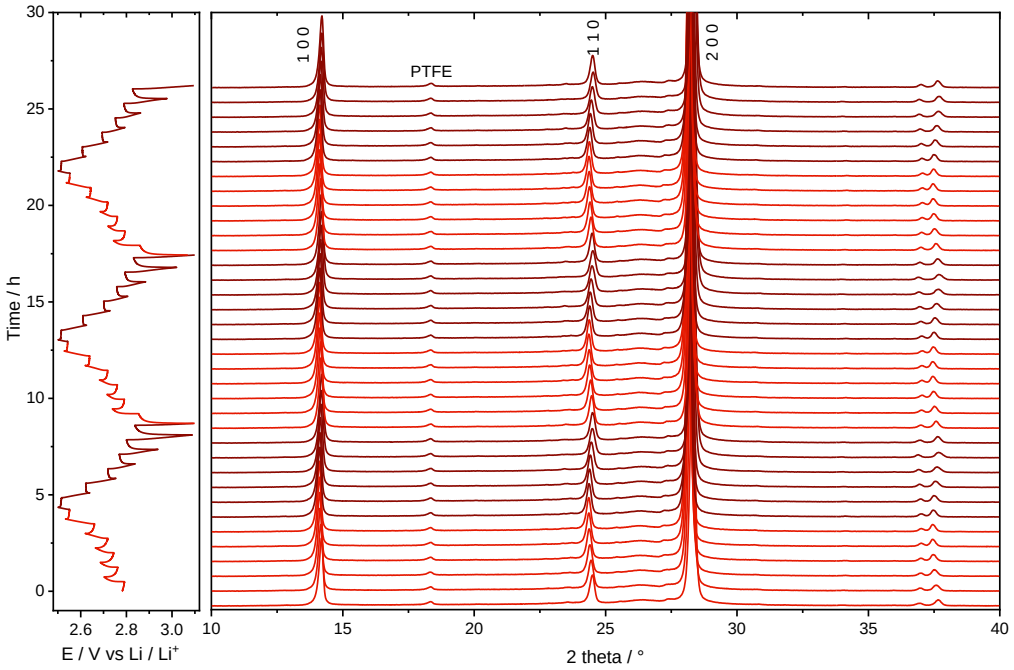

Figure IV-22. *Discharge and charge curves for Na HTB in $LiPF_6$ in EC-DMC and XRD pattern from 10-40° in 2θ.*

In the case of Na HTB, the behavior is very similar to the Li compound, as already aforementioned in Chapter III. Figure IV-22 shows the XRD patterns as a function of the charge/discharge curves. The shifting of the primary reflections seems to be less distinguishable than the Li HTB. Nevertheless, it looks similar. The main reflections observed correspond to *100*, *110*, and *200 hkl*, noticing the absence of the *001* planes.

As for Li HTB, the Li^+ intercalation does come from the *c* direction, more precisely from the end edges of the nanorods (Chapter III – Figure III-23). Figure IV-23 and Figure IV-24 show the color map of the observed peaks and the zoom-in of the *100*, *110*, and *200* hkl, respectively. The shrinking and the expansion of the lattice corresponding to the *a* and *c* are detailed in Figure IV-25 with the evolution of the cell parameters *vs.* pattern number obtained upon cycling.

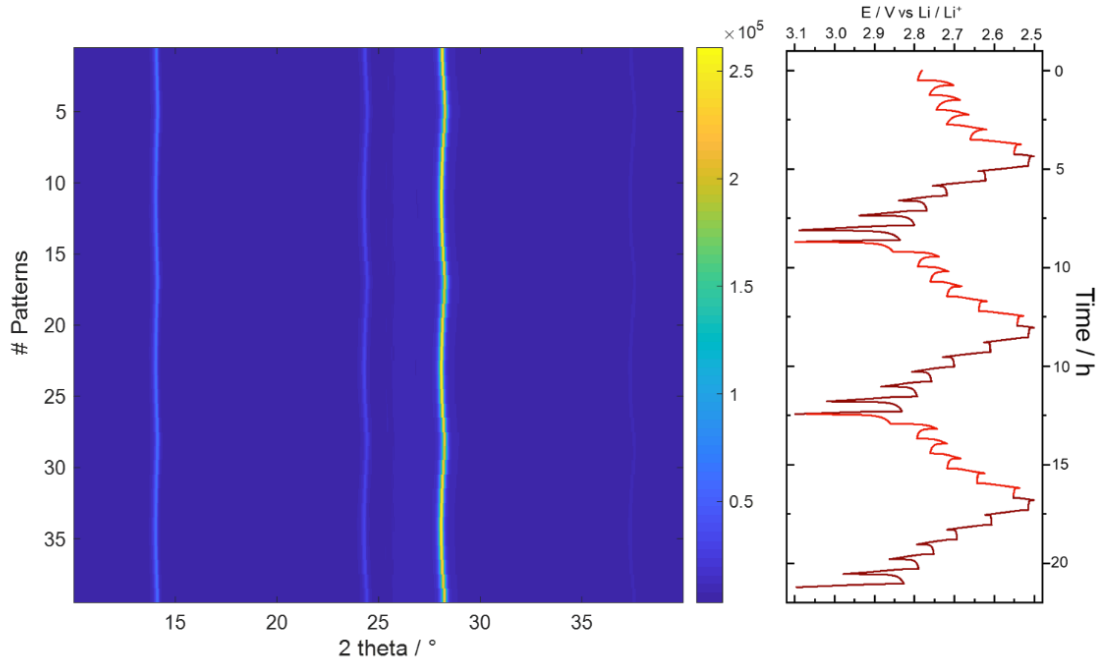

Figure IV-23. *Color map showing the shift of the peaks upon cycling and charge and discharge curves for Na HTB.*

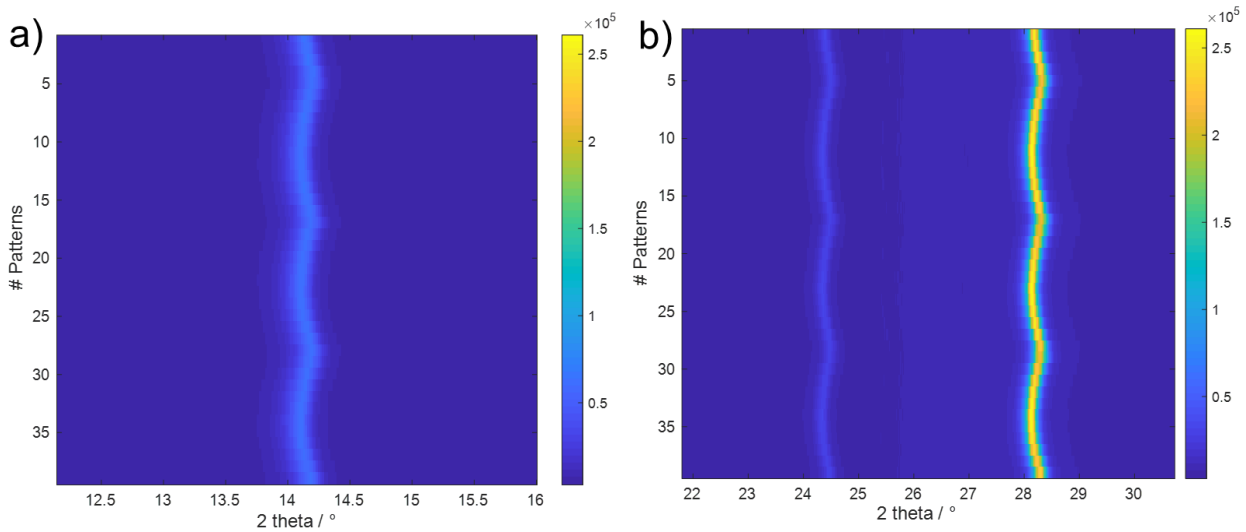

Figure IV-24. *Zoom-in of the a) 100, b) 110, and 200 main reflections shown in the in situ XRD for Na HTB.*

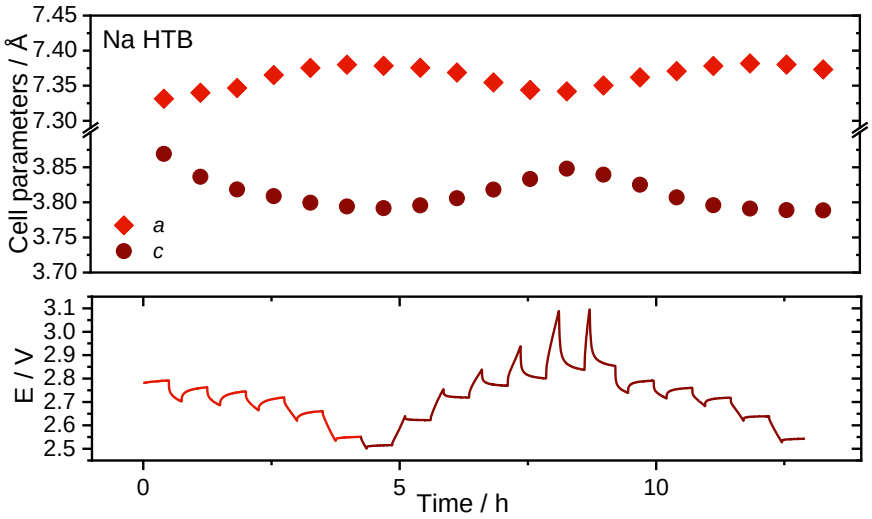

Figure IV-25. *Evolution of the refined cell parameters upon cycling of Na HTB in P6/mmm space group.*

IV.4.3.3. KTB

K compounds show almost no displacement of the peaks due to the cycling. As previously discussed, the potassium compound presents an opposite behavior to Li and Na HTBs. No faradaic response can be seen in its CVs. Moreover, both deconvolution electrochemical analysis and EQCM experiments were not successfully performed in such a compound. Figure IV-26 displays the XRD patterns in function of the charge/discharge curves, with the main and very low-intensity reflections corresponding to *100, 110, 002,* and *200 hkl*. As expected, no visible change can be observed.

Figure IV-27 and Figure IV-28 show the color map of the observed peaks and the zoom-in of the *002*, *110*, and *200* hkl, respectively. Almost no shift can be detected for the set of two peaks at ~23° and 24° in *2θ*. Figure IV-28 shows them clearer but, the low intensity makes it difficult to distinguish.

Finally, Figure IV-29 shows the evolution of the cell parameters *vs.* pattern number obtained upon cycling. As expected, no substantial variations can be observed. Thus, concluding that no Li^+ intercalation occurs in the lattice of the K HTB.

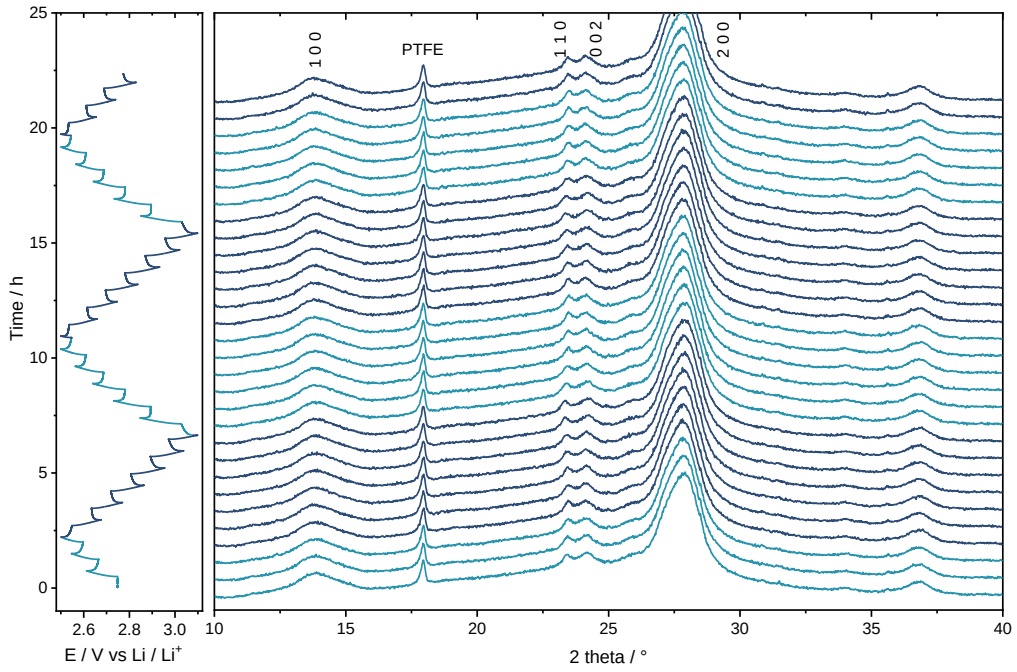

Figure IV-26. *Discharge and charge curves for K HTB in $LiPF_6$ in EC-DMC and XRD pattern from 10-40° in 2θ.*

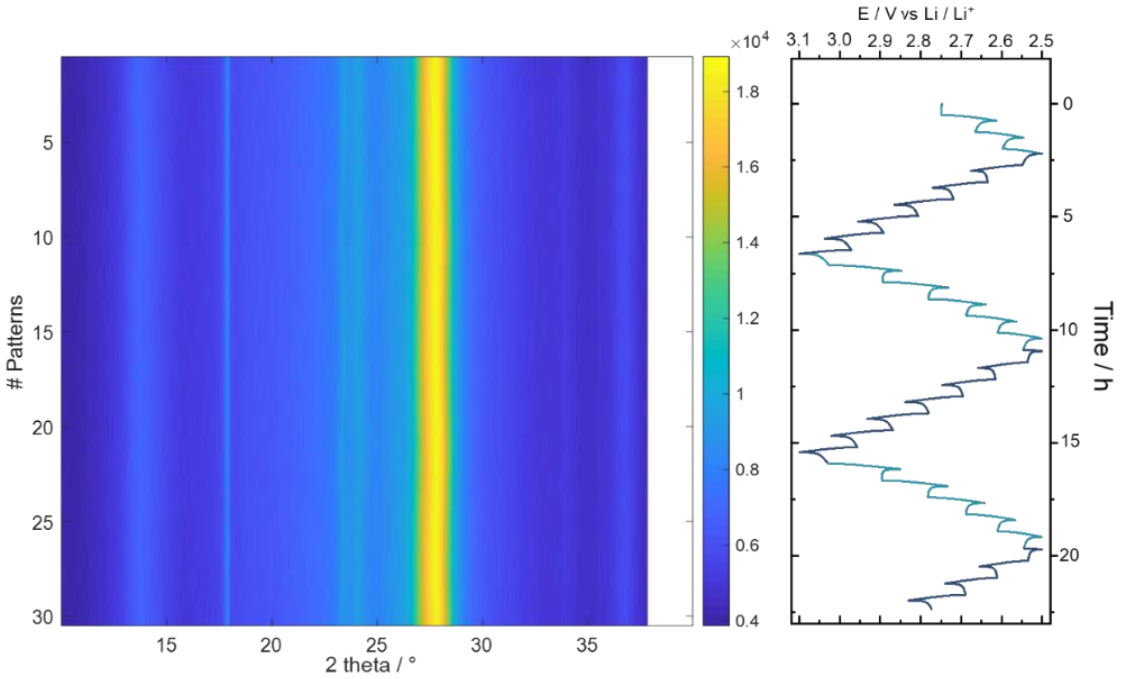

Figure IV-27*. Color map showing the shift of the peaks upon cycling and charge and discharge curves for K HTB.*

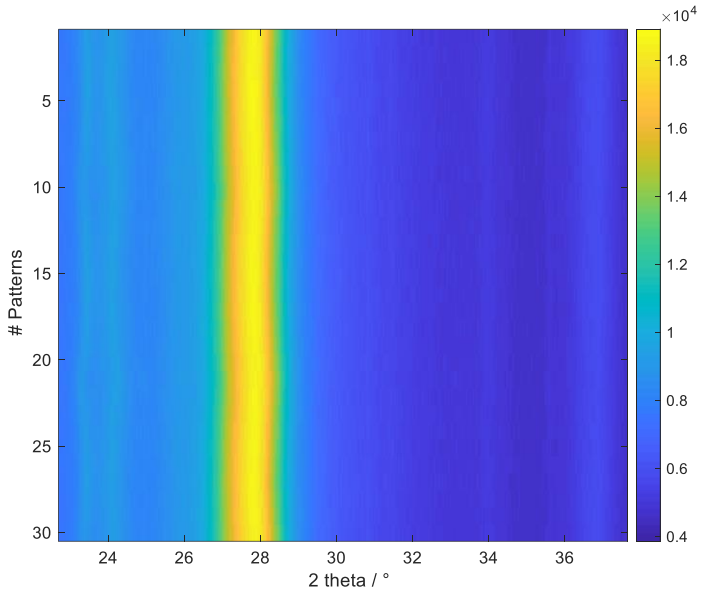

Figure IV-28. *Zoom-in of the 002, 110, and 200 main reflections shown in the in situ XRD for K HTB.*

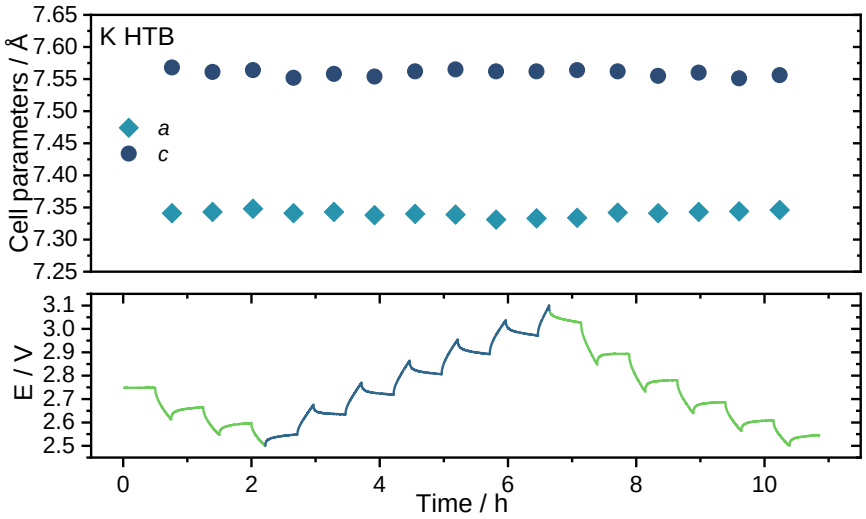

Figure IV-29. *Evolution of the refined cell parameters upon cycling of K HTB in $P6_3/mcm$ space group.*

IV.4.4. Preliminary conclusions on *in situ* XRD study

In this section, we confirmed the very slight structural changes caused by Li^+ cations intercalation into the hexagonal tungsten bronzes of Li, Na, and K. The results agreed to what was expected for both Li and Na HTBs, where an expansion and contraction of the lattice was observed upon Li^+ intercalation and deintercalation, respectively. On the other hand, K HTB

did not show any remarkable change, as expected for this phase with no faradaic activity. Even though the experiments were performed in an organic-based electrolyte, the results shed some light on the structural modifications, indicating thus Li^+ intercalation upon cycling. Moreover, because no significant volume changes were observed, we can conclude that these materials can present a relatively good cyclability upon charge and discharge.

IV.5. X-ray absorption spectroscopy (XAS)

IV.5.1. Introduction to XAS

Synchrotron sources present an outstanding unconventional alternative in the use of *operando* X-ray-based techniques. On the one hand, the high penetrative power of X-ray allows a better design for *operando* photon in-photon out experiments. This is really advantageous when dealing with different transition metal edges as the ones used as active materials in electrochemical energy storage devices. The X-ray can reach and interact with the metals, and they can go out in a signal where the corresponding information will be given. On the other hand, synchrotron X-rays can be tuned. A synchrotron's vast energy range can be tuned to a specific energy range to resonant with specific atomic transitions. These characteristics make it a great and valuable approach to better understand the phenomena occurring in the studied material.[43]

X-ray Absorption Spectroscopy (XAS) is a site-selective technique that provides both electronic structure (related to the chemical state) of the absorbing atom and its local atomic environment (*i.e.*, the bond distances, coordination, and geometry) at a very local scale (~4-5 Å). The X-ray absorption coefficient of the studied sample is measured as a function of the X-ray photon energy, scanned across the absorption edge of a certain element which corresponds to a well-defined electronic transition of a core electron to the available electronic states with the right symmetry. The XAS spectrum can be divided into two regions: 1) the XANES region (X-ray Absorption Near-Edge Structure), from -10 eV to 80-100 eV above the absorption edge, and 2) the EXAFS region (Extended X-ray Absorption Fine-Structure), which prolongs to 1000 eV above the absorption edge. Each region gives valuable information about the absorbing species (see Figure IV-30). For instance, the XANES region, including both pre-edge and edge,

will be more influenced by the unoccupied valence and the conduction band structure, giving information about the oxidation state and the coordination of the involved species. On the other hand, the extended region (EXAFS) will be actively influenced by the geometry positions of the neighboring atoms; consequently, it can be helpful to study the local structure, obtaining bond distances, coordination number, and the nature of the bonding atoms.[43]

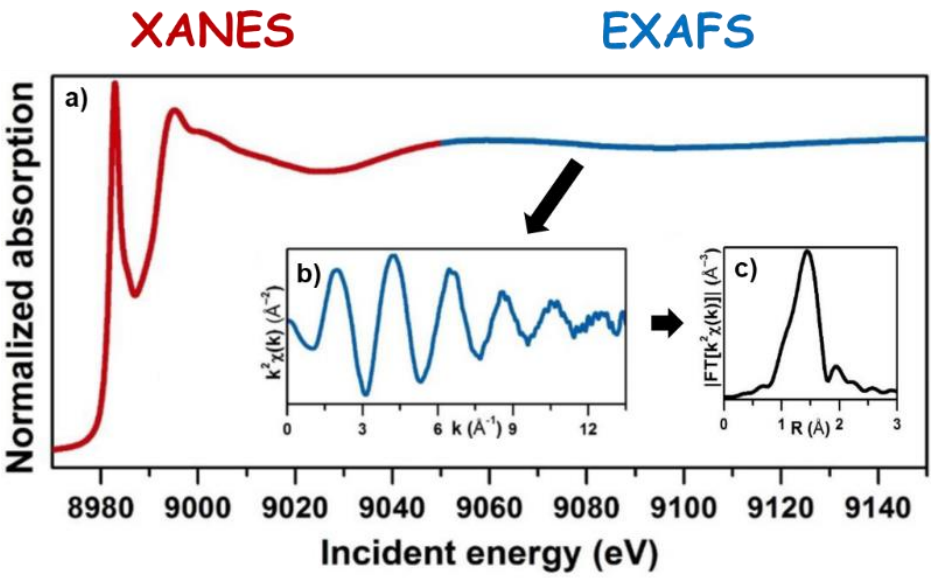

Figure IV-30. *a) XAS spectrum showing both XANES and EXAFS regions. b) k-space EXAFS spectrum and c) Fourier transform of the k-space EXAFS.*

When such a technique is applied to a working electrochemical cell, then real-time information about the changes in the electronic and atomic structure can be obtained to unravel the charge storage mechanism of the desired material.

IV.5.2. Application of XAS on energy storage systems

XAS has demonstrated to be very useful to study materials employed in different energy storage systems, from electrochemical capacitors to battery type materials, both with unique charge storage mechanisms. As previously mentioned in Chapter I, RuO_2 is an excellent pseudocapacitive material, being responsible for such mechanism the redox couple involving Ru^{3+} and Ru^{4+} demonstrated by *in situ* XAS under polarization at specific values of potentials

in acid media. This study revealed the changes in the white-line for both L_3 and L_2 edges, being attributed to a change in oxidation state from +3 to +4, a transition from $4d^5$ to $4d^4$. [31,32] Similar studies were performed in Mn and Fe oxides in aqueous electrolytes.[33–36] Reversible changes in the XANES spectra upon charge and discharge indicated a surface redox reaction between Mn^{3+} and Mn^{4+} as shown in Figure IV-31, where the Mn K-edge energy at different polarization potentials is plotted *vs.* references of known Mn compounds. Thus, the oxidation state changes in the selected material can be followed.

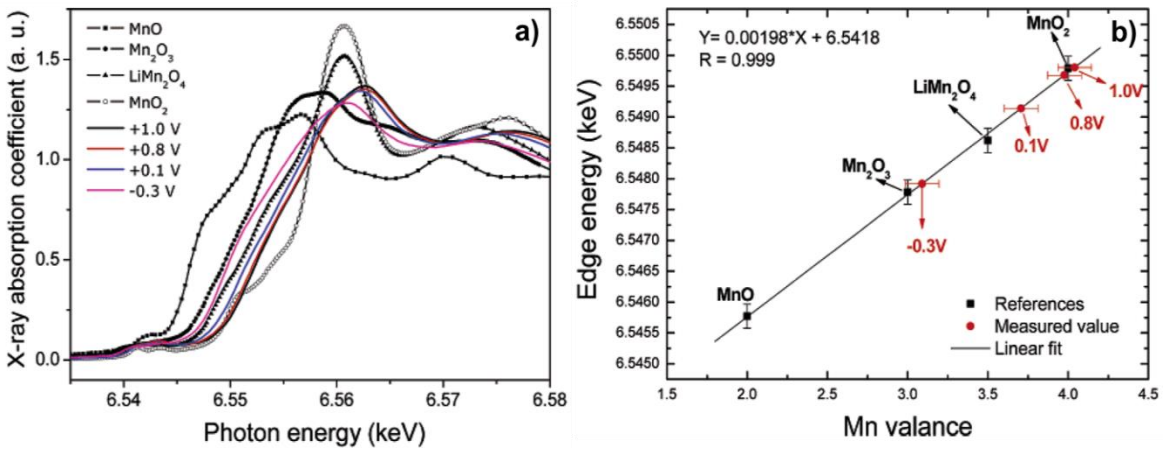

Figure IV-31. *(a) Mn K-edge XANES spectra of the electrodeposited manganese oxide at various applied potentials together with the reference manganese oxides. (b) Oxidation state determination of manganese oxide at applied potentials using the Mn K-edge energy shift of the reference Mn compounds*[33].

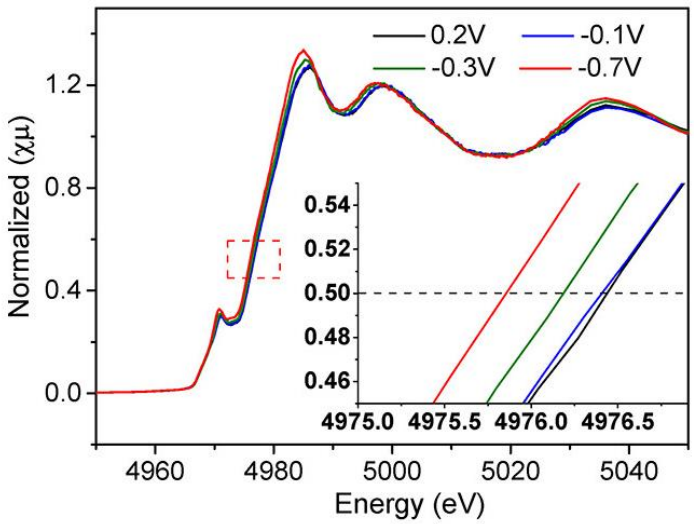

Figure IV-32. *In situ XANES analysis of P-MXene electrode in 1 M H_2SO_4 electrolyte.*[18]

Additionally, *in situ* XAS approaches have been applied to the famous MXenes phases ($Ti_3C_2T_x$) first reported by Gogotsi's group in Drexel university and after by Simon's group in Toulouse.[18,37] They measured the Ti K-edge of the pristine-MXene polarizing at different values of potentials *vs.* Ag/AgCl. They observed a shift to lower energies upon negative polarization, indicating thus a decrease in the oxidation state of Ti (see Figure IV-32).

Despite several *in situ* studies that have been reported, a few *operando* analyses have been performed. As mentioned above, the great advantage of the *operando* approach is the possibility of observing all the changes happening in real-time, as we were watching a film at a very low scale. Goubard-Breteshé *et al*.[38] applied *operando* XAS to understand the behavior of $FeWO_4$ as a pseudocapacitive material in aqueous electrolytes, as displayed in Figure IV-33. Three main thoughts have to be kept out of this study: 1) The prove of the pseudocapacitive behavior by the change on the oxidation state of Fe from 2.8 – 2.55 along with the studied potential window, 2) the zero contribution of tungsten to the charge storage mechanism and 3) this is the first experiment performed in a very rapid system in operando conditions, thus confirming the unique opportunity provided by operando XAS to investigate these fast energy storage devices.

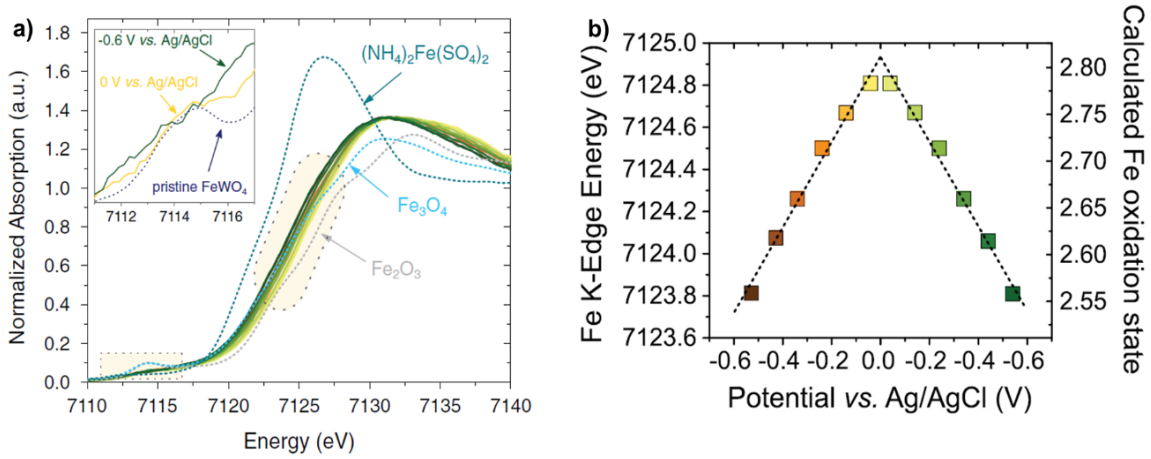

Figure IV-33. *a) Operando Fe K-edge XANES spectra for $FeWO_4$ comparing to several Fe references and b)Evolution of the Fe K-edge energy and mean oxidation state as a function of the electrode potential.*[38]

Nevertheless, the studies in battery-like materials are not outdone. With longer charge/discharge times needed to intercalate 1 mol of Li^+ or Na^+ (ion-exchanged), it allows a thoroughly study not only of the XANES region related to the electronic structure but also in the EXAFS, where we can quantify the deviations at the local scale from the average structure

allowing a complete understanding of the structural evolution, as seen in many examples reported in the literature.[39–45]

IV.5.3. Chemometrics to analyze operando XAS

Operando XAS has been mainly used in the study of energy storage systems, as presented above. However, the large amount of data captured, hundreds or thousands of spectra, makes an incredible and challenging task the analysis spectrum by spectrum. Therefore, chemometrics tools, based on statistical approaches, have flourished in the application to operando datasets. The use of these multivariate tools aims to decompose a large set of data matrices into linear models. The most common methods used PCA (Principal Components Analysis) and MCR-ALS (Multivariate Curve Resolution by Alternating Least Squares). Applying such approaches is possible, first to extract the orthogonal components explaining the utmost variance in the data. Second, unlike PCA, MCR-ALS can generate spectral components and their concentration profiles with a real physical and chemical meaning (Figure IV-34)[46]. These approaches will shorten the operando XAS dataset's analysis and allow a more unambiguous interpretation and enable the trail of unique features of the transient species possibly developed.

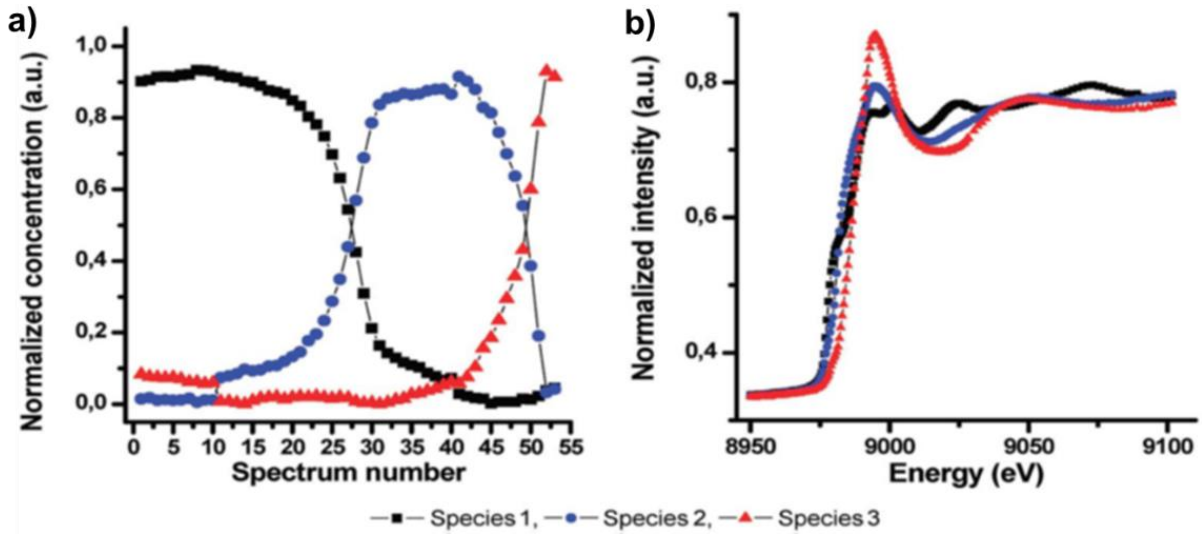

Figure IV-34. *Computed concentration profiles. a) obtained by the MCR-ALS data treatment of the operando XAS study of the charge of a $Cu_{0.1}V_2O_5$-base positive electrode and b) the corresponding pure reconstructed components.*[46]

IV.5.4. Operando electrochemical cell

In order to carry out the *operando* XAS, a special cell was designed in the laboratory Institut des Matériaux Jean Rouxel (IMN) and used for the first time in the doctoral dissertation of Nicolas Goubard-Breteshé[47]. This cell satisfied all specifications needed to perform the experiment in the best optimal conditions. One of them is the optical path of the cell, which depends on the electrode and electrolyte, as indicated in Eq. IV-7, I is the transmitted intensity, I_0 *is* the initial intensity, μ_l is the linear attenuation coefficient (cm^{-1}), and x is the optical path between the two windows.

$$I = I_0 e^{-\mu_l x} \qquad \text{Eq. IV-7}$$

The calculated optical path is fixed at 1.5 mm. Figure IV-35 shows a representation scheme of the *operando* cell, a polyimide film (Kapton®) as a transparent X-ray window is placed between the flange to prevent electrolyte leakage and to minimize the absorption of the photons.

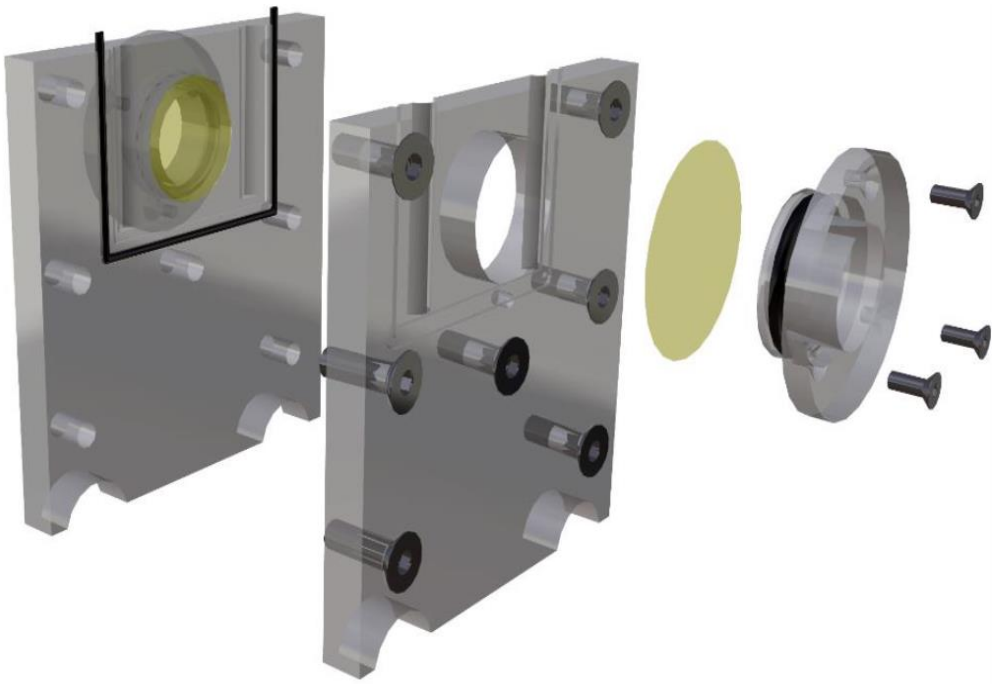

Figure IV-35. *Assembly of the operando cell used for the X-ray absorption spectroscopy experiments.*

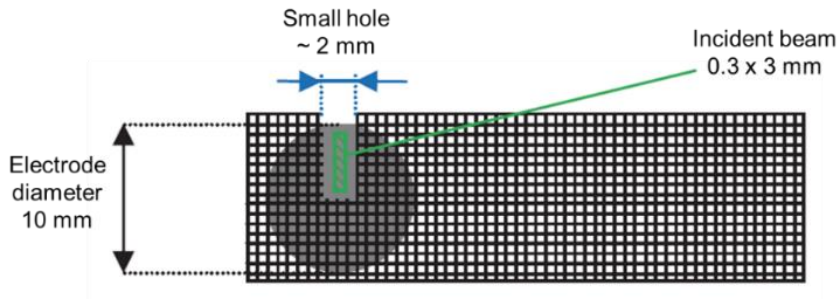

Figure IV-36. *Electrode drawing to be used in an operando cell for XAS.*

To acquire XAS operando spectra, HTBs electrodes were fabricated using the same method as for the classic electrochemical test. Therefore, composite pastes containing 60% active material (HTBs), 30% carbon black, and 10% PTFE were prepared. Small discs with a diameter of 10 mm and loading mass of 6 mg cm^{-2} (optimal value to perform this study) of active material were pressed in a stainless steel grid previously perforated in order to avoid the absorption of incident X-ray photons. The special aperture made in the current collector is shown in Figure IV-36, along with the size of the incident beam.

IV.5.5. Operando XAS experiment at ROCK beamline (SOLEIL)

Operando X-ray absorption spectroscopy (XAS) experiments were performed at ROCK beamline[48] (Rocking Optics for Chemical Kinetics) of SOLEIL. This beamline is dedicated to studying rapid kinetic processes, particularly in catalysis, batteries, and electrochemical capacitors. It enables working at energies ranging from 4 to 43 keV thanks to their two "Quick-EXAFS" monochromators, Si (111) and Si (220). They can oscillate up to a frequency of 30 Hz over small angle ranges (<0.5 °) and 20 Hz for larger oscillations. Therefore, very fast scans are possible with an acquisition time of up to 25 ms per spectrum. Thanks to its optical setup and acquisition chain, the ROCK beamline is the best option for studying fast energy storage systems, like those described in this manuscript.

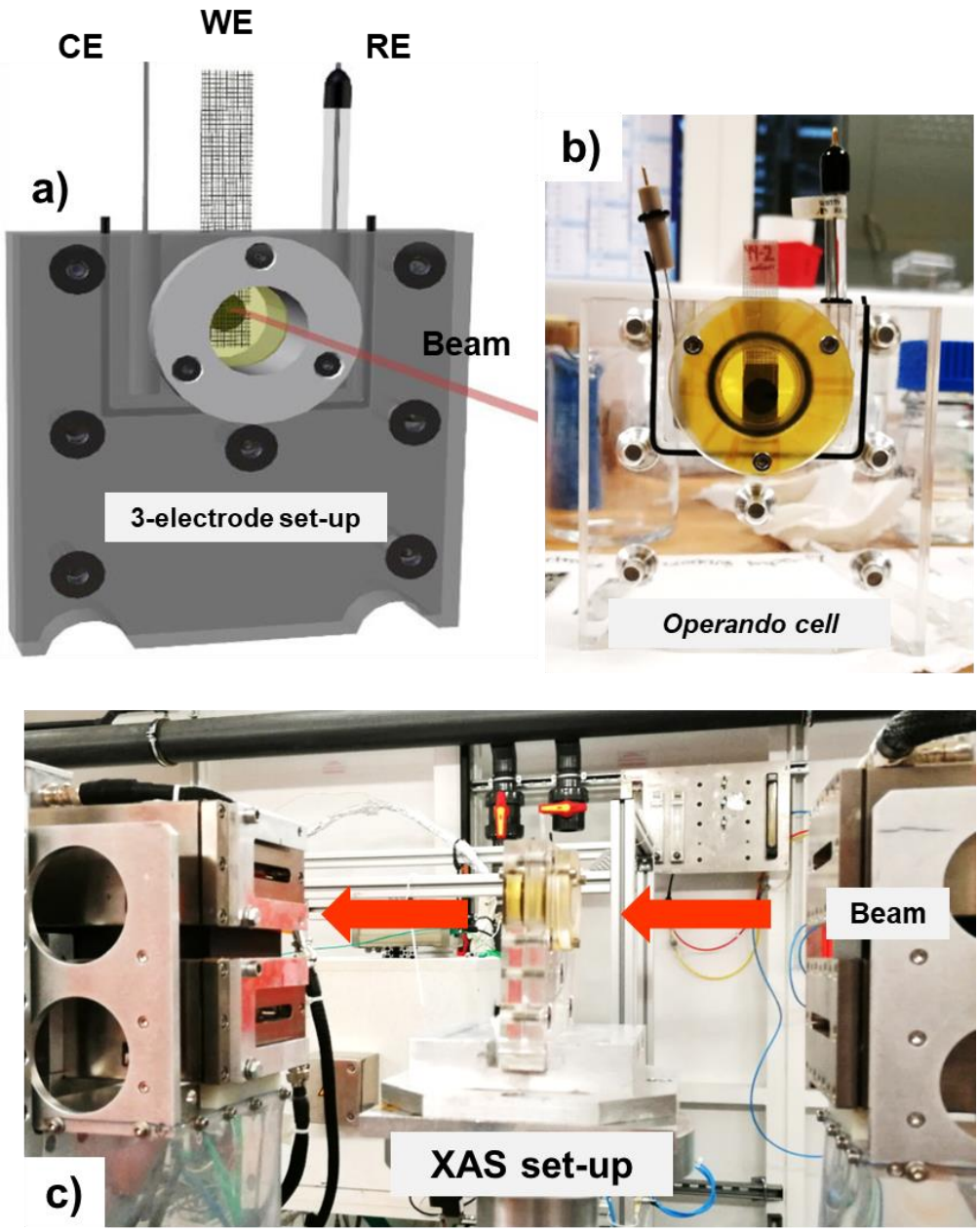

Figure IV-37. *Operando XAS cell. a) Scheme of the cell indicating the 3-electrode setup, b) Frontal view of the operando cell, and c) XAS setup in SOLEIL synchrotron facilities.*

The XAS spectra were collected at tungsten L_3 edge (10204 eV) on HTBs electrodes. Tungsten foil (W), WO_2 (W^{+4}), and WO_3 (W^{+6}) commercially available were used as references to assess the W oxidation state. First, the valence state of the pristine samples was evaluated at the open circuit potential (OCP) of the electrodes. Then, the electrodes prepared from the samples of the different HTBs were tested by cyclic voltammetry in aqueous $LiNO_3$ 5M, Li_2SO_4, Na_2SO_4, and K_2SO_4 starting with an activation test at 20 $mV.s^{-1}$ from 0.0 V to -0.6 V *vs.* Ag/AgCl. After a few cycles, the XAS spectra acquisition started cycling with a scan rate

of 2 mV.s^{-1} in the same potential window (*operando* conditions). XAS spectra were collected at a frequency of 2 Hz. The spectra obtained were averaged 10 by 10 in order to increase the signal-to-noise ratio. This procedure made it possible to obtain an averaged spectrum every 5 seconds (*i.e.*, every 10 mV cycling at 2 mV.s^{-1}) and thus to precisely follow the evolution and changes of the HTBs active materials upon real-time cycling conditions. Figure IV-37 illustrates the 3-electrodes *operando* cell XAS setup at the beamline just before the X-ray acquisition. Furthermore, the operando XANES results for the HTBs in 5 M LiNO3 will be presented next.

IV.5.6. Operando XANES analysis for the Hexagonal Tungsten Bronzes

Figure IV-38 shows the cyclic voltammograms for the three HTBs tested in *operando* XAS setup *vs.* the CVs obtained in the traditional cell (discussed in Chapter III) as a comparison. It is noticed that the classical shape for each compound is maintained, with Li response changing slightly from the standard CV. This is understandable due to the thickness of the electrode and the special setup of the cell. However, the signatures are clearly defined to continue and carry on the *operando* XANES experiments.

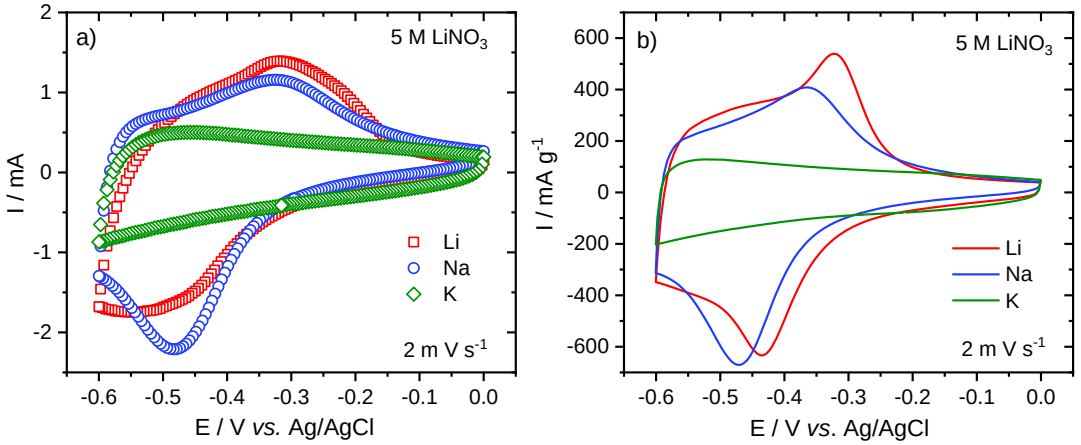

Figure IV-38. *Electrochemical response for the HTBs in 5M $LiNO_3$ at 2 mV.s^{-1}. a) HTBs CVs from the operando setup and b) HTBs CVs from the classical setup.*

The experiment started measuring the W L_3-edge XAS spectra upon cycling. Figure IV-39 shows the first results obtained, only showing as an example Na HTB spectra. This figure

shows the normalized absorption vs. the energy in eV of W L3-edge in both reduction and oxidation sweeps (Figure IV-39a and c). Moreover, Figure IV-39b and d, displays the respective zoom-in into the edge part. It can be noticed that the spectra shift towards lower energy values upon reduction and then goes back to higher energy values upon oxidation.

The W L_3-edge corresponds to the transition of $2p_{3/2}$ electrons towards 5d states. The single prominent peak above the edge is called the "white line," and its intensity is also proportional to the 5d empty state. The shift of edge energy to lower values is attributed to the decrease of the binding energy of the core level of the W absorber[49,50], meaning that W is being reduced from W^{6+} to W^{5+} due to the Li^+ intercalation into the lattice.

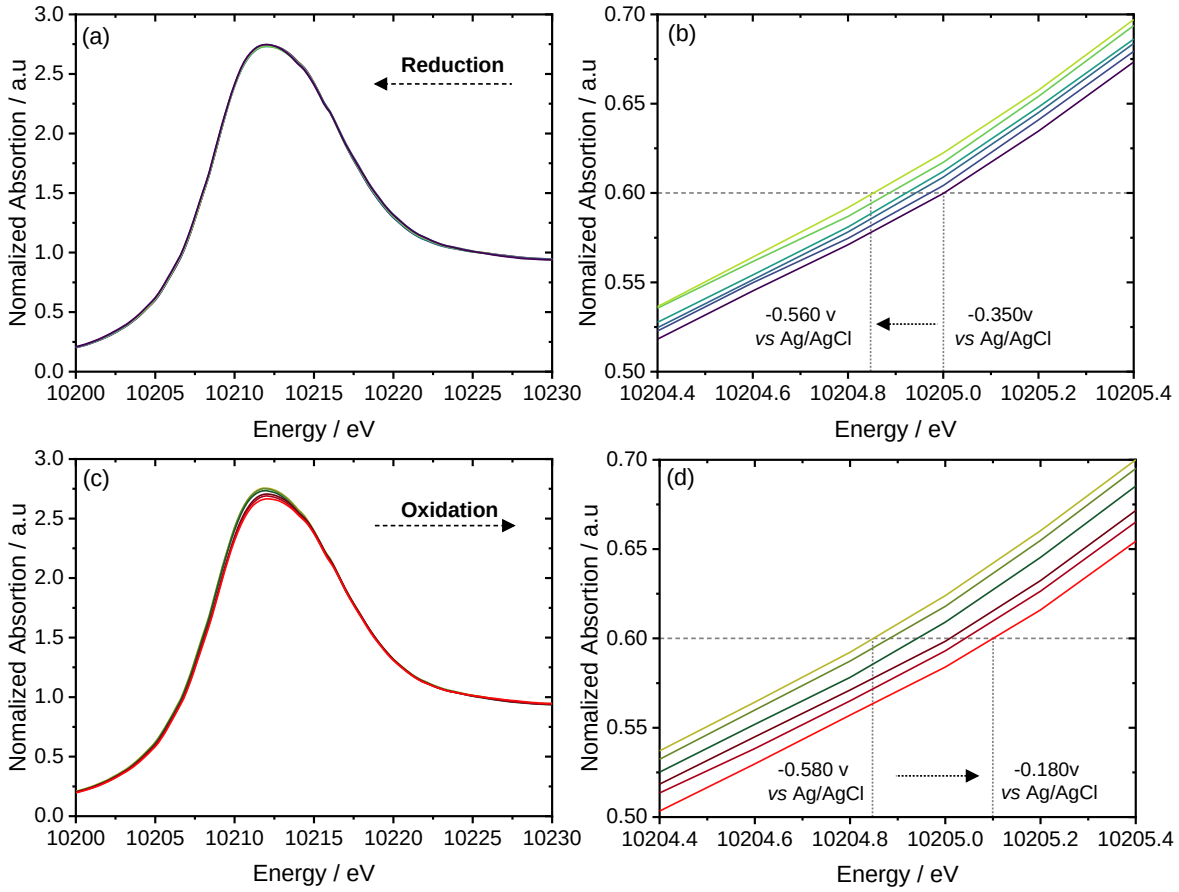

Figure IV-39. *Operando W L_3-edge for Na HTB. a) Upon reduction from 0.0 - (-0.6) V b) Upon oxidation -0.6 - 0.0 vs. Ag/AgCl. b) and d) respective enlargement of the normalized absorption evidencing the changes in W L_3-edge energy while cycling the electrodes between 0.0 V down to −0.6 V vs. Ag/AgCl at 2 $mV.s^{-1}$.*

The spectra shown in Figure IV-39 can be associated with a respective value of potential in the CV of the Na HTB. Moreover, in the same way, each value of potential is associated with a specific value in energy, in eV. Figure IV-40 displays this relationship more clearly. Thereby, the shift in energy depending on the sweep of potential towards more negative values and then towards more positive values can be further appreciated. In addition, it can be seen that such energy shift *vs.* potential is not totally linear, as in the case of pseudocapacitive materials already reported.[33–35] This non-linearity indicates that such a mechanism is not entirely pseudocapacitive and that intercalation must be the predominant process at specific values of potential.

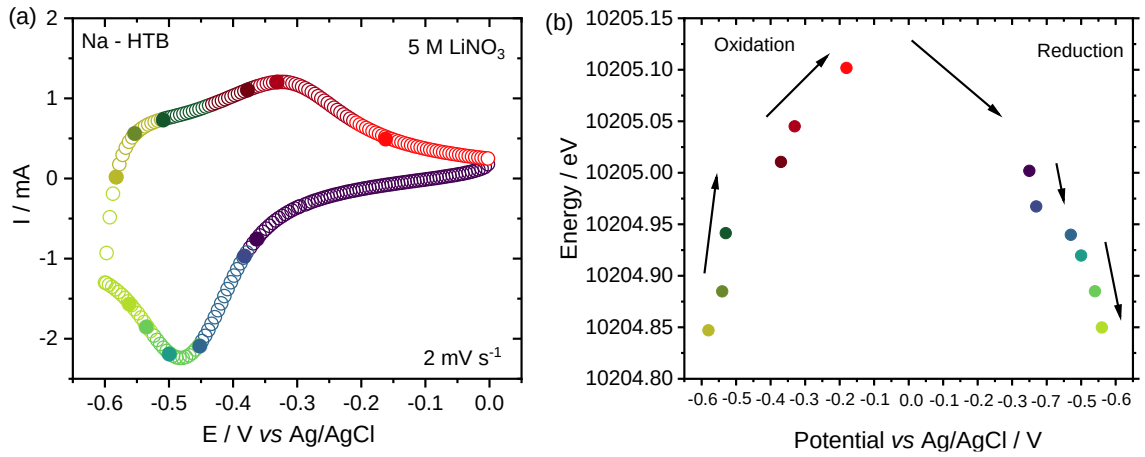

Figure IV-40. *a) Cyclic voltammogram for Na HTB at 2 mV.s^{-1} in $LiNO_3$ 5M (the color dots represent the XAS spectra acquisition selected for this representation. b) Evolution W L_3-edge energy shift in function of the sweep potential vs. Ag/AgCl.*

However, to better understand the shift in energy *vs.* potential in several cycles, the data analysis was performed using Matlab routine to treat a large data volume, specifically.

Figure IV-41 shows the comparison between the three Li (a, red), Na (b, blue), and K (c, green) HTBs. The electrochemical signature in current *vs.* time coupled with the energy shift *vs.* #scan (spectra number) is displayed. This plot makes it easier to follow the shift in energy upon cycling when the reversible sweep takes place from more negative to more positive potentials and back again. Li and Na HTBs follow a similar trend, even though the energy shift is very small (~0.1 eV). On the other hand, K HTB, as we already know, exhibits a different behavior compared to the other HTBs: the energy shift is in the signal-to-noise band, and it is difficult to identify a clear trend. Therefore, using the results obtained for Li and Na HTBs, a

Principal Components Analysis, PCA, was performed in order to extract the number of the main components involved in the electrochemical reaction when the HTBs are being cycled in aqueous 5M $LiNO_3$.

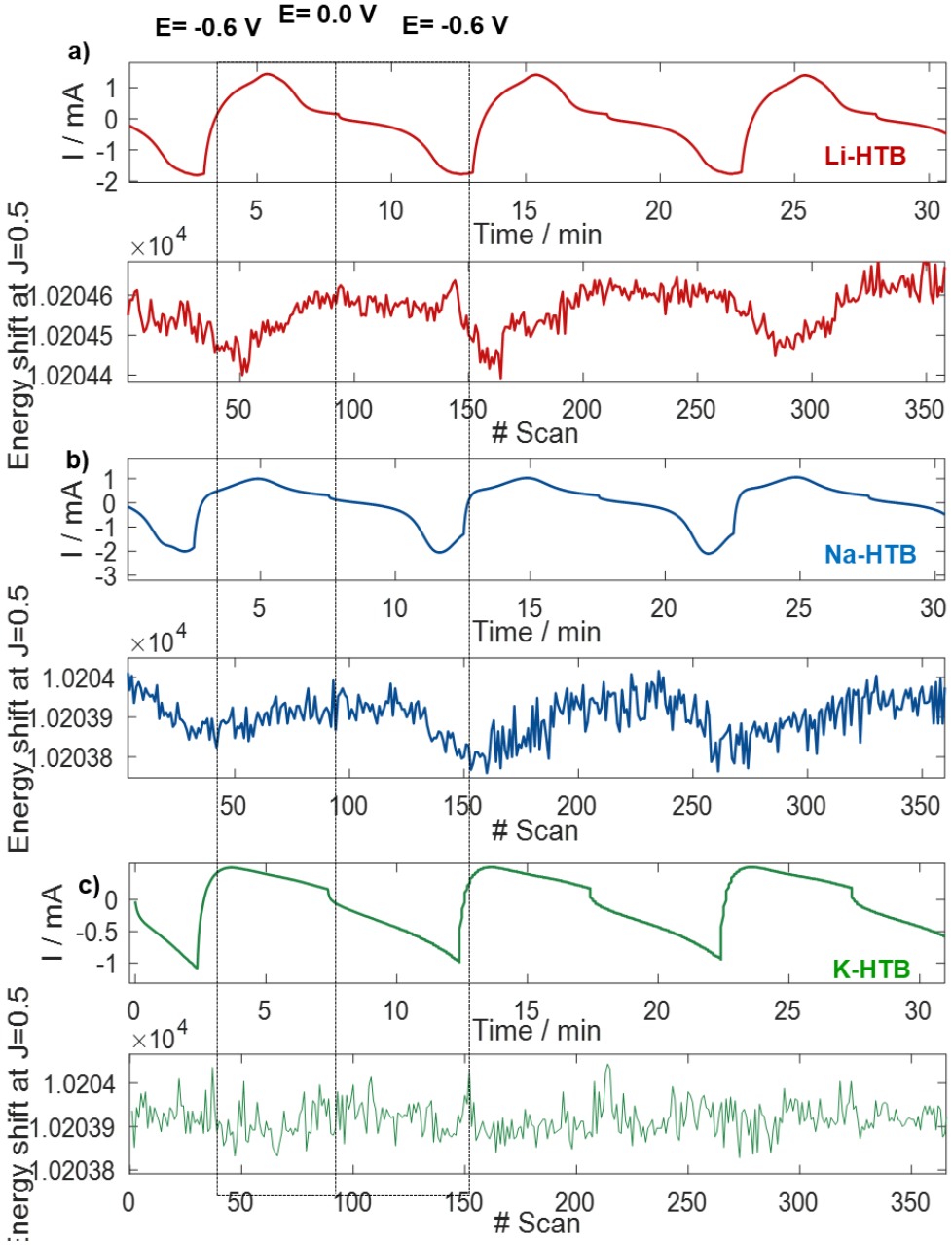

Figure IV-41. *Current vs. time curves for Li, Na, and K HTBs. And Energy shift in function of spectra number. The dotted lines indicate the values where the potential reaches -0.6 V and goes back to 0.0 V vs. Ag/AgCl.*

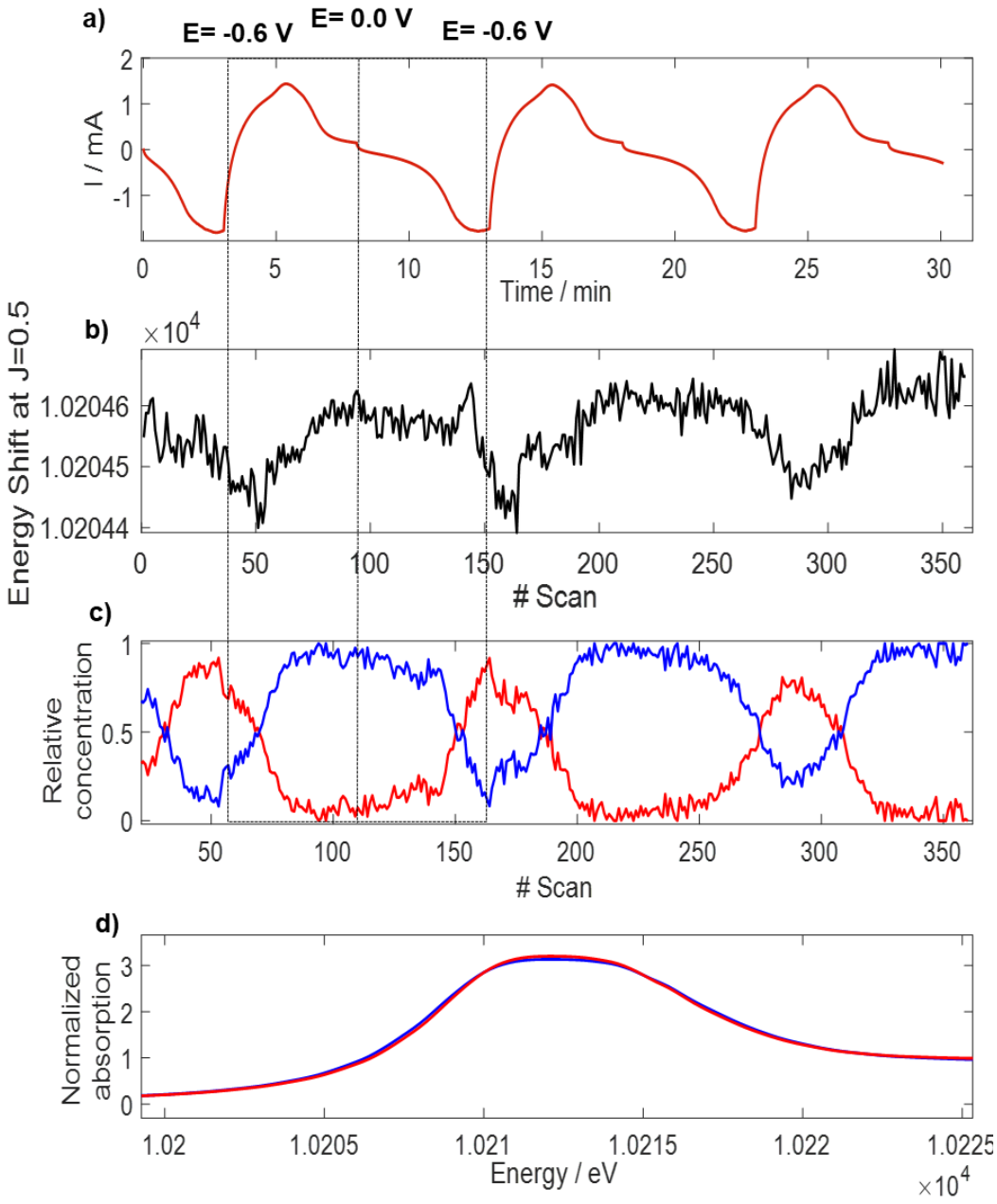

Figure IV-42. *a) Current vs. time curves for Li HTB. b) Energy shift in function of spectra number. The dotted lines indicate the values where the potential reaches -0.6 V and goes back to 0.0 V vs. Ag/AgCl. c) Concentration profile of the two principal components required to describe the operando XAS spectra (blue and red). And d) reconstructed XANES spectra of the two independent components required to describe the Li HTB system.*

Figure IV-42a and b show the electrochemical response *vs.* the energy shift for Li HTBs. Additionally, Figure IV-42c and d, display the concentration profile of the two principal components (blue and red). And the reconstructed XANES spectra of those two reconstructed components. For this case, at least two components are required to describe the operando XAS spectra. One increases (red) while the other decreases (blue) upon cycling. Looking at their

XANES profile, one is more oxidized, and one is more reduced, depending on the potential change.

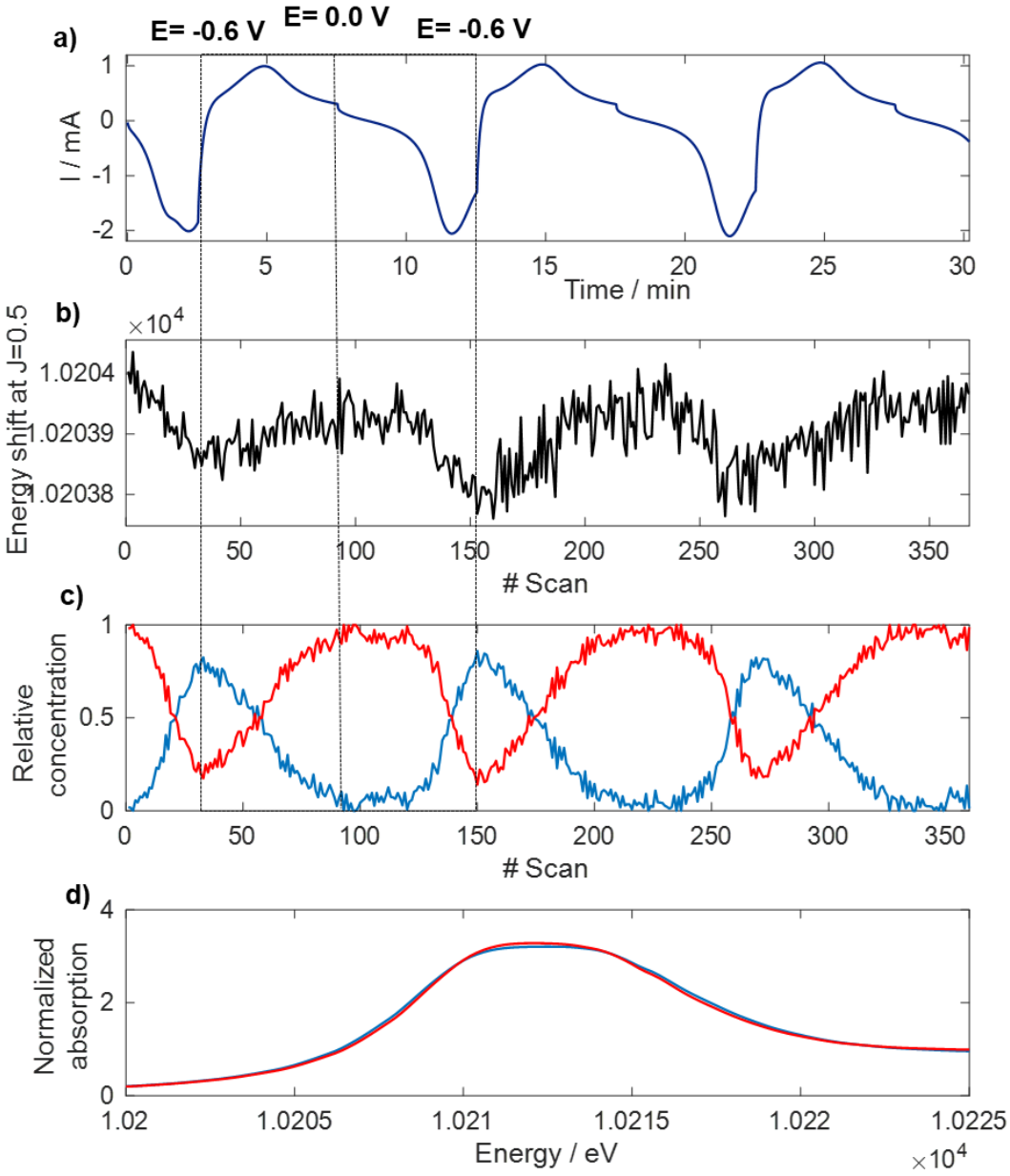

Figure IV-43. *a) Current vs. time curves for Na HTB. b) Energy shift in function of spectra number. The dotted lines indicate the values where the potential reaches -0.6 V and goes back to 0.0 V vs. Ag/AgCl. c) Concentration profile of the two principal components required to describe the operando XAS spectra (blue and red). And d) reconstructed XANES spectra of the two independent components required to describe the Na HTB system.*

Even though the energy shift upon cycling is very small, we need to consider that the redox contributions are limited to the interface of the electrode/electrolyte while the XAS measurements performed in transmission mode are bulk sensitive.

As with the Na HTB case, Figure IV-43 shows the respective results. The energy shift related to the electrochemical response is translated to the concentration profile of two main components necessary to describe the *operando* XAS spectra. As aforementioned, the same trend for Li HTB is followed for these components. Indeed, these two reconstructed components are most likely associated with one more oxidized (red) and one more reduced (blue) species being active in the material.

Bringing back the reference samples measured, WO_2 for W^{4+} and WO_3 for W^{+6}, the energy shift between the two was ~1.0 eV, which is related to 2 e- as shown in Figure IV-44 a) and b). Therefore, using the energy edge of the references, one can estimate the number of electrons being exchanged due to the change in energy provided by the XANES for the Li and the Na HTBs.

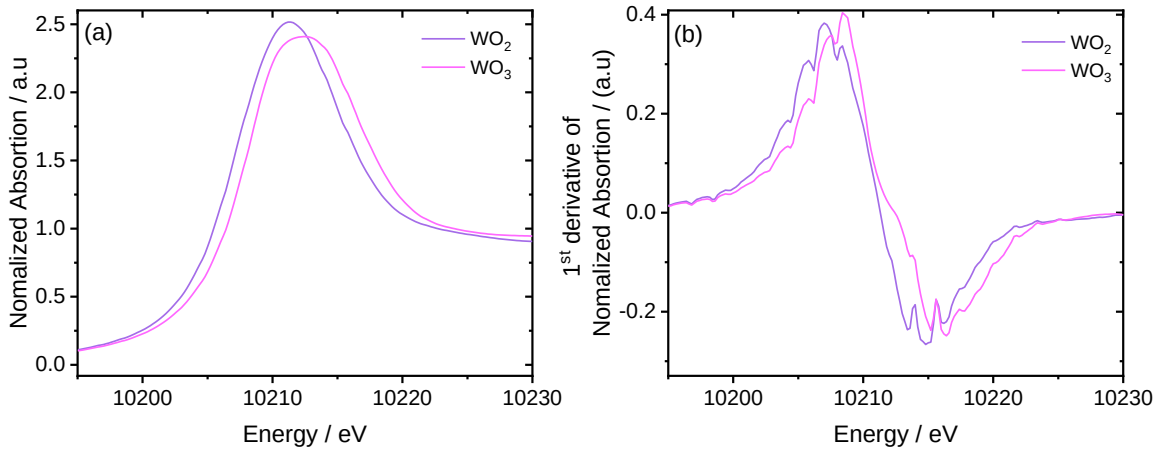

Figure IV-44. *a) XANES spectra of the references WO_2 and WO_3 and b) 1st derivative of the normalized absorption for WO_2 and WO_3.*

Table IV-4 shows the e^- exchanged calculated based on the capacity extracted from the electrochemical response. For this, we use Faraday's law (Eq. IV-8), where n is the number of electrons exchanged, M_w is the molecular weight of the respective HTB, and Q is the capacity associated with the electrochemical response.

$$Q = \frac{n\,F}{M_w} \qquad \text{Eq. IV-8}$$

These electrons are then compared to the e^- exchanged due to XANES energy shift. It can be noticed that the e^- calculated from both approaches are comparable.

***Table IV-4**. Electrons exchanged comparing electrochemical response vs. XANES energy shift.*

HTB	Capacity from CV in $C.g^{-1}$	# e^- exchanged	# e^- exchanged considering an average shift of 0.1 eV
Li	53	0.13	~0.1-0.2
Na	42	0.10	~0.1-0.2

Finally, we can conclude that XAS has resulted in a powerful technique to perceive the small changes occurring with the hexagonal tungsten bronzes when used as electrode material for relatively fast Li^+ intercalation. XANES followed the same trend shown by our previous studies. There is a more visible faradaic contribution due to the Li^+ intercalation for the Li and Na HTBs, which was confirmed by the slight energy shift of the W white line, confirming thus a slight oxidation state variation of tungsten upon intercalation. This was shown by Principal Component Analysis, where an interesting trend of two related species was depicted upon cycling of Li and Na HTBs. Moreover, K HTB seems to present only a surface capacitive behavior where no energy changes could be detected by XANES, thus neglecting any pseudocapacitive behavior.

IV.6. Conclusions – Chapter IV

This chapter presented an advanced electrochemical study and several in situ and operando characterization techniques. They were used to understand better the charge storage mechanism of the hexagonal tungsten bronzes of lithium, sodium, and potassium.

In the first section, the deconvolution of the main contributions for storing charge was made. It was found that both capacitive and diffusion-controlled predominate for Li and Na HTBs. In contrast, for K HTB, this study could not have been completed. However, it should not be taken lightly since the capacitive adds a pseudocapacitive participation, implying a charge transfer not limited by diffusion. Moreover, the shape of the cyclic voltammograms for Li and Na HTBs clearly indicates more a faradaic response in addition to a possible pseudocapacitive one. On the other hand, K HTB only reflects a most likely surface capacitive mechanism with no pseudocapacitive contribution as the normalized surface capacitance showed, comparable to those of metals with an electric double-layer behavior.

EQCM was presented in the second section. A relationship between the faradaic response observed in the CVs for Li and Na HTBs and the intercalation of Li^+ was further investigated. Li^+ cations are not being intercalated alone. They are accompanied by about 0.5 and 1.1 moles of water for Li and Na HTBs, respectively. As aforementioned in chapter III, there is a relationship between the concentration of Li^+ in the electrolyte and the feasibility of Li^+ to be desolvated and then intercalated into the lattice of the material. Thus, EQCM confirms the Li^+ intercalation into the HTBs in a water-based electrolyte at a moderate rate.

Both electrochemical and EQCM studies were performed in aqueous electrolytes. Later in the text, *in situ* X-ray diffraction was used to follow the evolution of the cell parameters during charge/discharge cycles in an organic-based electrolyte. It was found that the cell parameters are related to reversible Li^+ intercalation/deintercalation. During Li^+ intercalation, the *a* and *b* cell parameters lengthen, and the *c* parameter shortens. Thus, it was assumed that the intercalated Li^+ occupy the available trigonal/hexagonal crystallographic sites of the HTBs. This was demonstrated for Li and Na HTBs. On the other hand, the X-ray patterns of K HTB did not show any significant shift in the cell parameters. Therefore, it confirms the absence of an intercalation mechanism for this material, as indicated by the already seen quasi-rectangular CV shape.

Finally, to give further support and understanding on such interesting WO_3 hexagonal phases, synchrotron *operando* XAS studies were performed. We found a slight change in the oxidation state of tungsten is obtained by the shift in energy, in eV, upon electrochemical cycling. Notwithstanding that such a shift observed is very small, Principal Components Analysis (PCA) confirmed two main components necessary to explain the XANES spectra for Li and Na HTBs. These components were attributed to a more oxidized specie and a more reduced one. This confirms that when Li^+ is intercalated into the lattice, the W cations are possibly reduced, and when Li^+ deintercalates, the W gets re-oxidized in a fully reversible process. In addition, the electrons related to the electrochemical response and the ones associated with the energy shift of the W white line are comparable, demonstrating reliable results of this study.

Moreover, it must be mentioned that thanks to PCA, these changes can be visible considering that the electrochemical cycling takes only 10 min, charge/discharge included, being much faster than standard battery-like materials and slower than pseudocapacitive materials. In contrast, we can conclude that the K HTB only presents a possible surface capacitive mechanism due to the lack of energy changes in the W white line, and confirming thus, the results found electrochemically and by the *in situ* XRD study. Furthermore, PCA has not provided straightforward results for this compound because the detection limit was close to the signal-to-noise ratio.

IV.7. References – Chapter IV

1. Trasatti, S. & Buzzanca, G. Ruthenium dioxide: A new interesting electrode material. Solid state structure and electrochemical behaviour. *J. Electroanal. Chem. Interf. Electrochem.* **29**, A1–A5 (1971).
2. Ardizzone, S., Fregonara, G. & Trasatti, S. "Inner" and "outer" active surface of RuO_2 electrodes. *Electrochim. Acta* **35**, 263–267 (1990).
3. Lindström, H. *et al.* Li^+ Ion Insertion in TiO_2 (Anatase). 2. Voltammetry on Nanoporous Films. *J. Phys. Chem. B* **101**, 7717–7722 (1997).
4. Conway, B. E., Birss, V. & Wojtowicz, J. The role and utilization of pseudocapacitance for energy storage by supercapacitors. *J. Power Sources* **66**, 1–14 (1997).
5. Liu, T.-C., Pell, W. G., Conway, B. E. & Roberson, S. L. Behavior of Molybdenum Nitrides as Materials for Electrochemical Capacitors Comparison with Ruthenium Oxide. *J. Electrochem. Soc.* **145**, 1882–1888 (1998).
6. Wang, J., Polleux, J., Lim, J. & Dunn, B. Pseudocapacitive Contributions to Electrochemical Energy Storage in TiO_2 (Anatase) Nanoparticles. *J. Phys. Chem. C* **111**, 14925–14931 (2007).
7. Metrohm DropSens: Screen-Printed electrodes. https://www.dropsens.com/en/screen_printed_electrodes_pag.html.
8. Sauerbrey, G. Verwendung von Schwingquarzen zur Wägung dünner Schichten und zur Mikrowägung. *Z. Phys.* **155**, 206–222 (1959).
9. Buttry, D. A. & Ward, M. D. Measurement of interfacial processes at electrode surfaces with the electrochemical quartz crystal microbalance. *Chem. Rev.* **92**, 1355–1379 (1992).
10. Levi, M. D., Salitra, G., Levy, N., Aurbach, D. & Maier, J. Application of a quartz-crystal microbalance to measure ionic fluxes in microporous carbons for energy storage. *Nat. Mater.* **8**, 872–875 (2009).
11. Levi, M. D. *et al.* Electrochemical Quartz Crystal Microbalance (EQCM) Studies of Ions and Solvents Insertion into Highly Porous Activated Carbons. *J. Am. Chem. Soc.* **132**, 13220–13222 (2010).
12. Levi, M. D., Sigalov, S., Aurbach, D. & Daikhin, L. In Situ Electrochemical Quartz Crystal Admittance Methodology for Tracking Compositional and Mechanical Changes in Porous Carbon Electrodes. *J. Phys. Chem. C* **117**, 14876–14889 (2013).
13. Tsai, W.-Y., Taberna, P.-L. & Simon, P. Electrochemical Quartz Crystal Microbalance (EQCM) Study of Ion Dynamics in Nanoporous Carbons. *J. Am. Chem. Soc.* **136**, 8722–8728 (2014).
14. Pean, C. *et al.* Confinement, Desolvation, And Electrosorption Effects on the Diffusion of Ions in Nanoporous Carbon Electrodes. *J. Am. Chem. Soc.* **137**, 12627–12632 (2015).
15. Chmiola, J. Anomalous Increase in Carbon Capacitance at Pore Sizes Less Than 1 Nanometer. *Science* **313**, 1760–1763 (2006).

16. Tsai, W.-Y. Ion adsorption in porous carbon : from fundamental studies to supercapacitor applications. (2015).

17. Wu, Y.-C., Taberna, P.-L. & Simon, P. Tracking ionic fluxes in porous carbon electrodes from aqueous electrolyte mixture at various pH. *Electrochem. commun.* **93**, 119–122 (2018).

18. Shao, H. *et al.* Unraveling the Charge Storage Mechanism of $Ti_3C_2T_x$ MXene Electrode in Acidic Electrolyte. *ACS Energy Lett.* **5**, 2873–2880 (2020).

19. Shao, H. 2D $Ti_3C_2T_x$ MXenes pour le stockage électrochimique d'énergie. (2020).

20. Morcrette, M. *et al.* In situ X-ray diffraction techniques as a powerful tool to study battery electrode materials. *Electrochim. Acta* **47**, 3137–3149 (2002).

21. Amatucci, G. G., Tarascon, J. M. & Klein, L. C. CoO_2, The End Member of the Li_xCoO_2 Solid Solution. *J. Electrochem. Soc.* **143**, 1114 (1996).

22. Roberts, M. R. *et al.* Direct Observation of Active Material Concentration Gradients and Crystallinity Breakdown in LiFePO4 Electrodes During Charge/Discharge Cycling of Lithium Batteries. *J. Phys. Chem. C* **118**, 6548–6557 (2014).

23. Morcrette, M., Leriche, J.-B., Patoux, S., Wurm, C. & Masquelier, C. In Situ X-Ray Diffraction during Lithium Extraction from Rhombohedral and Monoclinic $Li_3V_2(PO_4)_3$ *Electrochem. Solid-State Lett.* **6** A80 (2003)

24. Mba, J.-M. A., Croguennec, L., Basir, N. I., Barker, J. & Masquelier, C. Lithium Insertion or Extraction from/into Tavorite-Type $LiVPO_4F$: An In Situ X-ray Diffraction Study. *J. Electrochem. Soc.* **159**, A1171–A1175 (2012).

25. Nguyen, L. H. B. *et al.* Monitoring the Crystal Structure and the Electrochemical Properties of $Na_3(VO)_2(PO_4)_2F$ through Fe^{3+} Substitution. *ACS Appl. Mater. Interfaces* **11**, 38808–38818 (2019).

26. Come, J. *et al.* Electrochemical Kinetics of Nanostructured Nb_2O_5 Electrodes. *J. Electrochem. Soc.* **161**, A718–A725 (2014).

27. Mitchell, J. B. *et al.* Confined Interlayer Water Promotes Structural Stability for High-Rate Electrochemical Proton Intercalation in Tungsten Oxide Hydrates. *ACS Energy Lett.* **4**, 2805–2812 (2019).

28. Wang, X. *et al.* Titanium Carbide MXene Shows an Electrochemical Anomaly in Water-in-Salt Electrolytes. *ACS Nano* (2021).

29. Mu, X. *et al.* Revealing the Pseudo-Intercalation Charge Storage Mechanism of MXenes in Acidic Electrolyte. *Adv. Funct. Mater.* **29**, 1902953 (2019).

30. Mitchell, J. B. *et al.* Confined Interlayer Water Promotes Structural Stability for High-Rate Electrochemical Proton Intercalation in Tungsten Oxide Hydrates. *ACS Energy Lett.* **4**, 2805–2812 (2019).

31. Mo, Y., Antonio, M. R. & Scherson, D. A. In Situ Ru K-Edge X-Ray Absorption Fine Structure Studies of Electroprecipitated Ruthenium Dioxide Films with Relevance to Supercapacitor Applications. *J. Phys. Chem. B* **104**, 9777–9779 (2000).

32. Stefan, I. C., Mo, Y., Antonio, M. R. & Scherson, D. A. In Situ Ru LII and LIII Edge X-ray Absorption Near Edge Structure of Electrodeposited Ruthenium Dioxide Films. *J. Phys. Chem. B* **106**, 12373–12375 (2002).

33. Nam, K.-W., Kim, M. G. & Kim, K.-B. In Situ Mn K-edge X-ray Absorption Spectroscopy Studies of Electrodeposited Manganese Oxide Films for Electrochemical Capacitors. *J. Phys. Chem. C* **111**, 749–758 (2007).

34. Chang, J.-K., Lee, M.-T. & Tsai, W.-T. In situ Mn K-edge X-ray absorption spectroscopic studies of anodically deposited manganese oxide with relevance to supercapacitor applications. *J. Power Sources* **166**, 590–594 (2007).

35. Kuo, S.-L., Lee, J.-F. & Wu, N.-L. Study on Pseudocapacitance Mechanism of Aqueous $MnFe_2O_4$ Supercapacitor. *J. Electrochem. Soc.* **154**, A34 (2007).

36. Lee, M.-T., Chang, J.-K., Tsai, W.-T. & Lin, C.-K. In situ X-ray absorption spectroscopic studies of anodically deposited binary Mn–Fe mixed oxides with relevance to pseudocapacitance. *J. Power Sources* 7 (2008).

37. Lukatskaya, M. R. *et al.* Probing the Mechanism of High Capacitance in 2D Titanium Carbide Using In Situ X-Ray Absorption Spectroscopy. *Adv. Energy Mater.* **5**, 1500589 (2015).

38. Goubard-Bretesché, N. *et al.* Unveiling Pseudocapacitive Charge Storage Behavior in $FeWO_4$ Electrode Material by Operando X-Ray Absorption Spectroscopy. *Small* **16**, 2002855 (2020).

39. Ouvrard, G. *et al.* Heterogeneous behaviour of the lithium battery composite electrode $LiFePO_4$. *J. Power Sources* **229**, 16–21 (2013).

40. Koga, H. *et al.* Operando X-ray Absorption Study of the Redox Processes Involved upon Cycling of the Li-Rich Layered Oxide $Li_{1.20}Mn_{0.54}Co_{0.13}Ni_{0.13}O_2$ in Li Ion Batteries. *J. Phys. Chem. C* **118**, 5700–5709 (2014).

41. Marino, C. *et al.* At the Heart of a Conversion Reaction: An Operando X-ray Absorption Spectroscopy Investigation of $NiSb_2$, a Negative Electrode Material for Li-Ion Batteries. *J. Phys. Chem. C* **118**, 27772–27780 (2014).

42. Bak, S.-M., Shadike, Z., Lin, R., Yu, X. & Yang, X.-Q. In situ/operando synchrotron-based X-ray techniques for lithium-ion battery research. *NPG Asia Mater.* **10**, 563–580 (2018).

43. Darwiche, A. *et al.* Operando X-ray absorption spectroscopy applied to battery materials at ICGM: The challenging case of BiSb's sodiation. *Energy Storage Mater.* **21**, 1–13 (2019).

44. Nguyen, L. H. B. *et al.* A Combined Operando Synchrotron X-ray Absorption Spectroscopy and First-Principles Density Functional Theory Study to Unravel the Vanadium Redox Paradox in the $Na_3V_2(PO_4)_2F_3$─$Na_3V_2(PO_4)_2FO_2$ Compositions. *J. Phys. Chem. C* **124**, 23511–23522 (2020).

45. Brennhagen, A. *et al.* Understanding the (De)Sodiation Mechanisms in Na-Based Batteries through Operando X-Ray Methods. *Batter. Supercaps* **4**, 1039–1063 (2021).

46. Fehse, M. *et al.* Applying chemometrics to study battery materials: Towards the comprehensive analysis of complex operando datasets. *Energy Storage Mater.* **18**, 328–337 (2019).

47. Goubard, N. Nouveaux oxydes pseudocapacitifs pour supercondensateurs aqueux à forte densité d'énergie volumique. (2016).

48. Briois, V. *et al.* ROCK: the new Quick-EXAFS beamline at SOLEIL. *J. Phys.: Conf. Ser.* **712**, 012149 (2016).

49. Khyzhun, O. Yu. XPS, XES and XAS studies of the electronic structure of tungsten oxides. *J. Alloys Compd* **305**, 1–6 (2000).

50. Pauporté, T., Soldo-Olivier, Y. & Faure, R. In situ X-ray absorption spectroscopy study of lithium insertion into sputtered WO3 thin films. *J. Electroanal. Chem.* **562**, 111–116 (2004).

General Conclusion and Perspectives

Conclusions

This thesis aimed to investigate different multicationic tungsten-based oxides, to study how the synthesis conditions will impact the desired phase, to fully characterize and to elucidate the crystal structure, and more importantly, to explore their use as potential electrode materials for fast energy storage devices. Furthermore, powerful non-conventional characterization techniques were used to unravel their charge storage mechanism in aqueous electrolytes.

The first material explored was iron tungsten oxide in its form of Fe_2WO_6 synthesized for the first time by a low-temperature polyol mediated route, in addition to the classic high-temperature ceramic synthesis. Different annealing temperatures were applied to the as-synthesized powder, which initially resulted in an amorphous phase. The best electrochemical performance was obtained for the sample annealed at 600 °C (FWO-600) as a negative electrode in an electrochemical capacitor using aqueous 5M LiNO3 as the electrolyte. A specific and volumetric capacitance of 38 F.g−1 and 240 F.cm−3 were obtained when cycled at 2 mV.s−1, respectively. Moreover, a quasi-rectangular shape corresponding to a pseudocapacitive behavior was depicted. This sample was characterized ex situ to understand such an interesting behavior at long-term stability (up to 10,000 cycles at 20 mV.s−1), which is not very common for supercapacitors oxide materials. All the experiments performed demonstrated that the morphology, crystallographic structure, and magnetic properties were not affected by the electrochemical cycling nor simple prolonged soaking in the electrolyte. No partial dissolution at the surface of the particles nor Fe^{2+} formation could be detected. Thus, we confirmed the relatively good stability of the material.

Moreover, an interesting crystallographic study of the high-temperature form of the Fe_2WO_6 powder was performed. We found an incommensurately modulated structure providing an additional understanding of the crystal structure of A_2BO_6-type polycrystalline compounds, which may be beneficial for future research to determine the structure-property relationship of analogous compounds. In conclusion, Fe_2WO_6 material represents an option of a multicationic oxide exhibiting exciting pseudocapacitive performance in terms of density, volumetric capacitance, and long-term cycling behavior.

The second part of this thesis was related to the study of the hexagonal tungsten bronzes (HTBs) A_xWO_3 (with A= Li, Na, and K and $0<x<0.33$. The size of the alkali cation explains the growth of the particles in nanorods/nanowires like morphology in hydrothermal synthesis conditions. The larger the cation, i.e., K^+, the thinner the wires will be. On the other hand, the smaller the cation, i.e., Li^+, the broader and spiky the rods will be. In the case of Na^+, the particles acquired much higher uniformity, as was shown in both SEM and TEM images.

Nonetheless, Li and Na HTB present the same SSA when compared to K HTB. Additionally, the Rietveld refinement and the chemical and thermal analysis studies revealed the general formulas: $Li_{0.167}WO_{3.083}(H_2O)_{0.25}$, $Na_{0.278}WO_{3.139}(H_2O)_{0.083}$, and $K_{0.33}WO_3$, for the Li, Na, and K compounds, respectively. Moreover, a new model of the atomic arrangement along the c axis was proposed for the Na HTB. Such a model, different from the already published one, is consistent in terms of Na-Na, Na-O, and O-O distances and presents a good agreement with the Na amount determined by EDX analysis. Contrary to Li and Na HTBs, the $K_{0.33}WO_3$ compound presents a doubled c parameter, and W atoms with an oxidation state of 5.67^+, resulting in more distorted WO_6 octahedra.

There is a strong relationship between the structure of the HTBs and electrochemical performance. Both Li and Na compounds exhibited similar structural features as well as very similar electrochemical signatures. They showed a faradaic CV shape with clear redox peaks indicating the intercalation of Li^+ into the structure. The capacity values obtained for such phases were 71 and 63 $C.g^{-1}$, respectively. On the other hand, K HTB resulted in a quasi-rectangular shape attributed to a capacitive behavior of 29.5 $C.g^{-1}$. Moreover, the critical ratio of H_2O/Li^+ was put on evidence when both Li and Na HTBs were tested in different concentrations of $LiNO_3$ and water-in-salt electrolyte.

Furthermore, a kinetic study deconvoluting the main charge contributions was carried out to better understand the charge storage mechanism. We found that both capacitive and diffusion controlled predominate the charge storage. However, it should not be taken lightly since the capacitive adds pseudocapacitive participation, which involves a charge transfer non-limited by diffusion. Moreover, the shape of the cyclic voltammograms for Li and Na HTBs indicated a faradaic response plus a possible pseudocapacitive one. On the other hand, K HTB only reflects a possible capacitive mechanism.

EQCM analysis put on shreds of evidence that Li^+ are being intercalated accompanied by 0.50 and about 1.06 moles of water for Li and Na HTBs, respectively. This agrees with the

possible desolvation process taking place at the electrode/electrolyte interface to make it easier for the Li^+ to go inside the lattice. In addition, in situ X-ray diffraction studies confirmed Li^+ cations can go inside the structure from the c direction for Li and Na HTBs. On the other hand, for K HTB, no intercalation mechanism was confirmed as the quasi-rectangular CV shape indicated.

Finally, synchrotron operando XAS analyses were performed on the HTBs. With such a powerful technique, we confirmed the changes in the oxidation state of tungsten attributed to the shift in energy, in eV, upon electrochemical cycling. Even though the shifts in energy are small, PCA confirmed the main components necessary to explain the XANES spectra. These components are attributed to a more oxidized species and a more reduced one. This confirms that when Li^+ gets into the lattice, W cations are reduced, and W gets re-oxidized when Li^+ goes out. Thanks to PCA, these changes can be visible, taking into account that the electrochemical cycling is taking only 10 min, charge/discharge included, times much faster than a standard battery-like- material and a bit slower compared to a standard battery-like- to a pseudocapacitive material.

In conclusion, we showed a complete study in solid-state chemistry combined with electrochemistry in this thesis. We used conventional and not conventional characterization techniques to shed light on the charge storage mechanism of multicationic tungsten-based oxides as electrode materials for electrochemical capacitors or high-rate batteries.

Perspectives

The hexagonal tungsten bronzes showed exciting structural and electrochemical properties. We observed the growth of the nanorods-like particles along the c direction, where the intercalation of Li+ takes place, proved by in situ XRD and *operando* XAS. In order to decrease the diffusion length for the cation intercalation, ball milling could be executed to break nanorods and evaluate if the electrochemical performance would improve. Hard ball milling and soft ball milling could be tested to evaluate the degree of particle break.

We performed the EQCM study in collaboration with Toulouse's group. We carried out several experiments in our lab, adjusting the adequate setup and calibration parameters to obtain reliable results. Unfortunately, we failed, and opportunely we sent the samples to the

CIRIMAT. EQCM is an exciting technique for studying the electrode/electrolyte interfaces in aqueous electrolytes. It would be beneficial for our group to keep developing this setup.

Similarly, we were able to perform in situ XRD in an organic electrolyte setup. We could design a specific in situ electrochemical cell to experiment with water-based electrolytes from a future perspective. Moreover, to follow the rapid evolution of the possible changes in the active material, synchrotron operando XRD could be performed.

DOCTORAT MATIERE BRETAGNE MOLECULES LOIRE ET MATERIAUX

UNIVERSITÉ DE NANTES

Titre : Oxydes multicationiques à base de tungstène comme matériaux d'électrode pour les dispositifs de stockage d'énergie à haute puissance.

Mots clés : condensateurs électrochimiques, oxydes pseudocapacitifs, tungstate de fer, bronze de tungstène hexagonal, *in situ*, *operando*

Résumé : Les condensateurs électrochimiques sont des dispositifs de stockage de l'énergie caractérisés par une capacité de puissance élevée. Leurs performances dépendent principalement des propriétés physico-chimiques et de la structure cristallographique de leurs matériaux d'électrode. Un fort intérêt pour les matériaux à base d'oxydes présentant un comportement pseudo-capacitif a récemment émergé en raison de leur densité d'énergie potentiellement plus élevée que les matériaux à base de carbone activé utilisés dans les dispositifs commerciaux.
De plus, il est nécessaire de rapprocher les performances entre les condensateurs électrochimiques et les batteries afin d'obtenir des dispositifs possédant à la fois des densités de puissance et d'énergie élevées.
Cette thèse visait à étudier différents oxydes multicationiques à base de tungstène en tant que potentiels matériaux d'électrode négative pour des dispositifs de stockage d'énergie rapides, tels que Fe_2WO_6 et des bronzes de tungstène hexagonaux, A_xWO_3 ($A = Li^+$, Na^+ et K^+).
Leur synthèse, leur caractérisation structurale et leurs propriétés électrochimiques ont été étudiées, en utilisant des techniques originales telles que l'EQCM ou du XAS en conditions *operando* afin de mieux comprendre les mécanismes de stockage de charges se produisant dans ces composés, combinant des concepts de chimie du solide et d'électrochimie.

Title: Multicationic tungsten-based oxides as electrode materials for fast energy storage devices.

Keywords: electrochemical capacitors, pseudocapacitive oxides, iron tungstate, hexagonal tungsten bronze, *in-situ*, *operando*

Abstract: Electrochemical capacitors are energy storage devices characterized by a high power ability. Their performance depends mainly on the physical, chemical properties and crystallographic structure of their electrode materials. The interest in oxide-based materials exhibiting a pseudocapacitive behavior has recently increased due to their possible high energy density compared to standard carbon-based materials used in commercial devices. Additionally, the gap between electrochemical capacitors and batteries needs to be reduced in order to reach high-rate devices delivering both high power and energy densities.
This thesis aimed to investigate different multicationic tungsten-based oxides as potential electrode materials for fast energy storage devices, such as Fe_2WO_6 and hexagonal tungsten bronzes, A_xWO_3 ($A=Li^+$, Na^+ and K^+).
Their synthesis, structural characterization and electrochemical properties were investigated, using original techniques such as EQCM and synchrotron operando XAS in order to fully understand the charge storage mechanism occurring in these compounds, combining solid state chemistry and electrochemistry concepts.